Magnetocaloric properties of $La(Fe,Si)_{13}$ compounds

Edmund Lovell

Ph.D. Thesis

Department of Physics, Imperial College London

Abstract

$La(Fe,Si)_{13}$-based compounds are extremely promising for use in magnetocaloric cooling applications. This thesis aims to address multiple challenges to their use in cooling systems, as well as contribute to the fundamental understanding of their first-order magnetic phase transition. A significant field rate dependence in the field-induced paramagnetic (PM) to ferromagnetic (FM) transition in the first-order composition is determined to be a result of non-isothermal conditions from the inherent heating or cooling from the magnetocaloric effect (MCE). Reduction of the magnetic hysteresis has been shown with improved thermal linkage with the thermal bath. Metastability between the phases is demonstrated by magnetic temporal evolution (relaxation). The completion of this evolution is arrested by physical cracks and the sample shape (demagnetising field effects). The onset of the transition is shown to be dominated by the demagnetising fields, and as such a method to reduce magnetic hysteresis via sample shape is demonstrated. These effects are shown to not dominate for samples which show a second-order transition.

Mn substitution on the Fe site decreases the strength of the first-order character which is correlated with the relaxation rate, the latent heat decrease and the heat capacity peak increase. Similar correlations are observed with increasing temperature and both the relaxation rate and latent heat go to zero at the critical point, defined by the temperature at which the first-order character (latent heat and hysteresis) disappears.

The electronic and spin wave contributions to the low temperature heat capacity are investigated and significant enhancement of the former is shown. This is further enhanced with increased Mn-doping but to a much lesser extent when interstitial hydrogen is introduced to the compound. Suppression of this further enhancement in magnetic field suggest that there are two enhancement mechanisms: a base enhancement likely from electron-phonon interactions, and a second which is magnetic in origin.

Declaration of Originality

I declare that the contents of this thesis are my own work and contain no material which has been previously published or written by another person, or substantial proportions of material which have been accepted for the award of any other degree or diploma at Imperial College London or any other educational institution, except where acknowledged. All figures and data reproduced from the published work of other persons are explicitly referenced as citations and, where necessary, the appropriate copyright and intellectual property permissions have been obtained and stated as such. All contributions to this thesis which have been carried out by others, with whom I have worked at Imperial College or other institutions, have been clearly acknowledged as such. The intellectual content of this thesis is the product of my own work, except where assistance from others in the project's conception, design and vital discussions, leading to its claims and conclusions, in addition to assistance to the presentation and style of the thesis, has been acknowledged.

Copyright Declaration

The copyright of this thesis rests with the author and is made available under a Creative Commons Attribution Non-Commercial No Derivatives licence. Researchers are free to copy, distribute or transmit the thesis on the condition that they attribute it, that they do not use it for commercial purposes and that they do not alter, transform or build upon it. For any reuse or redistribution, researchers must make clear to others the licence terms of this work.

Acknowledgements

My time at Imperial College and in London, during my Ph.D., has been highly enjoyable and has taught me an awful lot. Many people have contributed to the research I have conducted during this time, as well as to my training and development as a researcher and to making the four years I have spent here brilliant, and I would like to acknowledge these people for being instrumental to the progress and completion of my thesis.

Firstly, I would like to give a huge thank you to my supervisor, Prof. Lesley Cohen, who has given me the opportunity to carry out this Ph.D., has helped and supported me throughout the time I have spent as her student, has not been afraid to push me when needed, has unfailingly checked through my thesis drafts and article manuscripts, and has contributed enormously to all of my results, findings and publications. Secondly, to my supervisor, Prof. David Caplin, your support, ideas, suggestions, discussions, checking of my work and general company around the department have enabled me to reach this stage, for which I am eternally grateful. A huge thank you is given to Kelly Morrison and André Pereira, who were of invaluable help during the start of my Ph.D. and made sure I was able to stand on my own two feet before they left for pastures new. Much of their input during this time has had a very important effect on the direction of my research, and their support and scientific discussions, after leaving, have greatly aided me at all points since. Milan Bratko, Mikhail Kustov, Jérémy Turcaud and Garry Perkins have been calming presences in the lab and have directly influenced, via lab-work and vital discussions, many of my results. Thanks particularly to Milan, whose incredible microcalorimetry data and analysis are used in this thesis.

Thank you, of course, to Oliver, Chris and Jack for making H702 the greatest office there has ever been, and help in the lab (of secondary importance). No doubt we will spend many a time in the future having beers and recreating the good times! I extend a warm thank you to Katharina, Daan, Elysia, Luiz, Rob, Dom, Jan, Zsolt, Adam, Stephanie, Will and Karl, who have been of great help in the lab and excellent company at lunch, tea breaks and for pints

after work. I would also like to give thanks to Julia Lyubina, Luis Ghivelder and Vittorio Basso, who have directly contributed to the results in this thesis, for their kind help, excellent insight and vital discussions of the physics. I also acknowledge EPSRC for the funding grant EP/G060940/1 which has allowed me to undertake this project, in addition to the European Community's 7^{th} Framework Programme under Grant agreement 310748 'DRREAM'.

Thank you to Vikesh Mistry and Daan Arroo for kindly and meticulously proofreading the thesis, correcting my many errors and giving vital comments, including some controversial suggestions for this acknowledgement page (suggestions ignored). I also am at the behest of the housemates I have had during my Ph.D., Duncan, George, Vikesh, Tom, Jane Thu, Chris and Ahmed, who have all supported but, most importantly, kept me entertained at home and around London throughout my Ph.D. My parents and siblings have been of great support, as ever, with some even appearing at Imperial from time to time for an impromptu and very welcome catch up with food and beer. Lastly, I would like to thank Becca, who has given me her unconditional support and advice throughout, who has always made me smile, and who has made reaching the end of my Ph.D. so much easier.

Contents

List of Figures **9**

List of Tables **13**

1 Introduction and Physical Concepts **14**

1.1 Introduction and motivation 14

1.2 The magnetocaloric effect 16

1.2.1 The magnetic phase transition 19

1.2.2 The Maxwell and Clausius-Clapeyron relations 25

1.2.3 The active magnetic regenerator cycle and engineering details 28

1.2.4 Materials summary 29

1.2.5 Comparison with other caloric phenomena 31

1.2.6 A note about units 32

1.3 First-order phase transitions 33

1.3.1 Definition and properties 33

1.3.2 Nucleation and growth 36

1.4 Models 37

1.4.1 Itinerant electron metamagnetism 38

2 The La(Fe,Si)$_{13}$ System and Review of Relevant Literature 40

2.1 La(Fe,Si)$_{13}$ . . . 41

2.1.1 Structure and phase . . . 41

2.1.2 The magnetic phase transition . . . 41

2.1.3 Hysteresis . . . 46

2.1.4 Pressure, specific heat and latent heat . . . 48

2.1.5 Doping and interstitials . . . 49

2.1.6 Technological relevance of measurements on compositions far from room temperature . . . 52

2.2 Dynamics . . . 53

2.2.1 Rate dependence of the first-order transition . . . 53

2.2.2 High operating frequencies . . . 56

2.2.3 Relaxation across the phase transition . . . 57

2.3 Role of demagnetising fields . . . 60

2.3.1 Second-order systems . . . 62

2.3.2 First-order systems . . . 63

2.4 Heat capacity . . . 65

2.4.1 The low temperature limit . . . 65

2.4.2 Sommerfeld coefficient enhancement . . . 67

3 Experimental Methods 69

3.1 Sample preparation . . . 69

3.2 Regarding sample shape choice . . . 71

3.3 Vibrating Sample Magnetometry . . . 72

3.4 Scanning Hall probe imaging . . . 74

3.4.1 Hall probe sensors . . . 74

3.4.2 Imaging specifics . . . 76

3.4.3 Out-of-plane and in-plane imaging 78
3.4.4 Choice of sample shape and surface fly height 80
3.4.5 Other technical details 81
3.4.6 Local loops and dynamic Hall probe imaging 82
3.5 Heat Capacity 82
3.5.1 Two-tau model 84
3.5.2 Slope difference method 86
3.6 Microcalorimetry 88
3.7 X-ray diffraction 88

4 Dynamics and Magnetostatics of the Metamagnetic Transition in $La(Fe,Si)_{13}$ 89

4.1 The metamagnetic transition and entropy change 90
4.2 Dynamics: field-rate dependence 93
4.3 Dynamics: relaxation rate 96
4.4 Dynamics: field-driven transition rate 101
4.5 Influence of sample connectivity on magnetisation dynamics 105
4.5.1 Sample connectivity scenarios 105
4.5.2 Magnetic relaxation 107
4.5.3 Driving field rate dependence 111
4.6 Statics: role of demagnetising fields 114
4.6.1 Scanning Hall probe analysis of the shape dependence 116
4.6.2 The second-order phase transition 125
4.7 Summary 129

5 Temperature Dependence of $La(Fe,Si)_{13}$ and First-Order Character of the $La(Fe,Mn,Si)_{13}$ Series 131

5.1 Temperature dependence of the first-order transition 132

5.2 Temperature dependence of the relaxation feature 136
5.3 Role of manganese doping on the transition 143
5.3.1 Hysteresis and T_{crit} 146
5.3.2 dH_{c}/dT and Clausius-Clapeyron analysis 149
5.4 Role of composition on the relaxation dynamics 153
5.4.1 Magnetic relaxation 153
5.4.2 Comparison with specific heat and latent heat 159
5.5 Summary 163

6 Low Temperature Specific Heat of the La(Fe,Mn,Si)$_{13}$ Series 165

6.1 Summary of the La(Fe,Mn,Si)$_{13}$(-H) sample series 166
6.2 Specific heat of the metamagnetic transition 166
6.3 Extraction of the contributions to low temperature specific heat 170
6.3.1 The electron contribution: Sommerfeld coefficient 175
6.3.2 The phonon contribution: Debye temperature 179
6.3.3 The spin wave contribution 180
6.4 Magnetic field dependence of the specific heat contributions 182
6.5 Summary 185

7 Conclusions and Future Work 188

7.1 Summary of Results 188
7.2 Future Work 190
7.2.1 Study of sample shape benefits in a working cycle context 191
7.2.2 Multicaloric combinations 192
7.2.3 Further understanding of the enhanced Sommerfeld coefficient and implication on the MCE 193
7.3 Publications of work conducted during Ph.D. 194

Bibliography **196**

A Acronyms and Abbreviations **213**

B Hall Sensor Fabrication and Characterisation **214**

B.1 InSb/GaAs epilayer characterisation 214

B.2 Sensor fabrication 216

B.2.1 Diamond-tip scribing 216

B.2.2 Focused Ion Beam lithography 217

B.2.3 Sensor mounting 219

C Copyright Permissions **220**

List of Figures

1.1 The magnetocaloric cooling cycle 18

1.2 $S(T)$ of the MCE 20

1.3 The field driven magnetic phase transition 22

1.4 ΔS and ΔT_{ad} for first and second-order phase transitions 24

1.5 $S(T)$ of the MCE in hysteretic systems 25

1.6 The free energy landscape of the first-order transition 35

2.1 $LaFe_{13-x}Si_x$ structure 42

2.2 $LaFe_{13-x}Si_x$ $H-T$ phase diagram 43

2.3 $\Delta S_{\mathrm{m}}(T)$ and $\Delta T_{\mathrm{ad}}(T)$ of $LaFe_{13-x}Si_x$ 45

2.4 The Kuz'min and Richter energy diagram 46

2.5 $M(T)$ and $M(H)$ of the transition 47

2.6 Heat capacity, latent heat and magnetostriction of $LaFe_{11.6}Si_{1.4}$ 49

2.7 T_{C} and T_{crit} evolution with interstitial hydrogen 51

2.8 Field rate dependence of $LaFe_{11.71}Co_{0.19}Si_{1.11}$ 54

2.9 Isothermal and adiabatic $M(H)$ and ΔT_{ad} 57

2.10 Magnetic relaxation of $La(Fe_{0.88}Si_{0.12})_{13}$ 61

2.11 Spatial evolution of the local magnetisation at the transition 64

2.12 Seebeck measurements of the $La(Fe_{0.88}Si_{0.12})_{13}$ transition 66

3.1 VSM schematic 73

3.2 Hall probe sensor schematic 75

3.3 Scanning Hall probe imaging system 77

3.4 Direction of magnetisation and the stray field response 79

3.5 Hall sensor calibration curve 80

3.6 Heat capacity measurement platform 83

3.7 Two-tau measurement schematic 85

3.8 Heat capacity T relaxation curves at a first-order transition 86

4.1 $M(H)$ and phase lines of $LaFe_{13-x}Si_x$ with $x = 1.4$ and $x = 1.6$ 92

4.2 Entropy change of $LaFe_{13-x}Si_x$ with $x = 1.4$ and $x = 1.6$ 93

4.3 Field rate dependence of $LaFe_{11.6}Si_{1.4}$ 94

4.4 Field rate dependence of the second-order transition 95

4.5 Schematic of the $LaFe_{11.6}Si_{1.4}$ sample 97

4.6 Magnetic relaxation across the phase transition 97

4.7 Rate of relaxation with H_{pause} 99

4.8 Magnetic relaxation of $LaFe_{11.4}Si_{1.6}$ 100

4.9 Field driven transition rate of $LaFe_{11.6}Si_{1.4}$ 102

4.10 The transition rate vs the field driving rate 104

4.11 Schematics of four sample connectivity scenarios 106

4.12 Magnetic relaxation in each scenario 108

4.13 Field rate and scenario dependence of $M(H)$ 110

4.14 Hysteresis width and transition completion time with driving field rate 113

4.15 Field line schematic of the shape dependence 116

4.16 Field direction sample dependence of the transition I 117

4.17 Scanning Hall probe imaging of the $LaFe_{11.6}Si_{1.4}$, out-of-plane first-order transition . . . 120

4.18 Local Hall probe loops of the $LaFe_{11.6}Si_{1.4}$, out-of-plane first-order transition . 121

4.19 Schematic of the in-plane first-order transition . . . 122

4.20 Scanning Hall probe imaging of the $LaFe_{11.6}Si_{1.4}$, in-plane first-order transition 123

4.21 Hall probe line-scans of the $LaFe_{11.6}Si_{1.4}$, in-plane first-order transition . . . 124

4.22 Field direction sample dependence of the transition II . . . 124

4.23 Scanning Hall probe imaging of the $LaFe_{11.6}Si_{1.4}$, out-of-plane second-order transition . . . 126

4.24 Local Hall probe loops of the $LaFe_{11.6}Si_{1.4}$, out-of-plane second-order transition 127

4.25 Scanning Hall probe imaging of the $LaFe_{11.4}Si_{1.6}$, out-of-plane second-order transition . . . 128

5.1 $H-T$ phase line of $LaFe_{11.6}Si_{1.4}$ with T_{crit} . . . 133

5.2 T and field rate dependence of $M(H)$ . . . 134

5.3 T and field rate dependence of the hysteresis . . . 134

5.4 Intrinsic hysteresis extraction . . . 135

5.5 Extrinsic and intrinsic contributions to the hysteresis . . . 137

5.6 T-dependence of the magnetic relaxation . . . 139

5.7 T-dependence of the magnetic relaxation rate . . . 140

5.8 T-dependence of relaxation rate and latent heat . . . 141

5.9 $M(H)$ of the $La(Fe,Mn,Si)_{13}$ series . . . 145

5.10 $H-T$ phase lines and hysteresis of the $La(Fe,Mn,Si)_{13}$ series . . . 147

5.11 T_C and T_{crit} of the $La(Fe,Mn,Si)_{13}$(-H) series . . . 149

5.12 dH_c/dT of the $La(Fe,Mn,Si)_{13}$ series . . . 150

5.13 Maxwell and Clausius-Clapeyron analysis of the entropy change . . . 152

5.14 $M(H)$ of three selected $La(Fe,Mn,Si)_{13}$ compositions . . . 155

5.15 Magnetic relaxation of $LaFe_{13-x-y}Mn_xSi_y$ with $x = 0.18$ . . . 156

5.16 T and composition dependence of magnetic relaxation 157

5.17 T and composition dependence of the magnetic relaxation rate and ΔM . . . 159

5.18 C_p and latent heat microcalorimetry of the transition 161

5.19 Comparison of specific heat and latent heat 162

6.1 $M(T)$ of the La(Fe,Mn,Si)$_{13}$ compositions 167

6.2 Specific heat across a full T range 169

6.3 Specific heat of fully hydrogenated La(Fe,Mn,Si)$_{13}$-H 169

6.4 Contributions to low temperature specific heat I 171

6.5 Contributions to low temperature specific heat II 172

6.6 Low T c_p of the La(Fe,Mn,Si)$_{13}$(-H) composition set 174

6.7 Low T c_p of $LaFe_{13-x}Si_x$ with $x = 1.2$ and 1.6 176

6.8 The Sommerfeld coefficient 177

6.9 The Debye temperature 180

6.10 The spin wave component and stiffness 181

6.11 H-dependence of the low temperature c_p 183

6.12 H-dependence of γ, θ_{D}, α and D 184

6.13 H-dependence for $LaFe_{13-x}Si_x$ with $x = 1.2$ and 1.6 186

B.1 The van der Pauw measurement geometry 215

B.2 n and μ of the InSb films 216

B.3 FIB fabrication of Hall probe sensors 218

B.4 Sensor mount board schematic 219

List of Tables

1.1 MCE material summary 30

5.1 Composition and T_C of the La(Fe,Mn,Si)$_{13}$ compounds 144

6.1 Summary of non-hydrogenated and hydrogenated La(Fe,Mn,Si)$_{13}$ compounds 167

1 | Introduction and Physical Concepts

In this chapter, I introduce the magnetocaloric effect (MCE) and the motivations for carrying out the thesis work as well as providing a short summary of each of the following chapters. The MCE is then described in detail, beginning more generally with magnetic phase transitions, followed by a summary of the Maxwell and Clausius-Clapeyron relations widely used to calculate the magnitude of MCE within materials. Following this I introduce the cooling cycle, summarise the materials which exhibit MCE and also introduce some of the other caloric phenomena which are state-of-the-art. The second half of this chapter introduces concepts related to first-order phase transitions and summarises several models used, in particular the itinerant electron metamagnetism model specific to the compounds I have investigated here.

1.1 Introduction and motivation

This thesis presents, analyses and discusses many experimental results on $La(Fe,Si)_{13}$, within the field of the magnetocaloric effect (MCE) and its applications. The material has been much investigated over the last two decades and, along with one or two other material families, it is hoped that it will contribute to the solid-state element in a future technological cooling system.

The reason for the interest in the $La(Fe,Si)_{13}$ material stems from the significant magnitude of MCE it permits, with the ability to engineer a set of materials with a cascaded set of transition temperatures in order to produce high MCE performance over the application relevant range of temperatures (close to room temperature), using cheap and widely available constituent elements. Of particular promise are the small magnetic and thermal hysteresis, which allows its large entropy changes across the paramagnetic (PM) to ferromagnetic (FM) metamagnetic phase transition to be accessed without considerable, detrimental hysteretic energy losses. This is important for reducing the amount of rare-earth based permanent magnets used, which if the technology is able to become commercially competitive, will have considerable global impacts on the extraction of the expensive and rare elements required.

The majority of measurements in this thesis measures either the magnetic properties or heat capacity. The experimental methods are outlined in Chapter 3.

The motivation for this research is to extend the understanding of the magnetocaloric properties via studies of the physics of the magnetic phase transition, in particular concerning the nucleation and growth processes of the transition.

Field rate and sample size dependences reduce the advantage of large MCE and small hysteresis. This is relevant, since to be able to compete with existing cooling technologies, substantial mass of refrigerant (i.e. the MCE material) and high cooling pump cycling frequencies are required. In Chapter 4, I set out the main components associated with extrinsic hysteresis, much of which originates from dynamic processes, and clarify confusion existing in the literature regarding the cause of this extrinsic hysteresis by distinguishing between the fast and slow field rate regimes. Additionally, I propose a technique to further reduce the isothermal hysteresis based on engineering of the shape of the refrigerant in order to take advantage of the dependence of the nucleation sites on the shape as recently determined in the literature, and demonstrate how this is relevant for first-order but not second-order transitions in this system.

Most of the materials studied in this thesis show first order behaviour, and a considerable focus is placed on its form and evolution within this material in response to external parameters. This is a feature of Chapter 4 but has particular importance in Chapter 5, where relaxation growth dynamics, hysteresis and latent heat are discussed in terms of indications of first-order strength. In particular, the dependences of the relaxation growth and both extrinsic and intrinsic contributions to hysteresis (including their distinction), in the field-induced transition, are investigated as a function of temperature, in order to elucidate the dominating mechanisms at play, which have been discussion points in the literature. In addition, the evolution of the first-order character with composition is investigated with a series of Mn-doped compounds.

In Chapter 6, the focus moves to examine the behaviour of low temperature specific heat of this material as a function of composition and applied magnetic field. In particular, the Sommerfeld coefficient, Debye temperature and spin wave stiffness are examined across the series of Mn-doped compounds which, beyond several theoretical studies, have not been looked at in detail experimentally in this system. Comparisons with recent theoretical results on the compound in the literature are made.

1.2 The magnetocaloric effect

The worldwide energy use of cooling applications is continuously on the rise, for both domestic and industrial use. It is expected to overtake the energy expended on heating within decades and continue rising [1]. As a result, there is a pressing demand for refrigeration methods which are more efficient and environmentally friendly than the gas expansion and compression method overwhelmingly used in refrigeration systems worldwide. The latter is currently unsurpassed with regards to both cooling capability and cost-effectiveness, but unattractive because of the use of hydrofluorocarbons, a known greenhouse gas. One potential solution is to harness the magnetocaloric effect (MCE) in which the entropy changes of solid-state

magnetic materials can be used to remove heat from a system: so-called solid-state magnetic refrigeration.

The magnetocaloric effect can be described simply as the process of a material having an associated temperature change in response to a magnetic field [2]. This is not a new concept: adiabatic magnetic cooling is a technique used for decades employing paramagnetic salts to achieve milliKelvin temperatures. In this technique, the paramagnetic ordering of the electron spins, in response to an applied magnetic field, leads to a lowering of a system's magnetic entropy. This must result in the increase of a separate contribution to the overall entropy, namely the lattice contribution, which causes the material to heat [3]. Subsequent removal of the field results in cooling, in a reverse effect, and therefore a cycle with an appropriate heat-transfer method can allow cooling of a system, as shown in Figure 1.1. This technique previously has been only viable temperatures approaching absolute zero [4] due to the very small temperature and entropy changes involved.

Interest in the possibility of utilising this effect at room temperature was greatly magnified by the discovery of materials which show considerable temperature changes in response to magnetic field, such as Gd, which undergoes a conventional second-order transition at the Curie temperature which is close to room temperature, and many since reported systems usually with sudden magnetisation, M, and entropy, S, changes at a magnetic phase transition. Pecharsky and Gschneidner, in 1997, measured a huge magnetic entropy change, with a large associated adiabatic temperature change ($\Delta T_{\mathrm{ad}} \sim 15$ K), in the compound $Gd_5Si_2Ge_2$, when driven by magnetic field from $\mu_0 H = 0$ to 5 T between two magnetic phases [5]. This change in magnetic phase occurred simultaneously with a change in crystal structure (a magnetostructural transition). Similar effects have since been observed in a wide variety of materials, all associated with a magnetic field driven phase change [6, 7], and a search to determine the most ideal materials for magnetic refrigeration has resulted. A summary of some of the most promising materials is given in section 1.2.4.

In addition to the choice of MCE material, some of which contain expensive and rare elements

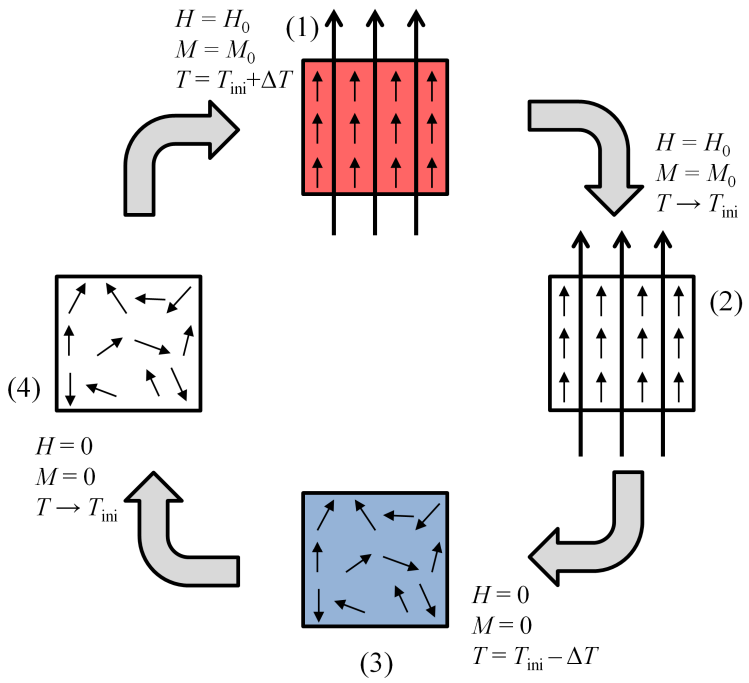


Figure 1.1: The magnetocaloric cooling cycle: (1) The magnetic field is applied, moments align and the material heats by ΔT, (2) The material is cooled back to the initial temperature, T_{ini}, (3) The field is removed, moments disorder and the material cools by ΔT, (4) The material is warmed back to T_{ini} and heat is extracted from the desired thermal mass. The cycle then begins again with (1).

such as gadolinium and rhodium (see Table 1.1), another aspect which has become important is the reduction in the use of neodymium and dysprosium based hard magnets - both rare earth elements which are expensive to obtain. Such magnets allow applied fields of up to $\mu_0 H = 2$ T. In order to achieve a reduction in their use, which will help to make the application of MCE cost-competitive, it is necessary to lower the maximum required field of the MCE material, such that a substantially lower mass of magnet can be used whilst retaining a suitably large field strength over the required distance from magnet to MCE material, or, further still, so that cheap, ferrite-based magnets with maximum fields of smaller than $\mu_0 H = 0.5$ T can be used in their stead [8].

1.2.1 The magnetic phase transition

A magnetic material which has both ordered and disordered magnetic states undergoes a magnetic phase transition between these states in response to temperature, T, and, in specific cases, magnetic field, H, and pressure, p, as well. Often this is between the ordered ferromagnetic (FM) and the disordered paramagnetic (PM) states, for which the transition temperature is known as the Curie temperature, T_{C}. In some cases, order-disorder transitions between other magnetic states are possible, such as the ordered antiferromagnetic (AFM) or ferrimagnetic states to PM, and order-order transitions, particularly AFM to FM.

The entropy of such a magnetic system has three principal contributions: magnetic, electronic and lattice. At a magnetic phase transition, the total entropy change, ΔS, can be written as:

$$\Delta S = \Delta S_{\mathrm{m}} + \Delta S_{\mathrm{elec}} + \Delta S_{\mathrm{latt}} \tag{1.1}$$

Where the last three terms correspond to the magnetic, electronic and lattice entropy changes respectively. In some systems these can be treated as independent terms and therefore to conserve entropy the decrease in one must lead to the increase in one or both of the others, as with the adiabatic cooling in paramagnetic salts described previously. For many magnetocaloric materials [3], this separation is not strictly valid due to interactions between the three contributions. For example, the MCE of 3d metal-based materials whose magnetism is due to non-localised, itinerant electrons, will have the same electrons contributing both magnetically and electrically. Additionally, interactions between the magnetic and lattice degrees of freedom can also be present, as will be discussed in section 2.1.2.

The entropy of a system can be visualised by the schematic in Figure 1.2. For large MCE materials, the $S(T)$ curve is strongly dependent on H and is thus moved significantly for different H, as indicated by a shift in the curve for two different fields, H_1 and H_2. Movement between the curves, or along the curves, can be achieved in several distinct ways: isofield (along one curve), isothermal and adiabatic. The latter two steps define the ΔS_{m} and ΔT_{ad}

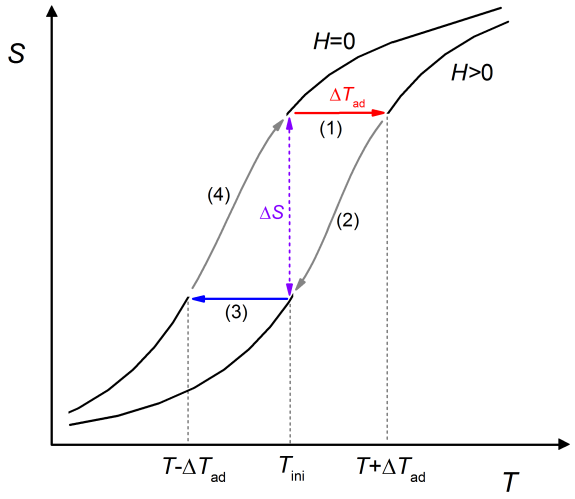


Figure 1.2: A general magnetocaloric cooling cycle in the entropy description. The $S(T)$ curves at zero field and finite, positive field are offset. This allows movement between them via an adiabatic temperature change, ΔT_{ad}, in response to field application or removal, steps (1) and (3) respectively, and isofield steps along the curves to return to the initial temperature, T_{ini}, by cooling and heating in steps (2) and (4) respectively. The latter step extracts the heat from the mass to be cooled.

material-specific properties respectively. Therefore, in general, the greater the gap between the two $S(T)$ curves, the stronger the MCE. The respective magnitudes of ΔS_{m} and ΔT_{ad} will be dependent on the specific shapes and separation of these curves, and this visualisation clearly demonstrates why both are equally important measures of MCE. These phase transitions are also signified by a dramatic increase in the heat capacity at temperatures close to the transition [9].

Phase transitions can be classified into two types: first-order, where there is a discontinuity in the first-derivative of the Gibbs free energy with respect to a state variable, and continuous, where there is not. The latter is often referred to as second-order, which is defined in the Ehrenfest classification as a transition where a discontinuity lies in the second-order derivative [10]. In reality a second-order and continuous transition, where there is no discontinuity in

any derivative, do not exactly refer to the same behaviour. However, the terms are commonly used interchangeably because typically only the first-order derivative is treated, in the case of many phase transitions, in which case second-order and continuous behaviour cannot be discriminated. Throughout this thesis I will refer to continuous phase transitions predominantly as second-order. For further details on the order of phase transitions, see section 1.3.1.

With regards to the MCE, first-order phase transitions are typified by a sharp change in magnetisation, entropy and volume (the latter discussed later) when there is a small change in environment, i.e. applied magnetic field, temperature or pressure. A sharp change of state resulting in large changes of entropy and material temperature, in response to modest changes in external variables, is the reason why first-order materials are so attractive [9]. This is with comparison to a second-order transition where the change in state is gradual and often requires large field or temperature changes. Further signifiers of the first-order transition are the release or absorption of latent heat, and irreversibility in the transition, i.e. hysteresis, which is a disadvantage for application. Irreversibility (and latent heat) do not exist for second-order transitions, where the physical state is always in thermodynamic equilibrium defined by the external environment at all points through and in either direction of the transition.

An example of a typical MCE material's first-order PM to FM transition is given in Figure 1.3. This type of field-driven transition is referred to as metamagnetic, implying the metastability of the two magnetic states at such a temperature that either can be induced with H. A large and discontinuous change of magnetisation transforms the material from its PM phase to FM at a critical field, H_{c}. Ferromagnetism is defined as a spontaneous alignment of spins (i.e. with no external field) leading to a non-zero moment and therefore magnetisation, at least locally. The nature of the metamagnetic transition, in which the magnetically ordered state is induced in large field, means that what has been termed here 'FM' is by definition not ferromagnetism since the ordering is not spontaneous. However, the spin alignment of the state shows the same ordering features locally as the FM state which does manifest below T_{C}, as indeed the $M(T)$ behaviour within large field demonstrates (see section 2.1.3). As a

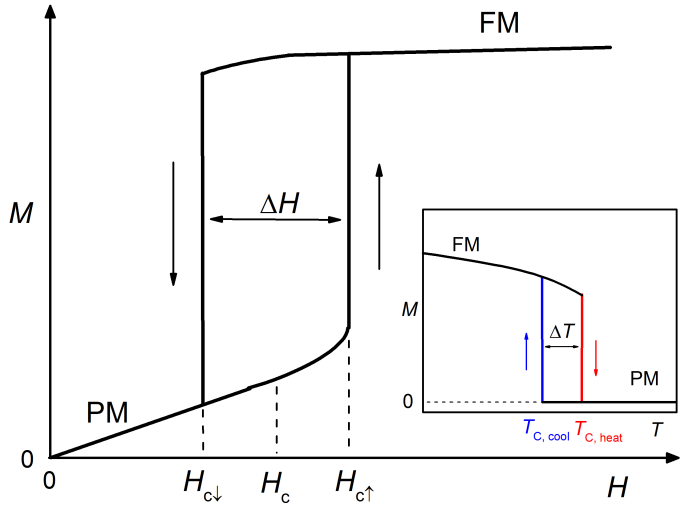


Figure 1.3: A typical field-driven first-order magnetic phase transition from the PM state (low field) to the FM state (high field) as visualised in magnetisation, M, with hysteresis, whose width is defined by ΔH as shown. The critical fields for field increasing and field decreasing are shown, $H_{c\uparrow}$ and $H_{c\downarrow}$ respectively, and H_c is the thermodynamic critical field. Inset: the equivalent transition with T with the respective heating and cooling Curie temperatures, $T_{c,\ heat}$ and $T_{c,\ cool}$, and the resulting hysteresis, ΔT, labelled. In both cases, the arrows show the direction of movement around the hysteresis loops.

result this state is commonly referred to as ferromagnetic in both the fields of magnetic phase transitions [11] and the magnetocaloric effect [5, 9], and will therefore be referred to as such in this thesis.

In the PM phase, the magnetic (i.e. electron spin) moments are disordered and react to increased applied external field by a weak, linear increase in magnetisation, as the moments begin to align with the field. The strength of this linear response is defined as the susceptibility, χ, where $M = \chi H$. Note that this is valid at the low H or low M regime and will saturate if H is sufficiently large enough to align all the moments. The FM state is characterised by the preference for the moments to align with each other. For so-called zero-remanence, or 'soft' FM materials, this magnetic ordering is on the micro-scale when no external field

is applied, causing the material to separate into differently-orientated FM domains with a net magnetisation of zero, (except for the case of nano-scale samples, in which domains may not form and a net magnetisation will exist). However within an external magnetic field the magnetisation of these domains will preferentially align with each other and with the field to give full alignment. This corresponds to the maximum possible magnetisation, defined as the saturation magnetisation, M_s [12]. It is this latter state that the field-induced first-order magnetic phase transition transforms the PM state into via the sudden change in M, as indicated in Figure 1.3, and it is saturated since a finite field is already present. The hysteresis (irreversibility) of the first-order transition emerges on subsequent decreasing of the field, where smaller H is required in order to induce the reverse discontinuous transition and return the material to its initial PM state. This is due to an energy barrier in the free energy description which must be overcome. Mechanisms for its existence will be covered in section 1.3.

For the above scenario to occur, the material must be in the PM state in zero applied field, which in many cases means it must be above T_C, therefore the working temperature of an MCE material typically refers to a range of T immediately above T_C. The T-driven transition in such materials is also discontinuous, and exhibits hysteresis (see the inset to Figure 1.3), in contrast to the conventional loss of magnetic order at T_C for standard FM materials, which is smooth and gradual [12, 13]. How the transition of the system responds to a variety of T and H is material specific; the case for $La(Fe,Si)_{13}$ is covered in section 2.1.2. Typically an increase in H leads to an increase in T_C as the FM phase is stabilised under larger applied fields, and equivalently a further T increase above T_C leads to an increase of H_c in the field-driven metamagnetic transition. The general behaviours of ΔS_m and ΔT_{ad} for first and second-order transitions, over variable H and T ranges, are shown in Figure 1.4.

The modification of the entropy, as shown in Figure 1.2, by hysteresis manifests as separate hysteresis loops for the two entropy curves at each field strength. A simplified schematic of such a situation is shown in Figure 1.5. By driving a system around either of the $S(T)$ curves, the black arrows must be followed. When a change in field is effected and the material is then

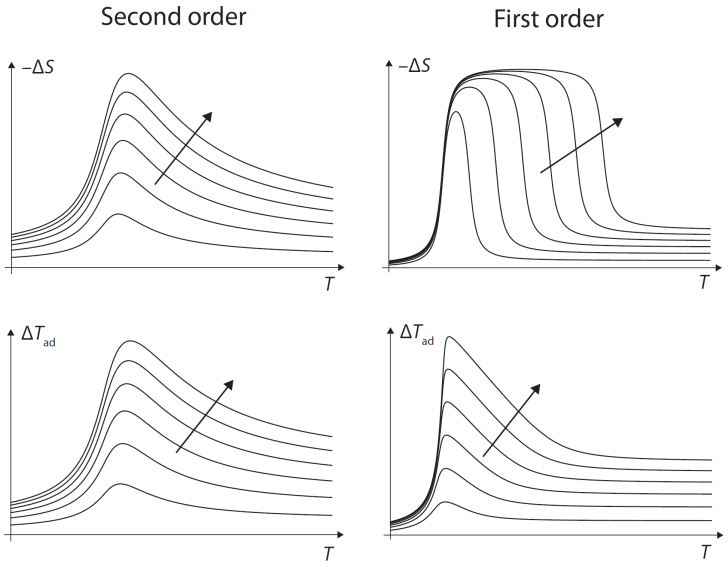


Figure 1.4: Reprinted from Ref. [9], schematics of the typical ΔS and ΔT_{ad} behaviours for second and first-order transitions. The arrows indicate increasing field range. © 2012 WILEY-VCH Verlag GmbH & Co. KGaA, Weinheim.

moved along a new $S(T)$ curve, it must also follow the arrows around the loop, which for an isofield step back to the original T is the branch closer to the initial field $S(T)$. Subsequent cycling then sees the material move around this 'inner' loop, as demonstrated within the shaded region, and the maximum ΔT_{ad} cannot be taken advantage of [14]. For a MCE cycle, this is an energy loss, and therefore a cycling efficiency loss [9, 15], which for an $M(H)$ hysteresis loop is equal to the area enclosed by the loop [16, 17].

One of the principal causes of such a large MCE is magnetostructural, magnetovolume or magnetoelastic changes, which occur in tandem with the magnetic phase change [18, 19, 20]. In the case of materials with magnetostructural coupling, for example, Pecharsky *et al.* [19] have used density functional theory to calculate the free energies and magnetisation of the two structures of $Gd_5Si_2Ge_2$, one monoclinic and the other orthorhombic, separately as a function of T. Each structure becomes magnetically disordered from FM to PM via the conventional second-order transition at their own respective T_{C} values. However, the comparative values of the free energies mean that the orthorhombic structure, which has a higher T_{C}, exists at low temperatures (below its T_{C}) but a crossing of the free energy curves means the monoclinic

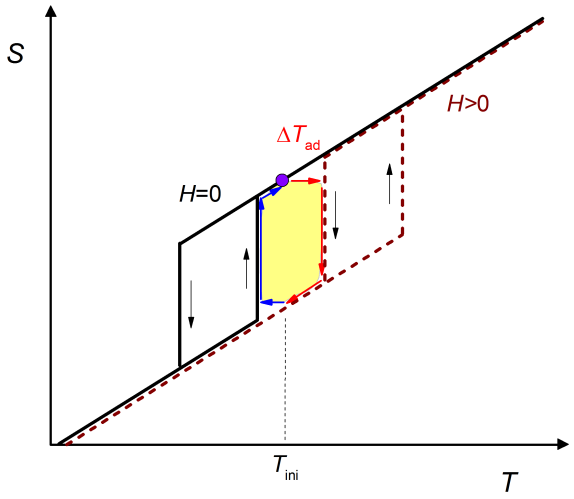


Figure 1.5: Schematic of the impact of hysteresis on the entropy curves. Following Figure 1.2, in two different field strengths (e.g. $H = 0$ and $H > 0$) the effect of hysteresis is to make the system cycle around the shaded region and thus ΔT_{ad} is significantly reduced.

becomes energetically favourable at higher T. Where this occurs is below the T_{C} of the orthorhombic but above that of the monoclinic structures. As a result, the structural change leads to a sudden, discontinuous loss of magnetic order.

In other cases, such as $La(Fe,Si)_{13}$, the change is isostructural, exhibiting a substantial change in volume (and in the separation between local moments) at the transition, with no change in crystal symmetry [6, 21]. For the other highly studied itinerant Fe_2P family, the transition is non-isotropic isostructural, showing magnetoelastic coupling, and often with minor volume change or volume conservation.

1.2.2 The Maxwell and Clausius-Clapeyron relations

The magnetic contribution to the entropy change, ΔS_{m}, can be derived, from the description of free energy of a magnetic system, to give a Maxwell relation. Beginning with the total

internal energy of an infinite, homogeneous system, U, its variation can be written according to the first law of thermodynamics as:

$$dU = TdS - pdV + \mu_0 HdM \tag{1.2}$$

Where T, S, p, V, H and M are the temperature, entropy, pressure, volume, magnetic field and magnetisation respectively. μ_0 is the permeability of free space, $4\pi \times 10^{-7}$ $\mathrm{H\,m^{-1}}$, and relates H to the magnetic flux density, B, by $B = \mu_0 H$.

The Gibbs free energy, G, describing the work a system is able to do, is defined as:

$$G = U - (TS - pV + \mu_0 HM) \tag{1.3}$$

By combining Eqn. 1.2 and 1.3, the change in free energy, dG, can be written as:

$$dG = Vdp - SdT - \mu_0 MdH \tag{1.4}$$

Which is a function of p, T and H. By partially differentiating G with respect to H then T, and separately with respect to T then H (keeping the other parameters constant in each case), using the principal that the quantity $\partial^2 G/\partial T \partial H$ does not depend on the order of differentiation, we arrive at the Maxwell relation:

$$\left(\frac{\partial S}{\partial H}\right)_{T,p} = \mu_0 \left(\frac{\partial M}{\partial T}\right)_{H,p} \tag{1.5}$$

This can be rearranged to give the isothermal ΔS_m between two values of H:

$$\Delta S_\mathrm{m} = \mu_0 \int_{H_\mathrm{i}}^{H_\mathrm{f}} \left(\frac{\partial M}{\partial T}\right)_H dH \tag{1.6}$$

A combination of M measurements in H and T allow the evaluation of entropy change between two fields at a set temperature [9]. This method is used widely and reliably in the magnetocaloric field to study the phase transition. The use of the Maxwell equation assumes

thermodynamic equilibrium, such as the case for continuous phase transitions. However, in the case of first-order phase transitions with irreversibility and associated hysteresis, the equilibrium demand is not necessarily met if the initial thermodynamic state is not the same as the final at the same H and T (for example, by beginning in the PM state but returning only in the FM, or a mixed state of the two). This will lead to subsequent measurements being made from a different initial state, and numerical analysis of such measurements can lead to artificial 'giant' peaks in ΔS_{m} [9, 22, 23, 24]. With comprehension of its failings and careful treatment during measurements, however, the use of Eqn. 1.6 for first-order transitions is appropriate. One example of ensuring this is by making certain the initial state is the same between measurements, which can be achieved by increasing T above the hysteretic region (into the PM state for example) and back to the initial temperature between measurements of the field-induced transition [23].

Another method to evaluate the first-order transition uses a magnetic version of the Clausius-Clapeyron equation, which describes the boundary curve between two phases where thermodynamic equilibrium holds [13]. This allows the direct calculation of ΔS from the abrupt change of magnetisation, ΔM, and the phase line in $H - T$ space, dH_{c}/dT [9, 22]:

$$\Delta S = -\mu_0 \left(\frac{dH_{\mathrm{c}}}{dT} \right) \Delta M \tag{1.7}$$

Where H_{c} is the critical field of the transition at a given T. Eqn. 1.7 assumes that a change in field causes only the transition itself to occur, since the two magnetic phases have the same thermodynamic potential at H_{c}, without changing any of the physical parameters (V, M, S) within either of the phases. This demonstrates explicitly how the entropy change increases for larger ΔM and a steeper critical phase line.

Regarding the quantity ΔT_{ad}, Zverev *et al.* analyse the theoretical maximum value with regards to ΔS_{m} [25], which Sandeman translates in terms of the quantity $\mu_0 dH_{\mathrm{c}}/dT$ [26] (appearing in Eqn. 1.7). Here it is assumed that $(\partial M/\partial T)_H$ is H and T invariant over a small range of both, close to T_{C}, and two limiting scenarios are discussed: at the large

dH_c/dT limit, ΔT_{ad} is inversely proportional to dH_c/dT, and at the small limit it is directly proportional to dH_c/dT. Maximum ΔT_{ad} occurs during a trade-off of these trends to give:

$$\Delta T_{ad}^{max} = \left(\frac{M_s T H_{max}}{C_p}\right)^{1/2} \tag{1.8}$$

Where C_p is the material heat capacity and H_{max} is the maximum field range. Zverev *et al.* estimate a theoretical ΔT_{ad} limit for a change of 1 T as 18 K, although they stress that this is in practice the upper limit of a strong inequality [25].

1.2.3 The active magnetic regenerator cycle and engineering details

Several cooling cycles have been proposed. The active magnetic regenerator (AMR) cycle, which is commonly expected for use, is based on the Brayton cycle, in which the four steps are:

a) adiabatic magnetisation, and therefore adiabatic heating, of the MCE material,

b) isofield cooling back to the initial T using a heat transfer medium,

c) adiabatic demagnetisation (and therefore cooling),

d) isofield heat transfer to heat the material back to the initial temperature.

The process leading to cooling of the desired mass then occurs during step d) [27, 28]. This cycle is the same as that shown and described in Figure 1.2 and requires the incorporation of fluid as the heat transfer medium, and therefore an appropriate design. In addition, the fluid and refrigerant (i.e. the MCE material) thermal conductivities, refrigerant and permanent magnet geometry, fluid viscosity and pressure drop between the hot and cold reservoirs must be taken into account, as summarised by Smith *et al.* [9] and Gschneidner *et al.* [6]. Other cycles, such as Ericsson, have also be proposed for use. However, Chen *et al.* demonstrated that, close to room temperature, the AMR cycle is the most efficient [29]. An example design

proposed by Zimm *et al.* [30] has the refrigerant rotate past a 1.5 T Nd-Fe-B permanent magnet in an AMR cycle, with an appropriate fluid flow designed to separate the hot and cold reservoirs. Using Gd and $La(Fe_{0.88}Si_{0.12})_{13}$, with rotation frequencies up to 4 Hz, they attain a cooling power of over 30 W, for a temperature span of 10 K between the hot and cold reservoirs.

The volume and structural changes intrinsic to the transition can lead to degradation of the solid refrigerant, where repeated cycling between the two structures or two volumes causes internal stresses, which in turn can cause the formation of cracks and even powderisation of the solid [31]. In some cases this has been seen to occur on first cycling only, after which the material stabilises with altered (and often reduced) MCE properties [32]. In general, mechanical breakdown of the material is seen as detrimental within the context of a heat pump set-up, although several methods to overcome this have been proposed, such as the introduction of porosity, which has been seen to greatly reduce the degradation of the MCE after multiple cycles [33]. Control of the thermal conductivity is also desired for efficient extraction of heat. Since this is reduced in porous samples, efforts to address this, for example incorporation of Cu into the pores, has demonstrated mechanical stability and a significant improvement of cooling power over non-composite porous samples [34].

1.2.4 Materials summary

Table 1.1 summarises the key properties of various material systems. Gd is usually referred to as the 'benchmark' MCE material to which all others are compared, and is therefore included here. Other than Gd, all systems considered in Table 1.1 undergo first-order transitions. A note should be made about the magnetovolume transitions of $(Mn,Fe)_2(P,Si)$ where, despite no structural change, there is a non-isotropic lattice expansion of its Fe_2P-type hexagonal structure, where the lattice constant in the plane and orthogonal to the hexagonal plane change oppositely, i.e. while one increases the other decreases, leading to a reduced net volume change [35].

Material	Structural or volume	Structure	Magnetic phases	ΔS_m (J-kg^{-1}K^{-1})	ΔT_{ad} (K)	T_C (K)	Ref.
Gd	N/A	Hexag.	FM to PM	5	5	293	[5]
La(Fe,Si)$_{13}$	Magneto-volume	Cubic, NaZn$_{13}$	FM to PM	25	8	180-250	[6]
(Mn,Fe)$_2$-(P,Si)	Magneto-volume	Hexag., Fe$_2$P	FM to PM	25	3	250-300	[36, 37]
FeRh	Magneto-volume	Cubic, CsCl	AFM to FM	17	13	315	[38]
La$_{1-x}$Ca$_x$-MnO$_3$	Magneto-volume	Ortho. perovskite	FM to PM	4	1	220-270	[6, 39]
Gd$_5$(Si,Ge)$_4$	Magneto-structural	Ortho., Gd$_5$Si$_4$ to monoc., Gd$_5$Si$_2$Ge$_2$	FM to PM	14	8	200-300	[5, 6]
MnAs	Magneto-structural	Hexag., NiAs to ortho., MnP	FM to PM	30	5	318	[40]
Ni$_2$MnGa	Magneto-structural	Tetrag., mart. to cubic, aust.	FM to FM	16	2	175-220	[6, 20]

Table 1.1: Summary of several key MCE material systems and their principal properties. ΔS_m and ΔT_{ad} values are given for 0 to 2 T. The order of the magnetic and structural phases refers to low T to high T.

Many of these materials suffer from very large thermal and magnetic hysteresis, on the order of tens of K and > 2 T, respectively. This is the case particularly for materials with magnetostructural transitions, such as Heusler alloys, Ni-Mn-Ga [41] or Ni-Mn-In [20, 42, 43, 44], which transform from martensitic to austenitic. Indeed, this system demonstrates more than one phase transition: a transition between two FM states concurrent with the magnetostructural transition, and a FM to PM transition at higher temperatures which is often the conventional second-order loss of moment order at T_C and therefore has no structural change. A similar situation exists for FeRh [45] with both an AFM-FM magnetovolume transition at low T and the conventional FM-PM at higher T.

1.2.5 Comparison with other caloric phenomena

In addition to MCE, materials can exhibit a caloric response to other changes in environment, where a thermal change occurs within electric fields (known as the electrocaloric effect, ECE), under hydrostatic pressure (barocaloric effect, BCE) or under uniaxial tension or compression (elastocaloric effect, eCE). Moya *et al.* present a review of these caloric phenomena in Ref. [46]. In ECE materials, the mechanism is analogous to MCE whereby changes of material polarisation in response to electric field cause an entropy change which is accounted for by a temperature change. Examples of systems in which the ECE is particularly strong are KH_2PO_4 or $BaTiO_3$ based materials. However, for bulk compounds such as these, the maximum entropy and adiabatic temperature changes are limited, e.g. $|\Delta S| = 2 - 4\ \mathrm{J\,kg^{-1}K^{-1}}$ and $\Delta T_{\mathrm{ad}} \leq 2$ K, in response to small field changes [47]. More recently, much larger $|\Delta S|$ and ΔT_{ad} values, significantly larger than for the bulk MCE materials listed in section 1.2.4, have been obtained in a range of ceramic and polymer films, with values of up to 130 $\mathrm{J\,kg^{-1}K^{-1}}$ and 28 K respectively being reported [48], albeit with large electric field changes. The lack of significant mass offered in film-based materials is a restricting factor for macro-scale ECE refrigeration applications, however this has the potential to be overcome with the use of multilayer capacitor devices [49].

The BCE is considerable in systems such as Ni-Mn-In, $Gd_5(Si,Ge)_4$ and $La(Fe,Si)_{13}$, and the eCE in NiTi and FeRh, for example. In particular, the BCE in ammonium sulphate (which is non-magnetic) has been reported with $\Delta S \sim 60\ \mathrm{J\,kg^{-1}K^{-1}}$ for a pressure change of 1 kbar [50] Note that since, in order to be large, these two effects require driving across structural transitions or considerable volume changes, predominantly of a first-order type. Therefore, many of these materials also fall into the MCE category, for which the large entropy changes involve magnetovolume or magnetostructural changes. In the case of the BCE, Mañosa *et al.* demonstrate that, in response to hydrostatic pressure changes up to $\Delta p = 2.6$ kbar, the Heusler alloy Ni-Mn-In has ΔS values larger than $-20\ \mathrm{J\,kg^{-1}K^{-1}}$, comparable to the MCE within the material, and indeed they predict similar effects in many MCE materials

that undergo volume changes at the transition [51]. Following this they show that, for a pressure change of 1 kbar, La(Fe,Co,Si)$_{13}$ exhibits $|\Delta S| = 20$ J kg^{-1}K^{-1} and $\Delta T_{\mathrm{ad}} = 1.5$ K, which is already larger than the MCE available within the field range of permanent magnets, for the same composition [52]. Since there are La(Fe,Si)$_{13}$ compounds of stronger first-order type with significantly larger MCE, such as LaFe$_{11.6}$Si$_{1.4}$, prevalent in Chapter 4 and 5 of this thesis, the BCE can also be expected to be as large. Indeed, theoretical work be de Medeiros *et al.* considering LaFe$_{11.57}$Si$_{1.43}$ predicts a large BCE [53].

Moya *et al.* also compare the relative efficiencies of these effects by way of a dimensionless efficiency coefficient, $\eta = |Q/W|$, where W is the magnetic or electric work (which can applied either electrically or mechanically) done, and Q is the heat flow, in a reversible cycle, from the material to the thermal bath [54]. They report that the maximum efficiency can be attained in MCE materials driven mechanically.

The fact that some of these materials show multiple effects leads to the possibility of multicaloric application: materials which have at least two of these properties and are used in such a way that their caloric versatility is taken advantage of [46]. This can be utilised by so-called tuning of the transition, e.g. using pressure to shift the working temperature of the MCE [55]. More recently there have been demonstrations of mixed caloric cycles which have the potential to reduce hysteresis [56, 57]. These examples show the promise in taking this approach for the future of the field, and indeed for application. However, difficulties in the application of different types of field create a barrier to the use of such cycles which may limit such use unless they are overcome.

1.2.6 A note about units

Within this thesis, the applied magnetic field, H, is written as $\mu_0 H$ so that the units are tesla, T (that of the magnetic flux density, B). Within the text, references to applied field will be given as H only.

There are multiple units of magnetisation, M, used across the literature of MCE, depending on the exact quantity being reported. In this thesis, emu g^{-1} is predominantly used, since all of the results have been directly measured as moment and normalised to mass. This unit is directly equivalent to another commonly used unit, A $m^2 kg^{-1}$, and both are directly related to the volumetric unit, A m^{-1}, by the material's density (in kg m^{-3}). This latter unit is the same as the SI unit for H. In the literature, other units are used, such as μ_B/Fe-atom. However, a significant portion of this thesis involves comparison between different compositions and therefore different Fe contents per unit formula. Therefore, this unit is not used.

In Chapter 6, specific heat measurements are reported in both J $kg^{-1}K^{-1}$ and J $mol^{-1}K^{-1}$ units, where the latter is given as moles per unit formula. To convert from the former to the latter, one multiplies by the molar mass (per unit formula) in kg mol^{-1}.

1.3 First-order phase transitions

1.3.1 Definition and properties

As discussed in section 1.2.1, the Ehrenfest classification defines first-order phase transitions as exhibiting a discontinuity in the first-derivative of the Gibbs free energy, G, with respect to a state variable, X, $\frac{\partial G}{\partial X}$, where X can be T, H, p, etc [10, 58].

A common example of a first-order phase transition is the change of physical phase at boiling and melting points. Using this example alone allows the description of many common phenomena associated with first-order transitions, which have direct analogues for the magnetic transitions studied in this thesis. Firstly, superheating or supercooling occurs, where the system can be pushed in T beyond its thermodynamic critical temperature of phase transition if there is no facilitator, such as an impurity or other nuclei, to begin the nucleation of the new phase, which costs energy [13]. Secondly, latent heat release or absorption at the transition (at constant T) originates as stored energy in the system required for the creation of the new

phase [10]. Thirdly, the transitions can be modified by other external factors, such as pressure, p, which when increasing, for example, moves the water-vapour boiling point to higher T. The result is the appearance of a phase-line denoting where in $p-T$ phase space the transition occurs. A fourth common feature is phase coexistence [59], where during transition (or if sitting at the transition boundary, for now ignoring that the reverse transition may have a different boundary) the system is on the equilibrium curve (in $p-T$ space) between two phases and therefore both phases are stable at the same temperature (or pressure) and occur together. This is a requirement for almost all first-order transitions since very rarely can the whole volume of a system undergo transition simultaneously, unless, for example, the system is very small such that the energy cost of a domain wall is prohibitive. In some instances, two separate phase equilibrium lines can meet at a point where three phases can coexist as a result, known as the triple point. An interesting and relevant phenomenon of the water-vapour transition phase line is that as the pressure is raised and T_{boil} increases, we eventually meet a point, known as the critical point, where the discontinuity between the phases disappears and there is no longer a transition.

For magnetism, the first-order transition can be visualised in the magnetic free energy in terms of order parameter, M. The requirement for first-order behaviour is the presence of two free energy minima separated by a maximum. As shown in Figure 1.6, the low and high M minima correspond to the PM and FM magnetic states respectively and the maximum, i.e. the energy barrier, ΔE, impedes transformation between the two. This free energy 'landscape' is modified by H or T such that the minima have equal energy at T_{C} and H_{c}. Therefore, the existence of either is possible in the same equilibrium conditions, but one minimum becomes preferable over the other as H and T vary, until the energy barrier is overcome at a change of field, $\Delta H/2$, or temperature, $\Delta T/2$, at which the transition takes place. It is this requirement to go beyond the equilibrium state, for both PM to FM and FM to PM transitions, which leads to hysteresis, ΔH or ΔT, the size of which is related to the barrier height, ΔE.

Often, the existence of the first-order transition is not well defined, since temperature or composition inhomogeneity, impurities, temperature variation and finite sample size effects,

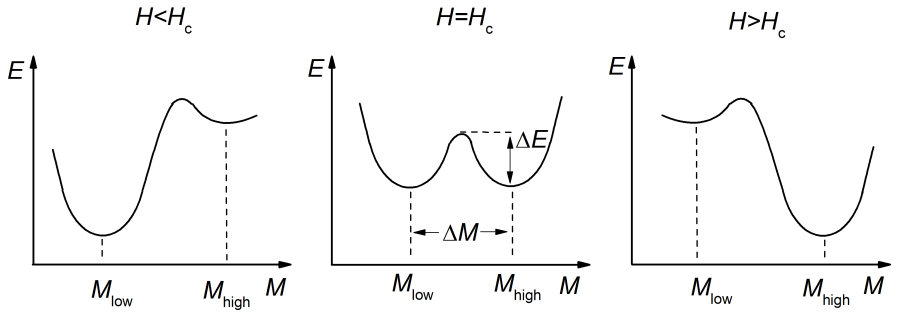


Figure 1.6: The free energy of a metamagnetic system at $H < H_c$, $H = H_c$ and $H > H_c$, showing the high M (e.g. FM) and low M (e.g. PM) minima, the adjustment of the free energy with field, and the requirement to overcome the energy barrier at H_c, ΔE, leading to magnetic hysteresis, ΔH.

amongst other causes, will in practice smear the sharp discontinuity [59], and extrinsic or dynamic effects can mask the existence of hysteresis. One useful representation of phase transition magnetisation data, which can clarify the presence of a first-order transition, is the Arrott plot, based on the Arrott-Noakes equation of state [60], $H/M = a\left(\frac{T-T_C}{T_C}\right) + bM^2$. When plotted as H/M against M^2, the first term on the right hand side is the intercept and b is the gradient. 'S'-shaped plots, due to negative b at the transition, are indicative of first-order character. However, transitions with a small extent of first-order character or close to a second-order crossover may also be ambiguous in this representation. As a result, the classification of first-order has also been defined more generally by the existence of latent heat release or absorption at the transition [61].

Throughout this thesis I will refer to concepts such as 'the strength of first-order behaviour/character' and 'more/less first-order'. By definition, a transition can of course only be defined as being first-order or not. However in many cases, and critically for the results and discussion represented here, the idea of differing degrees of first-order magnitude, for example different magnitudes of hysteresis, magnetisation, entropy and volume discontinuity and latent heat release, in addition to coexistence of both first and second-order behaviour, become very important. Therefore, these phrases above are intended only to give suitable descriptions of, and comparisons between, the phase transitions investigated.

1.3.2 Nucleation and growth

The first-order transition must begin with a nucleation process, and progression of the new phase within the old will be either in the form of further nucleation or growth around the previously nucleated regions. Growth in time (in constant T, H, p, etc) indicates metastability of states, and such behaviour is often referred to as relaxation.

The activation energy, E_a, is the energy required to overcome the barrier, and a common growth mechanism is activation by thermal $k_\mathrm{B}T$ energy in order to achieve this [13]. The rate at which this occurs, k, is modelled by the Arrhenius equation:

$$k = Ae^{-\frac{E_\mathrm{a}}{k_\mathrm{B}T}} \tag{1.9}$$

However, the first-order transition is complicated by factors which are not accounted for in such a simple model. For example, the energy required for nucleation can be very different to that required to thermally overcome the barrier, since a new boundary between two now-coexistent phases must be formed, and this can lead to supercooling or superheating without an appropriate impurity or other nucleation site to lower the barrier and allow nucleation to take place, as mentioned in section 1.3.1. In addition, the dynamics of growth become important.

Avrami formulated a description of nucleation and growth dynamics with the Johnson-Mehl-Avrami (JMA) model, which describes the time evolution of the phase fraction of new phase as a process of nucleation and subsequent growth of each nucleated region [62, 63]. In that formulation, the fraction of new phase, f, evolves with time, t, as:

$$f = 1 - e^{-kt^n} \tag{1.10}$$

Where here, k is related to the activation energy and n is the Avrami index which is related to the dimension of growth. Therefore, activation energy is still important but the geometry

of the surface and growth is included in the index. In the model, nucleation is assumed to be randomly distributed and the growth isotropic (within the dimensions of the index). As such, the latter part of the transition is dominated by reduced nucleation and the merging of growing regions, slowing the transition, and the rate of transition is independent of the extent of transformation already occurred. Further descriptions can be necessary, such as for interface effects between a new phase within the matrix of old phase in precipitation or solidification nucleation, as reported and modelled by Perez [64].

For MCE systems, coexistence has several specificities which will impact the growth. Strain fields arise within the sample from the two separate lattice constants of each phase, since magnetovolume and magnetostructural changes are a requisite of first-order behaviour, and dipole interactions may exist between the high moment and low moment regions of differing magnetisation [65], which would increase the role of the surface area of the interface between the two phases. Both of these will be influencing factors on the nucleation and growth, in addition to more general first-order characteristics such as latent heat release. Therefore, the nucleation and growth characteristics will be determined by which of these factors dominate and in what form. Specific examples are given in section 2.2.3.

1.4 Models

Several models have been developed to describe transitions in magnetic systems. Of significant relevance for the magnetocaloric effect is the Bean-Rodbell model [66], which describes the correlation of first-order behaviour with strong magnetoelastic effects by considering the Gibbs free energy as a sum of the contributions from the field, pressure, exchange, elastic and entropy terms. T_{C}, as a function of the strength of a magnetovolume coupling parameter, β, is given by $T_{\mathrm{C}} = T_0(1 + \beta\frac{V-V_0}{V_0})$, where V is the volume, V_0 is the equilibrium volume in the absence of magnetic interactions and T_0 is the Curie temperature of the system when V is constrained to V_0. This approach takes into account the role of interatomic spacing on the exchange

energy, and whether the lattice is deformable or clamped, and gives a general expression for the existence of first-order behaviour in terms of β and the lattice compressibility. Many groups have applied this model, or derivatives thereof, to magnetocaloric materials, such as the original authors to MnAs [66], and many others to other MCE materials or MCE transitions in general [67, 68, 69].

1.4.1 Itinerant electron metamagnetism

Because the Bean-Rodbell model uses molecular mean-field theory as its basis, its applicability is independent of the the origin of the magnetism. Magnetism of systems is usually classed as being due to two mechanisms: either from localised moments usually arising from strong interactions between valence electrons, or from itinerant electrons where the contributing electrons are not confined to atoms and so the mechanism is instead thought of as a correlation of moments within an electronic band structure [70]. In this case the electrons within the band contribute both to the magnetism and to the conduction so separation of the electronic entropy and magnetic entropy is not straightforward, as previously remarked. Additionally the two mechanisms are not necessarily separate either, for example magnetic systems such as $HoCo_2$ and $DyCo_2$ are best described by a combination of both localised moments and itinerant electron contributions [11].

In the case of field-induced transitions within itinerant systems, the transition is termed itinerant electron metamagnetism (IEM), and has been represented as a Landau-type expansion of the magnetic free energy up to the sixth power of the magnetic order parameter by Shimizu [11], following a previous description by Wohlfarth and Rhodes up to the fourth power [71]. The order parameter itself is represented by the magnetisation, M, which as previously stated is finite for systems with spontaneous magnetic ordering, and zero for disordered systems, e.g. the paramagnetic state. Starting with:

$$F = \frac{1}{2}aM^2 + \frac{1}{4}bM^4 + \frac{1}{6}cM^6 \tag{1.11}$$

Where a, b and c are the Landau coefficients, which are functions of T, the H field equation of state can be written generally as the following:

$$H(M) = \frac{dF}{dM} = aM + bM^3 + cM^5 \tag{1.12}$$

Within the IEM model, the role of spin fluctuations at finite temperature is considerable and modifies the coefficients a, b and c. For a first-order transition to occur, a and c are positive and b must be negative, as with the case of the Arrott plots (section 1.3.1). This gives the familiar free energy structure of a double minimum with an intervening energy barrier as represented in Figure 1.6. Shimizu defines the rigorous requirements of these coefficients in the IEM picture for first-order behaviour. Yamada investigates the impact of spin fluctuations as functions of T [72, 73, 74] and determines a temperature, T_{crit}, above T_{C} where the metamagnetic, double-minima behaviour (i.e. the energy barrier) is lost and therefore the first-order transition becomes second order. Additionally, the role of magnetovolume effects in the IEM transition has been formulated [73, 75].

These descriptions are very important with regards to the $La(Fe,Si)_{13}$ system studied in the following chapters, and more specific details are given in section 2.1.2 and during the discussion of the relevant results.

2 | The La(Fe,Si)$_{13}$ System and Review of Relevant Literature

Following the introductory summary of the magnetocaloric effect in Chapter 1, this chapter introduces the La(Fe,Si)$_{13}$ material system and focuses on literature concerning the first-order transition and the response of its characteristic features (namely: its magnetocaloric properties, hysteresis, criticality, heat capacity and latent heat) to the environment and composition. This is followed by a discussion of dynamic effects observed in the system and the importance of the demagnetising factor in magnetocaloric materials more broadly.

The final section of this chapter has a slightly different focus and concerns low temperature heat capacity measurements of similar material systems, resulting Sommerfeld coefficients, and theoretical predictions of the coefficient in La(Fe,Si)$_{13}$, to complement the results of Chapter 6.

2.1 La(Fe,Si)$_{13}$

2.1.1 Structure and phase

The $LaFe_{13-x}Si_x$ system has a cubic $NaZn_{13}$-type structure with space group $Fm\overline{3}c$ which has a stable phase region for $1.4 < x < 2.6$ [76, 77]. Note that the binary $LaFe_{13-x}$ cannot crystallise, and higher Si contents ($x > 3.2$) have tetragonal structure. A visualisation of the structure is shown in Figure 2.1. The unit cell comprises 8 formula units and Si atoms can occupy either Fe site, 8(b) and 96(i) (in Wyckoff space), and does so randomly [78], although occupation only on the 96(i) site has been reported to stabilise the magnetic properties described in the next section [79]. The compound crystallises in polycrystal form with regions of secondary-phase α-Fe, which usually comprise $\sim 5-8$ wt% of the material [78, 80]. Additionally a small amount of La-rich phase is often present: the presence and quantity of these secondary phases is dependent on and must be optimised (i.e. reduced, for studies of pure 1:13 $LaFe_{13-x}Si_x$) by the processing route, as outlined by Liu *et al.* [81].

2.1.2 The magnetic phase transition

$LaFe_{13-x}Si_x$ undergoes a magnetic phase transition between the itinerant electron ferromagnetic and paramagnetic (in which the electrons are also itinerant) states at the Curie temperature, T_C, as the spontaneous magnetisation disappears in response to increasing temperature [76]. T_C is in the range 185 K to 250 K, depending on Si content. Above T_C, the itinerant electron metamagnetic (IEM) transition from PM to FM can be induced with application of field; the reverse transition back to PM is induced by the subsequent removal of field [21, 82]. A very large volume increase of $\sim 1.5\%$ is exhibited across both the thermal and field driven PM to FM transitions [21, 82]. This is a magnetovolume change only, with the compound retaining its structure (this is not universal; other promising magnetocaloric systems, as described in section 1.2.1, such as the $(Mn,Fe)_2(P,Si,Ge)$ and $Gd_5(Ge,Si)_4$ families

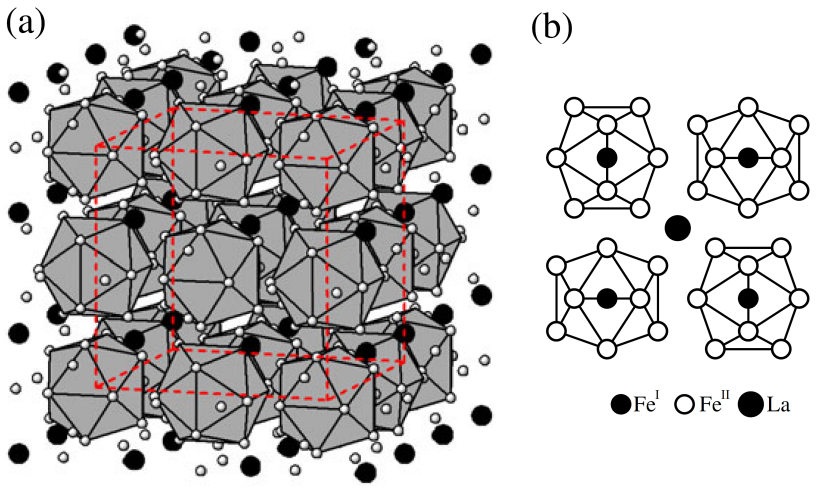


Figure 2.1: Reprinted from Ref. [78], (a) the structure of the $LaFe_{13-x}Si_x$ compound, where the dashed lines represent the edge of the unit cell, and (b) part of the unit cell shown in the (001) projection. The two Fe sites, Fe^{I} and Fe^{II}, represent the Wyckoff space positions 8(b) and 96(i) respectively. Note that in (a) the Fe^{I}, within the surrounding icosahedron of Fe^{II} atoms, is not displayed. © IOP Publishing. Reproduced with permission. All rights reserved.

undergo anisotropic lattice parameter changes and structural changes, respectively, during their magnetic transition [5, 83]). Additionally, due to the symmetry of the cubic crystal structure, there are no easy or hard axes to which it is preferential for the moment to align. The system thus shows no magnetocrystalline anisotropy.

For $x < 1.8$, the magnetic phase transition is first-order [55] and this becomes more pronounced for decreasing Si (as low as $x = 1.2$ has been reported [81, 84, 85]: below this the phase has difficulty forming, see section 2.1.1). For $x > 1.8$ the transition is second-order. Note, however, that there is some discrepancy in the literature between where the crossover to second-order is (Ref. [81] states $x > 1.6$) suggesting that it is not very well defined. Larger fields raise the transition temperature, $T_t(H)$ (where $T_t(H = 0) = T_C$), and equivalently, the further above T_C the system is, the larger the applied field required to induce the IEM transition is, as indicated by the $H - T$ phase diagram in Figure 2.2. The first-order transition undergoes an abrupt, discontinuous change in magnetisation, M, and volume, V, in response to temperature and field with small hysteresis. The transition occurs as a nucleation

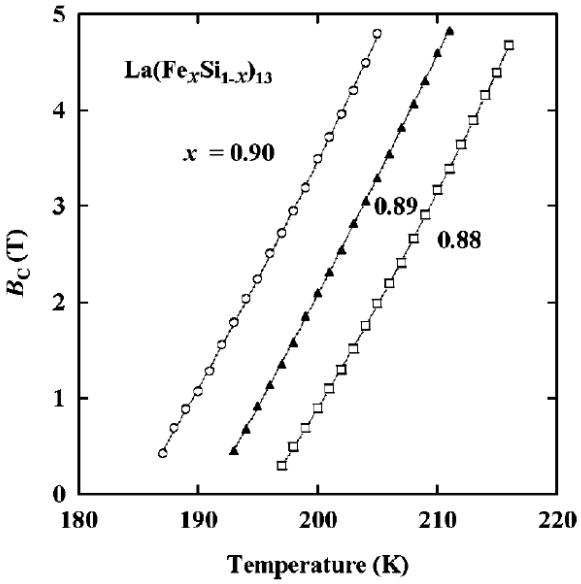


Figure 2.2: Reprinted from Ref. [88], the B $(\mu_0 H)$−T phase diagram for three samples of $LaFe_{13-x}Si_x$ showing for each the dependence of the PM-FM transition on field and temperature. T_C is represented by the intercept with $B = 0$ T and the regions to the left and right of each line represent the FM and PM phases respectively. See section 2.1.5 for details about the movement of T_C and the phase line with composition. Reprinted with permission. © 2003 by the American Physical Society.

and growth process of the new phase within the old, on the local scale. Therefore, as for many first-order transitions (an exception being if a system is small enough, i.e. on the order of the nucleation size, that the entire system transforms simultaneously), a period of mixed state results, with both the smaller volume PM and the larger volume FM phases coexisting, until the new phase is fully formed. As a result of the abrupt transition, ΔS_m values (extracted from the field-induced transition using the Maxwell relationship) of larger than -25 J kg^{-1}K^{-1}, with a corresponding ΔT_{ad} of up to 8 K have been reported for $x = 1.3$, with field applied between $\mu_0 H = 0$ and 2 T [86], and comparable values are given across the literature [7, 80, 84].

An increased field range will sometimes permit increased ΔS_m and ΔT_{ad} values; however for sharp, first-order systems, any extra benefit is only accessed from the temperature variation of

M within the FM state, which will be much less significant compared to that at the transition. Increasing the field range will however extend the temperature range above T_{C} across which the large ΔS_{m} and ΔT_{ad} are accessible. An example of the variation of these parameters with temperature, field range and composition is given in Figure 2.3, showing these observations clearly, and demonstrating how the attainable MCE reduces with increasing Si, as the material becomes less strongly first-order. It is these large values of ΔS_{m} and ΔT_{ad} within small field strengths, particularly in comparison to the benchmark material Gd [87] (note that permanent magnets based on the Nd-Fe-B compound allow maximum fields of $\mu_0 H < 2$ T), in addition to a wide temperature range of working temperatures (see section 2.1.5) that make this system one of the most attractive for use in magnetocaloric applications.

A large amount of literature, in particular the work of Fujita *et al.*, has described the behaviour of La(Fe,Si)$_{13}$ in terms of the IEM model, in particular the role of spin fluctuations on the Ginzburg-Landau expansion of free energy and the strong magnetovolume effect [21, 82, 86, 88, 89, 90, 91, 92]. The IEM itself originates from the itinerant Fe 3d electrons [21]. As described in section 1.4.1, a first-order IEM transition is characterised by a double-well structure in the free energy, with the low M and high M minima representing the PM and FM states respectively. The minima are well separated in M with a low barrier (therefore low hysteresis) and varies with H and T. Specifically, spin fluctuation theory explains the evolution of the landscape with increasing H and T such that both the separation between the two minima and the barrier height reduce, decreasing the first-order character until a point at which the barrier disappears and only one minimum remains. This point is known as the critical point, designated T_{crit} (in temperature), and denotes the disappearance of first-order behaviour.

Extending the theoretical approach, electronic structure calculations were made by Kuz'min and Richter [93] on LaFe$_{12}$Si, who showed that the free energy has several shallow minima and maxima as a function of M, strongly dependent on the lattice parameter, as shown in Figure 2.4. Such a flat free energy landscape implies small hysteresis and a fast magnetisation/demagnetisation process, beneficial to a magnetocaloric application. Regarding the role of the lattice itself, Gruner *et al.* [94] used density functional theory calculations to under-

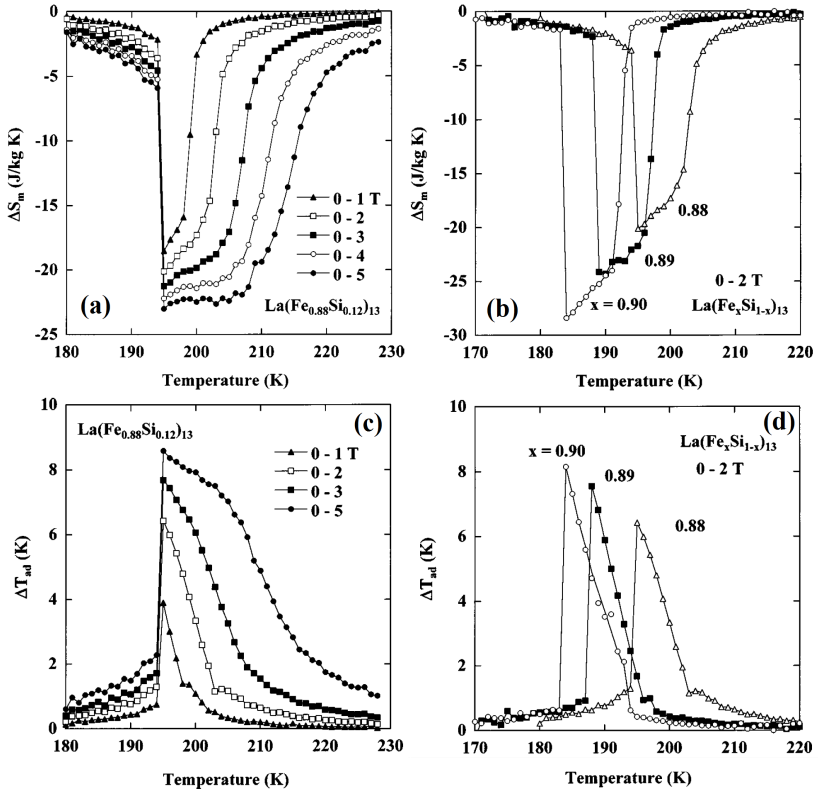


Figure 2.3: Reprinted from Ref. [86], $\Delta S_{\mathrm{m}}(T)$ of (a) La(Fe$_{0.88}$Si$_{0.12}$)$_{13}$ (equal to $x = 1.56$) for a variety of field changes and (b) three compositions for $\mu_0 H = 0 - 2$ T applied field, and $\Delta T_{\mathrm{ad}}(T)$ of (c) La(Fe$_{0.88}$Si$_{0.12}$)$_{13}$ for a variety of field changes and (d) the same three compositions again for $0 - 2$ T. T_{C} of La(Fe$_{0.88}$Si$_{0.12}$)$_{13}$ is 195 K, indicated by the peak in all of (a)-(d). See section 2.1.5 for details about the movement of T_{C} with composition. Reproduced with the permission of AIP publishing.

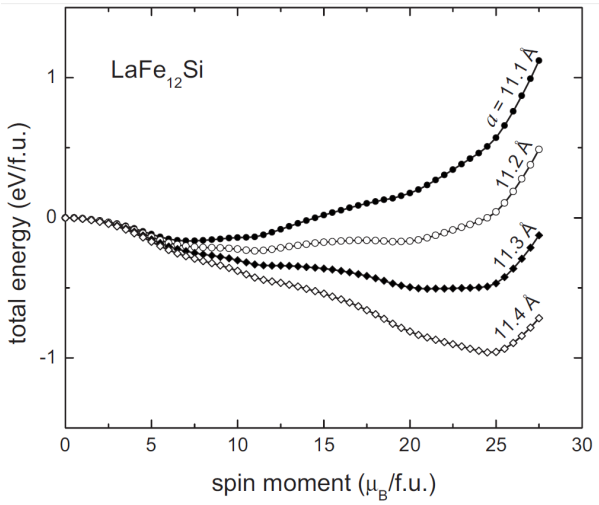


Figure 2.4: Reprinted from Ref. [93], the energy diagram as a function of spin moment (magnetisation) of $LaFe_{12}Si$, for several values of lattice parameter, shows a relatively flat landscape with multiple energy minima separated by low energy barriers. Reprinted with permission. © 2007 by the American Physical Society.

stand how the vibrational density of states is influenced by the magnetoelastic coupling across the transition. They showed that the excellent magnetocaloric properties had their basis in a cooperative contribution of the the structural lattice entropy change to that of the magnetic and electronic lattices.

2.1.3 Hysteresis

The inherent hysteresis of the first-order transition, due to the irreversibility between the PM to FM and the FM to PM legs of the cycle in both the thermally and field-driven transitions, results in energy losses (per normalisation unit) equal to the area of hysteresis within an $M - \mu_0 H$ curve. This means that in a cyclical process, the MCE parameters which have measured for one field direction only, such as those shown in Figure 2.3, will not be attainable to their maximum values. The hysteresis width and area of $LaFe_{13-x}Si_x$ decreases as compositional changes cause the first-order character to weaken (with increasing Si). For second-order compositions there is no hysteresis.

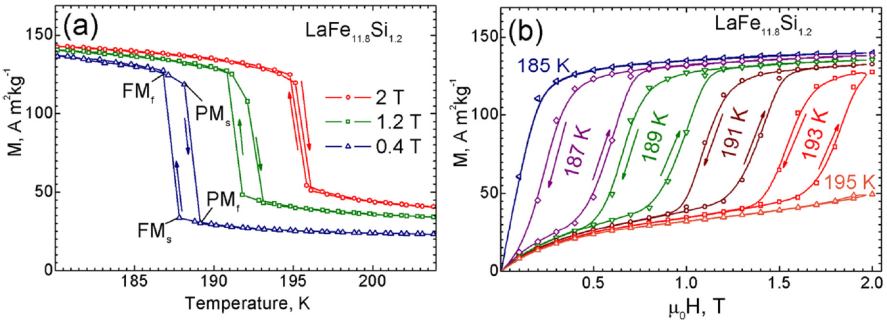


Figure 2.5: Reprinted from Ref. [85], (a) $M(T)$ in several fields and (b) $M(H)$ at several temperatures, for $LaFe_{13-x}Si_x$ with $x = 1.2$. The arrows indicate the direction of T/H change around the hysteresis loops. The 185 K data in (b) demonstrates the fully FM state. Reprinted with the permission of AIP Publishing.

An example of the the magnetic phase transition of $x = 1.2$ is shown in Figure 2.5 showing the movement of T_C and H_c with field and temperature respectively (see the phase diagram in Figure 2.2), and the hysteresis in both the thermally (ΔT_{hyst}) and field (ΔH_{hyst}) driven transitions. As discussed in section 2.1.2, the hysteresis is small in comparison to other systems due to the low barrier in the free energy, and decreases for increasing H and T until a point (in both H and T) where it and additionally the sharp feature (i.e. the abrupt change in M) of the transition disappear (T_{crit}). Fujieda *et al.* demonstrate that the energy loss from hysteresis increases for $LaFe_{13-x}Si_x$ compositions in correlation with increased ΔS_m (decreasing Si), representing strengthening of the first-order character, and, in addition, they explicitly show that this loss reduces to zero at T_{crit} [95, 96].

Despite the small intrinsic hysteresis, with regards to application, maximum reduction of its magnitude is desired, and several groups have looked at methods to achieve this. Hu *et al.* [97] showed the hysteresis in the $M(H)$ data to reduce with smaller samples, from the millimetre-scale to 20-50 μm in size. This was attributed to easing of heat transfer as the samples decrease in size (this is discussed in section 2.2.1), but additionally to the removal of strain and grain boundary effects. A similar reduction was observed for $x = 1.4$ when porosity is introduced to a bulk sample, in this case explained by the removal of internal constraints from

grain boundaries [33]. Fujieda *et al.* also explore reducing hysteresis losses via composition, in this case by partially doping the compound with Ce and Pr on the La site [95, 96, 98]. They observe that with either Ce or Pr the hysteresis, and therefore hysteretic losses, decrease but the large MCE is retained. This is in comparison with other dopants, particularly those on the Fe sites, which decrease the hysteresis but at a cost of a significant reduction in the magnitude of the MCE (see section 2.1.5 for a summary of the effects of dopants).

2.1.4 Pressure, specific heat and latent heat

Pressure impacts the IEM transition properties and can be introduced in two ways: application of hydrostatic pressure, p, to cause an isotropic unit cell volume, V, decrease, or the insertion of interstitial elements into the unit cell to create negative pressure and increase V (the latter is discussed in section 2.1.5). Due to the strong magnetovolume effects, the compound's properties are extremely sensitive to the lattice parameter change imparted by hydrostatic pressure, with T_{C} decreasing substantially with increasing p [55], but with a corresponding small decrease in the saturation magnetisation, M_{s}. These observations are characteristic of an itinerant system with spin fluctuations and a large magnetovolume effect according to the Landau-expansion, IEM theory, as reported by Fujita *et al.* [55] and Yamada *et al.* [74].

As with other phase transitions, there is a peak in the specific heat, c_p, at the transition. For second-order compositions of La(Fe,Si)$_{13}$, the peak has been shown to decrease in height for increasing temperature and field as the transition 'broadens' [87], indicating further weakening of the second-order transition, and this is also the case for applied field increases which move the transition from first to second-order, such as demonstrated by Fujita *et al.* [88] and Pecharsky *et al.* in magnetocaloric $DyCo_2$ [19]. However, care must be taken with first-order c_p measurements, since they involve the release or absorption of latent heat at the transition, which can give incorrect results. Morrison *et al.* [99], using a calorimetric method able to separate the specific heat and latent heat contributions, demonstrate, as shown in Figure 2.6, that the latent heat has a maximum peak and entropy contribution for zero field, which

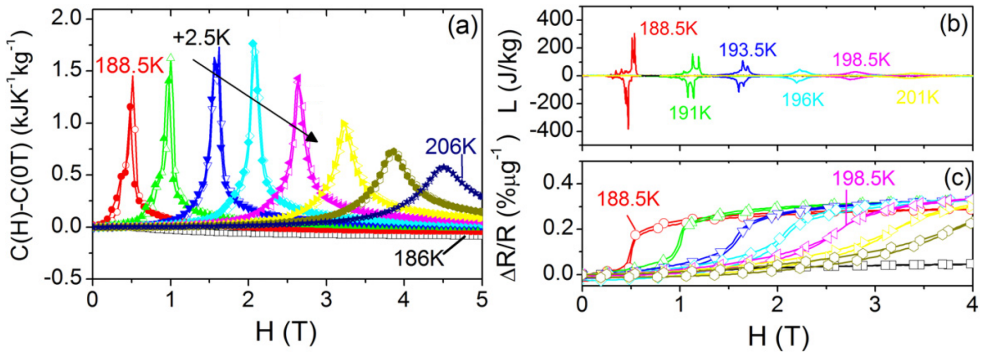


Figure 2.6: Reprinted from Ref. [99], (a) heat capacity, (b) latent heat and (c) magnetostriction measurements of the field-induced transition of $LaFe_{11.6}Si_{1.4}$ for several temperatures. © IOP Publishing. Reproduced with permission. All rights reserved.

drops off with increasing T and H until it disappears, at a temperature corresponding to the disappearance of hysteresis and the broadening of the magnetostriction (Figure 2.6(c)). This is another indicator of T_{crit} and the ending of first-order character. c_p, now separated from the latent heat, shows an initial increase of the magnitude of the peak with T/H before it drops. This increase of c_p, concurrent with a decrease of the latent heat, Q_{lh}, entropy contribution, has been described by Morrison *et al.* [100] as a common feature of a first-order transition evolving towards second-order, as H and T increase. This is complementary to the findings of Fujita *et al.* [92], which demonstrate that the Q_{lh} component's entropy change is in agreement with the Clausius-Clapeyron (CC) analysis (Eqn. 1.7) at the transition, and also decreases further from T_{C}. Since CC is calculated directly from the magnetisation change at the transition, ΔM, this equates the separation between the PM and FM free energy minima with the latent heat. The decrease in ΔM and therefore Q_{lh} is explained by the influence of spin fluctuations [90].

2.1.5 Doping and interstitials

The Curie temperature, T_{C}, and therefore working temperature of $LaFe_{13-x}Si_x$ is strongly dependent on composition and increases with Si content by approximately 55 K per unit

formula atom (x), from $\sim$ 195 K for $x = 1.56$ to $\sim$ 245 K for $x = 2.47$, whilst the magnetic phase transition becomes less strongly first order and crosses over to second-order type at $\sim x = 1.6 - 1.8$ [55, 81]. Specific doping also shifts T_{C}. For example, partial substitution on the La site with the lanthanides Ce or Pr lowers T_{C} [95, 96, 98, 101, 102], and on the Fe sites with Mn or Co decreases and increases T_{C}, respectively [87, 103, 104, 105]. Both Mn and Co also move the transition towards the second-order type. The absorption of interstitial hydrogen atoms into the compound has been shown by Fujita *et al.* to significantly increase T_{C} in a trend linear with the amount of hydrogen [88, 89]. For full hydrogenation, corresponding to the maximum number of hydrogen atoms permissible to enter the lattice ($\sim$ 1.65 atoms per unit formula), this increase can be up to 160 K (the extent of T_{C} shift varies somewhat between Fe/Si contents and the extent of doping [106]). Whereby increasing Mn and Co, by weakening the first-order character, decreases the peak values of the magnetocaloric properties, ΔS_{m} and ΔT_{ad} substantially [87, 105, 106], studies of interstitial hydrogenation suggest no significant changes, giving a shift in T_{C} without considerable change of the magnetic transition, maintaining the first-order character [88, 91, 107]. For this itinerant system, T_{C} is controlled by the negative pressure exerted by the interstitial atoms, leading to a volume and lattice expansion and influencing the magnetovolume coupling [74], which stabilises the FM phase by deepening the associated minimum in the free energy double-well landscape [108], with a direct correlation between T_{C} and unit cell volume due to hydrogenation [109]. This explanation of the FM minima deepening has also been supported theoretically by Gercsi *et al.* [110]. However, the H atoms themselves do not have a major impact on the electronic structure of the compound, namely the density of states at the Fermi level, which plays a significant role in the IEM transition properties; nor do they greatly change M_{s}. Again, this is expected for an itinerant system due to renormalisation effects of the spin fluctuations as the volume changes [74, 88]. The volume increase itself is up to 2% for full hydrogenation [89, 110], and follows a closely linear relationship with the hydrogen quantity.

Although the amount of hydrogen absorbed offers the advantage of fine T_{C} control, full hydrogenation is preferable since partially hydrogenated samples, sitting close to their transition

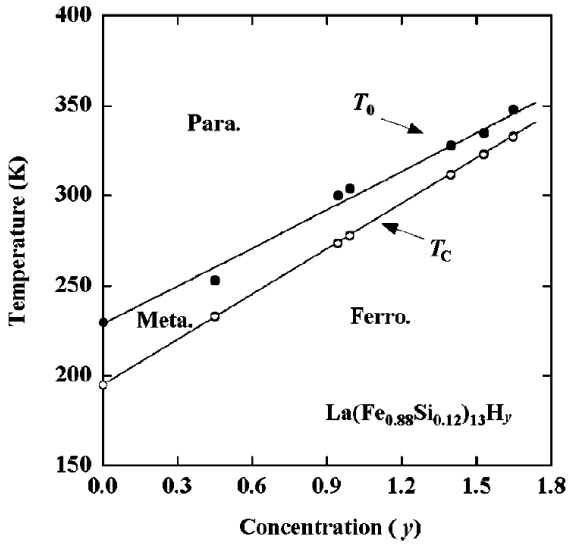


Figure 2.7: Reprinted from Ref. [88], the evolution of T_{C} and the critical point, T_{crit} (here designated T_0), with interstitial hydrogen, y, for La(Fe$_{0.88}$Si$_{0.12}$)$_{13}$H$_y$. The region within which the first-order IEM transition occurs is labelled 'Meta.'. Reprinted with permission. © 2003 by the American Physical Society.

temperatures, have shown a predisposition to split into two separate regions with distinctly differing T_{C} values over a time scale of days. This is because the hydrogen atoms tend to diffuse into FM regions, which have a larger lattice volume, resulting in an inhomogeneous distribution of interstitial hydrogen, and this scenario then stabilises. Thus, this results in undesirable changes to such samples' properties within reasonably short time scales [111, 112].

Despite the reports that hydrogenation does not greatly vary the magnitude of the magnetocaloric properties, as measurements of ΔS_{m}, ΔT_{ad} and M_{s} have demonstrated, this is not to say it is not having any impact whatsoever. Regarding the strength of first-order character, Figure 2.7 shows that the critical point, T_{crit}, which is also modified by renormalisation effects, does not scale with T_{C} as the hydrogen content is increased but increases by a lesser extent [88]. This means that after hydrogen is introduced, the range of the first-order transition is reduced and second-order behaviour is reached sooner (in increasing T and H): a reduction of the degree of first-order character.

However, the application of hydrostatic pressure, which is seen by Lyubina *et al.* to decrease

the magnitude of the MCE in non-hydrogenated $LaFe_{13-x}Si_x$ due to a broadening of the transition, increases it in the hydrogenated form due to a sharpening of the field driven metamagnetic transition feature [113]. It should be noted that conflicting behaviour is reported by Fujita *et al.* who see a sharpening of the transition in the hydrogen-free compound with p [55].

Absorption of other interstitial elements has also been studied, namely N, C and B. Unlike hydrogen, whose effect on the free energy double-well structure of the first-order transition is not substantial, these interstitials have been shown to have a much greater impact on the transition due to strong s-p band hybridisation, altering the free energy structure and significantly moving the transition to second-order [110].

In order to pinpoint precise T_C values through composition, for refrigeration application working temperature control, usually a combination of substitutions and interstitials are used, e.g. Mn doping and full hydrogenation [106], with the aim of trading off the benefits and detriments to the MCE of these substitutions.

2.1.6 Technological relevance of measurements on compositions far from room temperature

Much of the work of this thesis focuses on compositions of La(Fe,Si)$_{13}$ (with or without the addition of Mn) where T_C and therefore the working temperature is considerably lower than useful for the intended technological application. The conclusions, particularly concerning potential benefits and competitiveness in a working refrigeration cycle, can then justly be queried since such temperatures will not be relevant for practical use. However, the nature of this compound is that T_C is easily tunable with compositional doping and particularly with the insertion of interstitial hydrogen, which pushes T_C into a range close to room temperature without significantly changing the principal magnetocaloric mechanism and properties, other than altering the strength of the MCE (which indeed is investigated here) and of course the

temperature range at which it occurs. It is therefore reasonable to assume that the conclusions drawn can, in the best case scenario, be applied to the relevant hydrogenated $La(Fe,Mn,Si)_{13}$-H compounds with technologically appropriate working temperatures, and, in the worse case, be important as a study of the compound at an intermediate stage before the insertion of hydrogen. Similar arguments and assumptions have been made in other studies regarding this material system [85, 96, 114].

2.2 Dynamics

2.2.1 Rate dependence of the first-order transition

In order to further gauge the potential for use of first-order materials as a practical magnetic refrigerant with viable operational frequencies, the importance of time dependence and field-rate effects of the MCE has more recently become evident.

Specific to $LaFe_{13-x}Si_x$-based materials, several groups have investigated the apparent dependence of the first-order transition on the rate of change of applied field and temperature [115, 116, 117, 118, 119]. Moore *et al.* [115] have shown that the $M(H)$ transition features of both the field-driven PM to FM and FM to PM transitions of first-order $LaFe_{11.71}Co_{0.19}Si_{1.11}$ show 'flaring' of the hysteresis loop as the field-rate is increased, whereby the end of each transition, designated here H_{c2} and H_{c4} for PM to FM (increasing field) and FM to PM (decreasing field), move further up and further down in field, respectively, resulting in increased magnetic hysteresis, shown in Figure 2.8(a). This results in a so-called extrinsic contribution to the hysteresis, ΔH_{ext}, in addition to the time-independent intrinsic hysteresis, ΔH_{int}. One must be able to distinguish and understand how to remove the ΔH_{ext} component, for the purpose of accurate hysteresis measurement.

These types of effects have been suggested to be due to either extrinsic thermal effects from the inherent MCE heating of the sample [115, 116] or by an intrinsic nucleation and growth

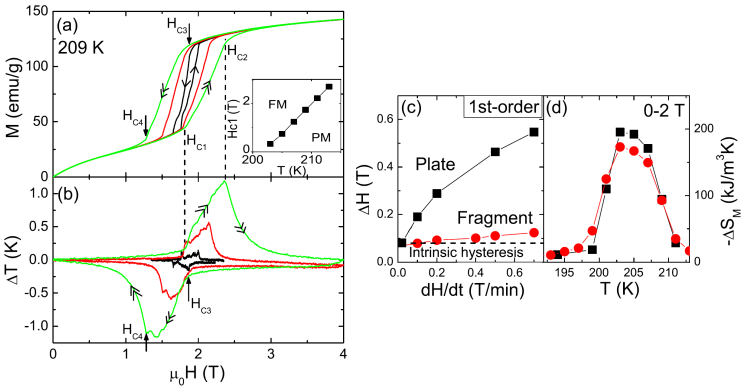


Figure 2.8: Reprinted from Ref. [115], (a) $M(H)$ hysteresis loops of a bulk plate sample of $LaFe_{11.71}Co_{0.19}Si_{1.11}$ taken at field rates of 0.02 T min^{-1} (inner loop), 0.2 T min^{-1} (middle) and 0.7 T min^{-1} (outer). The location of the critical fields H_{c1} to H_{c4} are marked. Inset: the $H-T$ phase line. (b) The simultaneously measured temperature of the sample for the three field rates shown in (a). (c) The hysteresis of the plate sample compared to a fragment of the same material and (d) the calculated entropy change curves for the two. Reprinted with the permission of AIP Publishing.

process [117, 118, 119]. In the former case, once the PM to FM transition has started at some part of the sample, the increase in temperature from the nucleated region heats the surrounding regions and therefore increases their critical fields (see the $H-T$ phase line in the inset to Figure 2.8(a)). Consequently, in such a quasi-adiabatic transition, increasingly larger fields are required for the remaining PM volumes to reach their critical field as more of the material transforms and the whole system heats. This occurs similarly and oppositely with cooling for the reverse FM to PM transition. Faster field-rates keep the sample out of thermal equilibrium longer if the heat has no easy means of transfer into and out of the sample, such as due to a poor thermal link to the thermal bath. This results in an increased hysteresis due entirely to extrinsic properties, the ΔH_{ext} contribution.

Moore *et al.* [115] support this view in two ways. Firstly, with simultaneous measurements of the temperature of the $3\times3\times1$ mm^3 plate-like sample (Figure 2.8(b)), they show that the temperature increases significantly at the fastest field rate (0.7 T min^{-1}), where the peak in temperature matches the peak flaring of the $M(H)$ loop, compared to the slowest (0.02 T min^{-1}).

Note that this observation requires a relatively poor thermal link to the bath such that the increased temperature change at the fast field rate is indicative of the heat energy having less time to leak away. Secondly, measurements on a sample of greatly reduced size, labelled 'fragment', show a much reduced increase in hysteresis with field rate in comparison to the plate, as shown in Figure 2.8(c). This is not due to a change in the intrinsic magnetocaloric properties, as shown in Figure 2.8(d), where the magnetic entropy change is in agreement between the two sizes of sample, but the thermal equilibration with the bath, which is considerably improved from the larger surface area to volume ratio of the fragment. This is in agreement with the sample size dependence of the hysteresis discussed in section 2.1.3 reported in $La_{0.7}Ce_{0.3}Fe_{11.6}Si_{1.4}C_{0.2}$ by Hu *et al.* [97].

This has been further supported by specific heat measurements by Kuepferling *et al.* [116] where a sample of $LaFe_{11.70}Co_{0.195}Si_{1.105}$ has been measured under varying field and temperature rates across the field-driven and thermally driven transition respectively. Comparing two contact media between the sample and bath, Apiezon N thermal grease (poor thermal contact) and silver paste (good thermal contact), they see that in the latter case, rate dependence effects and resulting ΔH_{ext} are greatly reduced, and can be corrected by a thermal contact resistance parameter which after removal leaves only ΔH_{int}. However, it is admitted that the method of extraction of this parameter could hide any intrinsic dynamic effect that may be present.

Alternatively in the latter case, it has also been suggested that this effect is an intrinsic nucleation and growth process dominated locally by heating/cooling at the phase boundary and the dipole interaction (by Yako and Fujita [117, 120]) or by thermal activation over the energy barrier (by Zhang *et al.* [119]). Therefore, disagreement over the origin of this extrinsic hysteresis still exists. In either case, the process would be unavoidable and the rate of transition limited by thermal conductivity, and also the time to magnetoelastically extend the phase boundary. Both cases, treating the rate dependence as an intrinsic property, are related to the feature of relaxation and are discussed in section 2.2.3.

2.2.2 High operating frequencies

With regards to fast field rates, there have been various studies of magnetocaloric systems at application operating frequencies (of the order of Hz). Kuz'min looks theoretically at the maximum frequency of a cyclic system consisting of a magnetocaloric coolant bed of regions of solid coolant material, separated by spaces occupied by heat exchange liquid [121]. The author finds a frequency limit of 200 Hz, dominated by the thermal conductivity of the coolant and the heat exchanger viscous friction. However, in addition to not addressing the significant eddy current heating which would occur at such frequencies, this neglects the temporal delay in the response of the magnetisation to the applied field, e.g. a non-instant return of the material to zero magnetisation with complete removal of field. This delay is in essence the principal feature of the rate dependence studies discussed in section 2.2.1, therefore this model cannot necessarily be applied to first-order systems; certainly, not for first-order $La(Fe,Si)_{13}$. From an experimental perspective, Trung *et al.* [122] use pulse-fields to measure the adiabatic regime of first-order $(Mn,Fe)_2(P,Ge)$ at a field-rate of 300 $T\,s^{-1}$, to a maximum field of $\mu_0 H = 20$ T (corresponding to cycling frequencies up to 25 Hz), specifically to extract values for ΔT_{ad}. They see (Figure 2.9(a)) the transition with increasing field considerably broadened in field from the isothermal transition (from a width of 2 T to more than 5 T) and a reduction in M, but propose that this is not a limiting factor to the working frequency, since there is minor hysteresis with the subsequent adiabatic transition with decreasing field (not shown). However, it must be acknowledged that this concerns considerable field strengths ($\mu_0 H > 5$ T) beyond the range of permanent magnets required for application, and more importantly does not account for extraction of the heat (i.e. work) between the two adiabatic processes of magnetisation and demagnetisation. When this latter point is accounted for, and the temperature of the material at the maximum field is returned to the initial temperature previous to field application, the resultant demagnetisation process will follow a different adiabatic curve, preferring larger magnetisation, and a much more considerable hysteresis will result.

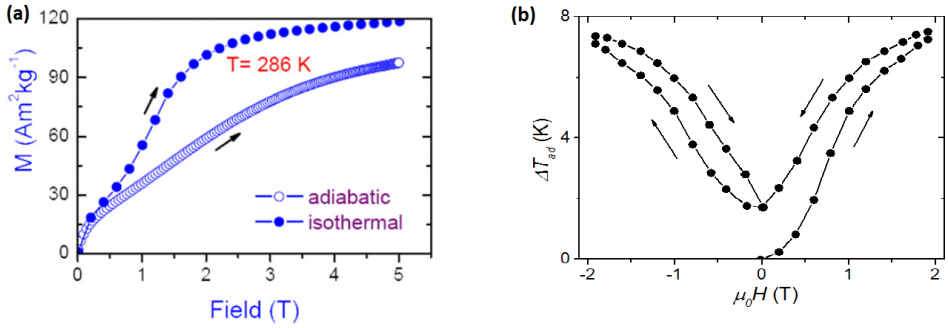


Figure 2.9: (a) Reprinted from Ref. [122]: the isothermal and adiabatic magnetisation response to increasing field of powder samples of $Mn_{1.2}Fe_{0.8}P_{0.75}Ge_{0.25}$ at 286 K. © IOP Publishing. Reproduced with permission. All rights reserved. (b) Reprinted from Ref. [33]: the ΔT_{ad} dependence on increasing and decreasing field, applied at rate 2 $\mathrm{T\,s^{-1}}$, of a $4 \times 4 \times 1$ $\mathrm{mm^3}$ sample of $LaFe_{11.6}Si_{1.4}$ at 191.3 K. © 2010 WILEY-VCH Verlag GmbH & Co. KGaA, Weinheim.

Specific to $La(Fe,Si)_{13}$, Lyubina *et al.* [33] use a Halbach type magnet set-up which allows field rates of 2 $\mathrm{T\,s^{-1}}$, up to 1.93 T, to make the same measurement (in this case, on bulk samples). As shown in Figure 2.9(b), in this field range, close to T_{C}, a ΔT_{ad} value of 7 K is reached. However, with closer examination of the $\Delta T(H)$ behaviour, there is no clear evidence of saturation of the temperature in increasing field, and reducing the field to zero returns the sample to a temperature 2 K above the initial temperature. This suggests that the full transition has not fully completed. Such a situation will therefore reduce the performance of the material due to an inability, at such frequencies, to use the full ΔT_{ad} and ΔS_{m} available.

2.2.3 Relaxation across the phase transition

As remarked in section 2.2.1, Zhang *et al.* [119] report a rate dependence equivalent to that shown in Figure 2.8 in $LaFe_{11.7}Si_{1.3}$, which was explained as a time-dependent process governed by thermal activation over the energy barrier. They show that with H and T held constant at the transition, the magnetisation evolves from large to small M over a time scale of 100 to 200 s in a 16.5 mg sample, indicating the occurrence of the FM to PM phase transition in a temporal evolution (or, relaxation) process. The increase of hysteresis at a fast

field rate is explained by the finite time for the transition to occur via relaxation, and these findings are complemented by simulated results using a thermal activation model.

However, for magnetic order phase transitions, the role of the magnetic dipole interaction is important and must be considered: here Zhang *et al.* discuss that the relaxation is slowed both by the dipole interaction between the PM and FM states, once the sample is in mixed phase (post-nucleation), and by the the change in internal field from changes in the demagnetising fields as M evolves, which increases the energy barrier height. The latter case, in the example of the PM to FM transition, can be described by the internal field decreasing as relaxation occurs, due to the increase of demagnetising fields as M increases (see section 2.3 for a fuller discussion of demagnetising field effects).

In Ref. [118], Fujita *et al.*, measuring the sample temperature directly, observe a degree of supercooling beyond T_C in the thermally driven transition of $La(Fe_{0.88}Si_{0.12})_{13}$. This indicates a energy cost to nucleation, after which the latent heat release balances the cooling rate, causing the temperature to remain mostly constant for a period of 72 s whilst the transition takes place. The process of this balanced period is discussed in terms of the volume energy gain from the release of latent heat, which, as the transition progresses, becomes dominated by an accelerated growth process related to the energy gain from decreasing the size of the PM-FM boundary and the dipole energy. For an increased cooling rate the time for the transition to complete decreases, indicating an quickening of the growth in response to a larger separation between the bath and sample temperature. They conclude that growth speed is principally dominated by the dissipation of the latent heat at the boundary. Further measurements, determining the evolution of the FM volume fraction in the thermally driven transition under different cooling rates, observe a good agreement with a Johnson-Mehl-Avrami (JMA) like transition process [117, 123]. Since the model assumes that the rate of transition is independent of the extent of transformation already occurred, the shape of the JMA curve is not affected by where on the curve the transition starts [62, 63]. In Ref. [89], the JMA curves of the three different cooling rates lie on a single curve, indicating a T-rate independence and intrinsic growth dominated process.

Since these measurements, on cooling, are not in isothermal conditions (i.e. a change in the external environment is driving the transition), it is not strictly a relaxation process. However, following this, Yako *et al.* [120] demonstrate relaxation at constant T and H, in which the onset of the transition is approached in field, which is then paused at various stages through the transition. Full relaxation from the PM to the FM state is observed, as shown in Figure 2.10(a). The variation between the curves is simply a hallmark of the different fractions of transition completed before the field is held constant. These curves fall unto a universal curve when the time axis of each is shifted, itself which again follows JMA behaviour. Since the PM and FM phases of the mixed phase, during the transition, have a magnetic dipole interaction, they cannot be treated as independent, and analysis of the JMA fitting indicates that the new FM volumes merge into a large region, as opposed to independently and randomly nucleating across the sample. However, again they conclude that the creation and dissipation of latent heat on the local scale, at the boundary, is the dominant factor of the relaxation growth process. It should be remarked that that these time scales, for all the samples in this literature, are comparable, in the range of tens to hundreds of seconds.

Further studies by Kuepferling *et al.* [124], using magneto-optical imaging of the thermally driven transition of $La(Fe_{0.9}Co_{0.015}Si_{0.085})_{13}$, have observed periods of continuous propagation of the new phase interspersed with so-called avalanches, which move the FM/PM boundary at a velocity over an order of magnitude faster, and which occur independently of the cooling/heating rate. This is interpreted as an athermal character of the phase transition, caused by boundary pinning at locations with high energy barriers due to microstructure, such as crystal defects or micro-scale cracks, since they were observed to always occur spatially in the same positions of the sample. This appears to be a form of relaxation which is fast in scale. However, it should be noted that the temperature range over which the 'athermal' character is claimed to be present is less than 1 K; this has important relevance to the results discussed in Chapter 5.

Related dynamic effects have been seen in other magnetocaloric systems, such as $Gd_5(Si,Ge)_4$

[125, 126] and Heusler alloys [127], demonstrating a certain commonality to these effects in first-order systems. In both cases, models of thermal activation over the energy barrier were able to describe the observations. However, the case of $La(Fe,Si)_{13}$-based materials, and the role of latent heat at the boundary, is not directly comparable, since the different competing processes at play, particularly the dominant effect of magnetostructural effects for $Gd_5(Si,Ge)_4$ and Heusler alloys, cause a very different free energy landscape, with larger energy barriers, for which large hysteresis is an additional result.

A result more similar to that of Yako *et al.* is observed by Manekar and Roy in the AFM to FM transition of FeRh [128], in which the relaxation follows a power law consistent with long-range dipole interactions between separate FM nuclei formed within the AFM matrix. These results demonstrate agreement with the JMA model and therefore suggests growth similar to the crystallisation of solids as derived by Avrami.

2.3 Role of demagnetising fields

Another variable whose relevance has become significant, and has a crucial role within the scope of the results detailed in Chapter 4, is that related to the effects of demagnetising fields, defined by the shape of the material under question. Demagnetising fields are a phenomenon of magnetic samples in which the field created by a sample's magnetisation, M, acts to oppose that magnetisation [12]. Under an applied field, H_{app}, this leads to a reduction of the sample's internal field strength, H_{int}, by an amount defined by a factor, known as the demagnetising factor, N, which is purely geometrically, i.e. sample shape, dependent:

$$H_{\text{int}} = H_{\text{app}} - N \cdot M \tag{2.1}$$

The demagnetising field is only uniform across the sample (in which instance N can be treated as a scalar) in the special case of ellipsoids, for which the infinite needle (field in the direction of the needle), infinite plate (field direction perpendicular to the surface) and sphere scenarios

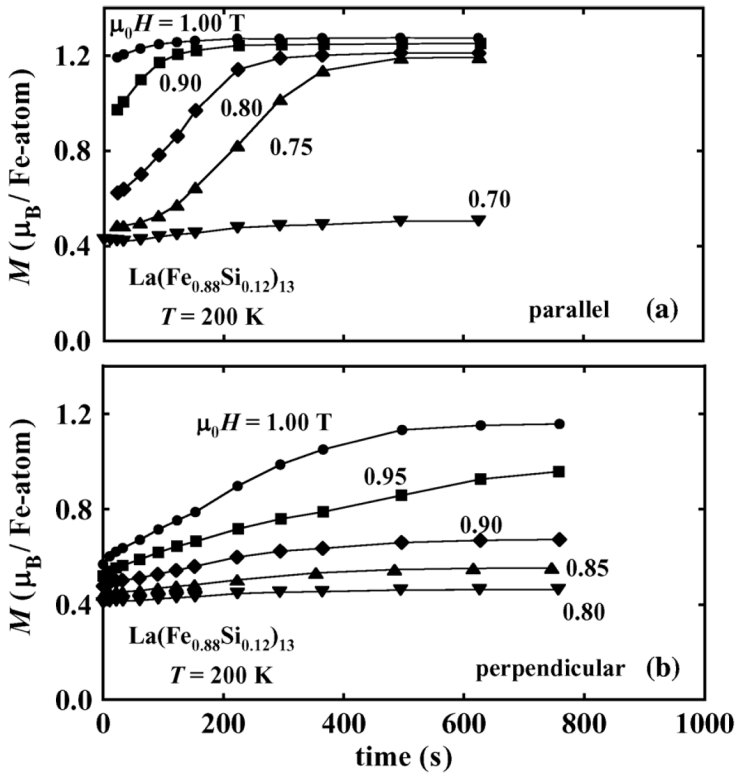


Figure 2.10: Reprinted from Ref. [120], time dependence of the magnetisation of $La(Fe_{0.88}Si_{0.12})_{13}$ under various constant applied magnetic fields, as labelled, swept from 0 T in directions (a) parallel and (b) perpendicular to the direction of the longest sample axis. © 2011 IEEE.

have $N = 0$, $N = 1$ and $N = \frac{1}{3}$, respectively. N in the three dimensions, x, y and z, sums to 1, therefore for field applied orthogonally to the previous needle and plate examples, $N = \frac{1}{2}$ and $N = 0$ respectively. For all other shapes, the demagnetising field is not uniform and is in most cases impossible to determine analytically. A numerical solution even for cuboid shapes can be very difficult to evaluate and is often simplified to an average N across the whole shape [129]. In addition, M itself will vary across the shape to further complicate any calculation of H_{int}, requiring an iterative process in the evaluation, since the local magnetisation at a given point depends on the local internal field which in turn is determined by the sample magnetisation, and so on [130].

2.3.1 Second-order systems

The importance of demagnetising fields, specific to MCE materials, has been studied in the bulk of work by the Risø group, TU Denmark [130, 131, 132]. Since all refrigerants will have a shape, whether they be regular bulk shapes or in packed powder form [132], the demagnetising fields present may greatly vary, and whether or not this has a negative impact on the magnetocaloric properties should be understood. In Ref. [131], the effects of demagnetising fields on the magnetic transition of a large $40 \times 25 \times 0.9$ mm^3 cuboid plate of second-order Gd is spatially analysed, both by a numerical model and from the adiabatic temperature change it undergoes, via the MCE measured by thermography, to calculate the change in internal field present in the material. By rapidly demagnetising the sample at a field rate of 1.5 T s^{-1} from a magnetised state ($\mu_0 H = 1.1$ T) to a fully demagnetised state ($\mu_0 H = 0$ T), the local magnetic field in the applied field scenario is determined indirectly from the temperature measured, using measured ΔT_{ad} as a function of local magnetic field reported by the group in Ref. [87]. They observed a variation of H_{int} between 1.1 T in the middle to 0.9 T at the ends of the sample, when the field is in the direction of the sample plane, and between 0.6 T in the middle to 0.4 T at the ends when the field is applied 90° to the sample plane. Using such an indirect method relies on the adiabaticity of the experiment during the field removal and that the temperature change is indeed reliably represenative of the internal field change. However, they observe good agreement with the numerical model. This result demonstrates a substantial variation across the sample, and a vast decrease in H_{int}, between the in-plane (low demagnetising factor) and out-of-plane (high demagnetising factor) orientations, which validates the importance of this effect with regards to magnetic cooling.

Trevizoli *et al.* [133] have explicitly looked at the influence of demagnetising fields on the performance of an active magnetic regenerator refrigeration cycle, using Gd plates as the coolant. They conclude that the reduced internal field strength of cuboid samples with a large demagnetising factor results in a considerable cooling capacity performance loss (by up to 27% between $N = 0.213$ and $N = 0.687$). This loss is therefore minimised by reducing N via shape

or field orientation. Several other studies on the impact of sample shape and demagnetising fields on ΔS_{m}, for second-order transitions, have demonstrated similar reductions with large N [134, 135, 136].

2.3.2 First-order systems

Extending this to first-order systems, those with moderate magnetocrystalline anisotropy will be dominated by the anisotropy feature in the magnetic and temperature transformation [3, 137, 138]. Thus, demagnetising fields, while clearly still significant, will not necessarily govern the response of the metamagnetic transition to external field. These include the families of $(\mathrm{Mn,Fe})_2(\mathrm{P,Si,Ge})$ and $\mathrm{Gd}_5(\mathrm{Ge,Si})_4$, and also the manganite series and Heusler alloys [7]. However the $\mathrm{La(Fe,Si)}_{13}$ family has no magnetocrystalline anisotropy and the subsequent domination of shape effects has been shown by Yako *et al.* [120] to have a significant impact on the magnetostatics and dynamics of first-order $\mathrm{La(Fe_{0.88}Si_{0.12})}_{13}$, as shown in Figure 2.10(a) and (b): by varying the direction of the field applied to the $4{\times}1{\times}1$ mm^3 cuboid sample, the low demagnetising factor orientation (field parallel to the long axis) demonstrated full relaxation between the PM and FM phases. However, in the high demagnetising factor orientation (field perpendicular to the long axis), the equivalent relaxation proceeds at a significantly slower rate, and becomes arrested in an incomplete, mixed-phase state midway through the transition. This is explained as being due to the energy loss from the magnetic dipole energy, as the PM-FM surface expands, exceeding the volume energy gain from latent heat release. Additionally, in this geometry, the transition is shifted to higher values of $\mu_0 H$ due to the resulting decrease of the internal field. Since in the two situations the thermal linkage within the sample and with the bath is identical, the authors conclude that the influence of the demagnetising effect on the dynamics is substantial.

Further development from the same group, Ref. [117], combining dynamic magnetisation measurements with Ginzburg-Landau model simulations, and additionally using Seebeck measurements of the MCE heat release and absorption in the field-induced transition (in the low

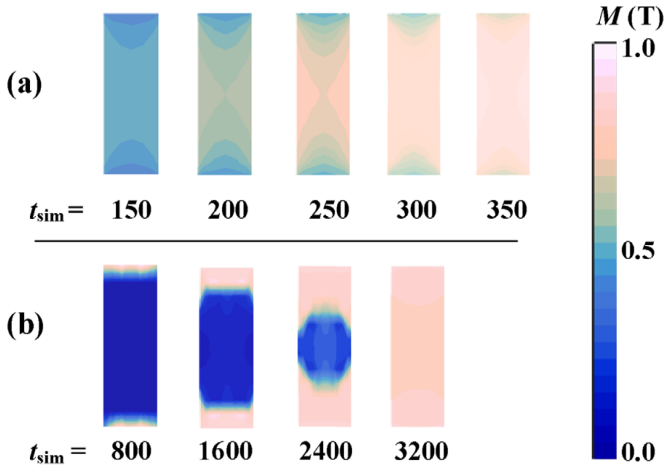


Figure 2.11: Reprinted from Ref. [117], the simulated time evolution of the local magnetisation at representative values of simulation time, t_{sim}, for (a) the field induced and (b) the thermally induced PM to FM transitions, in first-order systems. In the former, the field is applied in the direction parallel to the longest dimension, i.e. up/down with respect to the page. Note that the variable M should be multiplied by μ_0 for the unit to be correct. Reprinted with the permission of AIP Publishing.

demagnetising factor orientation), reveals a shape-symmetric growth of the new phase, but asymmetry between the two transitions, PM to FM and FM to PM. In the former case, the field driven PM to FM transition (Figure 2.11(a)) is shown to first nucleate in the middle of the sample with respect to the direction of field, but at the two edges in this region, as indicated by the contours of larger magnetisation as the transition progresses. This is due in part to the central region having the larger internal field, determined by the impact of the demagnetising fields on the rectangular shape, and in part to the preference of the nucleated region to have a shape favourable to the continuity of magnetic flux within and without the sample, leading to semicircular FM regions on either edges being preferable. The FM regions then grow towards the ends of the sample (in the direction of the field) to complete the transition. This is confirmed by the Seebeck voltage measurement (Figure 2.12), which uses the inherent temperature gradient, caused by the local variance of the transition across the sample, to infer the position of nucleation and growth of each phase. This is in agreement that the PM to FM transition begins in the centre and progresses to the ends, and additionally

shows that the reverse FM to PM transition conversely starts by nucleation of the PM state at the two opposite ends and finishes in the centre.

By comparison, Figure 2.11(b) shows the simulated behaviour of the thermally-driven PM to FM transition and demonstrates that, without the influence of applied field and the subsequent demagnetising fields, the FM region preferentially nucleates at the two furthest ends and grows towards the middle, affirming the importance of sample shape within applied fields to the transition.

2.4 Heat capacity

2.4.1 The low temperature limit

The heat capacity of a solid has been well described at low temperatures by the Debye approximation, which gives the phonon contribution as a cubic function of temperature:

$$C_p = \frac{12\pi^4 N k_\mathrm{B}}{5}\left(\frac{T}{\theta_\mathrm{D}}\right)^3 \tag{2.2}$$

Where N is the number of atoms, k_B is Boltzmann's constant and θ_D is a material, structure and environment specific parameter called the Debye temperature. This formula is accurate for temperatures where $T \ll \theta_\mathrm{D}$. Eqn. 2.2 can be simplified to:

$$C_p = \beta T^3 \tag{2.3}$$

Where:

$$\beta = \frac{12\pi^4 N k_\mathrm{B}}{5\theta_\mathrm{D}^3} \tag{2.4}$$

At high temperatures, the Dulong-Petit law, $C_p = 3Nk_\mathrm{B}$ or $c_p = 3R$ per mole of atoms, is recovered, where $R = 8.314\ \mathrm{J\,mol^{-1}K^{-1}}$, corresponding to all phonon modes having been excited and simply the degrees of freedom per atom. The temperature at which this is reached

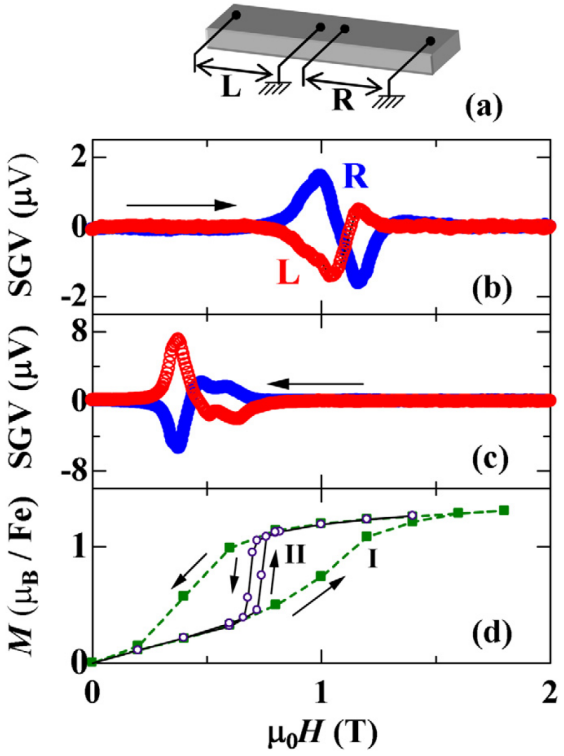


Figure 2.12: Reprinted from Ref. [117], (a) schematic view of the experimental set-up for the Seebeck voltage measurement of $La(Fe_{0.88}Si_{0.12})_{13}$. The Seebeck voltage response at 200 K, as a function of magnetic field applied in the direction parallel to the direction of the voltage measurement, is shown for (b) increasing and (c) decreasing magnetic field, at an applied field rate of 20 $mT\,s^{-1}$. (d) The corresponding magnetisation curve (I) at 200 K with the arrows indicating increasing and decreasing magnetic field. Curve II is taken 300 s after the field is varied and then paused at a variety of field strengths (equivalent to at an effective field rate of 0.5 $mT\,s^{-1}$), and illustrates the field rate dependence present in this composition (see section 2.2.1). Reprinted with the permission of AIP Publishing.

is determined by θ_{D} [139].

For many solids, phonons are not the only contribution to the heat capacity. For metallic and magnetic materials we must take into account the role of electrons and spin waves (otherwise known as magnons when thought of as quantised quasiparticles), respectively, the former which has a linear dependence on T and the latter which for ferromagnets follows a $T^{3/2}$ law [12]. Together these sum to the total heat capacity which in the low temperature Debye limit can be written as:

$$C_p = \gamma T + \alpha T^{3/2} + \beta T^3 \tag{2.5}$$

Here, γ is known as the Sommerfeld coefficient, proportional to the density of states at the Fermi level, $N(E_{\mathrm{F}})$, and α is related to the spin wave stiffness coefficient, D, at the low temperature approximation by [140]:

$$D = k_{\mathrm{B}}^{5/3}\left(\frac{0.113}{\alpha}\right)^{2/3} \tag{2.6}$$

D itself is represented in the parabolic dispersion of spin waves within a medium, $\hbar\omega = Dk^2$. It should be remarked that the $T^{3/2}$ form of the heat capacity is specific to ferromagnetic lattices (spin waves within an antiferromagnet have a T^3 heat capacity component, for example). However, only the ferromagnetic system is studied in this thesis (note that since Eqn. 2.5 and the extractions of the parameters are valid only at low temperature, we are far below the temperature at which the paramagnetic phase exists in all La(Fe,Si)$_{13}$ compounds).

2.4.2 Sommerfeld coefficient enhancement

The electronic heat capacity component, represented by the Sommerfeld coefficient, γ, is a function of $N(E_{\mathrm{F}})$, as stated in section 2.4.1. However, this direct relationship can be altered in many lattices by enhancement of γ by electron-electron, electron-phonon or magnetic interactions, which result in an increase of the contributing electrons' effective masses [139]. Such enhancements are prevalent in heavy fermion systems, which are often associated with

exotic low temperature behaviour such as superconductivity and quantum phase transitions, which can materialise at very low temperatures and in large applied fields or pressures. For example, Michor *et al.* [141] study the $NaZn_{13}$-structure compound $LaCo_9Si_4$ which for this Co/Si content sees a vanishing of the FM state (smaller Si contents, e.g. 3.9 per formula unit, have FM ordering at low T). Nevertheless, close to absolute zero, a first-order IEM transition into the FM state occurs in field. Unlike the IEM feature of $La(Fe,Si)_{13}$, which occurs at large T, that of this compound suggests the presence of a field-induced quantum critical point. Specific heat measurements reveal a large γ in zero field of 200 $\mathrm{mJ\,mol^{-1}K^{-2}}$, in comparison to that predicted theoretically from density of states (DOS) calculations of 45 $\mathrm{mJ\,mol^{-1}K^{-2}}$, indicative of a electron mass enhancement, which is claimed to specifically originate from spin fluctuations and strongly exchange-enhanced Pauli paramagnetism. γ increases significantly to above 230 $\mathrm{mJ\,mol^{-1}K^{-2}}$ in 5.3 T, at which the transition occurs for a temperature of 2 K, before dropping again in larger fields. The correlation between the presence of the IEM transition and the enhancement of the Sommerfeld coefficient gives an example of the important role of electron interactions in these types of compound.

For $La(Fe,Si)_{13}$ compounds, low T heat capacity measurements are well within the FM state and far from the phase transition where there will be a sharp peak. Several studies have used such measurements but have only reported θ_{D} values [88, 142]. However, there have been reports of γ values in compounds of $La(Fe,Si)_{13}$ as a product of DOS calculations [94, 143], giving γ for the FM state in the range 16-24 $\mathrm{mJ\,mol^{-1}K^{-2}}$. Since $La(Fe,Si)_{13}$ exhibits itinerant electron magnetism and spin fluctuations [21], with strong evidence for cooperative contributions between the magnetic, lattice and electronic entropy changes at the transition [94], a similar enhancement over the theoretical prediction is expected. A fuller summary of the results from the literature is given during the discussion of related results in Chapter 6.

3 | Experimental Methods

In this chapter I cover the sample preparation and principal experimental methods and techniques used in this thesis. All measurements, except where stated, were undertaken by the author. The x-ray diffraction data and analysis in Chapter 4 was undertaken by Dr. Julia Lyubina, and the 'microcalorimetry' heat capacity and latent heat measurements in Chapter 5 were performed by Dr. Milan Bratko.

3.1 Sample preparation

Two sample sets were studied in this work, from two separate collaborators. Samples of nominal composition $LaFe_{11.8}Si_{1.2}$, $LaFe_{11.6}Si_{1.4}$ and $LaFe_{11.4}Si_{1.6}$ were provided by O. Gutfleisch of TU Darmstadt, Germany, and prepared as described in Ref. [85] using induction melting in a purified Ar atmosphere. In order to obtain the $NaZn_{13}$-type single phase the samples were annealed at 1373 K for 7 days then quenched in water. The phase composition and homogeneity was inspected by energy dispersive x-ray spectrometry, which revealed compositional variation across the samples of less than 10^{-2} at. %, as detailed in the reference. Rietveld analysis of x-ray diffraction data of the principally studied composition, $LaFe_{11.6}Si_{1.4}$, revealed the secondary α-Fe phase to compose 6 ± 1 wt% of the composition, with the rest being the primary $NaZn_{13}$-type phase.

The series of $La(Fe,Mn,Si)_{13}$ compositions, with and without interstitial hydrogen, with vary-

ing Fe, Mn and Si, were provided by A. Barcza and M. Katter of Vacuumschelze GmbH & Co, and prepared using powder metallurgy as described in Ref. [111]. Master alloys were prepared by vacuum induction melting followed by mechanical milling steps to produce fine powders. The composition of each alloy was adjusted by blending master alloys with elemental powders. Compaction of the powder blends was performed by cold isostatic pressing. The green bodies were vacuum sintered at around 1373 K followed by an annealing treatment at 1323 K [144]. Hydrogenation was performed on granulate material with a particle size less than 1 mm by heating to 773 K in an argon atmosphere. At 773 K argon was replaced by hydrogen and the samples were cooled down to room temperature in hydrogen atmosphere in about 10 h. The hydrogen content (full hydrogenation) was determined by the hot gas extraction method, and has been shown to be stable over a long period of time [111]. All samples were estimated from magnetometry measurements of the Fe ferromagnetic response to have α-Fe contents < 5 wt%. Scanning electron microscopy analysis revealed a very small amount of La-rich secondary phase [106]. All samples were formed as bulk, structurally dense (not porous) polycrystals of irregular shape.

The sample properties are assumed to be dominated by the compositional differences and not significantly affected by the differing fabrication methods. The two sample sets for the most part are used for investigation of separate properties, however one specific result is shown to be consistent between samples from each set, supporting this assumption.

Inhomogeneity via compositional variation across the samples is expected to exist to some degree, although characterisation of the $La(Fe,Si)_{13}$ samples suggests here it is not significant. This is discussed specific to the results of Chapter 4 in section 4.5. With regards to the $La(Fe,Mn,Si)_{13}$ sample set, sample inhomogeneity is assumed to be minor compared to the changes of composition, and resulting impact on the properties, between the samples, and is discussed with the results in section 5.4.

For the shaping of samples as desired (see section 3.2 for details and discussion of sample shape choice), hand polishing was used. Samples were also chosen for their size and shape

from a large collection of samples with diameters of several mm. For scanning Hall probe measurements (see section 3.4, one surface was hand polished until level within 1 μm. For heat capacity measurements, samples were not chosen for their shape but required one side to be polished to a flat surface for good thermal contact to the heat capacity platform.

3.2 Regarding sample shape choice

Shaping of the samples is a key concern. Long, thin samples with a negligible demagnetising field would have an internal field equal to the applied field (in any other case, the internal field would be reduced), potentially leading to enhanced MCE properties reported and allowing more accurate comparison between materials or measurements. Alternatively, Bjørk *et al.* [87] have corrected for demagnetising fields using a numerical approximation in plates of MCE materials to give the correct (within the approximation) internal field; however, in general this issue is often ignored in MCE literature. Practically making long, thin samples is difficult, and exploiting this for application would require an appropriate design of heat-pump which may be affected detrimentally by an increased range of large field required. The work of Chapter 4 investigates the impact of demagnetising fields and thus specific sample aspect ratios are studied (as described in the relevant sections): indeed one of the key results demonstrates that samples with a small demagnetising field are not necessarily beneficial to a field cycle with respect to energy losses from hysteresis, and the importance of inhomogeneous demagnetising fields, resulting from irregular (i.e. non-ellipsoid) shapes, is a key discussion point. Therefore, samples have been shaped using polishing to close to the desired aspect ratio and size. In these results, the significant role of the demagnetising field is demonstrated within the limits of sample aspect ratios used, and therefore the extreme cases (infinite rod or infinite plate) are not required. In Chapter 5, instead the focus is on the comparison of one sample with temperature, and also between different compositions of $La(Fe,Mn,Si)_{13}$ in which irregular but similarly sized and shaped samples were selected (from a large choice of samples). This is important specifically so that the growth characteristic can be directly compared between the

samples without the influence of greatly varying demagnetising fields. Again, specific details of the samples are given in Chapter 5.

3.3 Vibrating Sample Magnetometry

Vibrating sample magnetometry (VSM) is a well established magnetic measurement technique that uses Faraday's law of electromagnetic induction, $V_{\text{emf}} = -d\phi/dt$, to measure the magnetic moment of a sample by means of sample movement within a pick-up coil. Since an induced electromotive force in the pick-up coil, V_{coil}, requires a change of magnetic flux in the direction of the axis perpendicular to the plane of the coil, movement of a sample in this direction can allow its moment to be measured if its movement is into and out of a coil, as $V_{\text{coil}} = \frac{\phi}{dz}\frac{dz}{dt}$, where z is the vertical position of sample with respect to the coil. In order to avoid induction caused by the rate of change of applied background magnetic field, H, the sample is vibrated between a set of two coils wound oppositely, cancelling all but the magnetic signal from the sample. The magnitude of the pick-up coil induced voltage signal is proportional to the sample's moment m and the movement speed, therefore at a set vibration frequency, f, and amplitude, A, with coupling constant, C, $V_{\text{coil}} = 2\pi f C m A sin(2\pi f t)$. The signal is easily calibrated to a sample with a known moment and hence moment readings are directly measured.

Two VSM set-ups have been used in this work: a vertical superconducting solenoid, supplying up to $\mu_0 H = 9$ T field, with a pick-up coil and rod vibration motor in a Quantum Design Physical Property Measurement System (PPMS), and an Oxford Instruments VSM superconducting horizontal split-coil, supplying up to 4 T, and pick-up coil, with vertical rod vibration movement. Schematics of the two systems are shown in Figure 3.1. The former has control over a temperature, T, range from 2 K to 400 K via helium exchange gas, and uses a rod vibration frequency of 40 Hz. The latter has a T range from 77.4 K to 295 K via nitrogen exchange gas, and uses a rod vibration frequency of 45 Hz. Due to differing thermal gradients

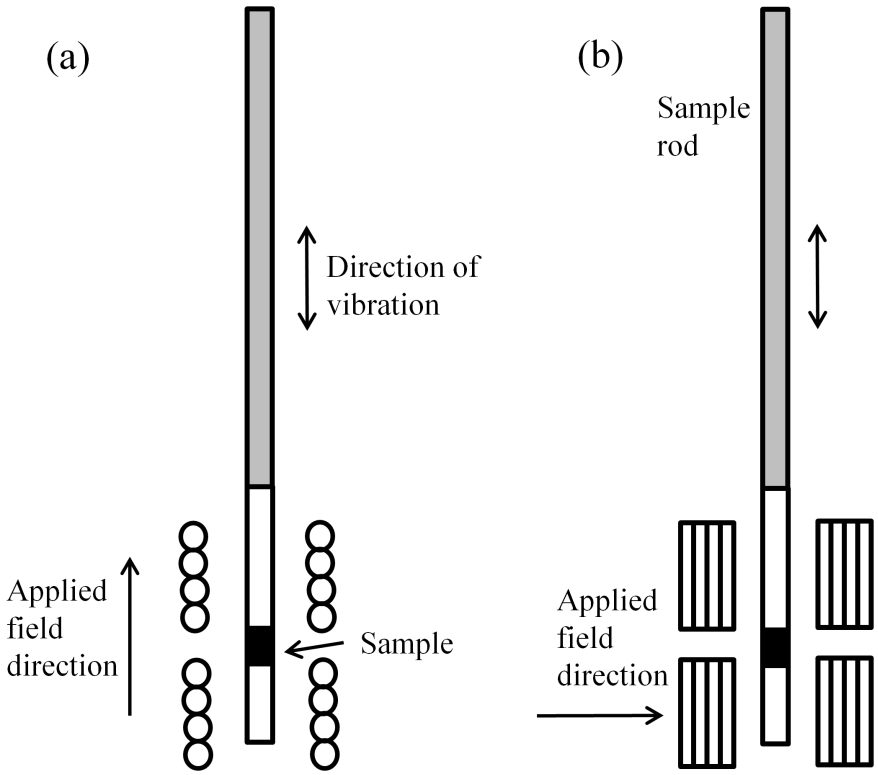


Figure 3.1: Schematic of the two VSM set-ups: (a) Quantum Design PPMS with field applied parallel to the direction of vibration and (b) Oxford Instruments VSM with field applied perpendicular to the direction of vibration.

between the T sensor and sample space between both systems, there is a small (up to several Kelvin) temperature discrepancy between the measured and actual sample temperatures in the Oxford Instruments VSM. Where possible, the data taken using the Oxford Instruments VSM have been adjusted to the thermometer of the PPMS. This has been achieved by comparing equivalent measurements undertaken in each systems. For all measurements, the samples have been attached to the measuring rod with polytetrafluoroethylene (PTFE) tape.

Due to the nature of the MCE being measured in this work, temperature changes of the sample are inherent during many measurements and correct handling of time-dependent results are important. The measurement time-constant (i.e. averaging time) is based on the vibration frequency, that is 40 or 45 Hz, and therefore on the order of 10^{-1} s. All time-dependent effects, measured as part of the results, are on time scales > 1 s. Thermal equilibration of

samples to the bath is estimated to be on time scales < 1 s.

3.4 Scanning Hall probe imaging

Scanning Hall probe imaging (SHPI) is a non-invasive, quantitative, raster scanning magnetic spatial imaging technique. The sensor used is an InSb Hall sensor. The Hall effect describes the Lorentz force deflection of moving electrons within a material in a perpendicular magnetic field. For a current moving in a field, this causes a charge imbalance in the direction perpendicular to both field and charge carrier movement, as the deflected carriers gather to one side. This results in a voltage build-up in this direction known as the Hall voltage, V_{H}, the magnitude of which is proportional to both the current flow and the field strength, $V_{\mathrm{H}} = (I \times B)/net$, where I and B are the current and magnetic flux density respectively, and n, e and t are the charge carrier density, electron charge and conductor thickness in the direction of the applied field, respectively [145]. The Hall voltage response is limited to flux incident on an area with current flow and probed by appropriate voltage leads, known as the active area, such that Hall cross or Hall bar structures are commonly used to either limit the area of material under inspection or reduce the scale of the active area to allow resolution of magnetic signals on the microscale or smaller.

3.4.1 Hall probe sensors

Hall effect sensors, which in the context of this thesis will be referred to as Hall probe sensors or simply Hall probes, are Hall cross structures usually fabricated into high carrier-mobility and low carrier density semiconductor films or quantum wells, which are highly sensitive to the magnitude of the perpendicular component of magnetic flux incident to the active area. The sensors used for this work are fabricated into the corner of wafers containing an epitaxial layer of InSb grown on GaAs, as shown by the schematic in Figure 3.2. For details of the film, mobilities and carrier densities, see Appendix B. The film used was 2.5 μm thick and

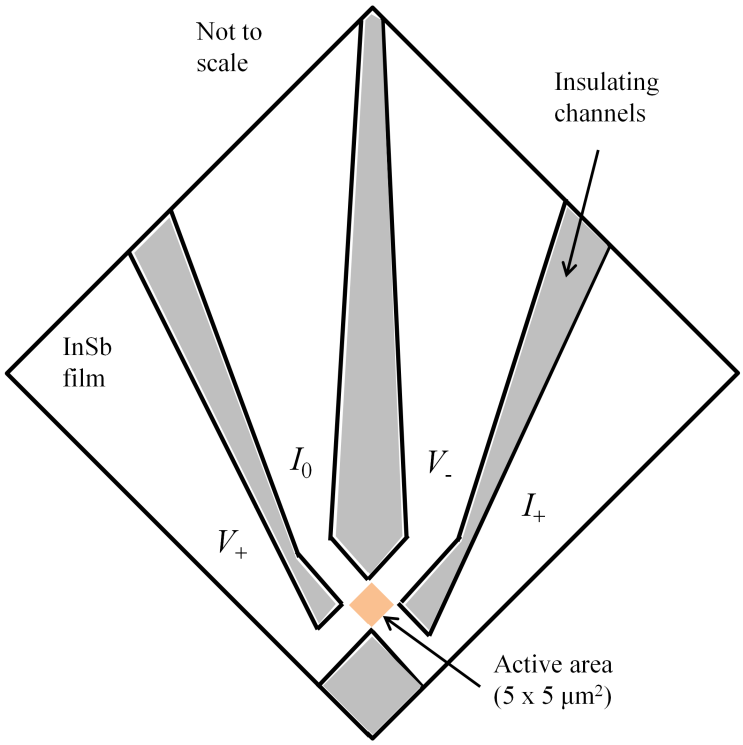


Figure 3.2: Schematic (not to scale) of a Hall probe sensor. Grey areas indicate insulating trenches in the InSb film (i.e. where there is no film) and labels show along which conduction channels the current is applied and voltage measured. The sensor is sensitive to the component of field in the direction corresponding to out-of-page.

sensor active area sizes of as low as 5 μm have been made, at distances of between 20 and 50 μm from the wafer corner to allow the sensor to be in close proximity (within 5 μm) to the sample under inspection. The films were measured to have a mobility at room temperature of $\mu = 12800$ cm^2/Vs. See Appendix B for further details of the fabrication process. Due to the linear dependence of V_{H} on H, sensors can be easily calibrated in known H and T allowing quantitative analysis of absolute field strengths.

3.4.2 Imaging specifics

The scanning apparatus [146], shown in Figure 3.3, consists of a vertical rod, at the bottom end of which is attached the Hall sensor, whose movements is controlled, via a pivot midway up the rod, by three stepper motors for the x, y and z directions at the top of the rod. The motors are housed together at the top end in order to easily allow the sensor, via the rod, to protrude into an Oxford Instruments cryostat with transverse split-coil superconducting magnet, permitting attainable magnetic fields, $\mu_0 H$, of up to 4 T projecting horizontally, and temperatures, T, of between 295 K and 77.4 K via nitrogen exchange gas. As such, the probe and sensor can be rotated horizontally so that the sensor is aligned in the direction either perpendicular or parallel to the applied field. The motors and pivoting rod set-up allow the sensor a maximum movement reach of 5 mm in both the x and y directions, with respect to the imaging plane, with sub-micron resolution capability. The sensor is set at an angle of approximately 5° to the imaging plane so that the distance between the sample and the corner of the film with the sensor is minimised. This is required since field strength falls off with distance, r, as $\frac{1}{r^3}$. The $x-y$ imaging resolution of magnetic information is therefore limited by the sensor active area size, d, and its proximity to the sample, z, and scales as $(d^2+z^2)^{1/2}$ [145].

The second principal feature of the probe is the sample attachment area, on one part of a pair of capacitor plates. The capacitor plate set-up is sensitive to movements of the sample attached, and this allows the sensor to maintain a constant and controlled fly height above the sample by constructing a sample surface plane via the following method: the sensor is slowly approached towards the sample in the z direction from a distance of approximately 200 to 400 μm until it makes contact, at which point the sudden movement of the sample and capacitor plate causes a sharp change in the capacitance signal. Where, in z, this jump occurs is then designated as the contact height position. The capacitor set-up allows this positioning to be accurate in z to within 1 μm. This process is repeated at multiple positions (chosen by the user) in a straight line along firstly the x then the y directions, to both of which a separate

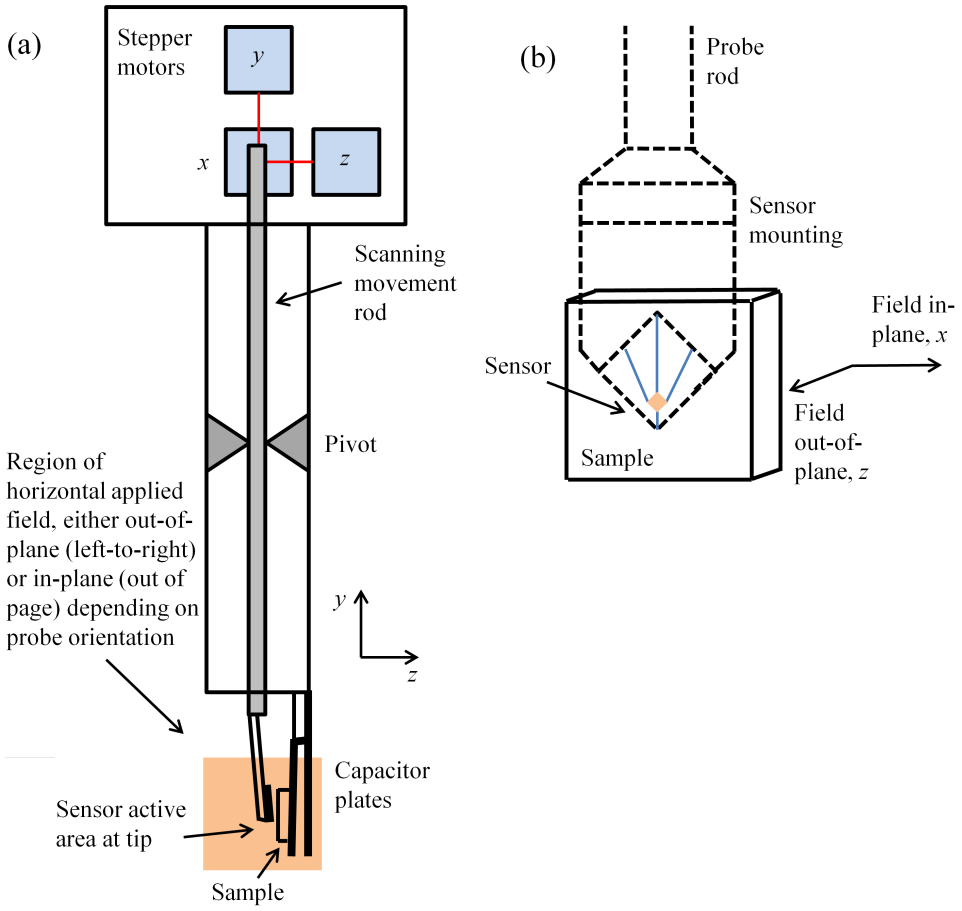


Figure 3.3: Schematic of the SHPI system: (a) an overview of the whole system and (b) a close-up of the sensor and sample.

parabolic curve is fitted (the natural movement of the probe rod can be closely approximated to a parabola). The imaging plane is then determined by these two fittings and the fly height can then be chosen separately before each image, during which the sensor raster scans across the chosen imaging window keeping constant height with respect to the sample.

3.4.3 Out-of-plane and in-plane imaging

A distinction can be made between what is termed as out-of-plane and in-plane imaging, and how they affect firstly the sensor signal and secondly the sample response. The set-up of the probe in the Oxford Instruments magnet means both are available in the same apparatus. Hall probe imaging is limited in that it is an indirect probe of a sample's magnetisation state via its stray field component perpendicular to the sample surface. A volume of sample, in a uniformly magnetised state directed out-of-plane to the surface being probed, will be detected by the sensor directly from the component of its stray field in the same direction as its magnetisation. Conversely, a volume magnetised in the plane parallel to the probed surface will either be detected indirectly by the signal from the magnetic poles at either end of a volume of uniform magnetisation, as the stray field in these locations bends out of plane to complete the field lines, or will not be detected at all, if the ferromagnetic domains are aligned in an interlocked pattern to minimise the stray field and magnetostatic energy (otherwise known as a 'soft' ferromagnet with zero net moment). Note that in this latter scenario, stray field is emitted from the domain walls, however in practice is not detected due to the domain wall size being well under the resolution of the sensor. See Figure 3.4 for examples of these situations.

Applying a background magnetic field, H, will solicit a response from magnetic materials, whether it is the appearance of a net moment in paramagnetic, diamagnetic or soft ferromagnetic materials, or bringing the magnetisation towards the direction of the field in hard ferromagnets whose moment is aligned along an easy axis. The total flux density measured by the sensor is $B = \mu_0(H_{\text{app}} + H_M)$, where H_M is the additional field induced by the sample's

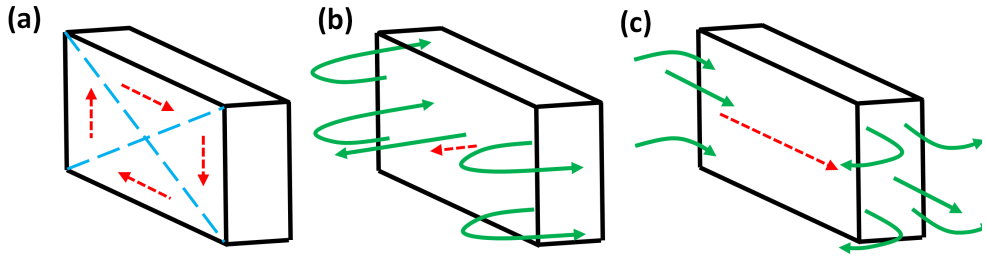


Figure 3.4: A simplified schematic of example stray field lines (solid arrows) from a plate-like magnetic material, such as those imaged in this thesis, with (a) Interlocked domains (a simplified example) and zero net magnetisation, (b) Field applied out-of-plane and uniformly magnetised in the same direction, and (c) Field applied in-plane and uniformly magnetised in the same direction. The sensor images the largest visible surface in all three cases. The dashed arrows give the magnetisation direction. For all three cases, the sensor is sensitive to flux in the direction parallel to the magnetisation direction indicated in (b). The dashed lines in (a) show the domain boundaries.

magnetisation. All of the magnetic states studied in this work are either paramagnetic or soft ferromagnetic, therefore an applied field is required in order to measure any sample stray field. In addition many of the properties studied are dependent on the external field. A Hall sensor will be sensitive to this applied field (termed background field) as with the stray field of a sample. Due to its uniformity across the imaging window, the background field, $\mu_0 H_{\mathrm{app}}$, is easily subtracted, leaving only the field response from the sample. This subtraction is used for all SHPI results in this thesis. Out-of-plane imaging therefore is defined as that where H is perpendicular to the image plane, and therefore the magnetisation and resultant stray field signal of a sample tends to align in the direction to which the sensor is sensitive. An increase in sample magnetisation, ignoring for now the effects of demagnetising fields, will lead to a close-to-linear increase in stray field and therefore sensor V_{H} response (the linearity of the V_{H} increase is dependent on the response of the InSb sensor used: in the case of this work the sensors have a close-to-linear $V_{\mathrm{H}}(H)$ characteristic as shown in Figure 3.5; the sensor can then be calibrated in order to give correct $\mu_0 H$ values). Such an increase of stray field strength is indicated in this thesis by an increase in brightness of the pixel.

Conversely, in-plane imaging is defined as the orthogonal case with H aligned along the

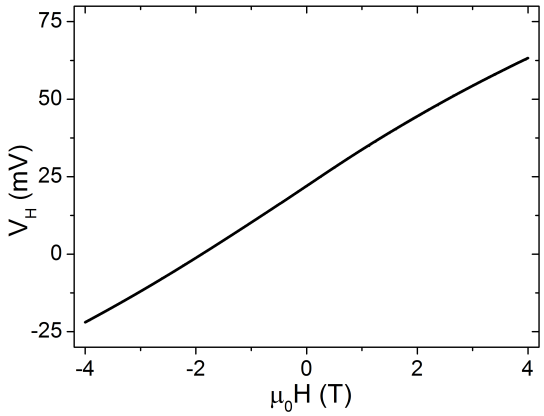


Figure 3.5: Example Hall sensor calibration curve at 295 K for a 5×5 μm^2 sensor in a 2.5 μm thick InSb film, with 1.2 V applied between I_+ and I_0 and a 180 Ω resistor in series to the applied voltage. The $\frac{1}{\mu_0} dV_{\mathrm{H}}/dH$ response curve is dependent on the current (approximately 5 mA) and carrier density, n. Further details are given in Appendix B.

imaging plane and thus in the direction to which the sensor is not sensitive. Therefore, the background applied field signal will not be measured and the sample's preferred in-plane magnetic state is detected via stray field from the poles formed where there are changes in magnetisation. An example is shown as part of the results in section 4.6.1. Having both out-of-plane and in-plane imaging options is required, due to the sample shape-dependent nature of many of the phenomena studied in this thesis, as outlined in Chapter 4.

3.4.4 Choice of sample shape and surface fly height

Because this imaging technique is a surface sensitive technique, another limitation is that it is not necessarily representative of the volume bulk of a sample, although some degree of depth below the surface will likely be represented by the stray field measured. To counter this, samples are preferably shaped so that the largest surface is imaged and the sample is relatively thin in the z-direction. The aspect ratio of the sample's shape, demagnetising fields and their importance in this work is discussed in detail throughout this thesis (see section 2.3

and 4.6), therefore specific sample dimensions will be described in the relevant sections. Due to the sensitivity of the stray field strength to distance from the magnetised sample, and the fall off of resolution with distance, samples measured using SHPI are required to have a polished surface, flat on the scale of micrometres, so that the sensor can easily remain at a constant fly height whilst imaging, as close to the surface as possible. For all imaging, a 10 μm thick layer of Teflon film is placed on the sample surface to protect the sensor from contact damage. The sensor is kept in contact with the Teflon film and therefore by that method maintains a regular 10 μm from the sample. To get an idea of the magnitude of field measured, at such distances, with the $La(Fe,Si)_{13}$ samples of this work fully magnetised in the FM state, stray field values of $\mu_0 H \sim 0.4$ T are commonly measured.

3.4.5 Other technical details

The Hall voltage signal from the sensor itself is obtained by applying a high frequency 9 kHz voltage at 1.2 V to the current leads (between I_+ and I_0 of Figure 3.2), with a resistor of 180 Ω (roughly an order of magnitude larger than R of the wafer) in series to maintain close to constant current of approximately 5 mA across the sensor. The resultant 9 kHz Hall voltage signal, $V_+ - V_-$, is picked out using phase sensitive detection with a lock-in amplifier. The lock-in amplifier achieves this by first amplifying the signal then multiplying it by a reference sine wave at the same frequency as the signal. The resulting waveform is passed through a low-pass filter to give a DC output proportional to $V_{\mathrm{sig}} cos\theta$, where $\theta = \theta_{\mathrm{sig}} - \theta_{\mathrm{ref}}$ is the phase difference between the signal and reference sine waves. This improves the signal sensitivity significantly and allows the measurement of very small signals by reducing interference and noise at unwanted frequencies, as well as 1/f noise which is reduced by the large frequency used. The lock-in amplifier can optimise its noise-reduction by the instrument's averaging time-constant. The larger the time constant, the more the signal is averaged and therefore the signal is improved. This, however, is at the expense of time resolution (the need for which is explained in section 3.4.6); therefore, optimisation is required. For this set-up, a 1 ms time constant is used allowing millisecond resolution: the sensor, whilst scanning during imaging,

measures up to 256 pixels (one line of raster) within several seconds. Each pixel (data point) is taken as a further average of ~ 5 to 10 time-constant averaged readings, to further improve its accuracy.

3.4.6 Local loops and dynamic Hall probe imaging

Each image takes between 10 and 30 minutes to complete, depending on the window size and pixel resolution. H and T are kept constant during each image and varied in between, depending on the property under inspection. As such, this is labelled as a static measurement, since any dynamic processes on the scale of a few minutes or less, upon which there is a strong focus in this thesis, is not probed and the material reaches its stable state, after changes in H or T, before the imaging begins. In order to probe the dynamic regime the Hall probe apparatus can perform dynamic local loops, for which the sensor is held at one position and the applied field is varied. This can be directly compared with static local loops collected from the same position across a set of static images.

An extension of this is dynamic Hall probe imaging, whereby performing a dynamic local loop (and therefore a separate field sweep) at each pixel, and building up a spatial image for each field point, allows sub-second, spatial resolution. This can be done with H applied both out-of-plane and in-plane to the imaging plane, and its use in this thesis has been developed specifically for this work. This technique can only be relevantly applied to transitions which proceed identically with every field-sweep and complete (i.e. fully reverse) within the field range used.

3.5 Heat Capacity

Heat capacity measurements were taken via the relaxation method using a commercial heat capacity puck designed for the Quantum Design PPMS. The puck consists of a platform

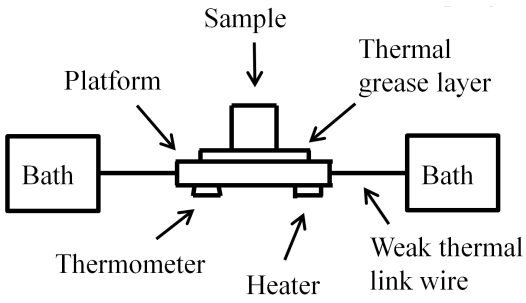


Figure 3.6: Schematic of the specific heat measuring probe, with the platform and its contents under high vacuum and isolated from the bath except via weak thermal linking wires.

which is connected to the thermal bath by a weak thermal link (wire) and operated under low pressure (less than 1 mTorr to remove unwanted thermal links through gas). Attached to the platform are a thermometer, heater and Apiezon N thermal grease to allow good thermal contact between the platform and a sample. A schematic is shown in Figure 3.6 [147]. The puck measures heat capacity at constant pressure:

$$C_p = (dQ/dT)_p \tag{3.1}$$

Assuming the platform and its contents to be thermally linked to the thermal bath via only the weak thermal conduction links, a square heat pulse of known power and duration $P(t)$ is applied by the platform heater and the temperature response of the platform is monitored in time, during the pulse and for some duration after, by the platform thermometer. Taking the assumption that the platform (including the heater and thermometer) and its contents are at the same temperature and in excellent thermal contact (with a thermal conductivity much larger than that of the weak links), the total heat capacity can be analysed from the corresponding heating and cooling curves of the platform temperature by use of a simple thermal model [147]:

$$C_{\text{total}} dT/dt = -K_{\text{w}}(T - T_{\text{b}}) + P(t) \tag{3.2}$$

Where K_{w} is the thermal conductivity of the thermal linking wires and T_{b} is the bath tem-

perature, which is constant. $P(t)$ is equal to P_0 whilst heating the platform, and equal to zero afterwards, while the platform cools. Solutions to this equation, $T(t)$, are exponential curves with a characteristic time constant, $\tau = C_{\text{total}}/K$, allowing calculation of C_{total}. The measuring of C_p of a sample is achieved simply by measuring C_p of the platform and thermal grease without the sample, called the 'addenda', before repeating the measurement with the sample attached. $C_p(T)$ of the sample is then calculated by subtracting the addenda from C_{total}, and the specific heat, c_p, can be calculated using the sample mass. Typically, multiple measurements are done as a function of T or applied magnetic field H. Because all materials have temperature dependence, and some have magnetic field dependence, in C_p, it is imperative that the addenda measurements be performed for all temperature ranges (and fields strengths if necessary) at which the sample will subsequently be measured. It is also important to remeasure the addenda each time new thermal grease is applied, as variations in its quantity will lead to different platform and grease combined heat capacity values.

For measurements of the platform heat capacity, this simple model is accurate, provided that the platform has good thermal conductivity and that the temperature increase induced by the heat pulse is small, compared to the absolute temperature, such that the heat capacity can be assumed to be constant in T. Typically a temperature increase of 2% of T is used. However, if a sample is present on the platform and in thermal contact via thermal grease, one cannot naively assume they are in perfect thermal contact. One must assume a second thermal conduction link of the thermal grease, between the sample and the platform, and use a more complicated model known as the two-tau fitting model.

3.5.1 Two-tau model

First proposed by Hwang *et al.* [148], the two-tau method assumes a second, separate thermal link of the thermal grease between the platform and sample, with conductivity, K_{g}, shown by the diagram in Figure 3.7. The sample and platform temperatures and specific heats are designated by T_{sample} and C_{sample} respectively for the sample and T_{platform} and C_{platform}

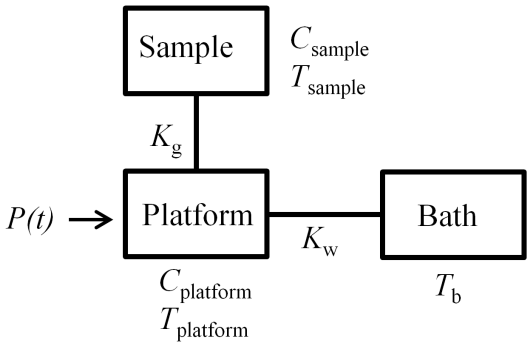


Figure 3.7: Schematic of the sample, platform and bath, and the thermal links, as described within the two-tau analysis.

respectively for the platform. The second thermal link has its own characteristic time constant τ_2 and adjustment of the model is required, given by the following equations:

$$C_{\text{platform}}(dT_{\text{platform}}/dt) = P(t) - K_{\text{w}}\Big(T_{\text{platform}}(t) - T_{\text{b}}\Big) + K_{\text{g}}\Big(T_{\text{sample}}(t) - T_{\text{platform}}(t)\Big) \quad (3.3)$$

$$C_{\text{sample}}(dT_{\text{sample}}/dt) = -K_{\text{g}}\Big(T_{\text{sample}}(t) - T_{\text{platform}}(t)\Big) \quad (3.4)$$

Eqn. 3.3 and 3.4 apply to the heating and cooling portions of the relaxation curves, respectively. The assumption is again made that the heater and thermometer are in excellent thermal contact with the platform and that the conductances of the platform and sample are much larger than K_{g} and K_{w}. Also assumed is that K_{g}, K_{w}, C_{sample} and C_{platform} are temperature independent for the temperature rise used. T_{platform} is the quantity being directly measured by the thermometer, not T_{sample}, since they are now treated separately. The heating and cooling curves can be fit via solutions to Eqn. 3.3 and 3.4 to extract C_{sample}, with knowledge of C_{platform} taken from the previously measured addenda (the addenda values themselves can be successfully measured using the simple model since $C_{\text{sample}} = 0$). This gives a powerful tool to measure the specific heat of a range of sample masses, at a range of temperatures, accurately.

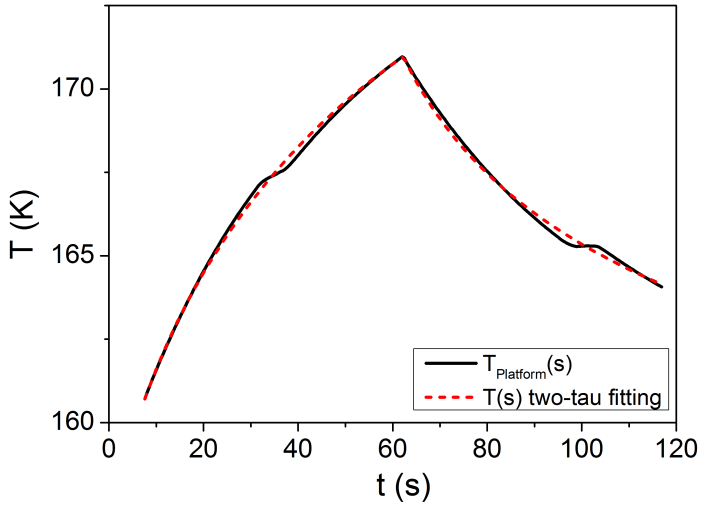


Figure 3.8: An example heating and cooling temperature relaxation plot across a first-order transition, showing the clear absorption and release of latent heat where the sudden flattening of the response occurs. A superimposed two-tau fitting to this curve shows its breaking-down in such circumstances.

3.5.2 Slope difference method

Further complications arise in materials which show either a significant change in C_p, within the temperature range of the heating and cooling curves of the relaxation method, latent heat release or thermal hysteresis. For materials with first-order magnetic and structural or volume phase transitions, all three will often be present. The standard two-tau relaxation fitting method will break down and give incorrect results. An example is shown in Figure 3.8, in which a plateau occurs in $T(t)$ for both heating and cooling, as latent heat absorption and release takes place, respectively. Using the slope difference method (SDM), careful analysis of the same heating and cooling relaxation curves can allow correct heat capacity values to be evaluated [149].

The in-built Quantum Design SDM analysis tool uses an algorithm based on the following formula:

$$C_{\text{total}}(T) = -K_{\text{w}}\Big((T - T_{\text{b}}) + P(T)\Big)/S(T) \tag{3.5}$$

Where $S(T) = dT/dt$ is the gradient of the temperature curve and $P(T) = P_0$ during heating and zero during cooling. Separate C_{total} evaluations can be taken for the heating and cooling curves, using the equation. However, due to the nature of properties being measured, specifically hysteresis and latent heat associated with first-order phase transitions, to achieve best results using SDM, considerable care must be taken regarding the choice of measurement and analysis parameters. Before measuring, it is necessary to know at which temperatures the transitions for both heating and cooling, designated $T_{\text{C, heat}}$ and $T_{\text{C, cool}}$ respectively, take place, and subsequently the magnitude of the thermal hysteresis ΔT_{hyst}. In order to capture the transition on both heating and cooling, the starting temperature, T_{i}, must be lower than $T_{\text{C, cool}}$, while the temperature rise, T_{rise}, must be larger than $T_{\text{C, cool}} - T_{\text{i}} + \Delta T_{\text{hyst}}$. Additionally, when latent heat absorption and release is present, the resultant plateaux ($dT/dt = 0$) in the $T(t)$ curves will give an infinity in the specific heat (by definition, the heat capacity during these periods is infinity, since there is no change in T even with the flow of heat energy). Therefore, these infinities must be handled with care. Use of a suitable moving average helps to smooth out the singularity and measure accurate $C_p(T)$ values, around the latent heat temperature region. However, separating the latent heat and heat capacity contributions using the relaxation technique is difficult and variations will often occur between samples measured and the choice of moving average used. Optimisation is required for each data set taken.

For all latent heat measurements, samples of mass between 1 and 8 mg were used, permitting both an accurate measurement of mass but with samples small enough in size to fit on the heat capacity platform. In some instances, multiple fragments were measured together to reach a suitable total mass. Before each sample measurement, an addenda measurement, over a range of temperatures, is carried out on the platform with a small amount of Apiezon N thermal grease attached. The platform does not have a measurable magnetic field dependence, therefore all addenda measurements were carried out in zero field. Samples were polished on one side before placement on the platform to allow good thermal contact.

3.6 Microcalorimetry

The calorimetric measurements, vital to the discussion in Chapter 5, were performed by Dr. Milan Bratko. Measurements are undertaken on small fragments (on the scale of μg mass), in a technique separate to that described in section 3.5. This technique allows the separation of latent heat and heat capacity, which can be accurately calculated. For details of this method, see Ref. [99]. To distinguish the technique in this thesis, it is referred to as 'microcalorimetry'. The determination of the latent heat, Q_{lh} from this technique was also carried out by Dr. Bratko and is described in detail in Ref. [150].

3.7 X-ray diffraction

Measurements and Rietveld analysis of x-ray diffraction data in Chapter 4 were carried out by Dr. Julia Lyubina on a powder of sample.

4 | Dynamics and Magnetostatics of the Metamagnetic Transition in $La(Fe,Si)_{13}$

The focus of this chapter is on two compositions of $La(Fe,Si)_{13}$: $LaFe_{11.6}Si_{1.4}$, referred to, for simplicity, by its Si content, $x = 1.4$, which shows first-order behaviour in its metamagnetic transition, and $LaFe_{11.4}Si_{1.6}$, referred to as $x = 1.6$, whose T_C is several degrees higher and whose transition displays second order behaviour. The principal aims are to investigate the first-order, $x = 1.4$ composition, predominantly at one temperature (194.5 K), with $x = 1.6$ used principally so that comparisons with a second-order transition can be made. In section 2.1.1, a discrepancy concerning what Si content gives second-order properties ($x < 1.6$ or $x < 1.8$) was discussed. In the case of materials measured for this thesis, the $x = 1.6$ composition is second-order, in agreement with much of the literature [81].

Following the analysis of the two compositions' MCE properties, via the $M(H)$ curves and evaluated entropy changes, the field sweep rate dependence and magnetic relaxation dynamics, as a function of approaching field rate, are measured and discussed in terms of extrinsic and intrinsic contributions to the growth characteristics and hysteresis width. These contributions, and a method to separate them, are analysed by field rate dependence and relaxation measurements on a series of sample scenarios, in which cracks are introduced into the sample.

The results are discussed in terms of the sample thermal contact with the bath and demagnetising fields. The effects of the latter are measured explicitly using scanning Hall probe imaging and the dominant role of the demagnetising factor is confirmed. The majority of results in this chapter are published in Ref. [151].

4.1 The metamagnetic transition and entropy change

Magnetisation curves at a variety of temperatures, close to T_C, are shown for both compositions in Figure 4.1, along with the corresponding $H - T$ phase lines designating the critical field of transition, H_c, for both increasing field (PM to FM) and decreasing field (FM to PM). The H_c values have been extracted for data where a field-driven magnetic transition occurs as the mid-point (in M) of the transition for both the field-increasing and field-decreasing portions. These types of figure representing, at fixed temperature, a response to field which exhibits a zero to finite magnetisation, and then a return to zero magnetisation, will be referred to as $M(H)$ plots throughout the following chapters. From Figure 4.1(b) and (d), the T_C values are estimated, from the intercept with the x-axis, as 191 K and 202 K for $x = 1.4$ and $x = 1.6$, respectively.

Such measurements are usually referred to in the literature as 'isothermal', since the change in state of the sample is often assumed to be slow enough that the thermal conduction between the sample and the temperature bath keeps the sample temperature constant. However, due to the finite field rate used in these plots and the nature of this magnetocaloric material and field rate dependence (see section 2.2.1), this is not strictly the case, as will be discussed in depth in section 4.2. This chapter will focus on the properties of the metamagnetic transition at a single temperature for each composition; features of the behaviour with T will be covered and discussed in Chapter 5. The curves at a range of temperatures are shown here as an introduction to the compositions.

In Figure 4.1(a), the characteristic field-driven first-order behaviour of $x = 1.4$ is shown:

above T_C, the transition from PM to FM, with increasing field, occurs as a sharp increase in magnetisation over a small applied field range. The reverse FM to PM transition, with decreasing field, takes place at a smaller field value, resulting in a hysteresis region. As T is increased the transition moves to larger fields in a close-to-linear relationship. The $H-T$ phase diagram in Figure 4.1(b) shows the phase line, and illustrates this behaviour. As T increases, the shift in H_c is accompanied by a decrease in both the hysteresis and magnetisation change between the PM and FM states, and a broadening of the transition towards second-order like behaviour. These features, indicative of the itinerant electron metamagnetic transition this material exhibits, will be discussed in detail in Chapter 5. Below T_C, the $M(H)$ curves follow the behaviour of soft ferromagnet, with small remanence (i.e. remaining net magnetisation at zero field), relative to saturation. Conversely, with higher silicon content, $x = 1.6$, above T_C, has a broad, second-order field-driven transition with little to no distinguishable hysteresis and continual broadening as T increases (Figure 4.1(c)). The saturation magnetisation is slightly reduced from that of $x = 1.4$, consistent with its linear decrease with decreasing Fe as observed in the literature [55, 76].

The entropy change, $-\Delta S_m$, determined from the $M(H)$ isotherms by the Maxwell relation (Eqn. 1.6) is shown in Figure 4.2. For $x = 1.4$, of the approximately 23 $\mathrm{J\,kg^{-1}K^{-1}}$ available for 0 to 4 T flux density change over a 10 to 15 K range, at least 20 $\mathrm{J\,kg^{-1}K^{-1}}$ is available for 0 to 2 T and 18 $\mathrm{J\,kg^{-1}K^{-1}}$ for 0 to 1 T, albeit over a 5 K range. This compares favourably against second-order $x = 1.6$ whose $-\Delta S_m$ for 0 to 4 T is 16 $\mathrm{J\,kg^{-1}K^{-1}}$, dropping considerably for 0 to 1 T as the shape of the entropy curve becomes more sharply pyramidal, with a peak of 10 $\mathrm{J\,kg^{-1}K^{-1}}$. This is a significantly smaller available entropy change, demonstrating the considerable advantage of first-order materials over second-order for low applied field cooling applications.

The effect of hysteresis is separate but also shown in Figure 4.2. A simple way to visualise the available entropy change after hysteretic losses in a cyclic process is the overlapping region of the two entropy plots calculated from the field-increasing and field-decreasing portions of the $M(H)$ curves. This simple method shows that for $x = 1.4$, hysteretic losses are

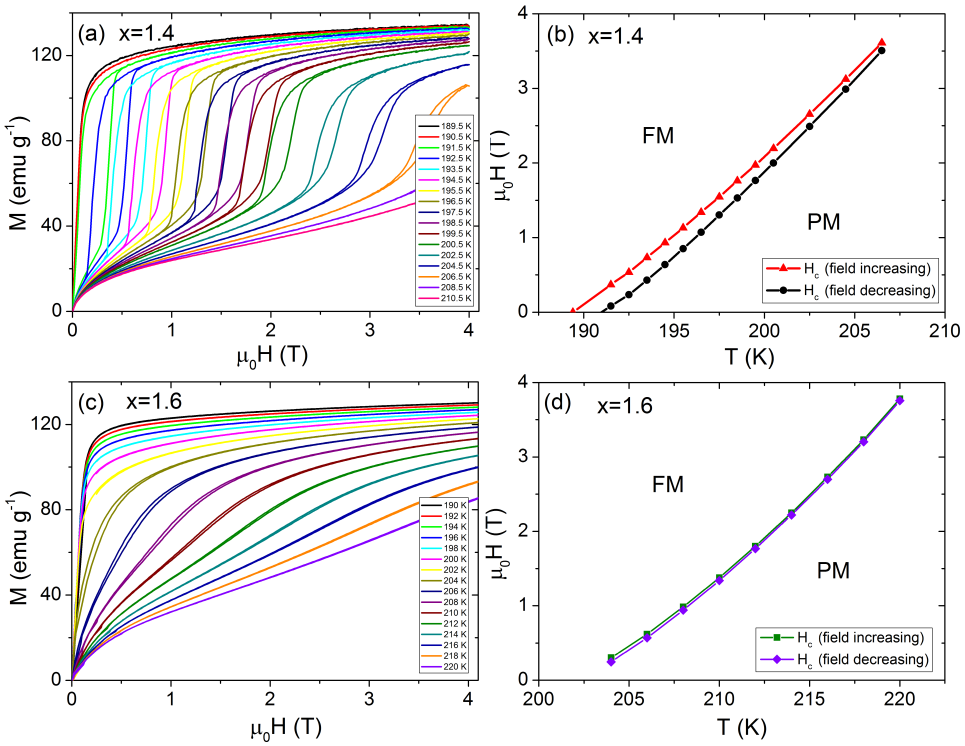


Figure 4.1: (a) $M(H)$ data of the metamagnetic transition of $LaFe_{13-x}Si_x$, with $x = 1.4$, for a variety of temperatures around T_C. The field sweep rate is 8.3 mT s^{-1}. (b) The extracted $H - T$ phase line measured at the mid-point (in M) of the transition, for both field increasing and field decreasing. (c) $M(H)$ data of the metamagnetic transition of $x = 1.6$ for a variety of temperatures around its T_C. The field sweep rate is 18 mT s^{-1}. (d) The extracted $H - T$ phase line measured at half saturation magnetisation for each temperature, for both field increasing and field decreasing.

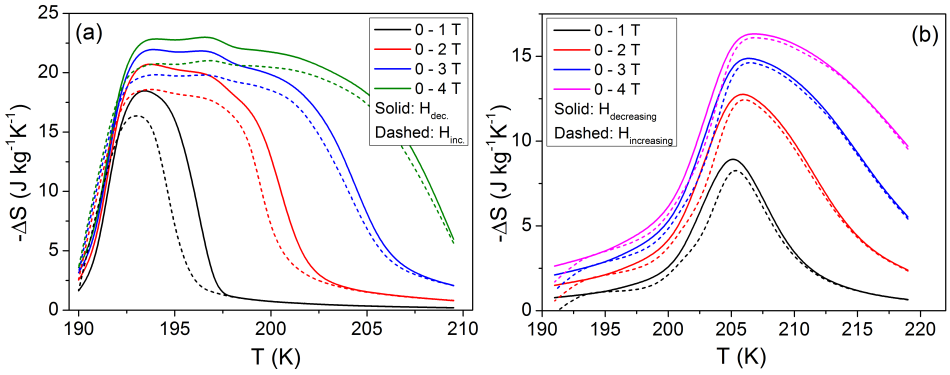


Figure 4.2: Calculated entropy changes ($-\Delta S_{\mathrm{m}}$) for a variety of magnetic field ranges for (a) $x = 1.4$ and (b) $x = 1.6$, calculated from the data of Figure 4.1. Separate curves for the entropy obtained for field increasing and field decreasing data are given.

significant. Hysteretic losses are apparent, although much less significant, for $x = 1.6$. This appearance of hysteresis in the second-order composition where, by definition, there should be none, is due to extrinsic factors from the finite field-rate and non-isothermal conditions, and is explained in section 4.2. Nevertheless, first-order La(La,Si)$_{13}$ compounds have small hysteresis in comparison to other many promising magnetocaloric materials (NiMnGa Heusler alloys, Gd$_5$(Si,Ge)$_4$ for example). A vital target for application purposes, using first-order materials, is therefore to reduce this hysteresis further without compromising the large entropy changes available within small fields.

4.2 Dynamics: field-rate dependence

Concentrating on the field-driven properties of the transition of $x = 1.4$ at one temperature, 194.5 K, much can be learned about the first-order transition. This temperature, 3.5 K above T_{C}, sits at the maximum entropy change for 0 to 1 T change, and indeed the full transition completes within this field range. Figure 4.3 shows the field sweep rate dependence of a sample with approximate prism dimensions of $1.7 \times 1.1 \times 0.4$ mm^3, and mass of 4.6 mg, for three field rates, $\mu_0 dH/dt$: 1 mT s^{-1}, 8.3 mT s^{-1} and 18 mT s^{-1} (a range of over an order of magnitude

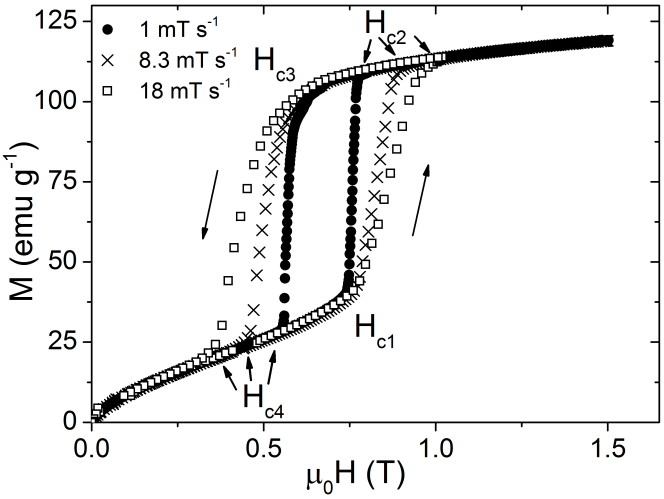


Figure 4.3: Magnetisation as a function of applied field for the $x = 1.4$ sample at 194.5 K (3.5 K above T_C) as the material transforms from PM (low-field) to FM (high field) and back. Data for three field sweep rates is shown, 1 $\mathrm{mT\,s^{-1}}$ (closed symbols), 8.3 $\mathrm{mT\,s^{-1}}$ (crosses) and 18 $\mathrm{mT\,s^{-1}}$ (open), and the definitions of H_{c1-4} are shown. The direction around the hysteresis loop is given by the arrows, which applies for all subsequent hysteresis loops shown in this thesis.

and including the field sweep limits of the Quantum Design PPMS). Following the results of Moore *et al.* [115] for a first-order compound within the $La(Fe,Si)_{13}$ family (Figure 2.8), an increase in the hysteresis, ΔH_{hyst}, is observed as the field rate increases. Here, for simplicity, for each loop, the fields at which the PM to FM transition begins and completes (reaches saturation) are defined as H_{c1} and H_{c2}, and the fields at which the FM to PM transition begins and completes are defined as H_{c3} and H_{c4}, respectively, as labelled in Figure 4.3.

For the slow field-rate shown (1 $\mathrm{mT\,s^{-1}}$), the quasi-static regime is approached and the first-order PM to FM transition appears sharp in field ($H_{c1} \sim H_{c2}$). A similar trend is seen at a lower field for the reverse transition, when the applied field decreases, although a more gradual drop in magnetisation occurs before the transition becomes sharp, suggesting a different nucleation process between the creation and early growth of the FM and PM phases. The fast field-rate loop (18 $\mathrm{mT\,s^{-1}}$) shows a considerably wider transition that deviates from the

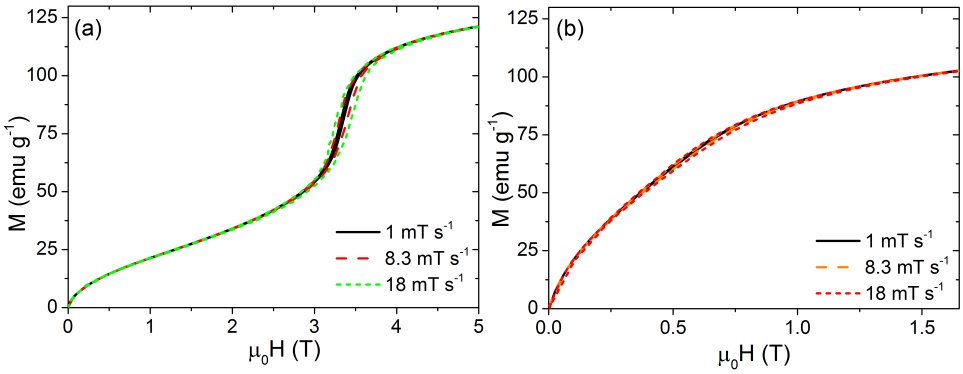


Figure 4.4: Magnetisation as a function of H at three field rates for (a) the $x = 1.4$ sample in Figure 4.3 at 206 K and (b) $x = 1.6$ at 206 K.

1 mT s^{-1} loop at both H_{c1} and H_{c3} to greater and smaller H_{c2} and H_{c4} values, respectively, resulting in an increased hysteresis width and area and therefore a time-dependent extrinsic contribution to the hysteresis, ΔH_{ext}. There are several possible sources of this extrinsic hysteresis, as discussed in section 2.2.1. One such source is heating from the inherent MCE of the material causing the sample to move along the phase line, resulting in increasingly larger fields required for the remaining PM volumes to reach their critical field (see the phase line in Figure 4.1(b)) and the sample remaining out of thermal equilibrium for longer. Therefore, whereas for the 1 mT s^{-1} field rate the system remains close to isothermal, faster field rates result in an increased hysteresis due entirely to extrinsic properties, as has been discussed in Refs. [115] and [116] where, respectively, smaller samples (fragments of maximum dimension $\sim$100 μm) with enhanced heat transfer through an increased surface-area to volume ratio, and improved thermal linkage to the bath have reduced or removed the rate dependent effects.

As such, one would expect such behaviour to be much reduced or lacking for second-order transitions, due to the smaller heat release of the MCE (and indeed the absence of sudden latent heat release), and the broadness of the transition in field. These two factors mean that, during field sweeps, the change in temperature from the inherent heating or cooling is smaller, and is spread out over a considerably larger time scale, with respect to an equivalent thermal equilibrium time, compared with first-order transitions. Thus, the second-order transition should remain close to isothermal. Figure 4.4(a) shows the transition induced by the same

set of three field rates, for the same sample of $x = 1.4$, at 206 K. This temperature is above T_{crit}, where the first-order behaviour crosses over to second-order (see section 5.1 for detailed discussion of T_{crit} in this composition). Firstly, ΔH_{hyst} for the 1 $\mathrm{mT\,s^{-1}}$ field rate is close to zero: this is still a finite field rate, so some hysteresis increase from the rate is expected to be present from the temperature change of the MCE (albeit much reduced). Increasing the rate opens up the loop and increases ΔH_{hyst}. Therefore, an extrinsic hysteresis component does still exist, but to a significantly lesser degree than when strongly first-order. Figure 4.4(b) has the equivalent results for second-order $x = 1.6$, of comparable dimensions $1.8 \times 1.0 \times 0.45$ $\mathrm{mm^3}$ and mass 5.0 mg, at a temperature corresponding closely to the peak in entropy change, 206 K. Here, the transition shape is very broad and hysteresis appears to be absent for 1 $\mathrm{mT\,s^{-1}}$, with only a small increase for faster rates.

4.3 Dynamics: relaxation rate

The second dynamic feature that dominates first-order $\mathrm{La(Fe,Si)_{13}}$ is temporal relaxation, as discussed in section 2.2.3: this is the progression of the transition between PM and FM (or the reverse) with no change in external environment, e.g. constant field and temperature. Zhang *et al.* [119] claim the relaxation to be dominated by thermal activation of the energy barrier, and Fujita *et al.* [120, 123] find a Johnson-Mehl-Avrami (JMA) behaviour of growth of new magnetic phase attributed to effects from the generation and dissipation of latent heat at the boundaries of growing regions, where locally the transition occurs. Additionally, as summarised in section 2.3, a strong dependence on demagnetising fields exists, such that the relaxation completes most quickly for samples with low demagnetising factor but becomes arrested mid-transition in a mixed state for high demagnetising factors.

With this latter point in mind, for the following, the $x = 1.4$ sample, which has approximate, cuboid shape with dimensions $1.7 \times 1.1 \times 0.4$ $\mathrm{mm^3}$, has been measured in the orientation with lowest demagnetising factor with respect to H; that is, with H parallel to the longest axis,

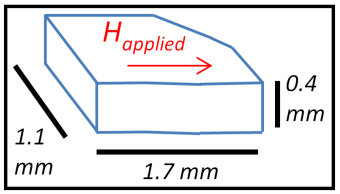


Figure 4.5: The schematic of the $x = 1.4$ sample with field direction as labelled.

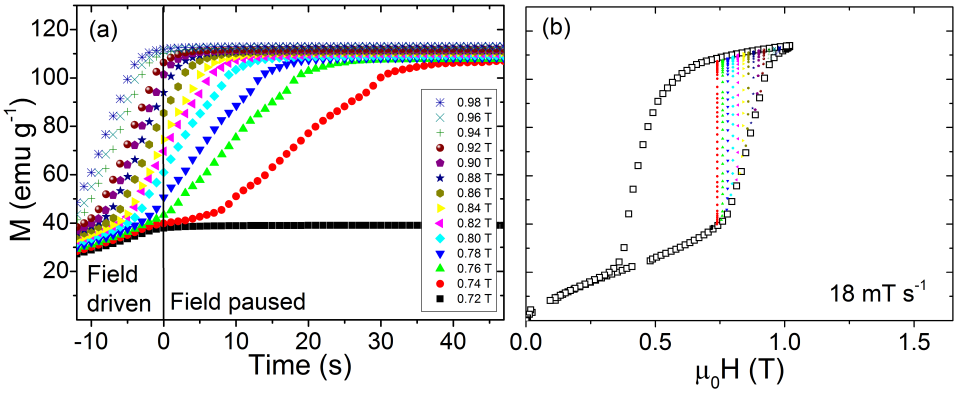


Figure 4.6: (a) Relaxation data in time for $x = 1.4$ at 194.5 K as the field is increased from $\mu_0 H = 0$ T at 18 mT s^{-1} and paused for 50 s at constant field at a variety of field values across the transition, as indicated. The field is returned to $\mu_0 H = 0$ T and increased again to the next target for each data set. (b) This same data is superimposed onto the 18 mT s^{-1} data set of Figure 4.3 as the vertical plots of increasing magnetisation, as the material relaxes fully into the FM state.

as shown in Figure 4.5. Variations in orientation, in subsequent measurements, will be stated explicitly.

With the temperature again at 194.5 K, and starting at $\mu_0 H = 0$ T (in the PM state), driving the field at 18 mT s^{-1} to above H_{c1} pushes the system out of equilibrium and closer to adiabaticity, and when the field sweep is paused and the field is held constant, the material relaxes into the FM state, shown in Figure 4.6. This relaxation is always to the full FM magnetisation, and so maps the 'fast-rate' 18 mT s^{-1} loop onto a relaxed 'static', time-independent intrinsic loop, with smaller hysteresis than that for 1 mT s^{-1} shown in Figure 4.3, with an infinitely discontinuous sharp transition (in H) via the vertical plots at each constant field. The relaxation time has been seen, during this study, to be highly dependent on the

size of the sample, in addition to the shape and demagnetising factor [120]. The latter will be discussed in more detail in section 4.5.

The relaxation rate, dM/dt, becomes faster as the field is paused further through the transition (between each measurement the field is reset to $\mu_0 H = 0$ T). This is shown in Figure 4.7, in which a linear gradient has been fitted to the $M(t)$ data to give dM/dt values for each relaxation plot. In contrast, if the field is paused just below H_{c1}, the magnetisation remains stable at its PM value (as is the case for pausing the field at $\mu_0 H = 0.72$ T). This result is interpreted as showing that the higher the 'pause' field, H_{pause}, the more FM nuclei are created, separate to the growth characteristic, and so there is faster subsequent growth of the FM phase when the field is paused, with the relaxation rate having a linear dependence on how far past H_{c1} this field is settled, here termed H_{pause}/H_{c1}. Approaching H_{pause}/H_{c1} at two slower field rates, 8.3 and 1 mT s^{-1}, shows that the relaxation rate is independent of field-rate preconditioning, as also shown in Figure 4.7, and the dependence on H_{pause}/H_{c1} is preserved for all field rates. As the value of H_{pause}/H_{c1} corresponds to different volume fractions of transformation for each rate, the relaxation rate is determined not simply by the fraction of material transformed before the field pause, but by some combination of this and the rate at which it was transformed, termed more simply as how far out-of-(phase) equilibrium the system is pushed before being allowed to relax. Due to the dynamic behaviour of the transition, each rate has, of course, different values of H_{c2} (represented by the plateauing of dM/dt after which the transition is fully driven): the slower the rate, the smaller the increase of field before H_{c2} is reached. This results in dM/dt plateauing at lower values for the slower field rates.

However, this result is not observed by Yako *et al.* [120] nor Fujita *et al.* [123], who report no increase in relaxation rate after field-inducing larger extents of the transition before pausing the field (see Figure 2.10(a)) or with varying cooling rates, respectively. As such they are able to fit a JMA model to the single resulting curve in each case. There are several possible reasons for this discrepancy. For example, a significantly larger sample and different field rate used in the field-induced case ($4 \times 4 \times 1$ mm^3 and 15 mT s^{-1}, respectively) [120], and

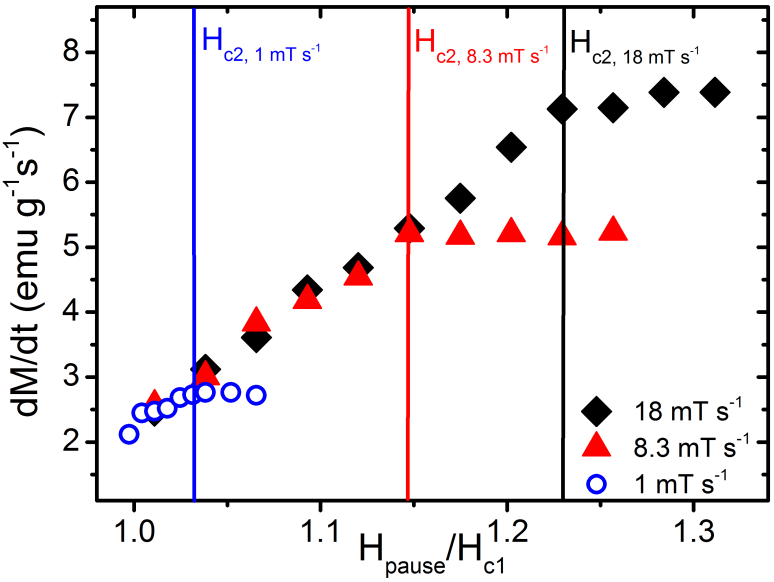


Figure 4.7: The line-of-best-fit gradient transformation rate dM/dt for the $x = 1.4$ sample at 194.5 K derived from the relaxation plots in Figure 4.6 as a function of $H_{\text{pause}}/H_{\text{c1}}$, where H_{pause} is the value the field is paused at to allow relaxation and H_{c1} is defined as the first field at which relaxation occurs: $\mu_0 H = 0.74$ T. Data of dM/dt when H_{pause} is approached at two additional field rates, 8.3 and 1 mT s^{-1}, is included and each rate's value of H_{c2} is labelled.

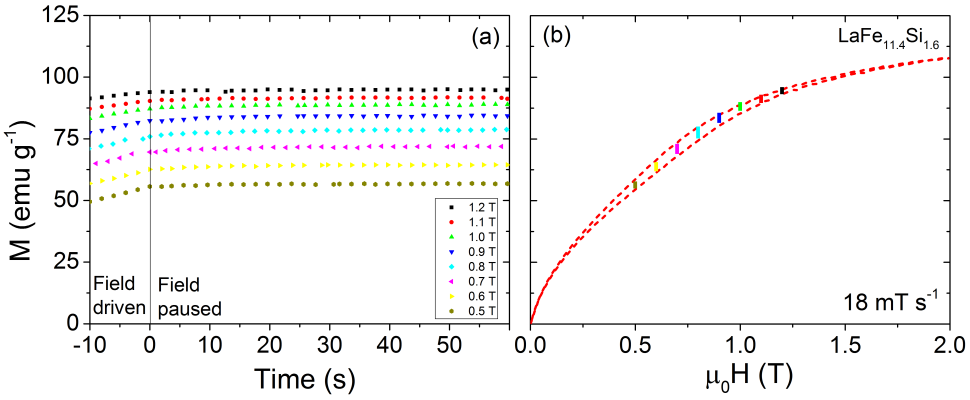


Figure 4.8: (a) Magnetisation response in time for $x = 1.6$, at 207 K, as the field is increased from $\mu_0 H = 0$ T at 8.3 mT s^{-1} and paused for 60 s at constant field, at a variety of field values across the transition, as indicated. The field is returned to $\mu_0 H = 0$ T and increased again to the next target for each data set. (b) This same data is superimposed onto a fully field driven 8.3 mT s^{-1} data set as the (very small) vertical plots of increasing magnetisation.

the different role of the dipole interaction when no field is applied, in the case of the T-induced transition [123]. Since one feature of JMA behaviour is that the rate of transition is independent of how much material has undergone phase change already, the results of Figure 4.7 indicate that the different field environment itself (i.e. higher H which shows faster relaxation) is enough to accelerate the relaxation. This could be via either an adjusted free energy landscape, which makes the existence of the new phase more preferable than lower H relaxation (i.e. the FM minimum having a lower free energy with respect to the PM), analogous to an enhanced supercooling effect, or an enhanced thermal energy impulse caused by an increased temperature deviation from the bath during fast rate approaches. Additionally, despite JMA suggesting the increased number of FM nuclei will have no impact, each nuclei has a greatly larger magnetisation than the surrounding PM regions and therefore it is possible that increased dipole interactions may be able to cause a deviation from the model.

In contrast, for $x = 1.6$, following the negligible rate dependence there is also negligible relaxation (Figure 4.8). Second-order transitions have no latent heat release or absorption

and no energy barrier to be overcome. Therefore, mixed phases and local processes during transition are not present to act as a driver of the growth process and the transition is broad, requiring a change in external conditions to progress (which occurs globally across the material [59]). The small relaxation that occurs after fast field change would then be consistent with the sample rethermalising along its phase line to the bath from the inherent and globally-scaled MCE pushing it out of thermal equilibrium. However, this is not a driving growth relaxation phenomenon but simply a result of thermal re-equilibration.

4.4 Dynamics: field-driven transition rate

Both the rate dependence and relaxation dynamic effects are related to the time over which the transition occurs. This is particularly important for application, since in order to be viable the heating/cooling cycle frequency will need to be at least on the order of a few Hz [121]; however, a slow transition rate, whether intrinsic to the system or extrinsic from external factors, will either limit the cycle frequency or result in only part of the transition being completed thereby, greatly reducing its effectiveness as a refrigerant. Figure 4.9 shows how the field-driven PM to FM transition as a function of time, t, for the $x = 1.4$ sample at 194.5 K depends on the field rate, where the start of each transition has been set to $t = 0$. As $\mu_0 dH/dt$ increases, there is a decrease in the transition time, t_{trans}, from approximately 30 s for 1 mT s^{-1} to 10 s for 18 mT s^{-1}. The transition times, approaching the 1 mT s^{-1} rate, show the approach of the relaxation regime, suggestive of the non-infinite t_{trans} that is observed at zero field rate (i.e. constant field). A relaxation plot, 'non-driven relaxation', is included explicitly in Figure 4.9 showing this, which has been obtained after H is increased from the PM state at 1 mT s^{-1}, towards the start of the PM to FM transition, and then paused at H_{c1} at $t = 0$. A key concern, with regards to application, is whether the transition time is dominated by the rate dependence and associated causes, as discussed in section 4.2, or an intrinsic growth process more closely related to the relaxation dynamics. It must be clarified whether, for field rates several orders of magnitude larger than those demonstrated here, the

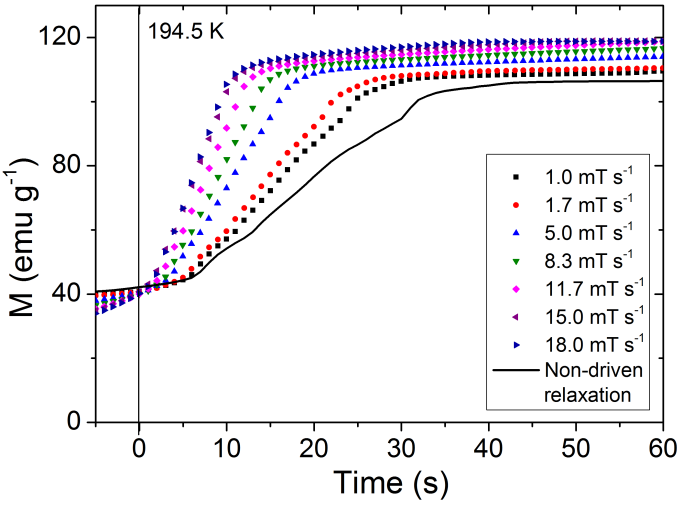


Figure 4.9: The field-driven $x = 1.4$ transition at 194.5 K shown as $M(t)$ at a variety of field-rates for the increasing field PM to FM transition. Included is also a non-driven relaxation plot across the transition for comparison (see Figure 4.6(a)). For all data sets, t is defined as zero at H_{c1}.

transition rate will continue to decrease, or whether it will reach a minimum transition time, determined either by sample size and thermal linkage to the thermal bath, or something more intrinsic. These questions and how this issue can be tackled, and the potential sources separated, will be returned to in section 4.5.

The dependence of the transition rate of the field driven transition, dM/dt, as shown in Figure 4.9 for $x = 1.4$, on field rate is shown in Figure 4.10 for $x = 1.4$ and $x = 1.6$, at the same respective temperatures as shown in Figure 4.3 and 4.4(b). Here dM/dt has been normalised to the saturation magnetisation, M_s, determined as the value of M at 1.5 T (where the sample has reached saturation), in order to compare how the transition rate with respect to a full transition behaves with rate of applied field, between the two compositions. For $x = 1.4$, as the field rate increases the increase of $d(M/M_s)/dt$ is sublinear, and is consistent with a logarithmic function as shown by the curve-of-best-fit. This sublinear behaviour may have negative implications where much larger field-rates are needed (e.g. of the order of 1 $\mathrm{T\,s^{-1}}$ for application) alongside a rapid dM/dt. Note that, if extrapolated to $dH/dt = 0$, the transition

rate is finite, consistent with the finite-time relaxation as previously discussed.

For application, the concept of transition rate is vital, since the hysteresis width is dependent on this time and if a magnetocaloric material is being cycled at, say, 1 $\mathrm{Hz\,T^{-1}}$, this leaves a maximum of 0.5 s for the full first-order transition to take place. This is an extremely conservative minimum time when one considers the time required, after each transition, for heat transfer with the environment to take place. Such a time scale is more than an order of magnitude quicker than the fastest transitions achieved here (see the 18 $\mathrm{mT\,s^{-1}}$ data plot of Figure 4.9), leading to the detrimental possibility that a full transition may not have time to complete, regardless of any decrease in isothermal hysteresis (such as that discussed in section 4.5.3).

However, it should be clarified that these remarks concern measurements in between the isothermal and adiabatic cases, but assuming an isothermal transition. This is because the entropy change from the Maxwell equation and the hysteretic energy loss are calculated in terms of these isothermal $M(H)$ loops, and both an incomplete transition and increased hysteresis indicate a significant degree of cooling power and efficiency loss. The effects of increasing the rate, as described earlier, push the system away from the isothermal regime towards adiabaticity, for which conditions will be met with appropriately fast field sweep rates or a large thermal resistance to the bath. Examples of adiabatic behaviour are shown in Figure 2.9. In the context of cooling applications, an isothermal transition is unlikely to be of practical use due its very nature of no temperature changes taking place (as well as the requirement of long time scales). The active magnetic regenerator cycle (AMR) instead has two adiabatic steps separated by isofield, thermal equilibration steps, during which the heat work is extracted from the system. Nevertheless, an adiabatic step for 0 to 2 T should still allow complete transformation in these materials, if we assume $\Delta T_{\mathrm{ad}} \sim 8$ K (see Figure 2.3) is the maximum temperature change, and $\mu_0 dH_{\mathrm{c}}/dT = 0.22$ $\mathrm{T\,K^{-1}}$ (see Figure 4.1(b)). This would give a maximum increase in H_{c} of 1.76 T, well within 2 T, if the transition starts close to 0 T, meaning that the transition to FM would complete in the adiabatic step instead of during the isofield stage (which is the cooling back to T_{initial}), and, therefore, the hysteresis

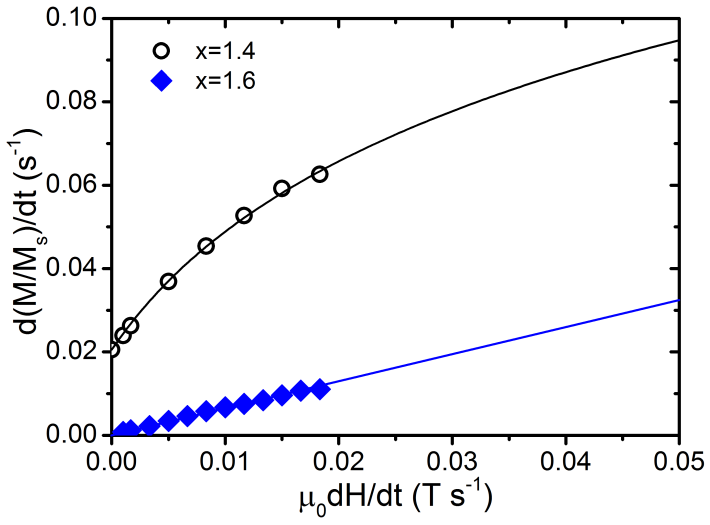


Figure 4.10: $d(M/M_\mathrm{s})/dt$ versus field rate for the driven transformation for the $x = 1.4$ sample at 194.5 K and the sample with $x = 1.6$ at 206 K.

in the field-induced transition is relevant as opposed to that in the T-induced transition.

The contrasting behaviour of second-order $x = 1.6$ is also shown in Figure 4.10. At slow field rates, the $d(M/M_\mathrm{s})/dt$ values are much smaller and cross the origin, since magnetic relaxation is absent and the system requires a change of applied field to produce any change of magnetisation. However, as the field rate is increased, $d(M/M_\mathrm{s})/dt$ also increases in an linear trend, confirming that there is not the complex dynamic behaviour that is prevalent in the first-order system. Thus, despite the fact that at the largest field rate available with the PPMS (18 mT s^{-1}), dM/dt for $x = 1.6$ is about $\frac{1}{6}^{th}$ that of $x = 1.4$, a continued linear trend towards the fast field rates needed for applications ($\mu_0(dH/dt) > 1$ T s^{-1}) suggests a second-order system will be significantly less constrained. Nevertheless, with regards to the preferable entropy change values of the first-order $x = 1.4$ (and first-order systems in general), mitigation of some of these detrimental effects is possible by judicious choice of sample geometry as discussed in sections 4.5 and 4.6.

4.5 Influence of sample connectivity on magnetisation dynamics

4.5.1 Sample connectivity scenarios

In order to understand better the contributions to these dynamic phenomena (field-rate dependence and relaxation) in the first-order transition, the influences of demagnetising fields (as seen in [120] and section 2.3) and sample connectivity were examined. At this stage, possible contributions from intrinsic nucleation and growth, extrinsic heating or other extrinsic effects cannot be entirely excluded.

To achieve this, an experiment was conducted with one sample of $x = 1.4$ in several different physical scenarios, shown in Figure 4.11, at a fixed temperature, as follows. Firstly, the sample, as measured in sections 4.2, 4.3 and 4.4, is denoted the first scenario, with field direction along the long axis, referred to in future as Scenario A. In this orientation, the demagnetising factor is minimised and, above H_c, there is complete relaxation (at constant field and temperature) between the phases as section 4.3 demonstrated. The sample was then broken along its length into three pieces and reassembled, with the smaller possible gap between the pieces, in the same orientation as A, labelled Scenario B. The field was applied in the same direction. Therefore, in this scenario, the global demagnetising factor and surface area-to-volume ratio are, apart from the effects of the new surfaces and edges, the same as Scenario A. However, effects of strain, domain growth and thermal contact between the pieces are eliminated or greatly reduced. The breaking was achieved by mechanically snapping the sample by positioning a portion of it over a ledge and applying a sharp force. This method was chosen in order to reduce any effects of localised heating from diamond saw cutting which may result in local compositional or phase differences in the sample between Scenario A and Scenario B, as well as reduce any significant loss of mass. It should be noted that deformation may result due to strain fields in the breaking method. However, no significant unintentional

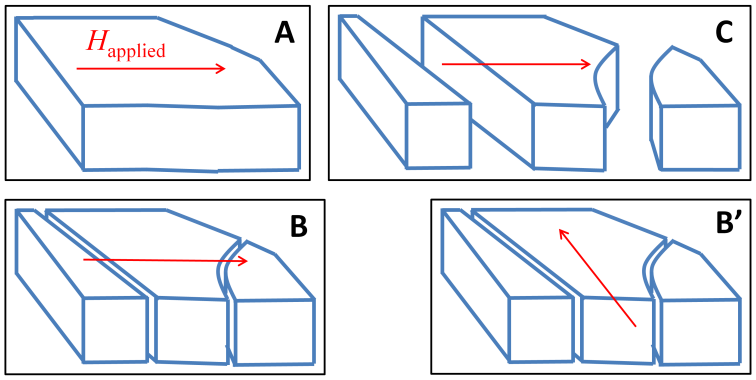


Figure 4.11: Schematics of the four scenarios for the $x = 1.4$ sample, A, B, C and B', as described in the text.

impact to the magnetic transition, such as substantial broadening, was observed. A small amount of mass (approximately 3%) was lost during this process. Thirdly, measurements were then repeated with the three pieces in the same orientation but separated by 0.4 mm (a distance of the order of their thickness), labelled Scenario C. The strain, domain growth, and thermal contact conditions are the same as Scenario B, but the magnetic coupling between the pieces is greatly altered and the global demagnetising factor is significantly larger, by approximately a factor of two, as determined from analysis of the magnetisation response to applied field in the FM state (not shown). Additionally, there is a small increase in the surface area to volume ratio due to the new faces. Finally, measurements of Scenario B were repeated but with H applied in the perpendicular direction as indicated, labelled Scenario B'. In this orientation, the connectivity is the same as Scenario B but the demagnetising fields are greatly altered.

With these experimental set-ups, undesirable results from variations in sample composition, which could potentially affect comparisons between scenarios, are removed. Inhomogeneity in the phase composition, which would lead to smearing of the transition or a spread of T_C, is expected (as are minority phases, in particular α-Fe regions which for this sample through Rietveld analysis of x-ray diffraction data are measured to be 6 ± 1 wt% of the material), therefore, in this study the same bulk of material was used for all scenarios to isolate spurious results from differences in any inhomogeneity present.

4.5.2 Magnetic relaxation

The relaxation curves, after H_{c1} is approached from zero field at the slow field rate, 1 mT s^{-1}, and paused at a variety of H_{pause} values, are shown for each scenario in Figure 4.12. The H_{pause} values are indicated in the legends. In Scenario A, full relaxation into the FM state can occur even if H_{pause} is several mT below H_{c1} (in contrast to the stable response at fast rates in Figure 4.6(b), sometimes after a delay of tens of seconds. If the assumption is made that some part of the transition has not already begun in a volume too small to be detected by VSM, we can say that the system is metastable at a so-called tipping point, such that the transition can be initiated by a small perturbation in the external environment, e.g. a temperature fluctuation. As summarised in sections 2.2.3 and 2.3, Yako *et al.* have shown relaxation with large dependence on the stray field and sample shape [120], demonstrating that full relaxation occurs when the field is applied in an orientation in which the sample has a low-demagnetising factor, but slows and becomes arrested for field directions with high-demagnetising factors coupled with a significant increase in all of H_{c1}, H_{c2}, H_{c3}, and H_{c4} (this latter point is discussed further in section 4.6).

Now comparing the relaxation of the sample in the three scenarios, A, B and C, Figure 4.12 shows that there is a considerable difference between them: in Scenario A (before breaking), the relaxation is smooth and the transition time is approximately 46 s (as measured from the start of the PM to FM transition to when the magnetisation reaches saturation as shown in Figure 4.12(a)); in Scenario B (broken and reassembled) the transition time is considerably longer (106 s) and transforms in at least three distinct stages. This may suggest that each of the three fragments transforms separately and consecutively, although as yet this can only be conjectured. The shapes of the relaxation curves are consistent on repeated measuring, however, which is a clear indication that the transition proceeds in the same way for each repeated measurement.

Figure 4.12 suggests that in both Scenarios A and B the transformation starts at one location

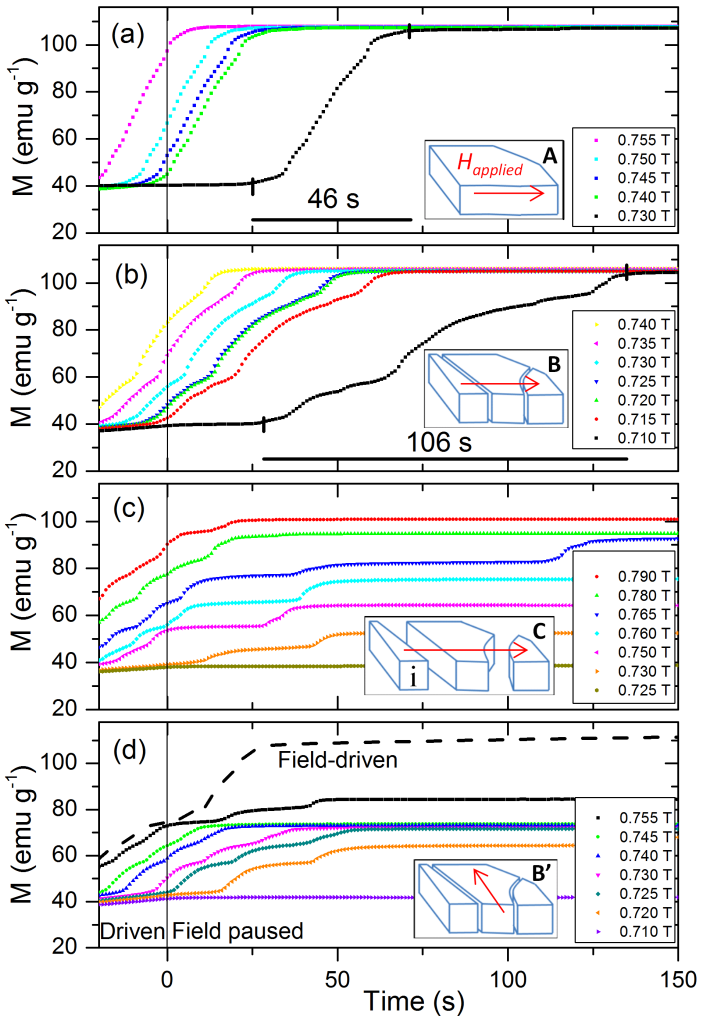


Figure 4.12: Magnetic relaxation in time at 194.5 K and schematics (insets) of the $x = 1.4$ sample in its three scenarios: (a) A, (b) B and (c) C, with H applied in the direction indicated. In each case the target applied field is approached from 0 T at 1 mT s^{-1}. The field is then held constant from $t = 0$ s for 150 s. Between each measurement, the field is returned to $\mu_0 H = 0$ T before being increased at 1 mT s^{-1} to the next field target. The horizontal lines indicated in (a) and (b) show the transition time and how it is determined. (d) Relaxation data of Scenario B with the field instead applied in the direction indicated, termed Scenario B'. Included is the data from the fully field-driven transition (from the $M(H)$ loop), represented by the dashed line. This demonstrates that the saturation magnetisation indicated is not attained during magnetic relaxation in paused field.

and grows until the entire sample has transformed. For the intact sample the growth can be assumed to be driven by any or all of strain, magnetic coupling, instability of the boundary between two magnetic phases, or thermal contact. The full relaxation of Scenario B suggests that nucleation occurs on only one of the fragments, but when relaxing into the FM state the growth can cross to an unconnected but adjacent fragment; or, more properly, the growth of new phase in the first nucleated fragment nucleates a volume on an adjacent fragment which grows, and so on until all three fragments have transformed fully to FM. The mechanism for this is proposed to be the increased stray field, created by the jump in magnetisation on the first fragment, permeating and influencing the next fragment via an increased local magnetic field, $H_{\text{local}} = H_{\text{app}} + f\Big(M_{\text{fragment 1}}(r)\Big)$, where the latter term is some function of the magnetisation of the fragment in the FM state at distance r to the nucleation site on the adjacent fragment; that is, a purely magnetic mechanism. Independent nucleation on all three fragments is possible but unlikely, since measurements of different sizes of material (not shown) have shown the relaxation time to generally decrease with decreasing sample size (and with increasing number of FM nuclei created, following the conclusions of Figure 4.6(b)) and therefore would be expected to be faster than in Scenario A, with all three smaller fragments transforming concurrently. Thus, since strain and heat flow between fragments will be inhibited, magnetic coupling between the fragments can enable a full transformation.

However, the overall relaxation in Scenario B is markedly slower than for Scenario A, implying that the strain field and/or thermal linkage play an important role. Since the sample expands when undergoing the transition, it is unlikely that strain field coupling enhances the transition (indeed, the opposite has previously been proposed [152]). Therefore, it can be concluded that thermal linkage across the transition is an important aspect of the transition dynamics, consistent with the conclusions reached by Yako *et al.* [120] and Fujita *et al.* [123] regarding the dissipation of locally created latent heat.

Scenario C (broken and separated) exhibits a substantial change to the relaxation and further confirms the magnetic coupling of Scenario B, since at this separation the stray field between the fragments is significantly weakened (this diminution of magnetic interaction has been

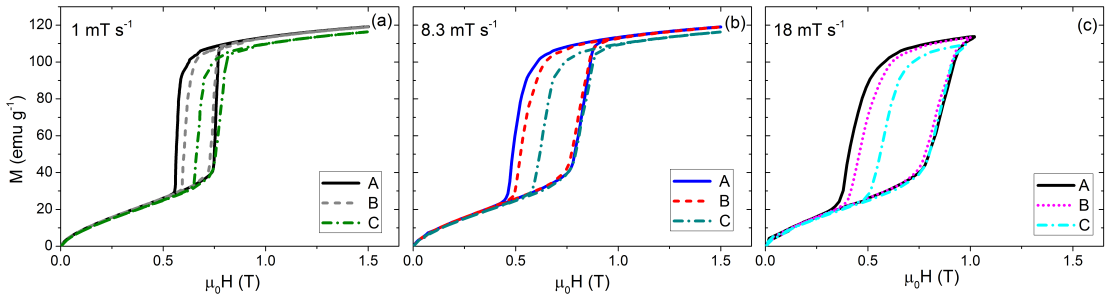


Figure 4.13: Comparison $M - H$ plots of the $x = 1.4$ metamagnetic transition at 194.5 K when the field is swept at (a) 1 mT s^{-1}, (b) 8.3 mT s^{-1} and (c) 18 mT s^{-1} for the three scenarios A, B and C.

supported by magnetisation measurements of each fragment separately, oriented in the same direction with field as they each appear in Scenario C: the addition of all three data sets shows magnetisation loops equivalent to the loops of Scenario C - not shown). There is no full relaxation from PM to FM until the system has been driven at least halfway through the transition, and instead there are small changes in magnetisation corresponding to small volumes within the fragments relaxing independently into the FM phase. It should also be noted that the demagnetising fields within each fragment are now much more significant, each approximately double those of Scenario A. Figure 4.12(c) shows that there are well-defined states of a mix of phases: there are at least five stable states with coexisting PM and FM regions arising from the three fragments, indicating that at least one of the fragments can itself become arrested in a mixed state.

To further examine the role of the demagnetising factor, Scenario B was examined with the field direction rotated by 90° , as shown in Figure 4.12(d) and designated Scenario B'. Under these conditions the sample is unable to transform fully but instead shows a series of arrested states similar to Scenario C. In Scenario B, magnetic flux linkage enables the transition, but in Scenario B', due to the fact that the flux lines run in the direction perpendicular to the sequence of the fragments, magnetic linkage between fragments is negligible.

4.5.3 Driving field rate dependence

Figure 4.13 compares the $M(H)$ loops of Scenarios A, B and C at three different field sweep rates, again 1 $\mathrm{mT\,s^{-1}}$, 8.3 $\mathrm{mT\,s^{-1}}$ and 18 $\mathrm{mT\,s^{-1}}$. For now ignoring the changes in hysteresis, which are discussed in section 4.6, the slow field rate regime shows the transition becoming less sharp in H as the sample is progressed from Scenario A to B then to C, indicative of the slowing (and arresting in the case of Scenario C) of the relaxation. However, at the fast rate regime, the transitions for both PM to FM and FM to PM broaden, as expected following Figure 4.3, to the same degree for all scenarios such that they fall on top of each other in the case of the PM to FM transition, and have the same shapes for FM to PM. Therefore, when driven at this fast field rate, the transitions, once started, behave identically, despite the physical differences between the three scenarios which are seen to play a major role in the dynamics when in constant field or slow field rates. This result also adds reinforcement to the claim that the breaking method between Scenario A and Scenario B was not negatively impacted by strain fields.

From this observation it can be stated that there are two regimes of sample behaviour. For slow sweep rates, the geometry and connectivity across the sample (thermal as well magnetic) play an important role; for fast sweep rates, the thermal connectivity across the thinnest dimension dominates, which in this case is the thickness of the sample that is a constant between Scenarios A, B, and C.

Therefore, under fast magnetic field driving conditions, the transition becomes independent of the growth mechanism: driving fast creates the necessary nucleation sites, as seen in the relaxation after driving partway through the transition in Figure 4.6(b). Further evidence for this can be extracted from measurements of the hysteresis against field rate (Figure 4.14(a)): the hysteresis widths are different, due to a shift in H_{c3} as will be discussed in section 4.6, but for rates faster than 5 $\mathrm{mT\,s^{-1}}$ the behaviours of Scenarios A and B show very similar gradients; increasing the field rate increases the hysteresis proportionally. Additionally, this is reinforced

in Figure 4.14(b), where the measured transition times match between the three scenarios. (The transition time measurement is defined in Figure 4.12(a)). Note that the transition time in Figure 4.14(b) represents a quantity roughly reciprocal to the transition rate, $d(M/M_\mathrm{s})/dt$, shown in Figure 4.10 (for Scenario A), and therefore the equivalent information.

For Scenario C, the gradient of the hysteresis, shown in Figure 4.14(a), is noticeably shallower (8.2 s compared with 10.7 and 10.3 s for A and B, respectively) and the transition times at the greatest field rates are shorter than for A and B. This suggests that the larger surface area-to-volume ratio improves heat transfer when the pieces are separated; therefore, there is marginally better thermal linkage with the bath, which allows the transformation to proceed more quickly [116]. This does not apply for rates slower than 5 $\mathrm{mT\,s^{-1}}$; here, we are approaching the relaxation regime where the effects of sample shape and connectivity, via the stray field and demagnetising factor, become dominant. Therefore, the crossover from the regime of extrinsic thermal effects to growth and magnetic coupling depends on the field rate and for this set-up occurs at approximately 5 $\mathrm{mT\,s^{-1}}$. How this crossover point varies with sample size, shape, and thermal linkage is important to elucidate: when fragments are small enough in nearby first-order materials (< 200 μm in all dimensions), effects due to both of these factors are greatly reduced, and the dynamics for the most part vanish at all field rates observed within laboratory time scales, as observed by Moore *et al.* [115] (see Figure 2.8(c)). Reducing the transition time, or equivalently increasing the transition rate, in the field driven regime can therefore be achieved to some extent by design of sample geometry in a way which improves the thermal equilibration time.

It should be clarified, however, that despite the sharpness of the transition broadening from Scenario A to B, as shown in Figure 4.13(a), it still remains sharp despite the introduction of cracks. This is complementary with the findings of Waske *et al.* [31], examining the structural changes of the magnetocaloric transition of $\mathrm{LaFe_{11.8}Si_{1.2}}$ in the heating and cooling cycle using in situ synchrotron measurements, in which the sharpness of the transition width (i.e. the H range between the commence and completion of the transition, or $H_{\mathrm{c2}} - H_{\mathrm{c1}}$, for example) in the presence of cracks in the material is also shown to be retained.

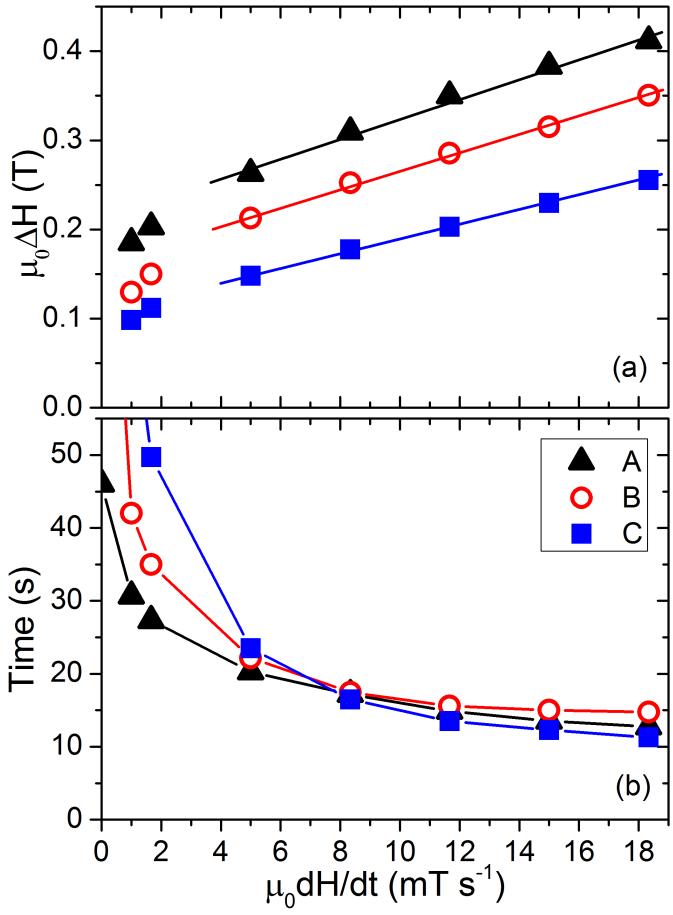


Figure 4.14: (a) Hysteresis width and (b) the PM to FM transition completion time as a function of dH/dt for the $x = 1.4$ sample in Scenario A (closed triangles), B (open circles) and C (closed squares) at 194.5 K. The hysteresis is measured as the difference between the mid-points of the PM to FM and the FM to PM transitions. The PM to FM transition time is measured for each field-rate loop as the time between the start of the transition and the point where the magnetisation saturates. The point at $\mu_0 dH/dt = 0$ represents the relaxation time of Scenario A in paused field as shown in Figure 4.12. This value is 106 s for B (off the graph) and does not exist for C.

4.6 Statics: role of demagnetising fields

Figure 4.13 also shows a considerable variation in the time-independent, magnetostatic features of the transitions between the three scenarios, A, B and C. In particular, the fragmentation of the sample has little effect on H_{c1} (at all three field rates) but causes a considerable shift in the commencement of the FM to PM transition at H_{c3}. H_{c3} is lowest for Scenario A, significantly higher for B (by 40 mT), and even more so for C (by more than 100 mT), resulting in hysteresis widths, as measured from the midpoints of the 1 $\mathrm{mT\,s^{-1}}$ PM to FM and FM to PM transitions, of 0.185, 0.130, and 0.098 T for the three scenarios, respectively (Figure 4.14(a)). In all three scenarios, the full FM to PM transition is preceded by a slight decrease in magnetisation before it transforms sharply; there are no such precursors for the PM to FM transition at H_{c1}.

The invariant H_{c1} but differing H_{c3} (assuming negligible temperature variation between measurements) for the three scenarios is unique to the first-order transition, suggesting asymmetry between the nucleation of the FM and PM phases. It is assumed that the PM phase is completely eliminated during the transition to FM, since the maximum applied field is considerably larger than H_{c2}, and therefore no nucleation sites remain to facilitate the transition back to PM. One possibility is strain relief [33]: in polycrystalline samples, such as these, where there is a period of mixed phase, the growth of the FM and PM phases is itself known not to be the same, as proven by Figure 2.12 [117]. Therefore, one would expect any relief from breaking the sample to dominate for the PM to FM case only, where the material increases in volume. Here, the PM to FM transition might be expected to be facilitated in Scenarios B and C with less volume constraint, whereas for the FM to PM transition, and its volume decrease, the difference between the three scenarios would not be significant. However, the difference in scale of the sample when intact and in its fragments is not substantial, and, therefore, the transformation would not be expected to be much influenced. Since, instead, a large difference between the scenarios for the nucleation of the PM phase in the FM state is observed, it can be inferred that strain makes no major contribution here. The dominating

factor would instead appear to be magnetic, and the large changes of H_{c3} but invariant H_{c1} is a direct result of the influence that the different demagnetising fields have on the nucleation of either phase. Although, globally, the demagnetising factors of Scenarios A and B are comparable, locally this is not the case, in particular at the new edges and asperities formed in B, where the local internal field will be very different to those in A. The data suggest that these local fields may greatly facilitate the onset of the PM phase in large field in Scenario B, but have little effect on the onset of the FM phase compared with A. The simulations and Seebeck voltage measurements carried out by Fujita *et al.* [117], on a rectangular sample as shown in Figure 2.11 and 2.12, suggest that the nucleation of the FM phase for the PM to FM transition occurs at the middle of the sample, whereas the FM to PM transition begins at the ends, with respect to the applied field direction.

This would be consistent with the findings in Figure 4.13, as described in the following and demonstrated in the schematics in Figure 4.15. The PM to FM transition begins in the high-field region of the sample, and the FM to PM transition in the low field. Due to the subtle changes in sample shape created by, firstly, introducing cracks into the original bulk sample, and then later, by separating the pieces in Scenario C (therefore, containing effectively three separate fragments and demagnetising factors), the local field within the high-field regions are not substantially decreased whereas the local low-field regions are, indicated by the spreading of the field lines. This causes a shift in all of H_{c2}, H_{c3}, and H_{c4} compared to the data of Scenario A, due to weaker internal fields which result from larger demagnetising fields, consequently requiring a larger applied field to drive the transitions. However, H_{c1} is not affected so the effect is substantial only after the PM to FM transition starts.

Directly measuring samples with two greatly different demagnetising factors (which indeed can be achieved by measuring one sample with high aspect ratio in two applied field directions) has shown a considerable shift in H_c, in both PM to FM and FM to PM transitions, between a low and high demagnetising factor orientation. This shows the dominant role of demagnetising fields, since all other features of the sample are unchanged between measurements [120]. For clarity, an example is shown in Figure 4.16 for a plate-like sample of $x = 1.4$ with approximate

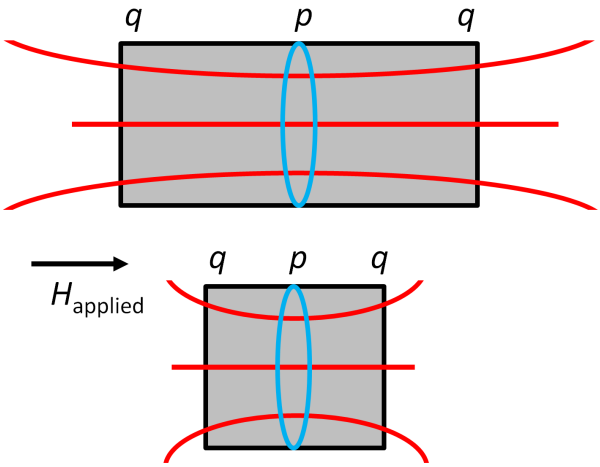


Figure 4.15: Schematics of field lines (red) within two rectangles in applied field showing the importance of sample shape for the first-order transition and where each phase nucleates. With the indicated field direction, demagnetising fields cause the total field to be strongest at p and weakest at q. By changing the dimensions as shown (bottom), the total field at q is considerably weakened without greatly affecting that at p (see the region indicated by the blue oval).

dimensions $1.5 \times 1.5 \times 0.35$ mm^3 and field applied in directions parallel and perpendicular to the largest plane. However, the behaviour of the $M(H)$ loops between orientations does not match that shown by the scenarios in Figure 4.13 since H_{c1} is not invariant. For the high demagnetising factor orientation $H_{\mathrm{out-of-plane}}$, the transition shape changes, becoming broader and with reduced hysteresis, a strong indication that the same processes as described by Figure 4.15 are taking place.

4.6.1 Scanning Hall probe analysis of the shape dependence

SHPI allows further investigation, permitting the spatial aspect of the transition to be directly probed, and revealing information that non-imaging measurement techniques cannot. The information available is limited to stray field, resulting from the magnetisation response to applied field, at the surface only. However, the samples, which have been polished on the imaging surface to allow a constant sensor fly height of 10 μm from the surface, are imaged on their largest surface, with the sample thickness in the direction orthogonal to the imaged

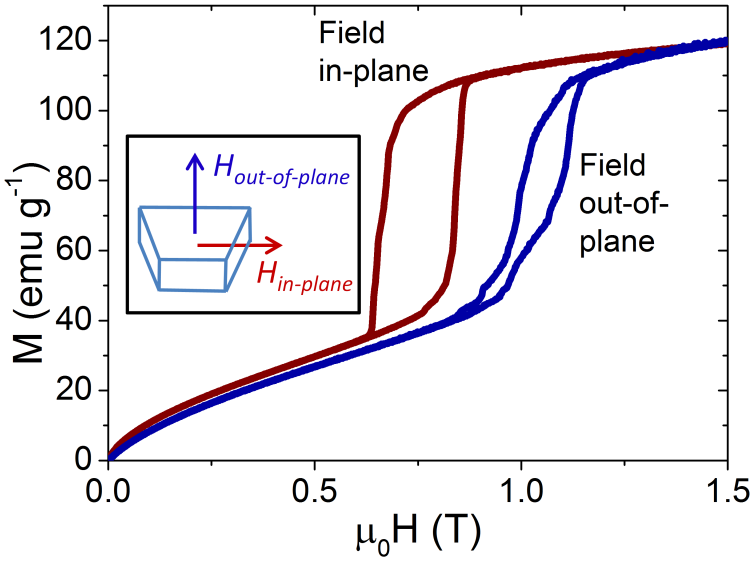


Figure 4.16: Magnetisation loops in applied field of a plate-like sample of $x = 1.4$, at 194 K, with a field rate of 1 mT s^{-1} and with the field applied in the directions in-plane and out-of-plane to the plate, as demonstrated in the inset, following Yako *et al.* [120]. The sample is roughly cuboid, as shown, and has approximate dimensions of $1.5 \times 1.5 \times 0.35$ mm^3. This shows a geometry where the global demagnetising factor is increased when the magnetic field applied is switched from in-plane to out-of-plane, leading to detrimental effects on the transition: the hysteresis is decreased but at the cost of a significant rise in applied field required for the whole transition.

surface being the smallest dimension. As a result, the surface stray field response can be approximated as closely representative of the bulk spatial magnetisation, as discussed in section 3.4. For the following sets of data termed 'static' imaging, an image is performed at a set temperature in a constant field for a sequence of field values across the transition. Each image takes approximately 30 minutes to complete, between which H is varied then held constant again at the next chosen field value. Therefore, it can be approximated that these measurements are in the fully static regime, after any relaxation present has occurred, and any dynamic effects previously discussed throughout this chapter (on the order of tens of seconds) will not be measured.

Using the situation exhibited in Figure 4.16, imaging the transition with H applied in the highest and lowest demagnetising factor directions will expressly confirm the simulations in Figure 2.11 and the explanation for the moving of H_{c3}. See section 3.4.3 and 3.4.6 for a description of the differences between in-plane, out-of-plane, static and dynamic imaging. A selection of static images for H applied in the direction of largest demagnetising factor (out-of-page) to a cuboid sample of $LaFe_{13-x}Si_x$ with $x = 1.4$, approximate dimensions $1.0 \times 0.4 \times 0.3$ mm^3 and at 194 K are shown in Figure 4.17. The image sequence shows both field increasing from $\mu_0 H = 0$ to 1.5 T and then decreasing back to 0 T, with the corresponding H values that each image corresponds to shown on the $M(H)$ loop in Figure 4.17(c). The field direction here is parallel to the direction of highest sensitivity of the Hall sensor. Therefore, regions with an increase in M, which will align with the field, will directly result in an increase in measured Hall voltage, V_H, from the stray field, which is indicated here by an increase in the brightness of the pixel. Since these images are in the maximum demagnetising factor orientation, the dynamic relaxation of the sample would be expected to be arrested mid transition resulting in a mixed state being present for a range of H during the transition. This is observed, such as during the field steps labelled '2' and '3' in the PM to FM transition (Figure 4.17(a)), and '6' and '7' in the FM to PM transition (Figure 4.17(b)). The bright regions represent the FM phase, and the duller regions (such as that for the entire sample at field '1') are PM, inferred from the expected stray field response respective of each phase's magnetisation, in addition to comparison of the sample in T and H known from magnetisation measurements, as shown in Figure 4.17(c). The images show that for the PM to FM transition, the FM regions first nucleate at the two ends of the sample with respect to its longest dimension, indicating the regions of largest internal field resulting from the spatial variation of demagnetising fields. The first-order characteristic is clearly shown at fields '2' and '3' in the contrast between new FM regions and those that have remained PM, with a distinct boundary which progresses towards the centre of the sample with increasing H, until the sample is fully FM. Between small field steps (not shown) the progression is smooth and the measurable phase boundary is broad showing no indication that microstructure is playing any role (magnetic features visible particularly in the PM state (e.g. at field '1') simply indicate physical surface features). The

FM to PM transition instead nucleates at the centre of the sample and progresses towards the edges where the FM phase originally nucleated until the sample is fully PM again.

Local behaviour, extracted from the images at a single position on the sample, shows explicitly that the transition is first-order locally and that the broadness of the transition in $M(H)$ is due to a spread of local sharp features (Figure 4.18), as the images in Figure 4.17 imply: positions A and C, as marked in the figure, transform from PM to FM very sharply, approximately 0.2 T below the transition of the region of sample at position B. Similarly, the reverse transition shows the same trend relative between the three positions, indicating that, locally, the hysteresis width appears to be comparable, and small (< 0.04 T), for all regions of the sample.

In order to measure the response of the sample with H applied in the lowest demagnetising factor, the imaging needs to be conducted instead with field applied in-plane and using dynamic imaging (see section 3.4.6 for details of this method). The reasoning for the latter is that following the results in section 4.3, in this geometry the sample will relax fully through the transition within tens of seconds and mid-transition states will not be revealed by static imaging. This means the location of nucleation and direction of growth would not be observed; only the initial and final states will. For a situation following Figure 2.11 [117] and with field applied in-plane to the sample and sensor, the predicted sensor response to stray field from FM regions growing from the central portion of a PM sample, and conversely PM regions growing from the ends, is shown in Figure 4.19. Dynamic imaging data is shown in Figure 4.20 at a selection of H values around the transition loop (again as indicated in Figure 4.20(c)): here the images are consistent with the predicted scenario in Figure 4.19, with the PM to FM transition nucleating in a central vertical band of the sample with respect to the image orientation, indicating the region of largest internal field, and progressing towards both ends of the sample in the direction parallel to the sample's longest dimension (and the field direction). Conversely, the FM to PM transition has the opposite behaviour. Line scans across the sample showing the stray field strength in the x dimension, at various applied fields, clarifies this situation, shown in Figure 4.21. This result shows a completely different sample

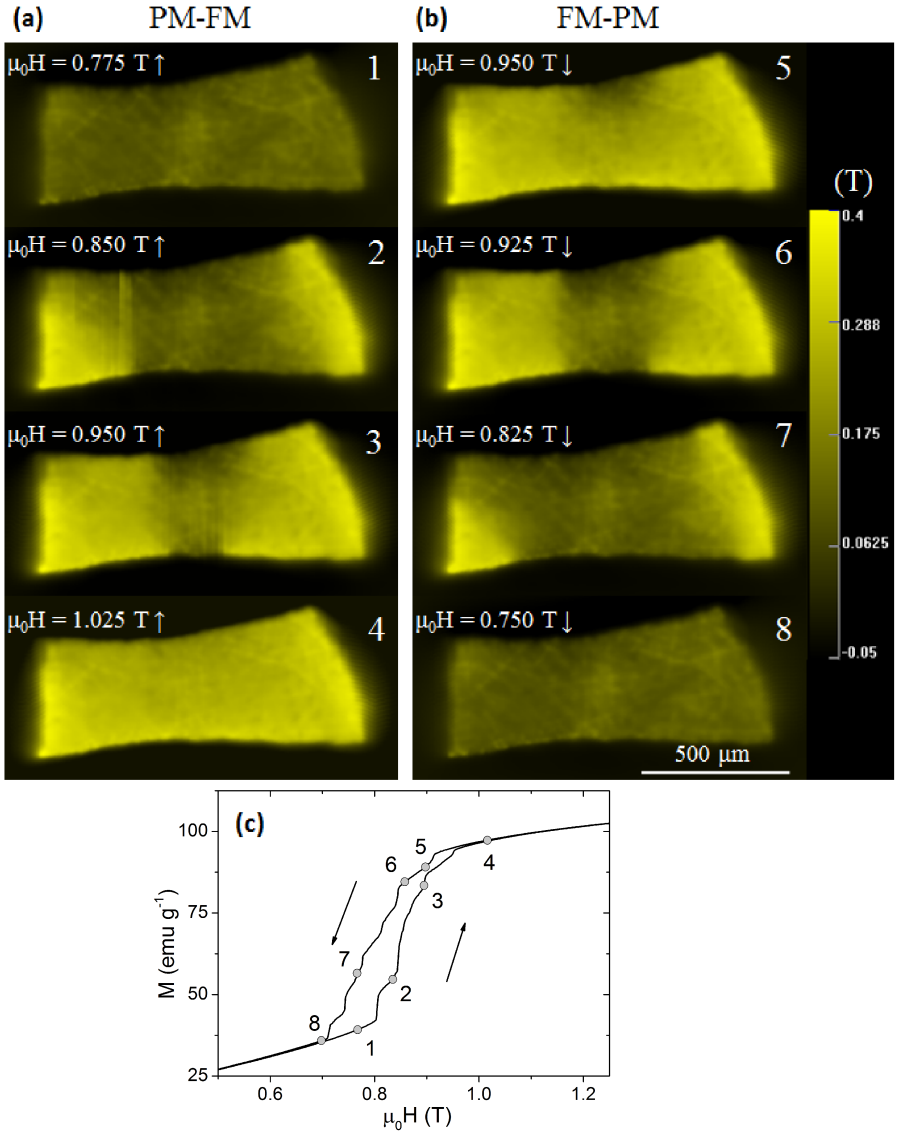


Figure 4.17: Series (top to bottom) of static Hall imaging captures of an approximately cuboid $1.0 \times 0.4 \times 0.3$ mm^3 sample of $x = 1.4$, at 194 K, with field applied out-of-page, showing (a) the PM to FM transition and (b) the FM to PM transition. The images show the 1.0×0.4 mm^2 surface. The field of each image is given and the up and down arrows represent the field increasing and decreasing, respectively. The scale bar indicates the strength of the stray field in Tesla. (c) A comparison $M(H)$ plot of the sample with the same field direction showing the approximate field values at which each image has been captured, as numbered. Small inconsistencies between (a)/(b) and (c) result from minor temperature variations between the two different measurement apparatus used.

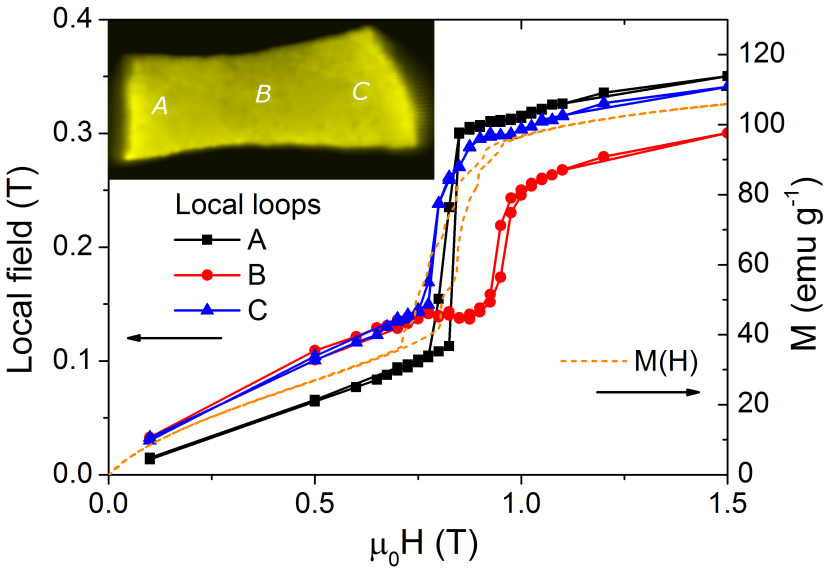


Figure 4.18: Local stray field data as a function of $\mu_0 H$ for three surface positions (shown in inset) extracted from the image set in Figure 4.17, compared against $M(H)$ data of the same sample with the same applied field direction.

response, in comparison to the high demagnetising factor orientation (out-of-plane), giving explicit proof of how the growth of each phase is strongly determined not by compositional or microstructure features, unique to specific regions of the sample, but by local geometry with respect to the field direction. Therefore demagnetising fields dominate the nucleation of both the FM and PM phases.

Taking this further still, this situation was clarified for a particular sample geometry, as shown with measurements on one of the fragments of Scenario B/C, labelled 'i' in Figure 4.12, which is approximately cuboid with dimensions $1.1 \times 0.4 \times 0.4$ mm^3. By measuring the response to field in two different orientations (Figure 4.22), the orientation with greater demagnetising factor (Orientation 2) showed a small increase in H_{c1} but a significant increase in H_{c3} compared with Orientation 1 resulting, counter-intuitively, in a considerably reduced hysteresis. This is clearly a balancing act as the geometries of Figure 4.16 show that shapes with too large an aspect ratio present a significant increase in H_{c1}, which is detrimental to the maintaining of a sharp transition, in low field, without a corresponding beneficial decrease in hysteresis.

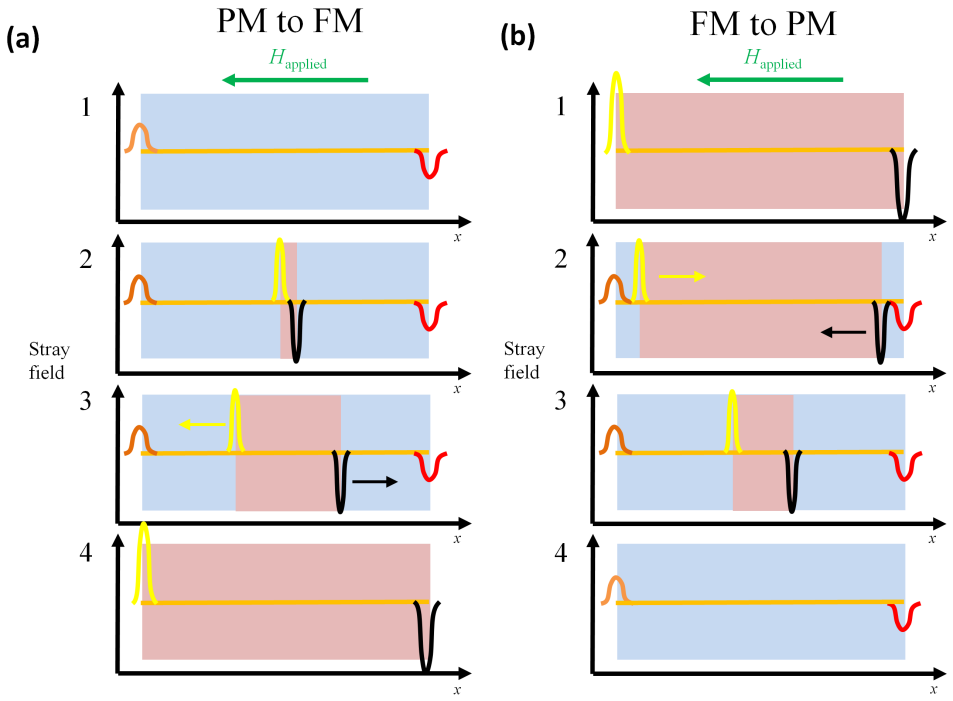


Figure 4.19: Time-evolution cartoons showing how dynamic Hall imaging of a rectangular sample, with the field applied in-plane to both the sample and the Hall sensor as indicated, would detect the first-order transition from (a) PM to FM and (b) FM to PM (steps 1 to 4 in each case). The schematic of the sample magnetisation state at four example stages of the transition is given by the blue and pink shading, representing PM and FM regions of the sample respectively. A simplified scenario of the stray field signal the Hall probe would measure is overlaid (colour-coded to approximately match the scale bar in Figure 4.20, where yellow and black correspond respectively to the positive and negative stray field emitted from the FM region and orange and red correspond respectively to the positive and negative stray field emitted from the paramagnetic regions to outside the sample).

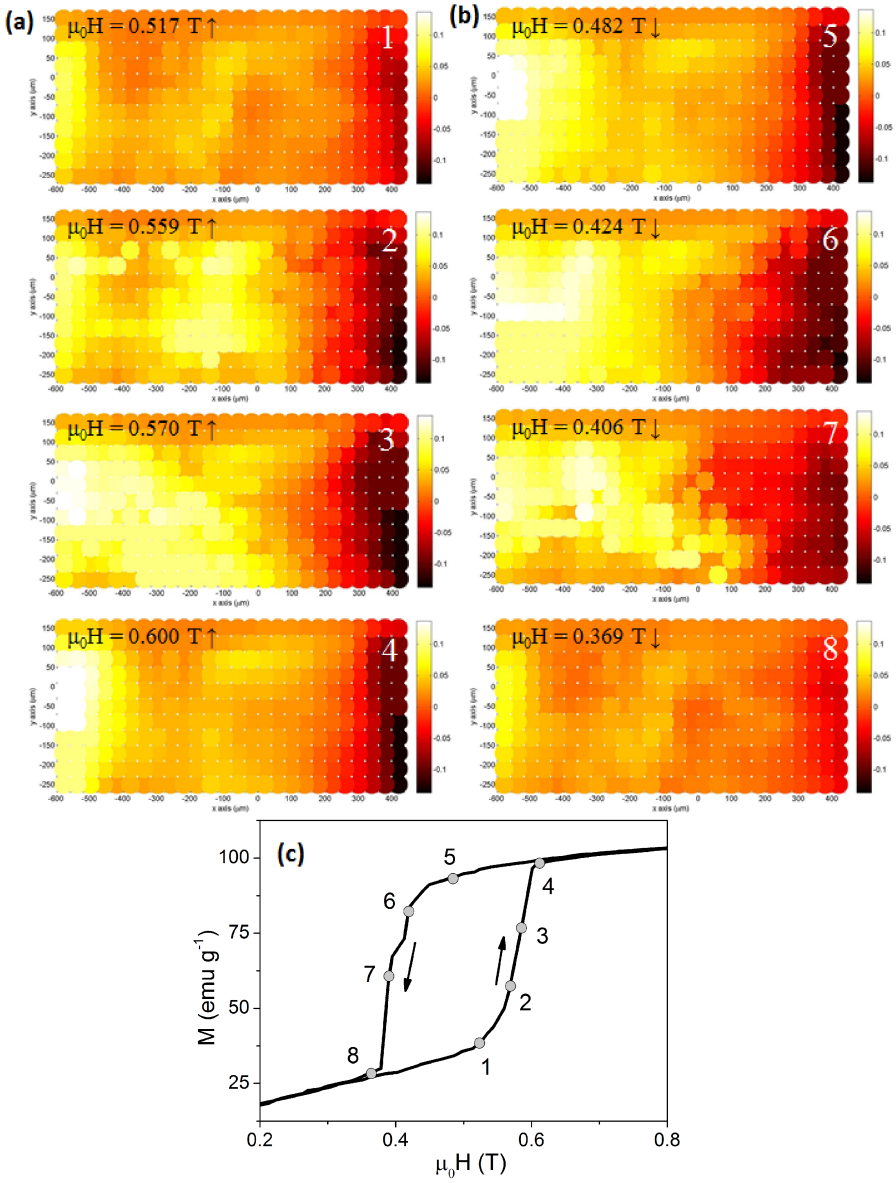


Figure 4.20: Series (top to bottom) of dynamic Hall imaging captures of the same surface of the sample of $x = 1.4$ as Figure 4.17, at 194 K, with field applied right to left (in-plane) at 8.3 mT s^{-1}. This shows (a) the PM to FM transition starting in the centre and (b) the FM to PM transition starting at the left and right ends, following Figure 4.19. The field for each image is given; ↑ and ↓ represent field increasing and decreasing respectively. The scale bar indicates the stray field strength in Tesla. (c) A comparison $M(H)$ plot of the same transition showing the approximate field values at which each image has been captured.

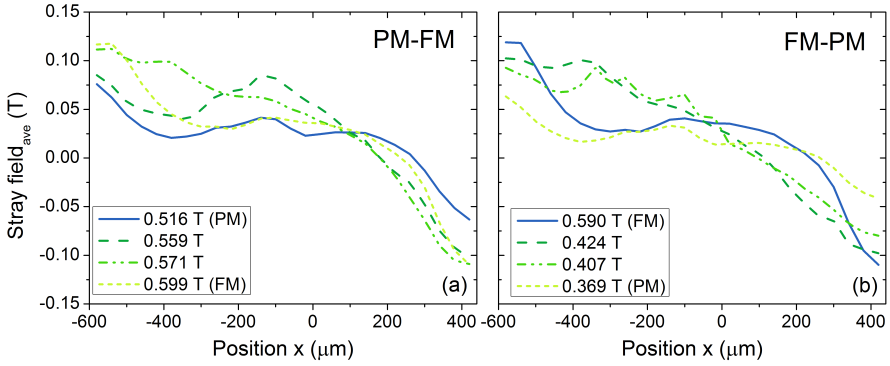


Figure 4.21: Line-scans along the x dimension (averaged along the y direction pixels) of the images shown in Figure 4.20, showing the evolution of the in-plane stray field signal as the transition is field driven from (a) PM to FM and (b) FM to PM.

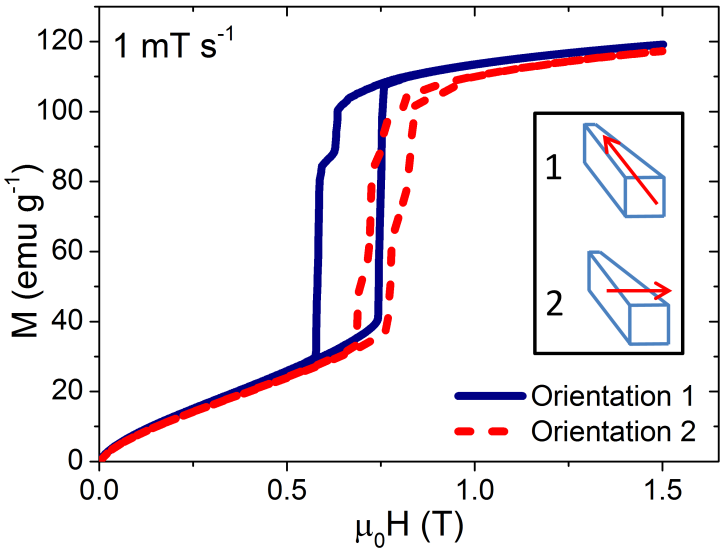


Figure 4.22: $M(H)$ loops at a field rate of 1 mT s^{-1} of Fragment 'i' (see inset to Figure 4.12(c)), measured in isolation with field applied in two different orientations, as indicated in the inset.

In this material family, there is no structural change (only ∼1% magnetovolume change) and no magnetocrystalline anisotropy. Therefore, features on both the unit cell scale and the grain size scale do not compete, allowing the macroscopic feature of demagnetising fields to dominate, in addition to microscale geometry features which will also contribute via demagnetising fields. Therefore, overall, these results demonstrate that demagnetising factor effects are able to be exploited usefully in first-order systems without structural changes or magnetocrystalline anisotropy, such as $LaFe_{13-x}Si_x$, in a way that has not been previously anticipated. Therefore, by careful choice of sample shape (such as that demonstrated in Figure 4.22), the local field within the high-field region (represented by 'p' in Figure 4.15) can be kept constant, while the local low-field region (represented by 'q') can be engineered to be significantly lower, so that the FM to PM transition occurs in higher applied field and consequently the effective hysteresis width is reduced.

4.6.2 The second-order phase transition

Thus far, the claim has been made that demagnetising fields dominate uniquely for the first-order transition. Comparing the behaviour of sample orientation and demagnetising fields on the second-order transition is important to consolidate this claim. Due to the broad characteristic in H, the variation in internal fields, which for the discontinuous, sharp transition of the first-order transition dominates remarkably, is expected to have a relatively muted effect, since the transition width in H (the range of H over which the transition occurs) is considerably larger. This is confirmed in Figure 4.23 for the same $x = 1.4$ sample in the maximum demagnetising factor orientation (out-of-plane) at a temperature above T_{crit} (205 K): the gradual change in magnetisation, indicative of the second-order transition, is global, and no significant local variations are detected. Comparison of local loops at several spatial positions, extracted from the images, with the global measured $M(H)$ data (Figure 4.24) shows retention of the broad transition shape both globally and locally. There is a suggested shift of the transition in H between positions A/C and B, but its impact on the broad global transition is not significant.

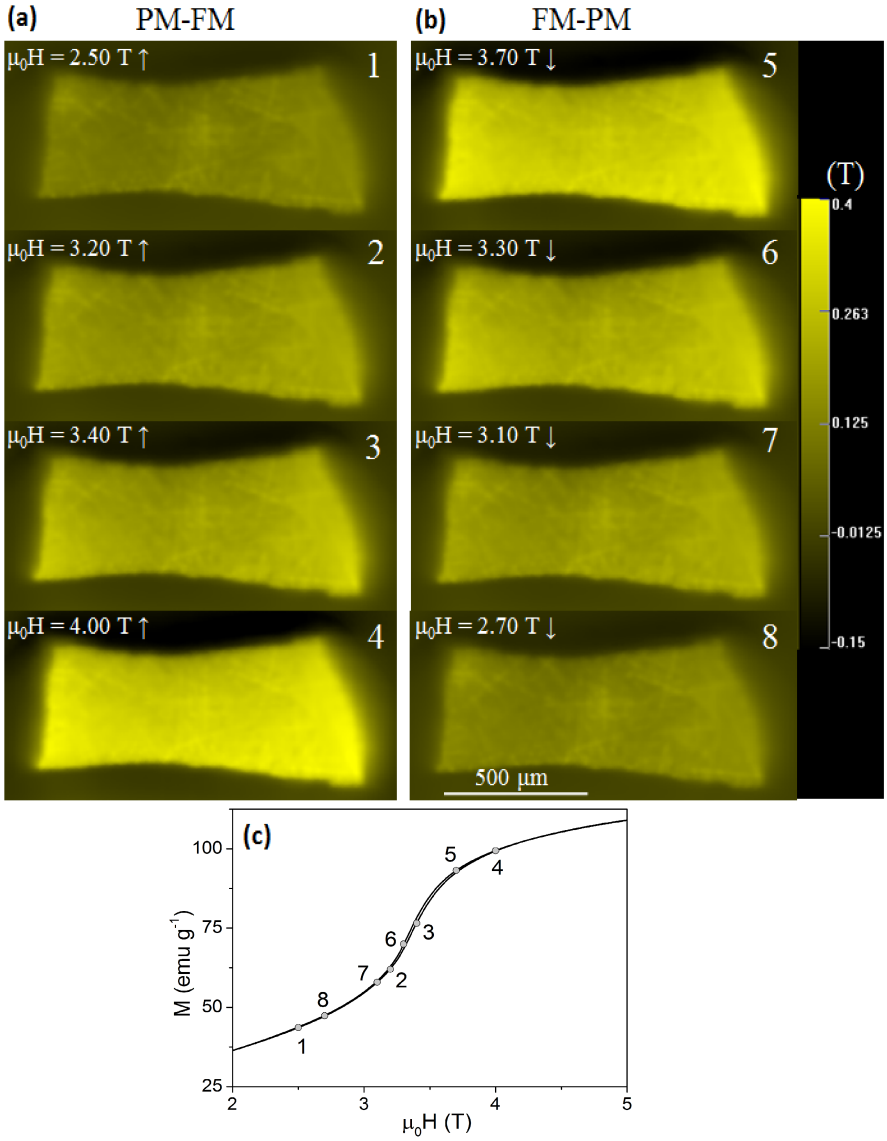


Figure 4.23: A series of static Hall imaging captures of the $x = 1.4$ sample at 205 K ($T > T_{\text{crit}}$) with field applied out-of-page. (a) The PM to FM transition and (b) the FM to PM transition are shown and, as before, the field of each image is given and the scale bar indicates the strength of the stray field in Tesla. (c) A comparison $M(H)$ plot of the sample at 205 K showing the field values at which each image has been captured.

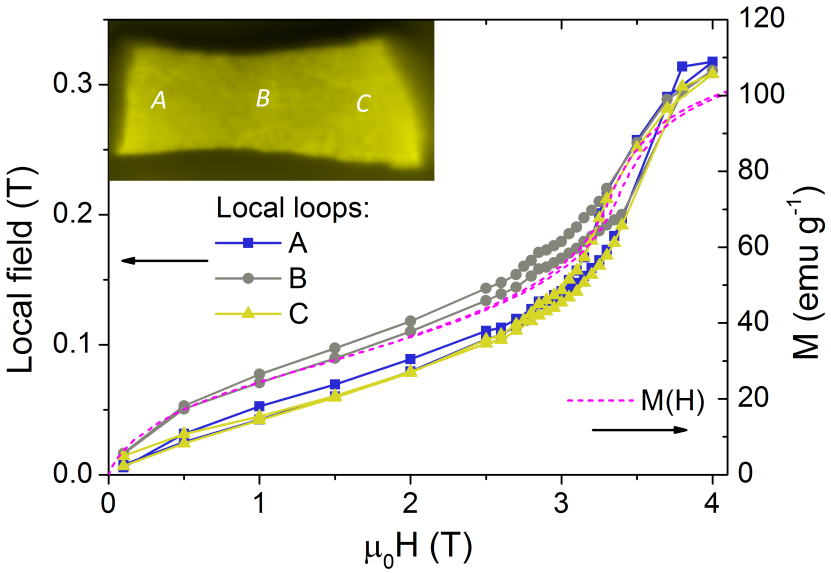


Figure 4.24: Local stray field data as a function of $\mu_0 H$ for three surface positions (shown in inset) at 205 K, extracted from the image set in Figure 4.23, compared against $M(H)$ data in the same orientation with respect to the applied field.

The second-order $x = 1.6$ sample, imaged in the maximum demagnetising factor orientation, gives an example of a transition close to T_C (Figure 4.25). Again, the transition, being very broad, shows no observable local variations: increasing and decreasing the field at 206 K reveals only gradual changes in magnetisation, as expected, with no clear local variations. This is not to say that there are not these variations, as Christensen *et al.* have shown [131] (see section 2.3), using thermography to measure the MCE of a rapidly demagnetised rectangular sample of second-order gadolinium, demagnetising fields result in measurable variations in internal magnetisation. Nevertheless, as has been shown here, the impact is minimal and thus remains a governing aspect of the first-order transition only.

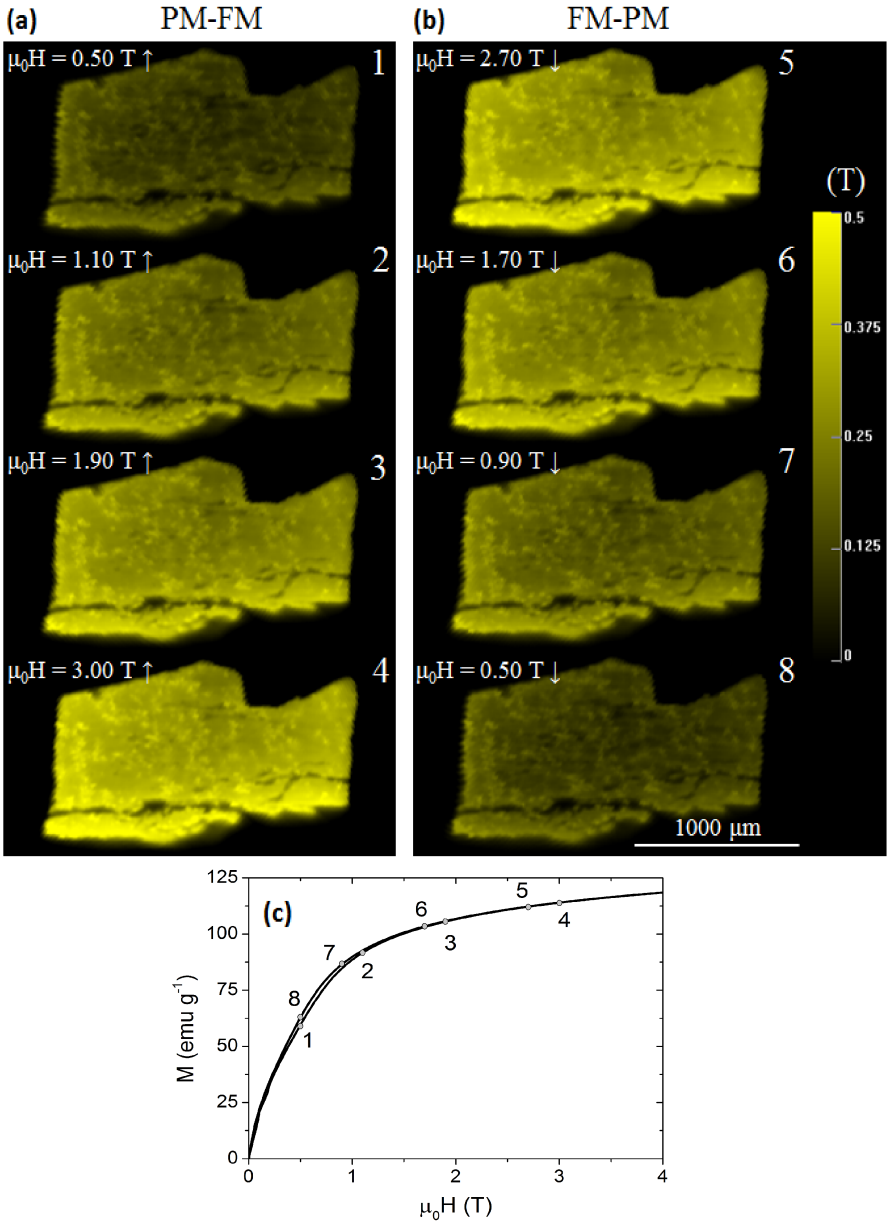


Figure 4.25: A series of static Hall imaging captures of the $x = 1.6$ sample of approximate dimensions $1.8 \times 1.0 \times 0.45$ mm^3 at 206 K, showing the 1.8×1.0 mm^2 surface with field applied out-of-page for (a) the PM to FM transition and (b) the FM to PM transition. (c) A comparison $M(H)$ plot of the sample at 206 K showing the field values at which each image has been captured.

4.7 Summary

By studying the metamagnetic PM to FM field-driven transition of first order $LaFe_{11.6}Si_{1.4}$ ($x = 1.4$), the transition width and hysteresis in field have been shown to be very strongly dependent on the field rate, which is much less significant in second-order $x = 1.6$. A relaxation process across the transition in time was observed in the first-order material, taking of the order of tens of seconds to complete the PM to FM transition. When field driven in a low-demagnetising factor orientation, the transition progressed more quickly than its relaxation in paused field implying that there is supplementary nucleation or the growth of nuclei is quickened. This result indicated a more complex growth process than that represented by the JMA equation, for which the transition rate is independent of the extent of sample transformation which has taken place prior to pausing the field, indicating that either the changed free energy environment in larger field, thermal equilibration back to the bath temperature, or a strong role of the dipole interaction between the FM and PM volumes, dominate the growth.

An experiment was devised with a bulk sample prepared in three scenarios in order to distinguish the intrinsic and extrinsic contributions to these dynamic effects: intact (Scenario A), in three fragments and reassembled in the original shape (Scenario B), and separated (Scenario C). With this sample size and shape, for field rates above 5 $\mathrm{mT\,s^{-1}}$, the three scenarios behave similarly, indicating that extrinsic heating from the MCE slows the transition, rather than it being limited by any intrinsic nucleation and growth mechanism. This reinforces the importance of thin samples and improved thermal contact for applications. In the slow field rate limit, the behaviour of the transition is dominated by nucleation and growth processes, which themselves are influenced greatly by the sample shape, size, and demagnetising fields. There is also evidence for magnetic coupling between fragments in close proximity, in the PM to FM transition, underlining the role of magnetic interaction for the progress of the transformation. However, this mechanism is a slower mechanism than that present within a single bulk of sample. Hysteresis was seen to greatly reduce with the fragmented and separated

samples, which has been shown to be caused principally by the shift in H_{c3}, whereas H_{c1} remains constant. This shift suggests that local changes in demagnetising fields, introduced by new edges, play an important and beneficial role for increasing the field at which the onset of the FM to PM transition occurs, but are much less significant for the PM to FM transition, leading ultimately to a decrease of hysteresis.

SHPI images confirm the findings of Fujita *et al.* [117] and clarify the dominant role of demagnetising fields and sample shape in determining spatially where the PM and FM phases nucleate and how they progress, which is shown to be greatly dependent on the sample's orientation to applied field. This observation has interesting implications concerning the design of refrigerant shape, and an example is given of a geometry where this is exemplified. Additionally, SHPI images of the second order transition, both in $x = 1.4$ above T_{crit}, and in the second-order composition, $x = 1.6$, show that these observed characteristics are unique to the first-order transition.

It has also been shown that despite purposely introduced breaks in the sample, the sharpness of the magnetic transition is not necessarily compromised. This is of considerable importance, since all first-order materials being considered for application have large magnetovolume coupling and often show the formation of cracks when cycled in field and temperature. This result implies that as long as samples retain their envelope shape, cracks will not necessarily be deleterious to the MCE properties.

5 | Temperature Dependence of $La(Fe,Si)_{13}$ and First-Order Character of the $La(Fe,Mn,Si)_{13}$ Series

The results of Chapter 4 were primarily limited to a single temperature, with additional data shown for the $LaFe_{13-x}Si_x$ with $x = 1.4$ at a temperature above T_{crit}, to show the behaviour of the system when it is second-order, for comparison. However, the meaning of T_{crit} was not covered in any detail. In this chapter, I extend these results and discuss the temperature dependence of the transition, including T_{crit}, with particular focus on its determination and the order of the transition. This begins with the rate dependence and intrinsic and extrinsic contributions to the hysteresis, followed by the evolution of the relaxation across the transition, as T_{crit} is approached.

This allows an examination of the role of composition on the order of the transition and its related properties, for which a series of Mn-doped $La(Fe,Si)_{13}$ compounds, with varying Mn, Si and Fe content, has been studied. The impact of increased Mn-doping on the hysteresis, T_{crit} and the contribution to the entropy change, as determined by the Clausius-Clapeyron relation, is discussed in terms of the strength of first-order character. Finally the impact of composition on the relaxation dynamics are examined and compared to 'microcalorimetry' data (specifically heat capacity and latent heat). Most of the results in this chapter are

published in Ref. [151], Ref. [150] (© 2017 by the American Physical Society.) and Ref. [153].

5.1 Temperature dependence of the first-order transition

The $H-T$ phase diagram for the $x = 1.4$ transition shown in Figure 4.1(b) is incomplete in that it does not take into account the disappearance of hysteresis, which is one definition of the ending of first-order behaviour, at a specific field and temperature, at which the critical point, T_{crit}, in the $H-T$ phase line occurs. The hysteresis width decreases with increasing temperature (as does the sharpness, or slope, of the transition), but due to the field-rate dependence of the hysteresis loop (discussed in section 4.2) and the finite field-rate used in extracting the phase lines, separately for PM to FM and FM to PM (8.3 $\mathrm{mT\,s^{-1}}$), there are both extrinsic dynamic contributions to the hysteresis, as well as the desired intrinsic hysteresis (that is, the hysteresis intrinsic to the material, independent of dynamic or external factors). Thus, due to extrinsic effects, T_{crit} and the onset of the second-order transition is masked. To remedy this, one must isolate the intrinsic transition only.

Figure 5.1 shows the $H-T$ phase lines showing only the intrinsic critical fields for the PM to FM and FM to PM transitions, $H_{\mathrm{c}\uparrow}$ and $H_{\mathrm{c}\downarrow}$, respectively, with the more precise measurement of T_{crit}. To arrive at this result, the extrinsic dynamic contribution to the hysteresis has been removed via two methods, which are in agreement with each other: firstly data performed (not shown) on a single fragment of the composition, with mass < 10 μg (estimated from comparison of its moment response to field with that of a bulk sample of known mass), shows a negligible field-rate dependence. This is due to its significant surface area to volume ratio - approximately two orders of magnitude greater than for the bulk samples in this study - resulting in a considerably faster temperature decay to the bath, and only evidence of the intrinsic hysteresis, even at the fast field sweep rates available in the PPMS. Figure 5.1 is derived from this data, with the critical fields of the transition, at each temperature, defined as the mid-point in field of the transition for both PM to FM (field increasing) and FM to PM

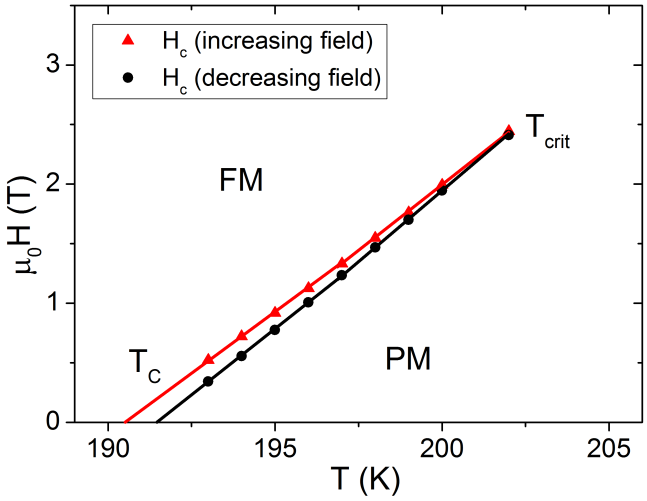


Figure 5.1: The $H-T$ phase line for the $x = 1.4$ sample as shown in Figure 4.1(b), updated to show the intrinsic critical fields on increasing and decreasing field, $H_{c\uparrow}$ and $H_{c\downarrow}$, respectively. This gives the estimated critical point, T_{crit}, defined here by the disappearance hysteresis. See text for details.

(field decreasing). The intersection of the phase lines gives T_{crit} between 202 K and 204 K, and the extrapolated T_{C} value is consistent with the bulk value (Figure 4.1).

The second method is obtained from magnetometry on bulk samples, which exhibit field rate dependence, as described in the following. Figure 5.2 shows $M(H)$ data for a range of temperatures close to and above T_{C} at three different field rates, 1.0, 8.3 and 18 $\mathrm{mT\,s^{-1}}$ (as before, covering the limits of field rate experimentally available). The hysteresis width is shown to increase with increasing field rates for all temperatures, indicating an increase in the extrinsic contribution. However, a decrease in all three hysteresis widths is evident with increasing temperature away from T_{C}, as shown in Figure 5.3: below 200 K, the gradient of hysteresis decrease, for all field rates, is comparable, and only above this temperature does it start to deviate from this trend, with the hysteresis width for faster field rates decreasing more rapidly with increasing T than the slow field rate.

At all temperatures, the increase of hysteresis with increasing applied field rate shows close to a

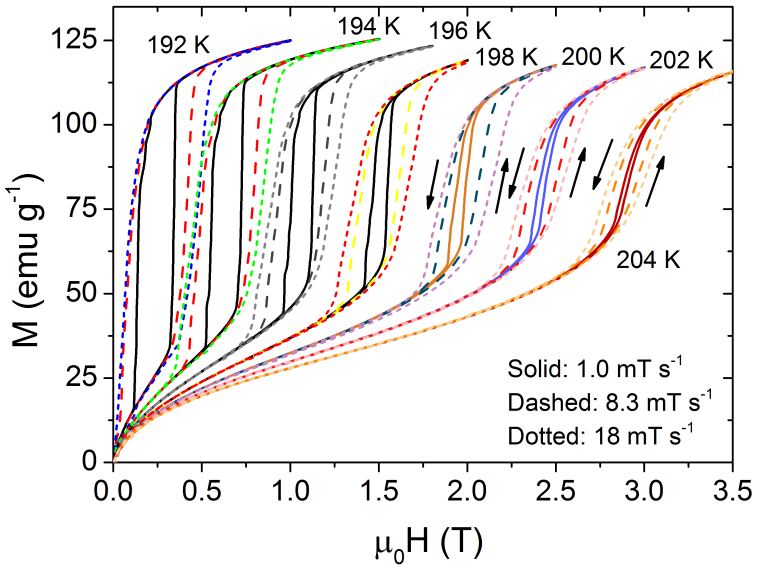


Figure 5.2: $x = 1.4$ $M(H)$ data on a bulk plate-like sample with $m = 3.47$ mg, at multiple T close to and above T_C, and with three different applied magnetic field rates. The arrows show the direction of transition around the hysteresis loops.

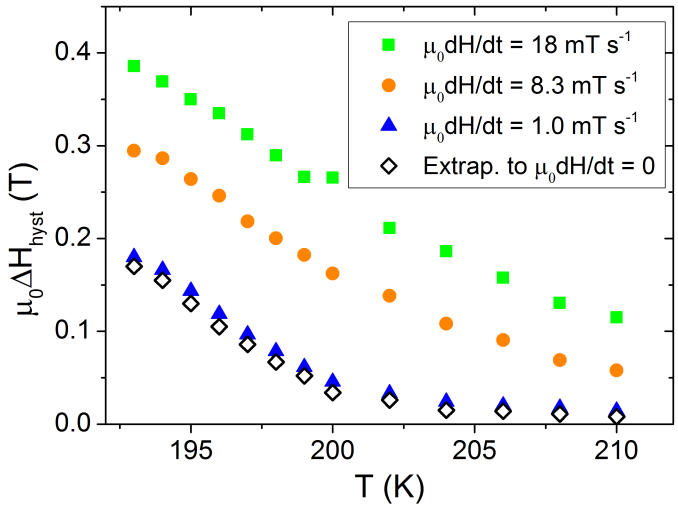


Figure 5.3: Hysteresis of the metamagnetic transition data in Figure 5.2, defined as the difference between the critical fields $H_{c\uparrow}$ for increasing field and $H_{c\downarrow}$ for decreasing field (measured from the mid-point of the respective transitions), for three field rates. Additionally, data is shown for the zero field sweep rate extrapolated hysteresis (open symbols), calculated as shown in Figure 5.4.

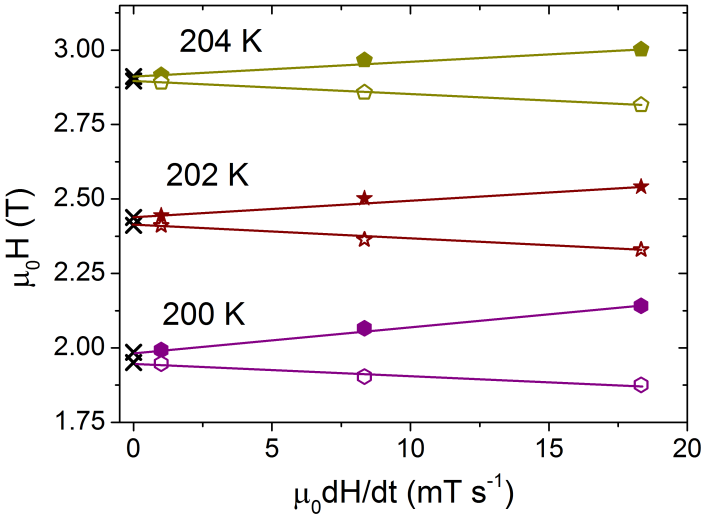


Figure 5.4: Examples, for three temperatures, of the extrapolation of the zero field rate critical fields (crosses), from the $H_{c\uparrow}$ (closed) and $H_{c\downarrow}$ (open) values at finite rate, extracted from Figure 5.2.

linear trend (Figure 5.4 shows examples at three temperatures) [115]. To extract the intrinsic, zero field rate hysteresis, the two critical fields for field increasing and field decreasing (again as measured at the mid-point of the transition) as a function of field rate can be extrapolated to zero using a linear fit, and the magnetic hysteresis, ΔH_{hyst}, is calculated as $H_{c\uparrow} - H_{c\downarrow}$. These resulting values are shown in Figure 5.3. In order to best estimate T_{crit}, the hysteresis for the fastest field rate, 18 mT s^{-1}, is plotted in Figure 5.5 with the so-called extrinsic hysteresis, calculated as $\Delta H_{\mathrm{hyst,\ 18\ mT\,s^{-1}}} - \Delta H_{\mathrm{hyst,\ 0\ mT\,s^{-1}}}$, where the latter term is the extrapolated zero field rate, and therefore intrinsic, hysteresis, ΔH_{int} (see section 2.2.1). The convergence of the two data sets gives T_{crit} consistent with that measured using the first method using the < 10 μg fragment. This represents the disappearance of the intrinsic contribution to the hysteresis from the 18 mT s^{-1} field-rate data.

The benefit of using this second method on a bulk sample is twofold: firstly, it demonstrates that, with appropriate knowledge about the dynamic response of the material and care in measurement collection, the key parameter, T_{crit}, can be extracted accurately, independent of sample size or shape. This method will be repeated for a variety of bulk samples in sec-

tion 5.3. Secondly, one can learn about the temperature dependence of the extrinsic hysteresis contribution: in particular, the observation that, despite the substantial decrease in overall hysteresis, the extrinsic addition, ΔH_{ext}, remains constant for the whole range of T between T_{C} and T_{crit}, and only at temperatures above T_{crit} does it decrease. It has been confirmed in section 4.2, following the findings of Moore *et al.* [115] and Kuepferling *et al.* [116], that this observation is caused by deviation from the isothermal condition, as a result of inherent heating or cooling of the MCE in conjunction with poor thermal contact with the bath. Here, between measurements at different temperatures, the thermal contact is unchanged, and only the MCE itself, and the rate at which it can be accessed (that is, via the sharpness of the transition in field and over what period the field rate crosses it), is independent of T. Therefore, it can be said that the MCE, via the adiabatic temperature change, ΔT_{ad}, is constant between T_{C} and T_{crit}, and any decrease in the sharp behaviour of the transition, with increasing T, is not significant. This is because the impact of this would be to decrease ΔH_{ext}, due to ΔT_{ad} being smoothed over a larger field range at the same finite field rate, and therefore more thermal transfer with the bath being allowed to take place. It is important to note, however, that this is neglecting the role of varying material heat capacity C_p, which cannot be separated at this stage; this will be discussed in section 5.4. This result of Figure 5.5 is consistent with the entropy change ΔS_{m} representation of the MCE, shown in Figure 4.2, and its plateau-like behaviour over large field ranges. Only above T_{crit}, where the material moves further into second-order behaviour, does ΔH_{ext} drop steadily, as the MCE becomes greatly diminished.

5.2 Temperature dependence of the relaxation feature

The dependence of the relaxation of the transition can now be examined, in particular the temperature dependence. Recent temperature cooling-rate dependence studies of the transition in first-order $LaFe_{11.7}Co_{0.195}Si_{1.105}$ have suggested an athermal character to the transition [124]. However, all the results so far discussed have strongly implied that the order of the

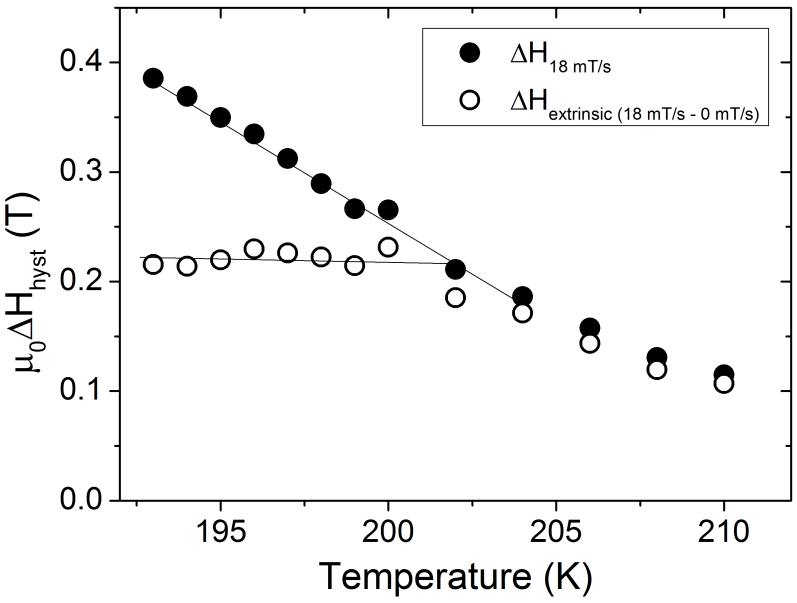


Figure 5.5: Hysteresis derived from 18 $\mathrm{mT\,s^{-1}}$ $M(H)$ data as shown in Figure 5.3 (closed) with the extrinsic dynamic contribution of the 18 $\mathrm{mT\,s^{-1}}$ data (open), calculated as $\Delta H_{\mathrm{hyst,\ 18\ mT\,s^{-1}}} - \Delta H_{\mathrm{hyst,\ 0\ mT\,s^{-1}}}$. The area between the plots represents the intrinsic hysteresis and the convergence of the plots (indicated by the guides to the eye) gives T_{crit}.

transition greatly affects the MCE properties, and the strength of the first-order character is highly dependent on temperature. By undertaking relaxation measurements, using the same method used in section 4.3 (Figure 4.6 and 4.7), but at a variety of temperatures from T_C to above T_{crit}, the relaxation feature can be compared against the strength of first-order character. Again, these measurements are performed by approaching the transition with increasing field, from the PM state, and holding the field constant at a variety of fields close to the first initiation of the transition, H_{c1}. These measurements allow a study of the relaxation into the FM state as a function of T.

Figure 5.6 shows field driven (left) and relaxation (right) data, at a selection of temperatures, for a bulk, plate-like sample of $x = 1.4$ with approximate dimensions $1.5 \times 1.5 \times 0.35$ mm^3, and with field applied in the plane of the sample. Here, the PM to FM transition is approached from zero field at rate $\mu_0 dH/dt = 8.3$ mT s^{-1}, and magnetisation data is acquired for 300 s after the field is held constant, at a variety of field values, as shown and defined in the figure. Between each measurement the field is reset to $\mu_0 H = 0$ T. The resulting relaxation shows a period of a close-to-linear increase in magnetisation, which can be directly taken as the relaxation rate, dM/dt, representative of the specific pause field value and temperature. As with the data of Figure 4.6 at 194.5 K, the relaxation curve observed steepens as H is increased above H_{c1} (and field-driven further through the transition) before being allowed to undergo its relaxation. Also observed is the decrease in slope with increasing T, irrespective of pause field value (i.e. how far through the transition the sample is driven before the field is paused).

A collection of extracted linear fits, for a range of pause fields and at a range of temperatures, can be displayed to clarify and quantify the situation. This is shown in Figure 5.7 (more temperatures are included than shown in Figure 5.6). In all cases, the linear stage of increasing M is extracted as the gradient value, dM/dt. Since, for increasing temperature, the values of H_{c1} increase (following the phase line), in order to allow simple comparison between data taken at different temperatures, the x-axis is plotted as $\mu_0(H_{pause} - H_{c1})$, where H_{c1} is estimated as the mid-point between the largest field pause value with no relaxation and the lowest where relaxation occurs (for example, mid-way between 0.28 T and 0.32 T in Figure 5.6(b)). The

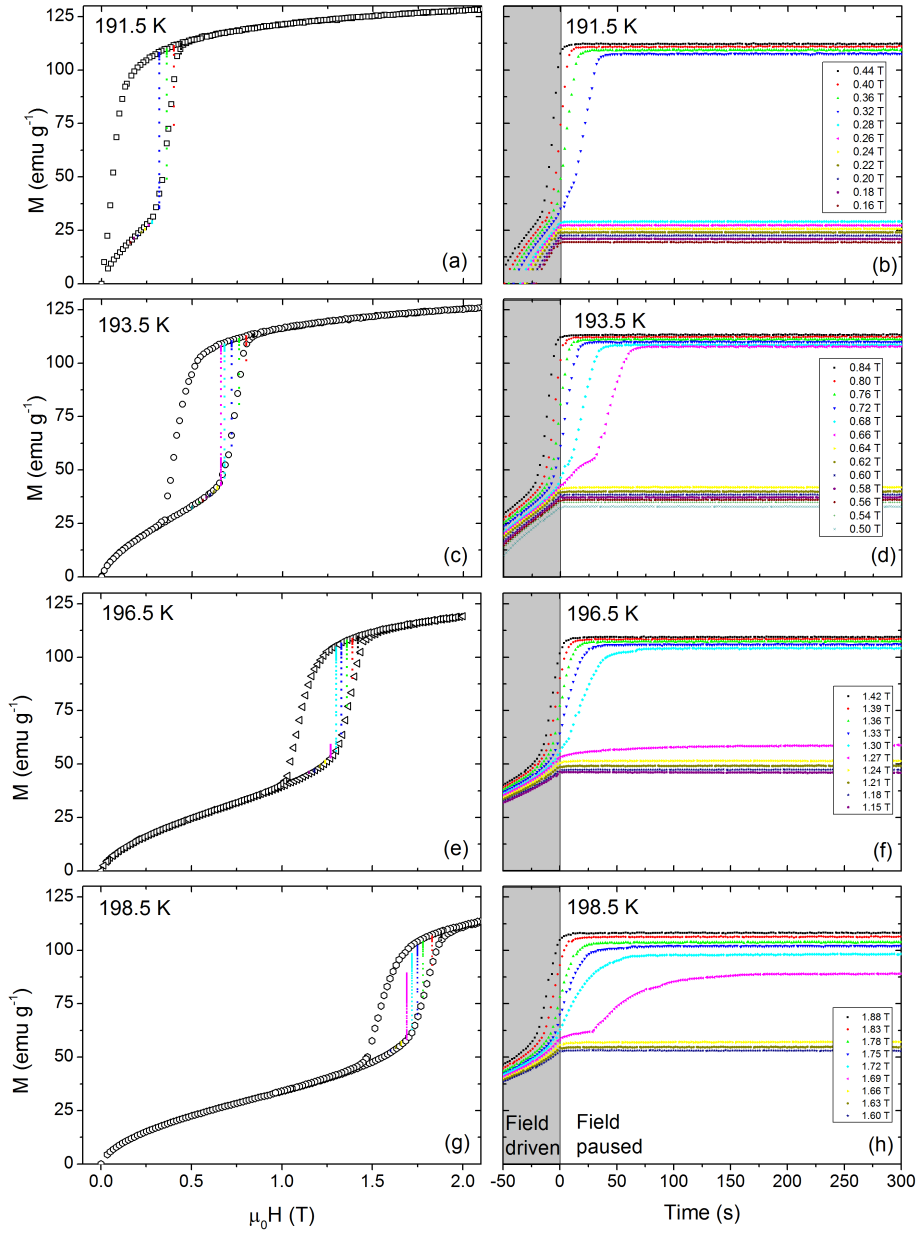


Figure 5.6: Magnetisation relaxation data for the PM to FM transition of the $x = 1.4$ sample of Figure 5.2, at four selected temperatures. (a), (c), (e) and (g) show the driven loop at 8.3 mT s^{-1} (open symbols) as a function of applied field, and (b), (d), (f) and (h) show the corresponding relaxation data in time, for 191.5 K, 193.5 K, 196.5 K and 198.5 K, respectively. For each data set, the field is varied at 8.3 mT s^{-1} from $\mu_0 H = 0$ T (PM state) and, at $t = 0$, is paused for 300 s at the target field indicated in the legend. The relaxation data are represented in (a), (c), (e) and (g) as the vertical plots, at constant field, evolving from the field-driven data.

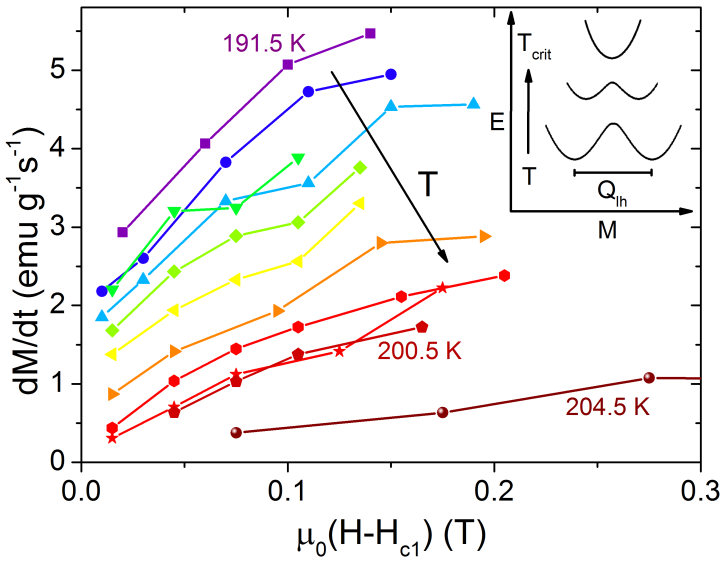


Figure 5.7: Relaxation rate in paused field for several temperatures (in 1 K steps between 191.5 K and 200.5 K) of $x = 1.4$, above T_{C}, as a function of how far past each temperature's respective H_{c1} values the 8.3 $\mathrm{mT\,s^{-1}}$ field rate sweep is paused. The black arrow denotes the direction of increasing T. Note: for each T, once H_{c2} is reached the rate levels off as the driven rate. Inset: schematic of the free energy of the system as T is increased towards T_{crit}, with a representation of the latent heat, Q_{lh} labelled. The curves at different T are offset for clarity.

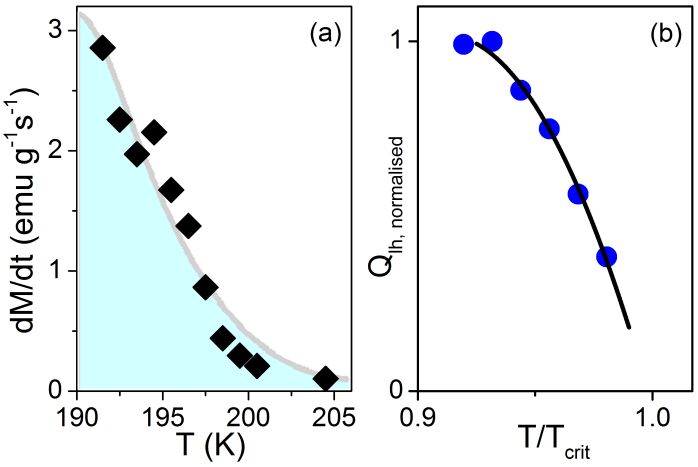


Figure 5.8: (a) Rate of relaxation from PM to FM as a function of temperature (extracted from Figure 5.7), close to H_{c1} at $\mu_0(H_{pause} - H_{c1}) = 0.01$ T for each T. The curve is a guide to the eye. (b) A representation of the $x = 1.4$ latent heat (Q_{lh}) temperature dependence, derived from Morrison *et al.* [154].

behaviour of dM/dt with H_{pause} is consistent with Figure 4.7, and additionally, its trend with T is explicit: it is found that as T increases and approaches T_{crit}, dM/dt decreases.

Figure 5.8(a) plots the rate dependence explicitly in temperature, as extracted close to H_{c1} at $\mu_0(H_{pause} - H_{c1}) = 0.01$ T, showing a clear drop of dM/dt with T, which reduces to zero close to 204 K (T_{crit}). The free energy landscape of the first-order transition requires at least two minima separated by an energy barrier which is overcome during transitions (see section 1.3.1). A thermal activation model of k_BT over this barrier cannot explain these observations, since such a model, of the form given in Eqn. 1.9, where dM/dt represents k, would imply an increase of rate with temperature. This, however, would assume an unchanging free energy landscape and barrier height, whereas a change in this landscape with both H and T is an attribute of the IEM transition [11], in particular for the evolution towards the second-order transition. In the inset to Figure 5.7, a schematic illustrates how the free energy landscape evolves away from T_C. When the material is close to T_C, there is a measurable energy barrier dividing the PM and FM phases and latent heat, Q_{lh}, associated with the change of magnetisation. As the temperature is increased towards the critical point (at which the transition becomes second order), the

latent heat diminishes. Q_{lh} has the experimental advantage of being measurable and relatively explicit in its presence, as an indicator of first-order character, whereas a discontinuous change in the magnetisation state may not necessarily be (e.g., due to broadening of the transition caused by impurities [59] or inhomogeneity from composition, varying grain orientations and strain fields, even if minor, in the composition). The same difficulty is true for hysteresis, as outlined in section 5.1. However, the release or absorption of heat will affect the growth itself, as described by Yako *et al.* [120], because the temperature change occurs on the local scale at the phase boundary, and its magnitude and subsequent dissipation will, hence, impact on how the subsequent neighbouring regions undergo transformation. Whether this is by impeding the transition of neighbouring regions by pushing them thermally along the phase line away from the isothermal condition, facilitating it via thermal activation, or perhaps some other more complex process, is important to understand.

Since latent heat information on this material is available this can be further examined. Figure 5.8(b) shows a representation of the temperature dependence of the latent heat that has been determined previously in this material system by Morrison *et al.* [99, 154]. Comparing its trend with the relaxation rate, there is a strong suggestion that the dynamics reflect the intrinsic free energy difference between the FM and PM phases. It may additionally suggest that the transition is driven by the local latent heat released once the transition starts, as a local thermal activation process that reduces as the latent heat reduces. Certainly, the trend is opposite to that which would be expected if larger latent heat, close to T_{C}, impeded the relaxation. Naturally, the latent heat decreases as the critical point is approached, and then vanishes: dM/dt drops accordingly. Thus, for the extrapolation to $dH/dt = 0$, the intercept representing the relaxation rate, in Figure 4.10, should diminish as the material composition moves from first-order towards second-order. The relaxation across the FM to PM transition has not been investigated here, and since this transition involves a latent heat absorption, the dynamics cannot be presumed as identical. The dissipation of heat to or from the boundary, depending whether latent heat absorption or release has occurred, can, assuming no significant change in the specific heat between the PM and FM phases, be

said to be equivalent at these temperatures far from absolute zero. On the other hand, a thermal activation scenario will differ, since new PM regions during the FM to PM process undergo cooling. However, Yako *et al.* [120] have compared the PM to FM and FM to PM relaxation dynamics (at one temperature) and observe the differences in relaxation rate to be minor, and instead explained by the different magnetic situations (i.e. dipole interaction and demagnetising fields) present.

5.3 Role of manganese doping on the transition

Whilst the temperature and field dependence of the presence and strength of the first-order transition has been examined in detail, its relationship with composition and to what extent a universal measure of 'order', across differing compositions and environments, is applicable is important to elucidate. Between different material systems, such a universality is unobtainable due to the extensive variety of dominant mechanisms and properties of the transition, for example, a local moment ferromagnetic system against an itinerant, or substantial magnetostructural changes against magnetovolume, for which different models apply for different origins of metamagnetic behaviour. Additionally, the wide ranges of hysteresis widths, magnetisation changes or field and temperature dependences that exist across the zoo of material systems all make the definition of a first-order strength non-trivial. Within the $La(Fe,Si)_{13}$ family, however, variations in composition and the impact on the IEM transition can be investigated for this purpose. An example of a comparative $La(Fe,Si)_{13}$ with increased Si content (on the Fe sites) resulting in a second-order transition at (and therefore also at temperatures above) T_C was shown in Chapter 4 with $x = 1.6$. However, being already in the second-order regime, no comparison about the strength of first-order character can be made. In this section, a series of samples with different Mn, Fe and Si contents have been studied.

Increased Mn content (at the expense of Fe atoms) results in a monotonic decrease of T_C [103] as well as a movement of the transition towards second-order behaviour [106]. Seven compo-

Sample	A	B	C	D	E	F	G
T_C	116	129	138	150	158	167	173
Fe	11.22	11.33	11.41	11.49	11.58	11.66	11.74
Mn	0.46	0.37	0.30	0.23	0.18	0.12	0.06
Si	1.32	1.30	1.29	1.27	1.25	1.23	1.20

Table 5.1: Nominal composition and T_C of the seven $LaFe_zMn_xSi_y$ samples.

sitions of $La(Fe,Mn,Si)_{13}$ have been measured. Their compositions and T_C values are given in Table 5.1. The Mn contents vary from 0.06 to 0.46, a range covering more than a factor of 7, leading to a decrease of T_C from 173 K to 116 K. There are also variations in the Si content between 1.20 and 1.32. This variation in Si content is unintentional. This is a less significant change in content compared to that in Mn with regards to the material's properties. For example, this change of Si alone can be expected to alter T_C by no more than 8 K [106], in contrast to the change of T_C with Mn, which for this series is almost 60 K. $M(H)$ data for samples B, C, E, F and G are shown in Figure 5.9. A general trend of decreased hysteresis and broadening of the transition is evident with increased Mn content, and additionally a corresponding change is observed for each with increasing T. Additionally, a discontinuity becomes particularly apparent for the lowest Mn compositions close to T_C.

Mn addition has been established to decrease the saturation magnetisation M_s of the system to an extent greater than expected from simple dilution of the Fe moment, which has been explained [103] and confirmed theoretically [143] by the dopant atoms coupling antiferromagnetically in the compound. A drop of M_s is correspondingly observed across the set of $M(H)$ plots. Figure 5.10(a) shows the $H-T$ phase lines for the series, with each H_c value determined as the mid-point (in M) of the transition at zero field rate, extrapolated using the method described by Figure 5.4. The shift of T_C across the series, defined here half-way between the increasing field and decreasing field H_c intercepts with $H=0$, is clear, showing that increased Mn content reduces the FM coupling and therefore reduces the stabilisation of the FM phase [103]. Additionally, the set of phase lines appear to have similar gradients, although a deviation of linearity can be seen. These observations will be returned to later in

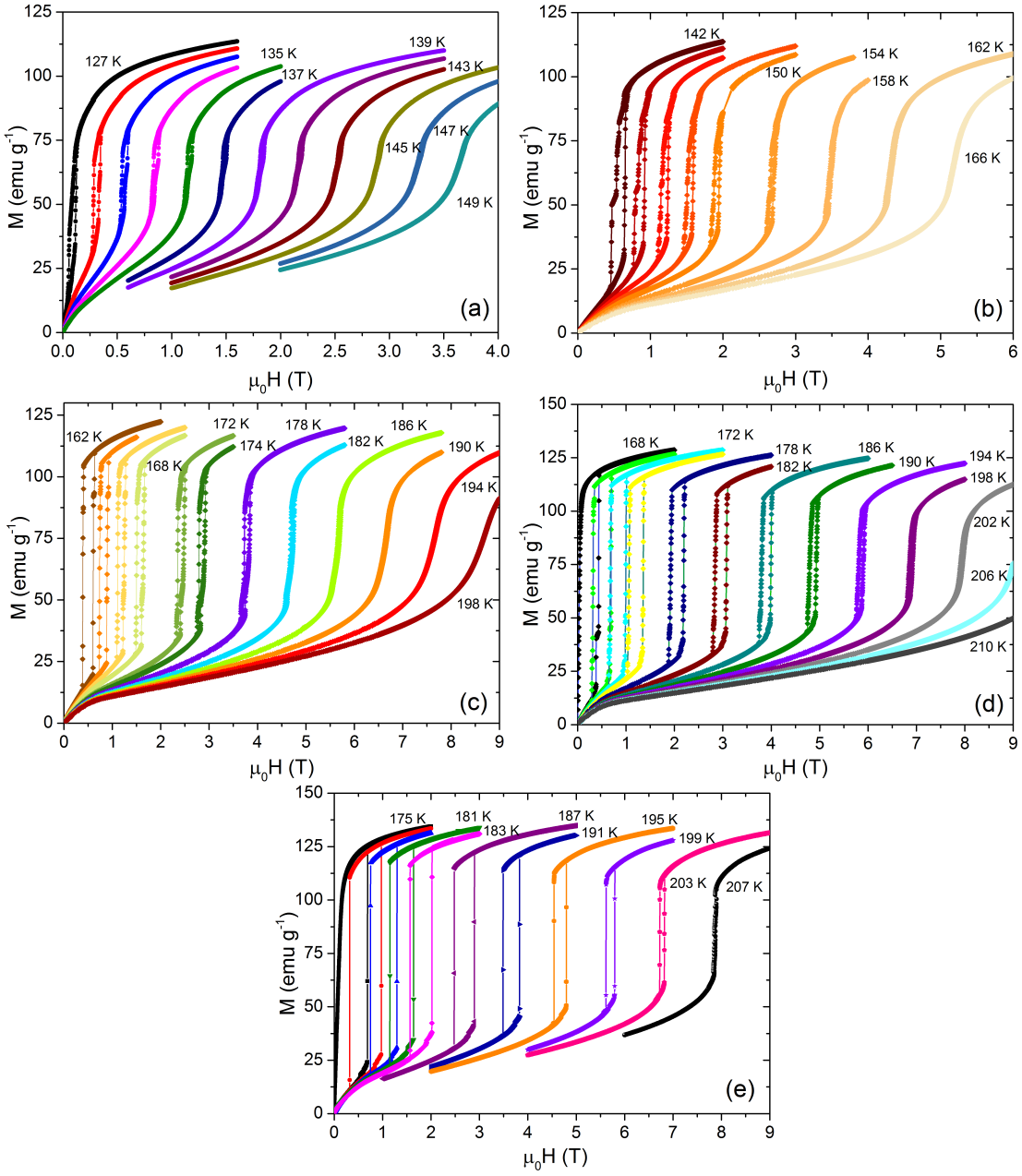


Figure 5.9: Example $M(H)$ data, measured in field rate $\mu_0 dH/dt = 1.0$ mT s^{-1} at various temperatures above T_C, for selected samples of $LaFe_{13-x-y}Mn_xSi_y$, (a) B ($x = 0.37$), (b) C ($x = 0.30$), (c) E ($x = 0.18$), (d) F ($x = 0.12$) and (e) G ($x = 0.06$).

section 5.3.2.

5.3.1 Hysteresis and T_{crit}

The values of T_{crit} are marked in Figure 5.10(a) (identified by the disappearance of intrinsic hysteresis): this is shown by the variation of magnetic hysteresis with T in Figure 5.10(b), with an uncertainty, caused by difficulties in resolving $\mu_0\Delta H_{\mathrm{hyst}} < 0.01$ T, represented by the grey shaded regions. This figure shows explicitly the trend of hysteresis decrease with increasing Mn content, in addition to a $\mu_0\Delta H_{\mathrm{hyst}}(T)$ trend which is linear with temperature. Therefore, the implication is that the systematic change in the free energy barrier height with T and H is retained for all the samples.

As shown in Figure 5.10(a), T_{crit} decreases substantially as Mn increases (G to A) with the separation quantity, $T_{\mathrm{crit}} - T_{\mathrm{C}}$, evolving from 36 K (corresponding to a field range of $\mu_0 H = 8.6$ T) for composition G to only 5 K (and $\mu_0 H = 0.9$ T) for composition A. The position of T_{crit}, with respect to T_{C}, can be thought of as one measure of first-order strength, since it represents how easily the first-order character, and thus how the free energy double well feature and the related magnetovolume coupling measure of first-order (described in the Bean-Rodbell model [66], see section 1.4), is suppressed in T and H. Mn addition achieves this. The dashed line in Figure 5.10(a) shows that the linear evolution of T_{crit} is roughly consistent across the series. However, one must be careful not to interpret this, necessarily, as a universal behaviour of the series as a function of T_{C} (i.e. with any change of Mn and Si). This is because, despite the variation of both elements in these compositions, they both vary monotonically, and the behaviour of T_{crit} with Si is also monotonic [55]. Therefore, a linear trend in both instances independently (which is suggested) should result in linearity in combination.

An equivalent plot for the interstitially hydrogenated (H content = 1.65 per unit formula) sister compositions of this set, with significantly increased T_{C} values as is expected after

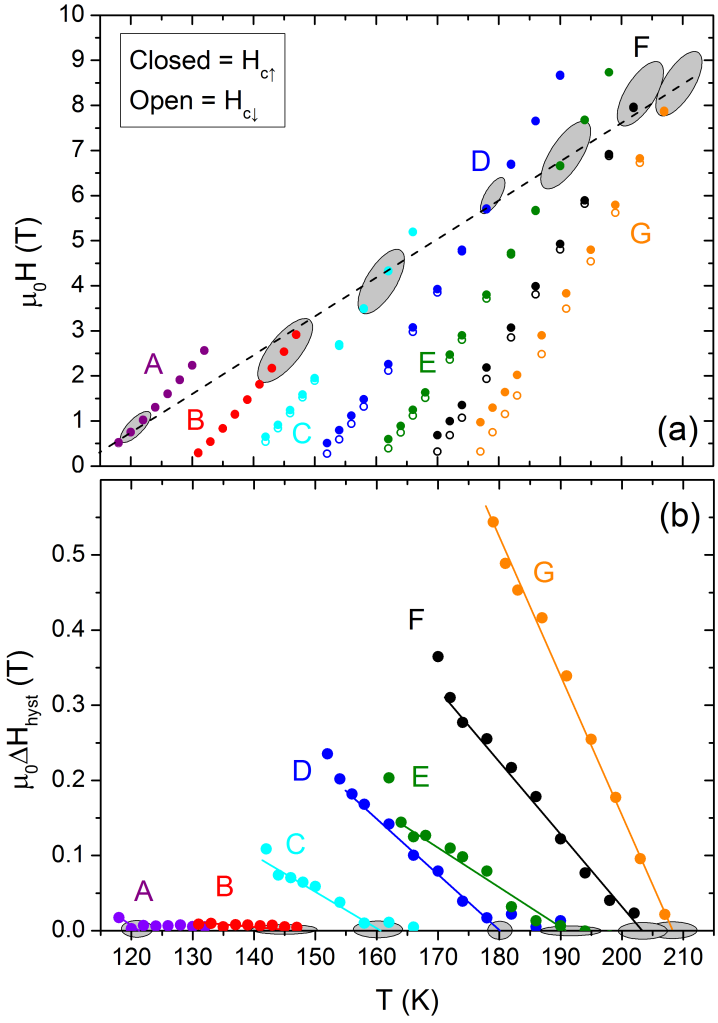


Figure 5.10: (a) H_c values determined from magnetometry (Figure 5.9) as the midpoint of transition for field increase, $H_{c\uparrow}$, (closed) and field decrease, $H_{c\downarrow}$, (open), in temperature, for the seven $LaFe_{13-x-y}Mn_xSi_y$ samples. Each H_c is extracted as the zero field rate value following the method in Figure 5.4. (b) Magnetic hysteresis calculated as the difference between $H_{c\uparrow}$ and $H_{c\downarrow}$ in (a). T_{crit} is defined (with uncertainty) where $\mu_0\Delta H_{hyst} = 0$ T and denoted by the grey ovals. These are also shown in (a).

hydrogenation, exists in Ref. [155], where T_{crit} values have been calculated by the diminishing of hysteresis, as determined by specific heat measurements. There, a systematic decreasing behaviour of both T_{C} and T_{crit}, with increasing Mn (and Si), also occurs. However, T_{crit} is greatly reduced in T and H, in comparison to the non-hydrogenated series, by almost a factor of three (comparing H_{crit}) for G, the composition with 0.06 Mn content, and its equivalent hydrogenated sister. Plotting the values of T_{C} and T_{crit} for non-hydrogenated and hydrogenated compounds together as a function of Mn content, with the hydrogenated data obtained from the above reference, a linear trend of both T_{C} and T_{crit} with Mn is displayed, and the substantial decrease of $T_{\mathrm{crit}} - T_{\mathrm{C}}$ with hydrogen is made explicit (Figure 5.11). This includes sample A (Mn = 0.46), where this quantity reduces from a small but evident value of 5 K to zero after hydrogenation, implying that hydrogenation has completely removed the first-order character.

These data are consistent with measurements included in the figure for a Mn-free $La(Fe,Si)_{13}$ compound with higher Si content from Ref. [88]. The substantially higher Si content (Si = 1.56) impacts the transition as expected, with a rise in T_{C} and a reduction of $T_{\mathrm{crit}} - T_{\mathrm{C}}$ for the non-hydrogenated sample, with respect to the Si = 1.20 content of sample G. When hydrogen is introduced and T_{C} is substantially increased, $T_{\mathrm{crit}} - T_{\mathrm{C}}$ decreases to a value comparable to the hydrogenated sister composition with the same Mn content as G. Therefore, despite the observation within that reference that the large MCE (ΔS_{m} and ΔT_{ad}) and therefore the first-order character is retained after hydrogenation, due to the interstitial hydrogen atoms not affecting the free energy structure but only impacting T_{C} via magnetovolume effects, it is noted that the volume dependence of T_{crit} is less than that of T_{C}. Within the picture of $T_{\mathrm{crit}} - T_{\mathrm{C}}$ being a measure of first-order strength, hydrogen introduction therefore decreases the strength. This has been confirmed by a greatly increased rate of drop-off of latent heat release at the transition with increasing T above T_{C}, between a sample with zero and full hydrogenation, in Ref. [150].

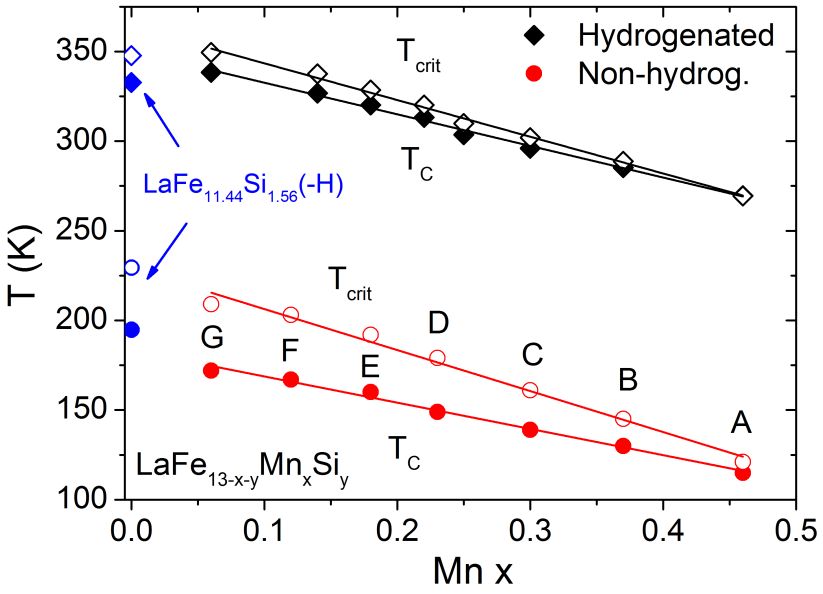


Figure 5.11: The evolution of T_C and T_{crit} with Mn content for the series (non-hydrogenated/'no H'), extracted from Figure 5.10(a). Also included are the values for the interstitially hydrogenated sister compositions (H content = 1.65 per unit formula), taken from Ref. [155], and a comparison non-hydrogenated/hydrogenated (H = 1.65) pair of zero manganese content $LaFe_{11.44}Si_{1.56}$ taken from Ref. [88].

5.3.2 dH_c/dT and Clausius-Clapeyron analysis

Figure 5.10(a) also reveals several additional observations about the transition of each composition from the slope of the phase lines. Over a relatively small temperature range ($\Delta T = 8$ K), Fujita *et al.* [92] observe that $\mu_0 dH_c/dT$ for $LaFe_{11.44}Si_{1.56}$ is almost constant in T with a value of 0.22 T K^{-1}. This linearity (or closely linear behaviour) in $\mu_0 H_c(T)$ was also observed for decreased Si content, with an increase of $\mu_0 dH_c/dT$ to 0.25 T K^{-1} for a Si content of 1.3 [88]. The latter observation is shown in Figure 2.2. This has been explained as due to the dependence of $\mu_0 dH_c$ on spin fluctuations, which leads to a T^2 behaviour at low T evolving to become proportional to T at high T. La(Fe,Si)$_{13}$ compounds, with their high temperature transition (with comparison to absolute zero), fall into this latter category. Note that, for

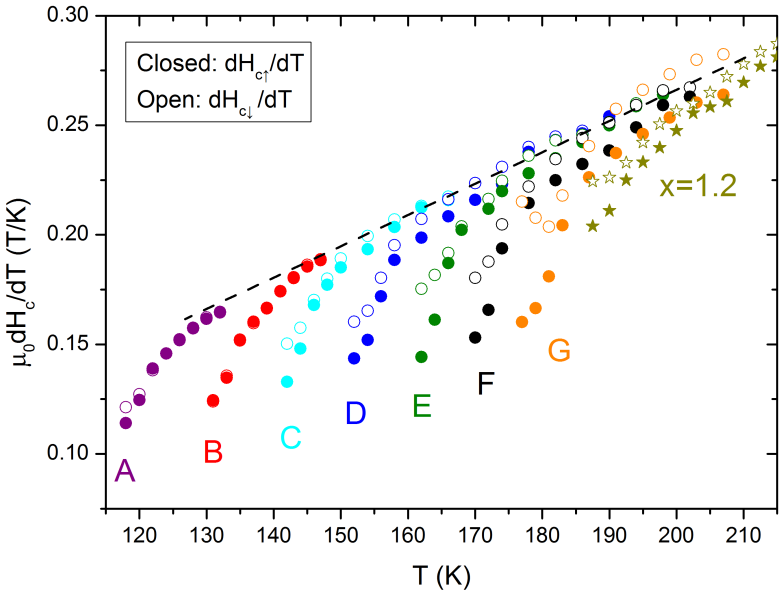


Figure 5.12: The differential of the $H-T$ phase lines for the full series of Mn-doped compositions, evaluated from Figure 5.10(a). Also included is the comparison plot for $LaFe_{13-x}Si_x$ with $x = 1.2$ (labelled). The dashed line represents an apparent universal behaviour.

several Si contents in Ref. [88] (shown in Figure 2.2), the $H-T$ slope does not change significantly, in comparison to the shift in T_C, and the phase lines appear to nest, characteristic of this IEM transition. This is also evident for the change in Mn of Figure 5.10(a).

Figure 5.12 gives the derivatives of Figure 5.10(a) demonstrating that, for all compositions, $\mu_0 dH_c/dT$ is not invariant and increases with T, as well as with decreasing Mn towards the more strongly first-order compositions. In addition, the behaviour of $\mu_0 dH_c/dT(T)$ evolves at a temperature several Kelvin above T_C onto an apparent universal line, consistent across the series. For comparison, $LaFe_{11.8}Si_{1.2}$, which corresponds to a composition with Mn = 0 with similar Si content to sample G, is also included in Figure 5.12 and is not T invariant, unlike the other zero-Mn compositions observations of Fujita *et al.* [88, 92]. However, its change of slope is less evident. This suggests the variant $\mu_0 dH_c/dT(T)$ behaviour may be a feature related to the presence of Mn, particularly at the strongly first-order transition.

Regarding the determination of the degree of the first-order contribution to the entropy change, to further extend this discussion of the degree of first-order strength, the variation in $\mu_0 dH_c/dT$ has a another important role in the evaluation of entropy change using the Clausius-Clapeyron relation (Eqn. 1.7). This relation measures only the contribution of the first-order transition. In Ref. [92], Fujita *et al.* compare the entropy changes for $LaFe_{11.44}Si_{1.56}$ determined from the Maxwell relation (Eqn. 1.6) and the Clausius-Clapeyron relation. Here they find that the entropy change calculated using the latter relation, ΔS^{CC}, is 100% of the value from the Maxwell relation at T_C, but decreases steadily, and to a larger extent than for Maxwell, as T increases. This is due to the increasing contribution from the entropy changes purely in the PM and FM states, which are included in the Maxwell analysis and keep it retaining plateau-like behaviour (such as that in Figure 4.2(a)), even as the first-order strength lessens. To obtain ΔS^{CC}, ΔM is defined as the change in magnetisation at the first-order transition, measured at H_c and representing the separation in M of the two minima in the free energy. This, however, is not necessarily trivial to define, particularly for weakly first-order transitions, where extrinsic broadening of the discontinuity is often very prevalent, and identification of the region of first-order transition (e.g. by the presence of hysteresis) is difficult. To address this, a technique designated the 'minor loop' method is employed, whereby the limits of the hysteretic region are carefully measured by approaching and then retreating the field in small steps close to H_c, for both the PM to FM and the FM to PM transitions. The field at which the hysteretic region begins can be closely measured from the onset of irreversibility in the $M(H)$ behaviour, indicating the opening of the hysteresis loop, at which the value of M at H_c is taken, for both the PM and the FM states, defined as $M_{c,\,PM}$ and $M_{c,\,FM}$, respectively. The magnetisation change is then defined as $\Delta M = M_{c,\,FM} - M_{c,\,PM}$.

Figure 5.13(a) shows for three of the compositions, B, E and G, the opposite trends of ΔM and $\mu_0 dH_c/dT$ with T which, particularly for the two most first order samples (E and G), result in a slight increase followed by a plateau in ΔS^{CC}, where the changes in the phase line slope dominate, before a fall off towards T_{crit} takes place. This plateau differs considerably from the results of Ref. [92] where $\mu_0 dH_c/dT$ is unchanging, and replicates the functional

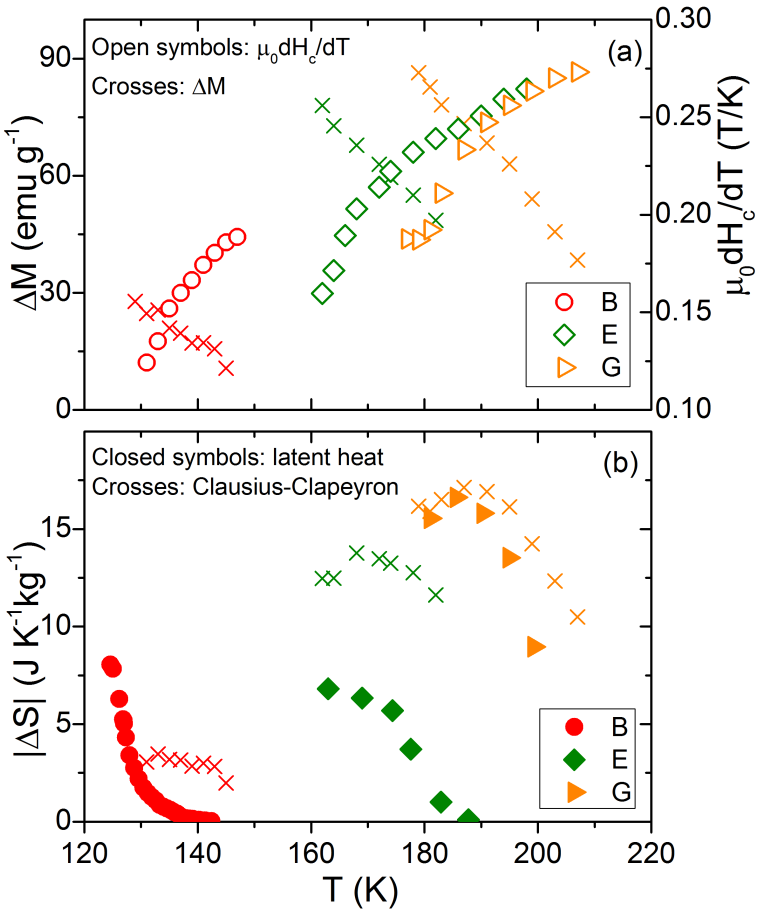


Figure 5.13: (a) ΔM and dH_c/dT estimates from magnetisation data show opposing trends. A finite ΔM is estimated even at the T_{crit} determined from hysteresis. (b) ΔS directly measured from latent heat, compared with Clausius-Clapeyron evaluation. All data points are averages of the transitions in both field directions.

form of $\Delta S(T)$ determined from latent heat measured on fragments of a few μg (included in Figure 5.13(b)). The latent heat at the transition represents the same separation of the free energy minima as that from Clausius-Clapeyron analysis and is thus expected to be in agreement. However, significant discrepancies are evident: firstly, sample E has a considerably lower latent heat contribution, at all T, to the entropy change than that measured from magnetisation; secondly, all samples show deviations between the forms close to T_{crit}. The latter can be explained by the value of ΔM extracted remaining non-zero at T_{crit}, despite the use of the minor loop method, indicating the difficulty in accurate determination of this property for transitions which are close to second-order. Regarding the former, it is suggested that further discrepancies may arise from variations between samples of one composition, since only sample E has such a disagreement.

5.4 Role of composition on the relaxation dynamics

5.4.1 Magnetic relaxation

To look at the relaxation feature for the series of $LaFe_{13-x-y}Mn_xSi_y$, and its relationship with the strength of the first-order character with compositional changes, the three compositions, as focused on in Figure 5.13, are selected, representing a range of Mn contents: $LaFe_{11.33}Mn_{0.37}Si_{1.30}$ (B), $LaFe_{11.58}Mn_{0.18}Si_{1.25}$ (E) and $LaFe_{11.74}Mn_{0.06}Si_{1.20}$ (G), referred to for simplicity in this section by their Mn contents, $x = 0.37$, $x = 0.18$ and $x = 0.06$, respectively (changes in Si content, y, are here assumed to be irrelevant). To compare dynamic features between the compositions, it is imperative that differences in the extrinsic properties of the samples themselves are eliminated: that is, specifically, variations in sample size (i.e. mass, assuming negligible differences in the densities of the materials) so that the thermal relationship with the bath is constant, and sample shape, since the effects from demagnetising fields have shown to be significant. As such, a sample of each was carefully chosen with comparable shapes and sizes: approximately cuboid, with dimensions $2.0 \times 1.0 \times 0.4$ mm^3 and

masses (3.3 ± 0.1) mg. Small variations between the samples shapes and masses are expected to have an effect, but one diminished with respect to the impact of composition itself.

$M(H)$ data showing the metamagnetic transition of these samples, for a selection of T values close to T_{C}, at a relatively slow field rate, 1.7 $\mathrm{mT\,s^{-1}}$, are shown in Figure 5.14. As with the $M(H)$ behaviour in Figure 5.9, with increasing Mn content, the transition is broadened and the jump in magnetisation at the transition, ΔM, as well as the hysteresis width, ΔH_{hyst}, are reduced. For each sample, these two quantities also reduce as the temperature is increased. ΔM at the PM to FM transition has been determined simply, in these specific samples, using the onset of hysteretic character of the $M(H)$ loops, as shown in Figure 5.14; however again this becomes increasingly uncertain for transitions with weaker first-order behaviour, in particular for $x = 0.37$, and an extent of uncertainty in this measurement is to be expected. In addition, the two most first-order compositions, $x = 0.06$ and $x = 0.18$, were seen to show a broadening of the transition upon initial field-cycling (not shown), due to permanent microstructural changes of the sample caused by the large and sudden magnetovolume changes, creating a range of distinct effective H_{c} values [31], after which the transition loop was always reproducible. This is particularly clear for $x = 0.06$ (Figure 5.14(c)) where several small steps have formed in the transition shape. Therefore, all samples were cycled across their transitions multiple times (> 8 cycles), before measuring.

Firstly, it is necessary to check the consistency of the relaxation behaviour against the zero manganese composition ($\mathrm{LaFe_{11.6}Si_{1.4}}$) to confirm that the same processes are present and the same conclusions can be drawn, after Mn is introduced, as in section 4.3. Figure 5.15(a) shows the magnetic relaxation for $x = 0.18$ at several fixed magnetic fields, specified in Figure 5.15(c). The lowest field at which the transition occurs, $\mu_0 H = 0.64$ T in this case, is denoted as H_{c1}, as for the results of section 4.2. Due to the tendency for the strongly first-order compositions to crack after first cycling, the post-virgin relaxation curves for both $x = 0.18$ and $x = 0.06$ show several distinct stages of relaxation. For example, for $x = 0.18$ in Figure 5.15(a) there is a period of varying dM/dt (such as from 0 to 15 s for the data with H paused at 0.64 T) before a stage of nearly constant dM/dt takes place after 15 s. This

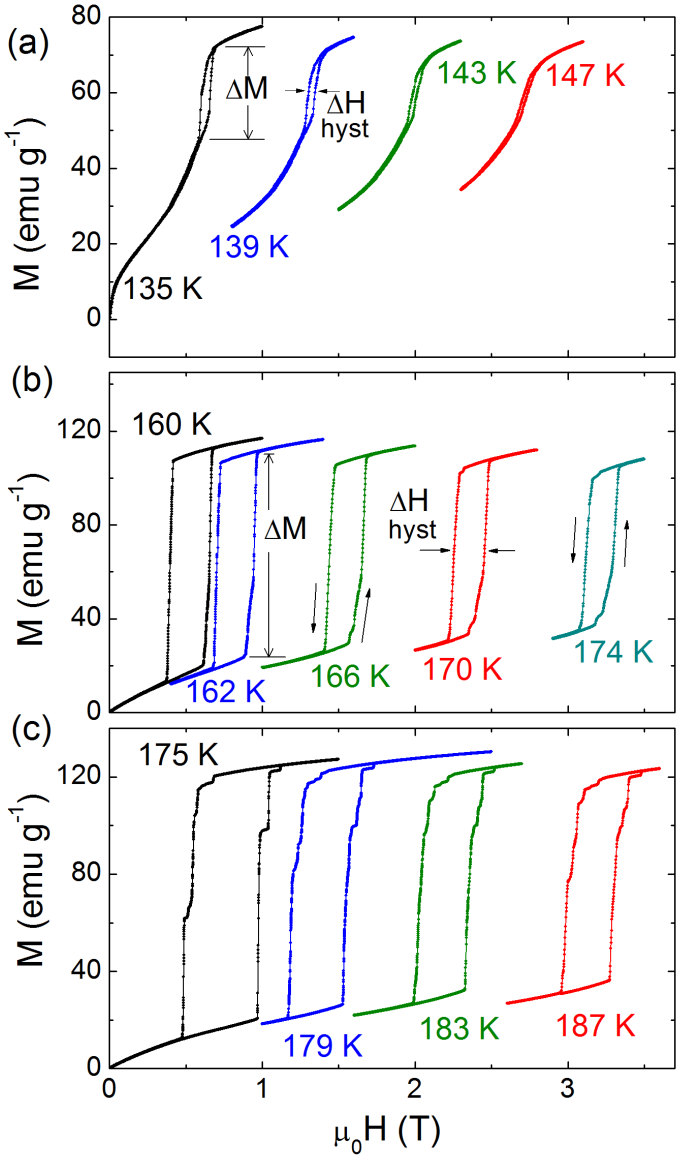


Figure 5.14: $LaFe_{13-x-y}Mn_xSi_y$ magnetisation loops at selected temperatures for (a) $x = 0.37$, $y = 1.30$ (B), (b) $x = 0.18$, $y = 1.25$ (E) and (c) $x = 0.06$, $y = 1.20$ (G). The field sweep rate for the curves shown was 1.7 mT s^{-1}. The definition of ΔH_{hyst} and ΔM is shown in (a) and (b).

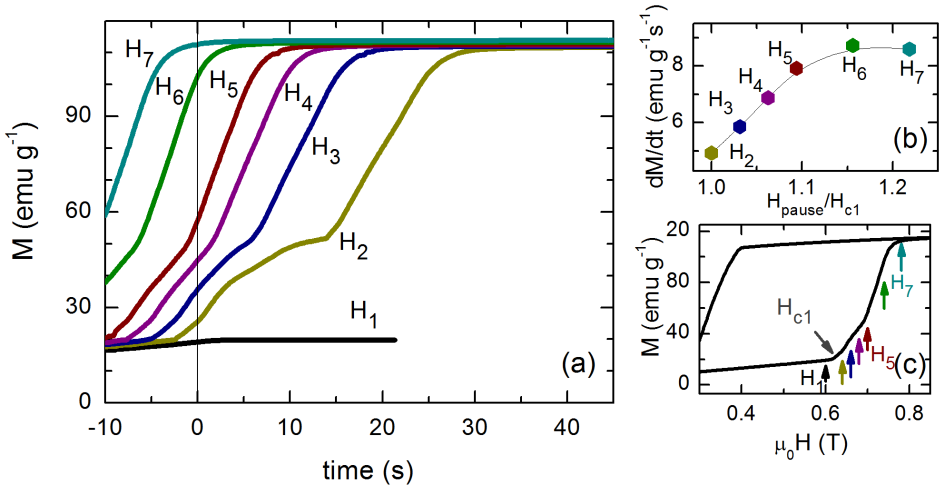


Figure 5.15: For $LaFe_{13-x-y}Mn_xSi_y$ with $x = 0.18$, (a) Temporal evolution of the magnetisation at 160 K as the PM to FM transition is approached in field, at a field sweep rate of $\mu_0 dH/dt = 8.3$ mT s^{-1}, and then held constant at $t = 0$ s at several fields along the magnetisation loop (see (c)), and allowed to relax through the transition in constant H and T. Between each measurement the field is reset to $\mu_0 H = 0$ T. The labelled field values are: $\mu_0 H_1 = 0.60$ T, $\mu_0 H_2 = 0.64$ T, $\mu_0 H_3 = 0.66$ T, $\mu_0 H_4 = 0.68$ T, $\mu_0 H_5 = 0.70$ T, $\mu_0 H_6 = 0.74$ T and $\mu_0 H_7 = 0.78$ T. (b) dM/dt, extracted from a linear fit to the principal stage of the transition in (a), as a function of the pause field value normalised to H_{c1} (see text for details).

latter stage, commencing at a time denoted t_0, can be easily identified in each measurement and, therefore, was used to define the relaxation rate, dM/dt, via a linear fit. Figure 5.15(a) and (b) show that dM/dt, for this composition, also increases linearly with increased paused field value H_{pause}/H_{c1} through the transition (consistent with Figure 4.6 and 4.7 for the $LaFe_{11.6}Si_{1.4}$ composition, discussed in section 4.3). Again, a plateau in dM/dt is reached when the fixed field is high enough for the transition to complete during the field-driving stage, before H is paused (see Figure 5.15(b)).

Figure 5.16(a), (b) and (c) show the relaxation of the magnetisation at fixed magnetic field H_{c1}, as a function of T for the $x = 0.37$, $x = 0.18$ and $x = 0.06$ samples, respectively. At each temperature, H_{c1} varies as the material moves along the $H - T$ phase line, as labelled. In this instance for each temperature and each sample, the transition has been approached

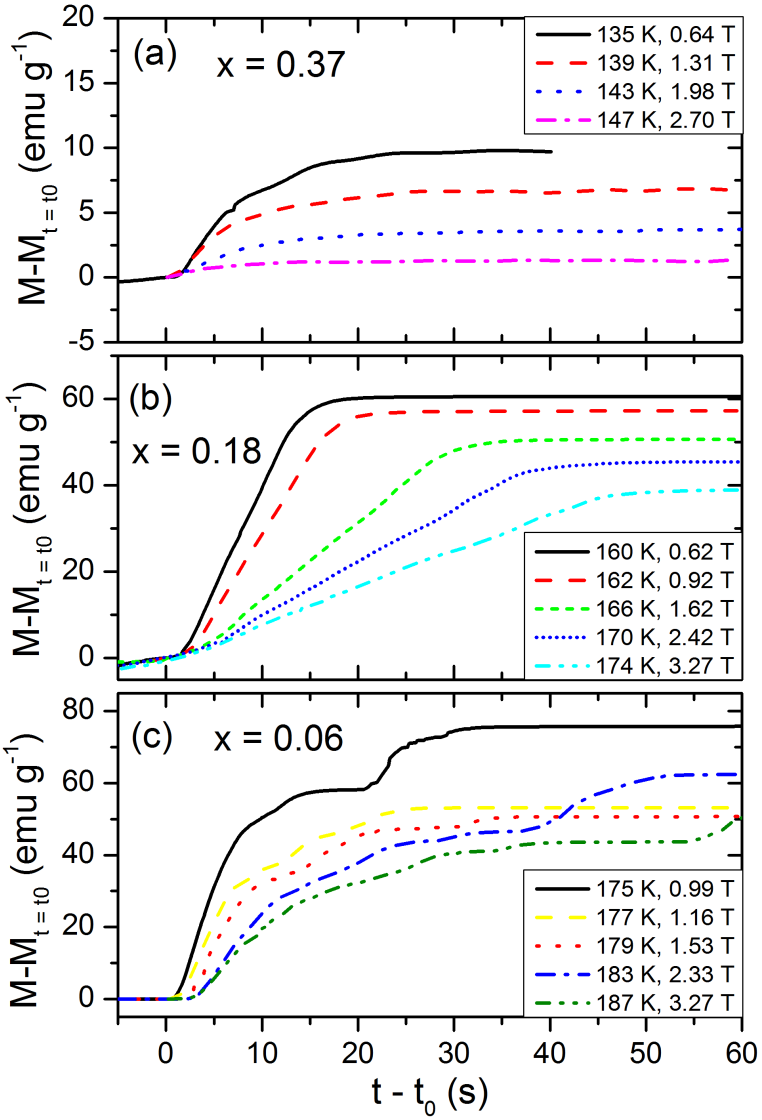


Figure 5.16: Relaxation of the magnetisation at fixed field H_{c1} for different fixed temperatures after approaching H_{c1} at 1.7 mT s^{-1}, for (a) $x = 0.37$, (b) $x = 0.18$ and (c) $x = 0.06$. H_{c1} increases with increasing T for all samples, thus T and $\mu_0 H_{c1}$ values have been labelled for each data set. The data has been offset in both M and t to the point where the principal relaxation across the transition begins for each temperature. For all data, the field has already been paused at or prior to $t - t_0 = 0$.

from zero field at 1.7 $\mathrm{mT\,s^{-1}}$ and paused at or just below H_{c1} for 60 s. The start of the principal stage of relaxation has been identified and designated t_0, and therefore, to make the comparison clearer, the y-axis has been plotted as $M - M_{t=t_0}$. The T-dependence of the relaxation slope is retained for all compositions, the $M(t)$ slope steepens for decreasing Mn content, and in the case of $x = 0.06$, the breaking of the sample caused upon first cycling (again not shown) is shown to impact the relaxation, since the different stages of the evolving magnetisation in time appear to separate with increasing T. However, relaxation to the fully FM state, in $x = 0.06$, still occurs, implying a situation very similar to Figure 4.12 and its separated pieces. This indicates that the transition is able to progress across cracks formed after first cycling, albeit at the cost of an increase in the total relaxation time.

The collected temperature dependence of dM/dt is shown in Figure 5.17(a) for all three samples, extracted from the $M(t)$ data following the method described for Figure 5.15. In order to make a direct comparison between compositions, the temperature axis has been normalised to T/T_C. The relaxation rate of all three compositions decreases as T increases, with an exponential decay (this is particularly clear for $x = 0.18$ and $x = 0.06$), as marked on the graph. The data are consistent with the relaxation rate reducing to zero at T_{crit}, which, for $x = 0.37$, $x = 0.18$ and $x = 0.06$, T_{crit}/T_C is 1.12, 1.20 and 1.22, respectively. The clear differences in the relaxation rate between the compositions demonstrate that this feature is dominating over any compositional or demagnetising field inhomogeneity that may be present between the different samples of each composition. Figure 5.17(b) plots the absolute magnetisation jump at the transition, $\Delta M(T)$, for each sample, and Figure 5.17(c) shows dM/dt normalised by $\Delta M(T)$. The three sets of data approximately collapse onto a single curve suggesting that for compositional changes, the separation between the free energy minima of the two magnetic phases is mirrored in the relaxation rate. However the behaviour in T is retained.

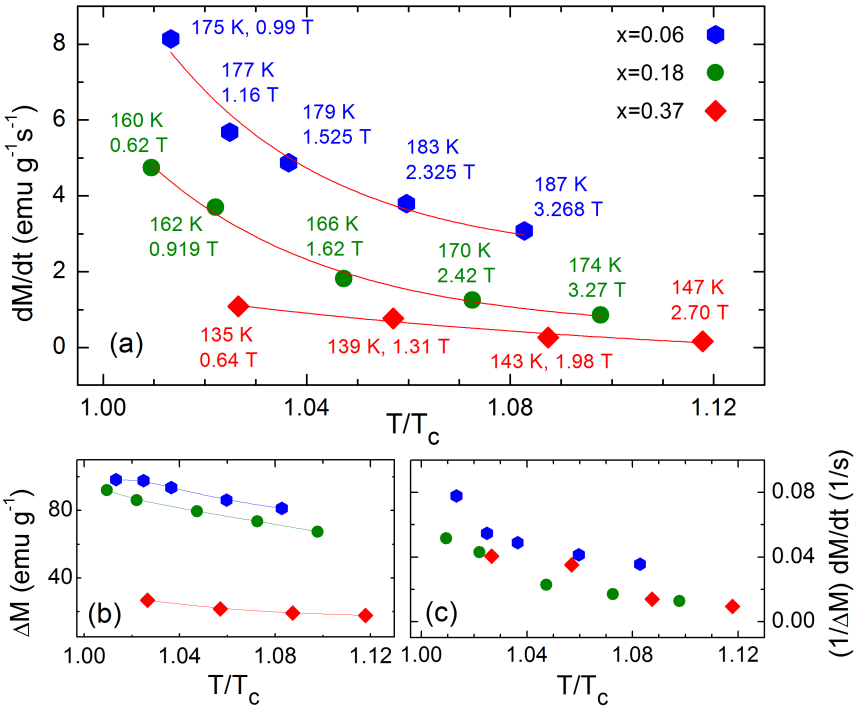


Figure 5.17: (a) Absolute relaxation rate dM/dt as a function of reduced temperature T/T_C for the three samples. The curves are the fit to an exponential form. The temperature and applied field for each relaxation curve is labelled individually. (b) Measured jump in magnetisation of the PM to FM transition $\Delta M(T)$, calculated from Figure 5.14, the curves in this case are a guide-to-the-eye to highlight the trend only, and (c) The temperature dependence of the normalised relaxation rate.

5.4.2 Comparison with specific heat and latent heat

In order to explore further the origin of the temperature dependence of the relaxation rate, the temperature dependence of the latent heat and the heat capacity is examined. In section 5.2, the latent heat, $Q_{\rm lh}$, as reported by Morrison *et al.* [154], as a property representative of the free energy landscape, was compared against the relaxation rate and was found to decrease with T, until, with dM/dt, it disappeared at $T_{\rm crit}$ (Figure 5.8). However, a discrepancy between the two functional forms is evident, indicating that the comparison to the latent heat does not fully describe the relaxation dynamics. This disagreement in form is particularly

magnified following Figure 5.17(a), which shows the exponential behaviour of dM/dt to be retained for the three Mn-doped compositions measured. Figure 5.18(a) and (b) show the heat capacity and Figure 5.18(c) and (d) the raw latent heat (shown as the variation of the thermopile voltage), for compositions $x = 0.18$ and $x = 0.06$, respectively, as a function of increasing field and temperature. These measurements were carried out on fragments taken from the bulk samples with approximate diameters of 100 μm. For these data, the use of the microcalorimetry technique allows the separation of the latent heat and specific heat contributions, as described by Morrison *et al.* [99]. Compared to the magnetisation data on bulk samples, the considerable difference in size of the fragments, in addition to greatly differing thermal environments (the latent heat and heat capacity has been acquired in vacuum to ensure the weak thermal linkage to the bath required for measurement), will be expected to greatly impact the observed dynamics of the transition [116, 156, 157]. For these measurements the interest is therefore on the intrinsic properties independent of sample size and shape: the magnitude of the heat capacity at the transition is intrinsic (with respect to time), and the existence and relative behaviour in T of the latent heat can be used to compare against the bulk magnetic relaxation.

For both compositions, the heights of the heat capacity peaks increase with T away from T_{C}, and, for $x = 0.18$, are seen to reach a maximum at T_{crit} (for $x = 0.06$, T_{crit} is above the maximum available field range so this peak is not attained). Meanwhile, the latent heat peaks generally decrease in amplitude with T, disappearing at T_{crit}, for $x = 0.18$, showing, as with Figure 5.8(b), the absence of any latent heat release (or absorption) once the material is second-order. The existence of multiple latent heat peaks at each T indicates separate transitions occurring within the fragment, separated in H due to inhomogeneity in the sample, which, as previously discussed, can have multiple sources.

With regards to the dynamic growth, the role of these latent heat peaks (and the extent of instantaneous heat release) on the growth of phase on the local scale, which impacts the subsequent macroscopic relaxation rate, is expected to be critical. However, the varying specific heat with temperature will be important regarding the resulting temperature change

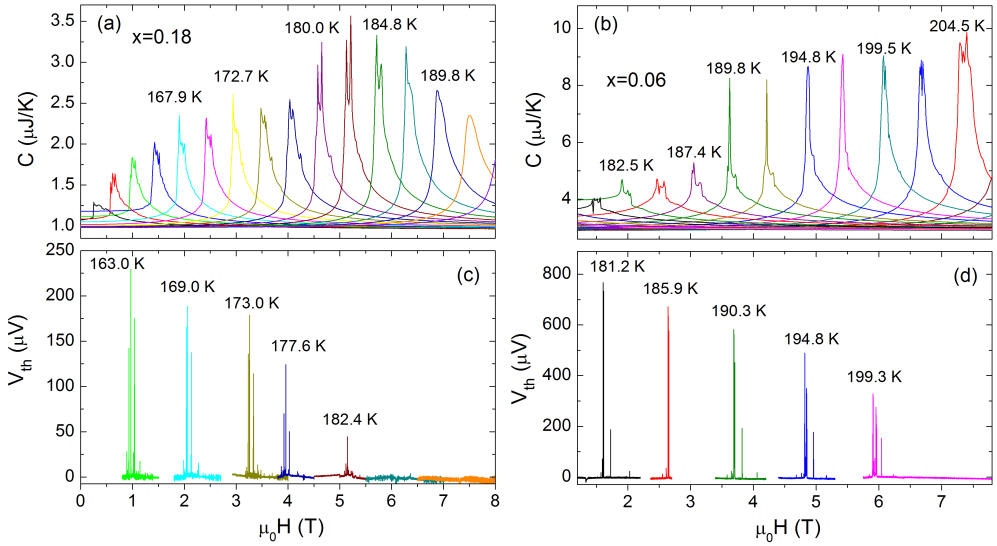


Figure 5.18: Heat capacity for (a) $x = 0.18$ (sample E) and (b) $x = 0.06$ (sample G), and latent heat (thermopile voltage signal, $V_{\rm th}$) measured for (c) $x = 0.18$ and (d) $x = 0.06$, at different temperatures as a function of applied field, using the microcalorimetry technique. The measurements in this figure were all conducted by Dr. Milan Bratko.

in the region of transition. Figure 5.19 compares the evolution of the latent heat (integrated from the peaks in Figure 5.18) and the inverse of the specific heat peak (proportional to the thermal diffusivity) as a function of temperature, for $x = 0.18$ and $x = 0.06$. The magnetic relaxation (Figure 5.17), the latent heat and the inverse specific heat all generally decrease as the temperature approaches $T_{\rm crit}$, although in detail there are still differences in their functional form. Nevertheless, the decreasing trend of these values with T is similar for both samples and consistent with a picture of spatially-localised behaviour of the evolution of the transition in terms of nucleation, latent heat release, thermalisation, time for the system to re-equilibrate with the bath (both times will increase as the heat capacity increases), and then subsequent growth of the high-field FM phase.

Therefore, the growth dynamics (i.e. relaxation) can be said to have a strong correlation with the order of the transition, and its absence will signal second-order behaviour in these

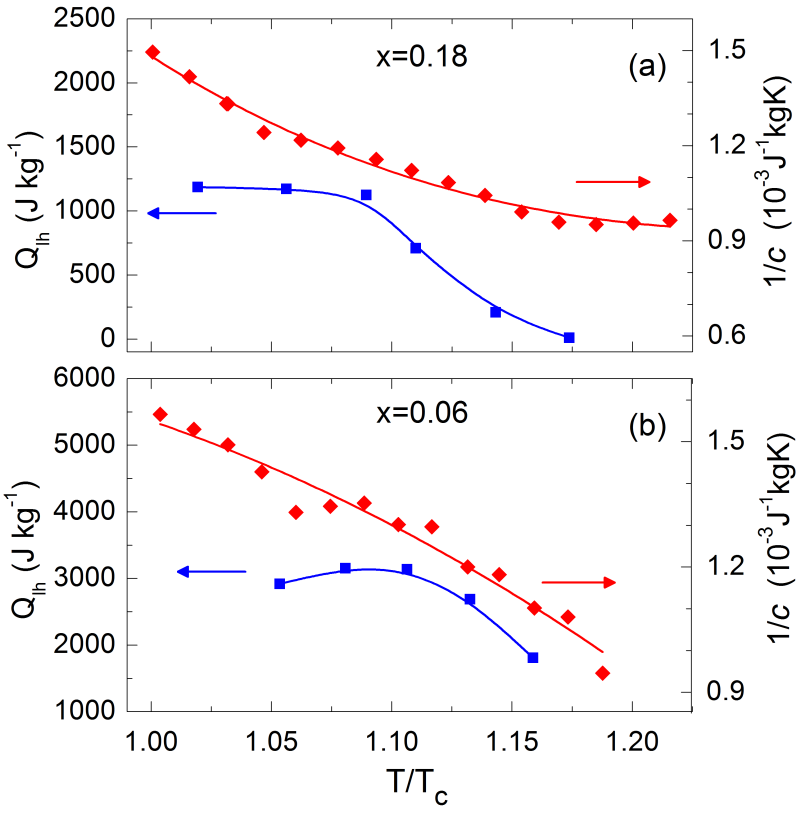


Figure 5.19: Normalised temperature dependence of the latent heat, $Q_{\rm lh}$, integrated from the latent heat peaks (left axis) and inverse of the specific heat at the peak, $1/c$, (right axis) taken on a fragment of the sample for $LaFe_{13-x-y}Mn_xSi_y$, with (a) $x = 0.18$ and (b) $x = 0.06$.

materials.

5.5 Summary

The rate dependence of the field driven transition in $x = 1.4$ has been observed as a function of T, and a method to extract the intrinsic and extrinsic contributions to hysteresis is shown. This shows an almost constant extrinsic hysteresis contribution as T increases, whilst the intrinsic contribution shows a linear decrease to zero at 202 to 204 K, T_{crit}. Above this, in the second-order regime, the extrinsic contribution decreases indicating a reduction of the MCE.

The relaxation rate also decreased with increasing T, showing that the growth is not dominated by a thermal activation model but by a variation in the free energy landscape. This is supported by a similar decreasing trend in the latent heat. Both disappear at T_{crit} and are therefore strong indicators for the existence of first-order behaviour.

Mn-doping into the $\mathrm{La(Fe,Si)_{13}}$ compound decreases T_{C} substantially, by 57 K for a change of 0.06 to 0.46 Mn atoms per unit formula. Concurrent with this is a marked weakening of first-order behaviour, demonstrated by a broadening of the $M(H)$ transition feature, reduction of the hysteresis width, and the dramatic decrease of the quantity $T_{crit} - T_C$. This quantity also decreases after hydrogenation. Focusing on three compositions, the contribution of the first-order transition to ΔS_{m} was discussed and the Clausius-Clapeyron analysis was shown to replicate the plateau-like shape of ΔS evaluated from latent heat data, due to a significant T-dependence of dH_{c}/dT which has not been previously appreciated, albeit a discrepancy in the absolute magnitude of ΔS being present in one of the compositions. Lastly, relaxation data of similarly sized and shaped cuboid samples from the same three compositions were compared, and the relaxation rate of the PM to FM transition was shown to decrease with both T and Mn content, indicative of a weakening of first-order behaviour. These are compared to the latent heat and ΔM, which decrease, and additionally the heat capacity, which increases towards T_{crit} for each composition. These observations suggest that, in addition to

the relaxation mirroring changes in the free energy landscape, the magnitude of the latent heat generated locally and the increased thermal equilibration time resulting from the increase of heat capacity impacts the relaxation rate and therefore the growth of new phase, during the metamagnetic transition.

6 | Low Temperature Specific Heat of the La(Fe,Mn,Si)$_{13}$ Series

In this chapter, six of the same set of La(Fe,Mn,Si)$_{13}$ compositions, introduced in sections 5.3 and 5.4, with a corresponding set of six samples which have undergone absorption of interstitial hydrogen (referred to throughout this chapter as hydrogenated), are studied to investigate experimentally the role of composition and hydrogen on the low temperature specific heat. This chapter focuses on the three principal contributions to the low temperature specific heat: electronic, lattice and spin waves, and their dependence on composition and hydrogenation. After summarising the relevant properties of the extended set of samples, this chapter discusses the fitting of the Debye model, the temperature ranges over which it can be used reliably, and the relative contribution of each component in this material. Following this, the results of the fittings are shown and discussed systematically. For further comparison, two samples of LaFe$_{13-x}$Si$_x$ (without Mn) are studied, with $x = 1.2$ and $x = 1.6$, in order to isolate the roles of Mn and Si within the compound. The final section of this chapter focuses on the impact of applied field on these components. Most of the results in this chapter are published in Ref. [158], © 2016 by the American Physical Society.

6.1 Summary of the La(Fe,Mn,Si)$_{13}$(-H) sample series

The nominal compositions and Curie temperatures of the twelve samples studied in this chapter are given in Table 6.1. The six hydrides are all fully hydrogenated (H=1.65), as described in section 3.1, and samples M, N and O are the hydrogenated sister compositions to A, B and C respectively. The remaining six compositions are not direct compositional pairs, however G and R have the same Mn content with a small difference in Si/Fe. The $M(H)$ characteristics have been shown for some of the non-hydrogenated samples in Figure 5.9. Figure 6.1 shows the temperature dependence of magnetisation for all twelve samples, taken in field cooling and warming in a 1 T. As shown previously, the addition of hydrogen raises the magnetic transition temperature; here by 154K, 156K and 157K in samples M, N and O from A, B and C respectively, consistent with T_{C} changes observed in La(Fe,Mn,Si)$_{13}$(-H) compounds with similar compositions after full hydrogenation by Krautz *et al.* [106]. As expected, the thermally driven magnetic transition is sharpest and has largest hysteresis for the lowest Mn content samples for both the hydrogenated and non-hydrogenated series, and the decrease in saturation magnetisation with Mn addition is explicit in the non-hydrogenated series.

6.2 Specific heat of the metamagnetic transition

The specific heat, c_p, in zero field over a temperature range of 2 to 290 K is shown in Figure 6.2 for a representative pair of samples of the same composition with and without interstitial hydrogen, M and A respectively. Plotted on this wide temperature scale, the T_{C} values of both samples are evident by the sharp peaks in each curve, and it can be seen that at low temperatures away from their respective T_{C}, the two curves are in close correspondence. It is this behaviour that led Fujita *et al.* [88] to comment that the addition of hydrogen does not change the Debye temperature, θ_{D}, and to suggest that hydrogenation does not significantly change the electronic or phonon density of states. These comments were made in reference to

Sample	La	Fe	Mn	Si	H	T_C (K)
A	1	11.22	0.46	1.32	-	116
B	1	11.33	0.37	1.30	-	129
C	1	11.41	0.30	1.29	-	138
D	1	11.49	0.23	1.27	-	150
F	1	11.66	0.12	1.23	-	167
G	1	11.74	0.06	1.20	-	173
M	1	11.22	0.46	1.32	1.65	270
N	1	11.33	0.37	1.30	1.65	285
O	1	11.41	0.30	1.29	1.65	295
P	1	11.54	0.22	1.22	1.65	310
Q	1	11.62	0.15	1.20	1.65	319
R	1	11.76	0.06	1.18	1.65	339

Table 6.1: Labels, nominal composition and T_C of the six non-hydrogenated samples A-G (also given in Table 5.1) and the six hydrogenated samples M-R. M, N and O are the hydrogenated sister compositions to A, B and C. G and R also have the same Mn content but with slight variations in Fe and Si.

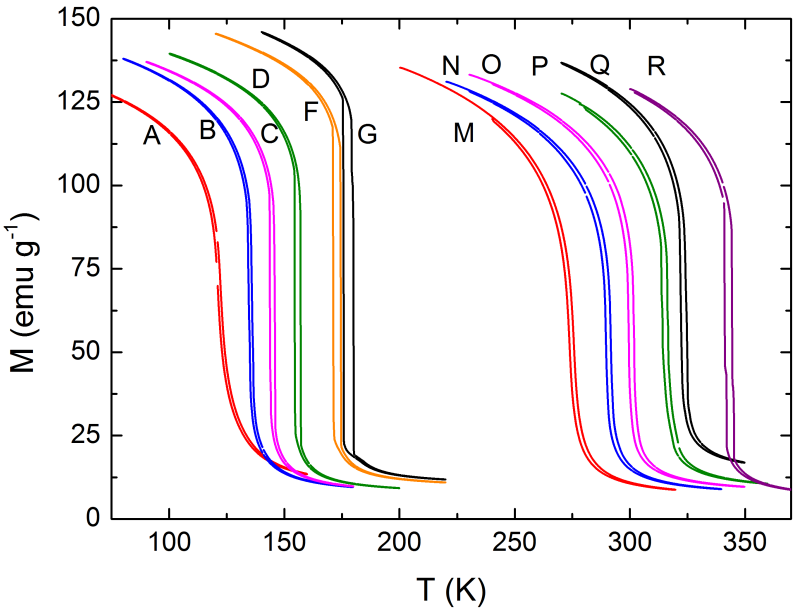


Figure 6.1: Magnetisation as a function of temperature for the twelve compositions (labelled), six with and six without interstitial hydrogen, in 1 T, with a heating/cooling rate of 1 K min^{-1}.

the fact that the increase of T_{C} with hydrogenation is primarily an effect of negative pressure from the interstitial atoms. This, however, should be expected to modify the electron and phonon density of states. The inset to Figure 6.2 shows that there are subtle changes in the specific heat as a result of hydrogenation at intermediate and low temperatures, where the electronic term begins to dominate. As will be shown in the following sections, these features result in significant changes to the Sommerfeld coefficient, γ, and the Debye temperature, θ_{D}, that have a dependence on composition across the systematic series of samples. A clear difference in c_p materialises for the temperature range between the two composition's T_{C} values, with sample A above T_{C}, in the PM state, having a significantly more shallow gradient of $c_p(T)$ compared to sample M below T_{C} (FM), which at approximately 150 K becomes the larger of the two. This is in opposition to their relative magnitudes at low T (see inset) where c_p for non-hydrogenated A is larger. Sample M also appears to remain the larger above its T_{C}. At these temperatures we are far from the Debye approximation's applicability and any change in the phonon contribution will not impact the specific heat, as we are approaching the Dulong-Petit classical limit. Indeed, if we take the number of atoms into account, 14 per formula unit for A and 15.65 per formula unit for hydrogenated M (an increase of 12% with the hydrogen), at 280 K the specific heat per mole of atoms reduces to 25.6 $\mathrm{J\,mol^{-1}K^{-1}}$ and 26.8 $\mathrm{J\,mol^{-1}K^{-1}}$, respectively, consistent with 3R.

Basso *et al.* [155] show, across the hydrogenated set of the compounds, that the peak in c_p at the magnetocaloric transition, measured using differential scanning calorimetry (DSC), generally decreases in height for increasing Mn. This is shown in Figure 6.3. Additionally, the peak decreases with increasing applied field. The temperature at which it occurs also increases with decreasing Mn and increasing field, indicating the change in T_{C}, as expected. In Figure 6.2 we see that hydrogenation also decreases the height of this peak, indicating a reduction of the first-order character.

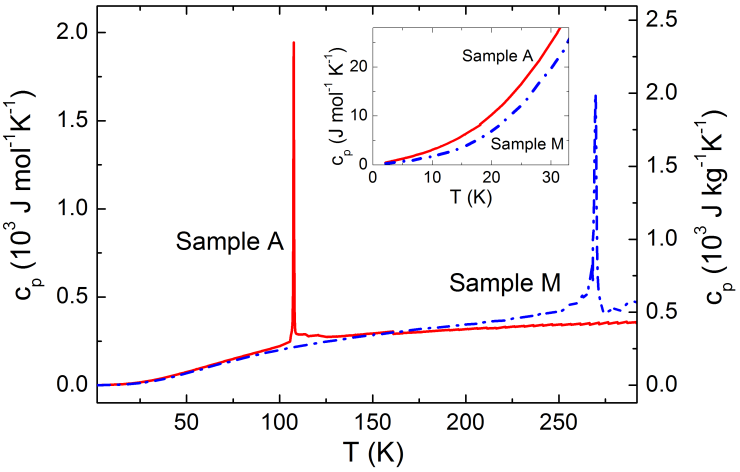


Figure 6.2: Specific heat $c_p(T)$ for sample A and the hydrogenated equivalent M, in zero magnetic field. The inset shows a blow-up at low temperatures. $c_p(T)$ values were obtained using a combination of the relaxation, two-tau method away from the magnetic phase transition at T_C, and slope difference method (SDM) in a small range of temperature (20 K) about T_C, using a moving average of 2 K. See section 3.5.1 and 3.5.2 for more details regarding these methods. Units are given both per kg and per mole (formula unit). The latter will be used predominantly in this chapter.

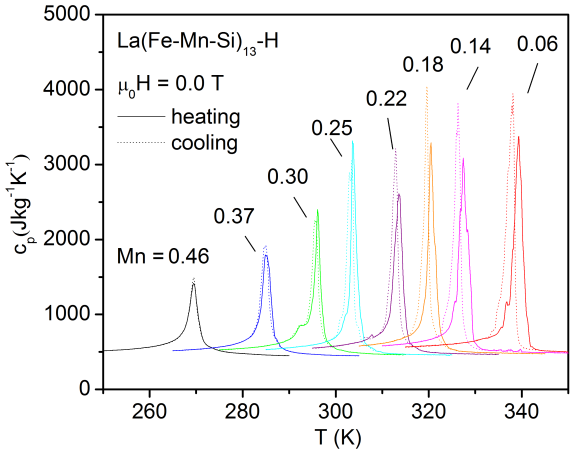


Figure 6.3: Reprinted from Ref. [155], the specific heat peaks, measured using DSC (see text), of $LaFe_{13-x-y}Mn_xSiy$-$H_{1.65}$ at the transition, in zero field, for heating and cooling. Mn=0.46, 0.37, 0.30 and 0.06 are the compositions M, N, O and R, respectively. Reprinted with the permission of AIP Publishing.

6.3 Extraction of the contributions to low temperature specific heat

This chapter relies heavily on the fitting of the Debye model, and its appropriate extensions for the substantial electronic and spin wave contributions for a metallic ferromagnet, to the specific heat (Eqn. 2.5). To justify this model and the fittings, prevalent in this section and section 6.4, it is prudent and indeed necessary to evaluate carefully the fitting parameters and appropriate temperature ranges to which they must be limited, since the T^3 Debye approximation is appropriate at low temperatures only. The fitting was carried out using an Origin Pro software function fitting procedure. Prior to fitting, the data was plotted as c_p/T against T^2 so that in Eqn. 2.5 the linear γ term is a constant, the cubic β term is linear and the α term goes as $(T^2)^{1/4}$. The fitting was done over the range 2 K to 14 K and is shown in Figure 6.4 for samples A and M (the T range represents 0 to 15 K; differences observed between the samples are discussed later). The uniqueness of the fitting, confidence in which must be verified, can be visualised explicitly in these axes. Figure 6.5 shows the same fitting, for sample A, over two temperature ranges as c_p against T. The full fitting is given by the dashed line and each separate contribution, as determined from each component extracted by the fitting procedure, is shown by the solid lines in order to explicitly show how each contribution compares in magnitude and behaviour. Note that the temperature range used means that we are measuring the FM state only (variations between the extracted parameters in the FM and PM state are expected and have been predicted, discussed in later sections). It is clear in Figure 6.5(a) that the fitting is reliable below 15 K and that the linear electronic contribution, labelled γ, is dominant below approximately 8 K. Looking at the T range up to 80 K (Figure 6.5(b)), we see that the cubic phonon contribution (β) begins to dominate above 20 K and then indeed the fitting and model breaks down above 35 K. Lastly, the spin wave $T^{3/2}$ component (α) is small at all temperatures. The significant electronic and small spin-wave components are, of course, specific to this metallic and ferromagnetic sample, yet across the series it is expected that the same concerns, regarding the comparative magnitudes of the

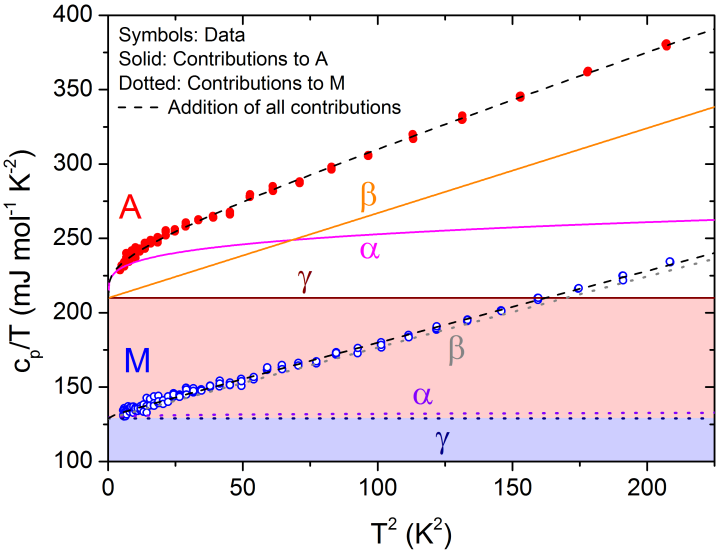


Figure 6.4: Fitting of the specific heat components as c_p/T against T^2. With these axes, the electronic contribution is constant, the phononic is linear, and the spin wave component goes as $(T^2)^{1/4}$. Comparison fits are shown for samples A and M, demonstrating behaviours with a large and small spin wave component (α) respectively. For clarity, the α and β components for both samples have been translated in the y-axis by the magnitude of their respective γ, which itself is designated by the shaded regions.

three contributions, will be retained. This means that the robustness of the α extraction is likely to be a compromising factor.

Nevertheless, at low temperatures (below 8 K) the $T^{3/2}$ term is dominant over the T^3 β term. This is made most evident with axes c_p/T against T^2 as shown for both samples A and its hydrogenated counterpart M in Figure 6.4. For sample A, the contribution from the spin-waves is explicit, but at low T only. Sample M, on the other hand, is an example where α is practically negligible (for discussion of the variations between compositions, see the following sections) and the resulting plot is close to linear. A material showing a zero spin-wave specific heat component would allow the simple extraction of the electronic and phonon components as the intercept and gradient respectively. Therefore, fitting of the model below 20 K is appropriate, extracting reliable γ and β parameters and differentiating between finite and close-to-negligible α, as shown by the examples. For the following data, the specific heat has

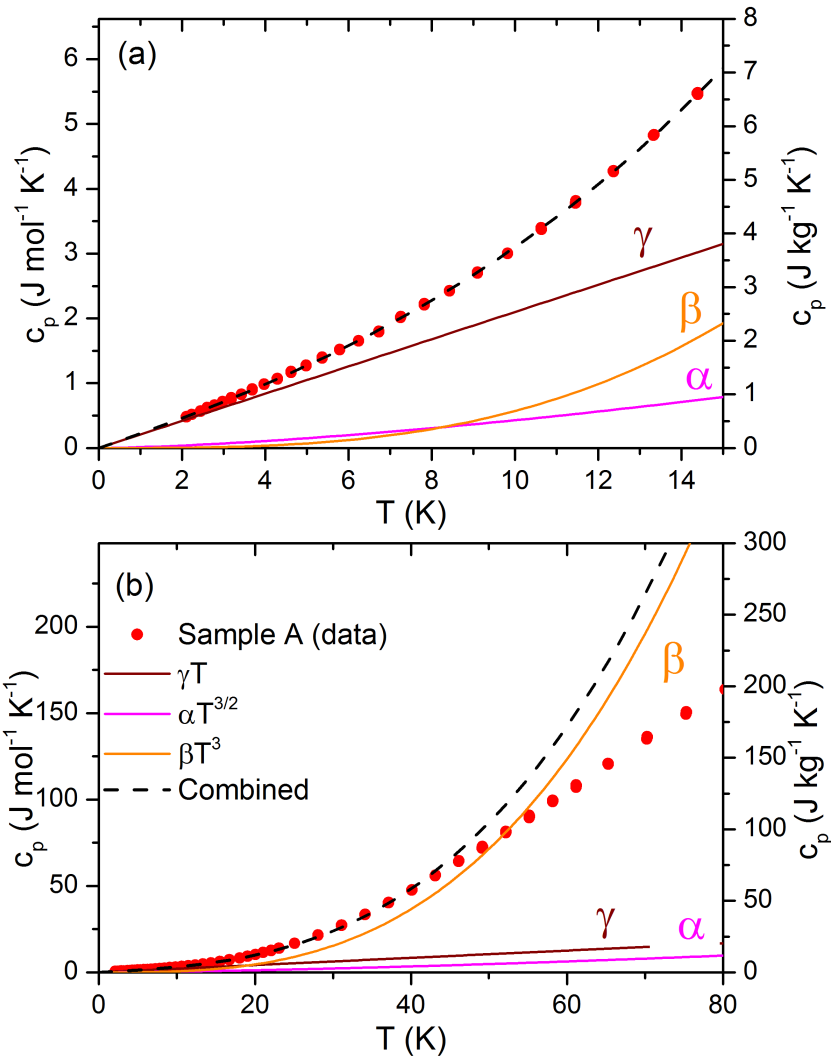


Figure 6.5: Specific heat data as shown in Figure 6.4, as $c_p(T)$ for sample A, showing how the three terms representing the electronic (γ), spin wave (α) and phonon (β) heat capacities contribute to the total c_p, in (a) the low T range, where the Debye model is robust and (b) a larger T range, 0 to 80 K, showing the breakdown of the model above 35 K.

been measured down to 2 K, and all fittings of the model have been done between 2 and 14 K.

The specific heat for all twelve La(Fe,Mn,Si)$_{13}$ compositions in the range 0 to 15 K is given in Figure 6.6. When plotted as c_p against T (Figure 6.6(a)), the spread of behaviours is clear, with an additional separation into two distinct groups, non-hydrogenated (A-G) and hydrogenated (M-R). When plotted as c_p/T against T^2 (Figure 6.6(b)), the comparative contributions of each parameter are shown much more clearly, with the $T = 0$ intercept and slope an indication of γ and β, respectively, and the extent of deviation from linearity at the low temperature limit corresponding to the magnitude of α. Immediately, it can be seen that there is a significant variation in γ across the two series, systematic with composition and, in general, larger for the non-hydrogenated against the hydrogenated sample set. The slope (and therefore the β parameter) is distinctly larger for non-hydrogenated, representing a larger lattice contribution to c_p and consequently the Debye temperature, θ_{D} will be lower than the hydrogenated samples. In addition, a finite α component is also clearly evident in the non-hydrogenated samples in comparison with the hydrogenated compositions which, in continuation of the trend shown in Figure 6.4, retain their linearity at low T, representative of a small or absent $T^{3/2}$ contribution. The fittings of the Debye model leading to the extractions of γ, α and β are also shown.

In addition, two samples of LaFe$_{13-x}$Si$_x$, both without Mn and without interstitial H, and with varying Si/Fe, $x = 1.2$ and $x = 1.6$, are measured, with the aim of isolating the roles of Mn and Si. The $c_p/T(T^2)$ behaviours, with the fittings included, are shown in Figure 6.7 and show a reduced variation for a significant change in Si content. Indeed, from quick inspection, the slope at higher temperatures and the intercept at $T = 0$ K are very similar between the two compositions, and the separation between plots appears to be due to variation in the $T^{3/2}$ behaviour evident close to $T = 0$ K. In the following, analysis of the three different contributions for all samples and their dependence on composition will be discussed.

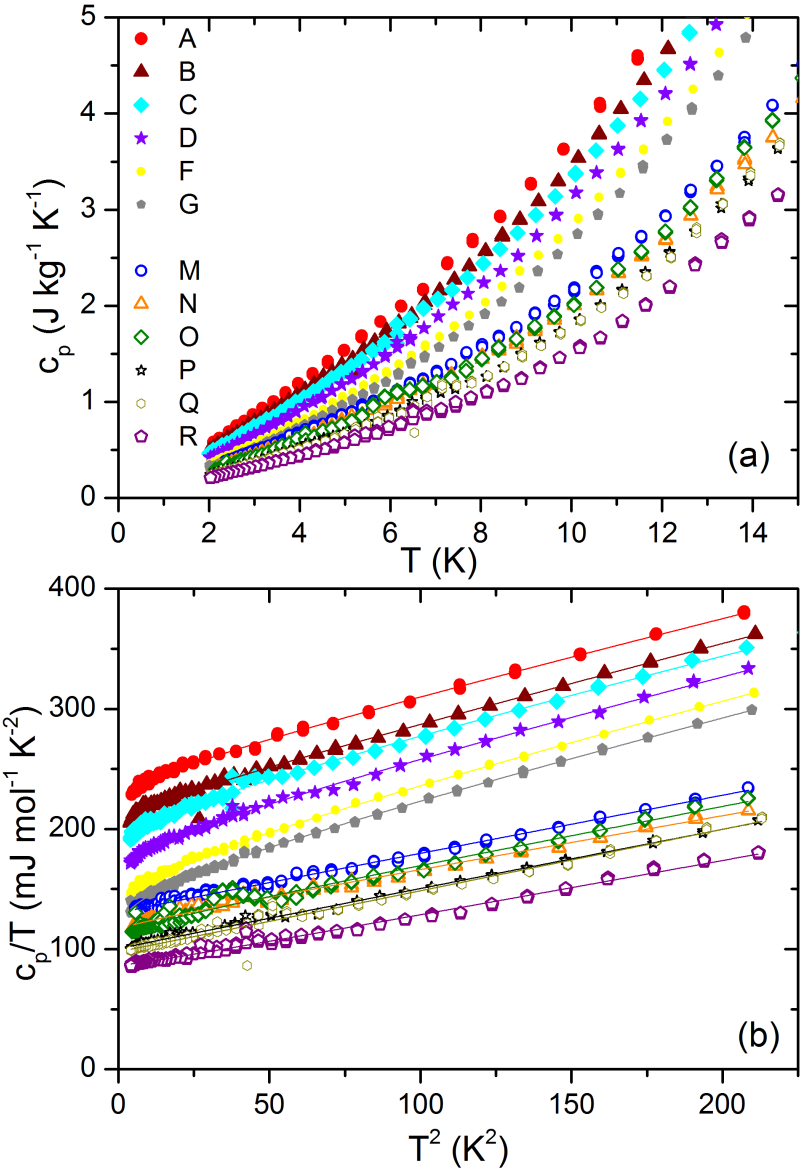


Figure 6.6: Specific heat data (symbols) for all twelve La(Fe,Mn,Si)$_{13}$ samples shown as (a) c_p vs T (units per kg) and (b) c_p/T vs T^2 (units per formula unit mole), with fittings to the Debye model shown (lines).

6.3.1 The electron contribution: Sommerfeld coefficient

The value for γ at the magnetic transition emerges from density functional theory calculations, which have been made on these systems by several groups. For example, Gruner *et al.* [94] have predicted the Sommerfeld coefficient for $LaFe_{11.6}Si_{1.4}$ to be 46.3 $mJ\,mol^{-1}K^{-2}$ (56 $mJ\,kg^{-1}K^{-2}$) in the PM state and 23.8 $mJ\,mol^{-1}K^{-2}$ (29 $mJ\,kg^{-1}K^{-2}$) in the FM state. The large change in the density of states (DOS) across the transition, associated with the change of lattice parameters, demonstrates the strongly correlated nature of the metamagnetic transition and the significant contribution of the electronic entropy change to the total entropy change in these itinerant systems. Zero temperature density functional calculations [143] predict that the bare electronic density of states increases with Mn substitution, and that for a change of Mn doping from $y = 0$ to $y = 0.5$, γ should vary from 16.07 to 18.07 $mJ\,mol^{-1}K^{-2}$ (19.2 to 21.6 $mJ\,kg^{-1}K^{-2}$), a change of about 13%.

The experimentally extracted values of the Sommerfeld coefficient, γ, are shown in Figure 6.8, and multiple observations become clear. Firstly, for all samples there is a striking discrepancy between the measured and the DFT predictions (also included in the figure). The data cluster for low or zero Mn around 90-110 $mJ\,mol^{-1}K^{-2}$ (here and throughout this report the unit mole is given per formula unit) is about a factor of 5 higher than the DFT calculation. There is therefore clearly an enhancement effect over DFT.

Secondly, the full set of measured γ values, which here are observed experimentally in the ferromagnetic state, show that there are clear systematic changes with Mn substitution across the sample series and lie in the range 88-210 $mJ\,mol^{-1}K^{-2}$ (106-254 $mJ\,kg^{-1}K^{-2}$). Adding Mn increases γ significantly for the non-hydrogenated samples, by over a factor of two between Mn contents of 0.06 and 0.46, and to a much lesser extent for the hydrogenated counterpart set. Both these trends follow linearity with Mn content. The corresponding trend of γ with T_C is shown in Figure 6.8(b), and shows two independent and close-to-linear dependences. Since T_C has a roughly linear dependence on Mn content [103], this is expected. In principle,

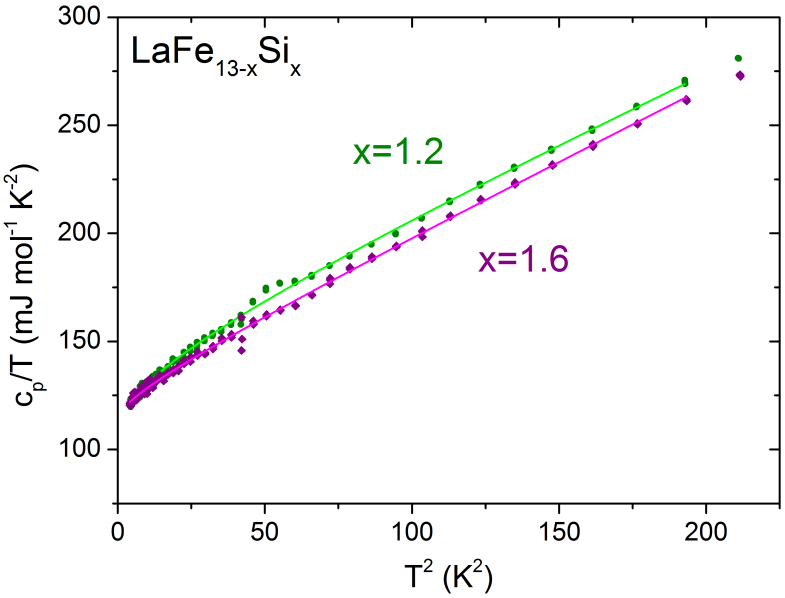


Figure 6.7: Specific heat data (symbols) for $LaFe_{13-x}Si_x$ with $x = 1.2$ and 1.6. The fittings to the Debye model (lines) are shown.

we should take into account the effects of finite temperature on the energy dependent band structure, but the change in the DOS between T_C and at low temperatures is expected to be relatively subtle compared to the PM to FM transition itself.

This leads directly to a third observation: the increase of γ with Mn predicted by DFT to be 13%, for 0 to 0.5 Mn content (Ref. [143]), is much less significant than that measured, estimated to be 60% from 0 to 0.5 Mn content for the hydrogenated samples and over 150% for the non-hydrogenated set over the same range. Wang *et al.* [159] discuss the effect of hydrogenation on the magnetic properties, suggesting that it is due mainly to 3d band-narrowing, caused by the decrease in the overlap of the Fe 3d orbitals, as the distance between the Fe-icosahedral clusters increases. The additional enhancement effect, which occurs when Mn is added, is less significant when there is band narrowing in the hydrogenated case. Most fundamental studies agree that hydrogen does not strongly affect the density of states at the Fermi level. However, also shown in Figure 6.8(a) are the results for $LaFe_{13-x}Si_x$ with $x = 1.2$ and $x = 1.6$, both non-hydrogenated and with zero Mn content. There is an increase in γ with increased Si content, although this increase is less significant than that from changes in the

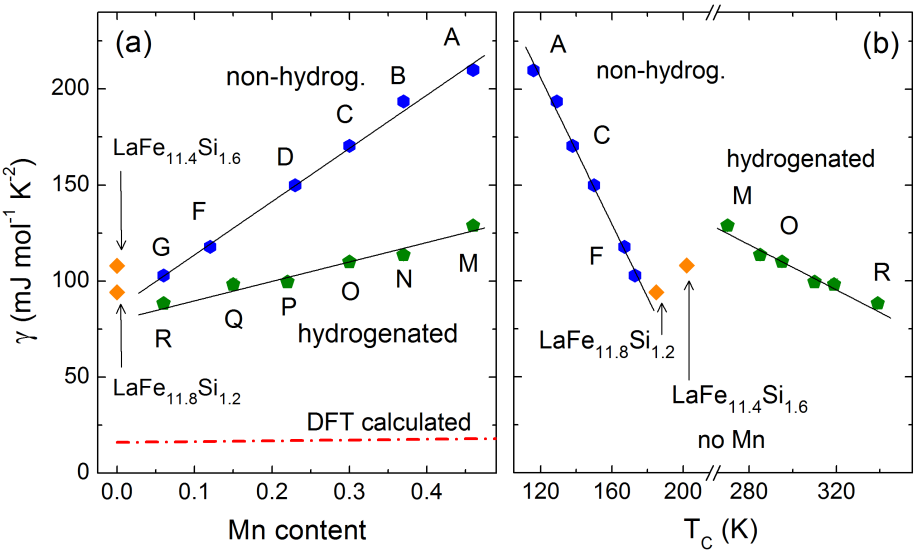


Figure 6.8: (a) The extracted Sommerfeld coefficient, γ, as a function of Mn content (per unit formula). The solid lines are a guide to the eye and values of non-hydrogenated and zero Mn content $LaFe_{11.8}Si_{1.2}$ and $LaFe_{11.4}Si_{1.6}$ are also included. The dashed line is the DFT prediction taken from Ref. [143]. (b) The Sommerfeld coefficient as a function of each composition's T_C, also including the compositions $LaFe_{11.8}Si_{1.2}$ and $LaFe_{11.4}Si_{1.6}$.

Mn content. This may be indicative of a change in the density of states, however it is likely that the impact of such changes are masked by the enhancement effect itself.

Finally, the values of γ for the samples without Mn or with low Mn content are rather similar, in the range 88-110 $\mathrm{mJ\,mol^{-1}K^{-2}}$, demonstrating little variation with hydrogen or Si content. This is indicated clearly by the apparent intersection of the trends for non-hydrogenated and hydrogenated $La(Fe,Mn,Si)_{13}$ as Mn goes to zero. Therefore, this would suggest that there is a base enhancement in the $La(Fe,Si)_{13}$(-H) system largely independent of both Si and interstitial hydrogen, which becomes further enhanced with Mn doping, but to a less significant extent in the hydrogenated forms.

Looking at related literature, there are several reports of related itinerant magnetic systems which also have large γ values. For example, Wang *et al.* reported, in $Nd_xLa_{1-x}Fe_{11.5}Al_{1.5}$

compounds, $\gamma = 193.9\,\mathrm{mJ\,mol^{-1}K^{-2}}$ ($236\,\mathrm{mJ\,kg^{-1}K^{-2}}$) for $x = 0$, and $\gamma = 222.1\,\mathrm{mJ\,mol^{-1}K^{-2}}$ ($270\,\mathrm{mJ\,kg^{-1}K^{-2}}$) for $x = 0.2$ [160]. Since enhanced values of γ are thought to be related to strong mass enhancement effects (here, the term mass enhancement refers to enhancement of the equivalent mass of d-band electrons), it is generally thought that these effects are brought about by d electron correlations due to spin fluctuations in transition metal ferromagnets [161, 162, 163], or interband exchange enhancement [164]. It is interesting to note that the mass enhancement is not limited to ferromagnetic compositions only. As described in section 2.4.2, Michor *et al.* [141] report $\gamma = 45\ \mathrm{mJ\,mol^{-1}K^{-2}}$ ($58\ \mathrm{mJ\,kg^{-1}K^{-2}}$) theoretically and $\gamma = 200\ \mathrm{mJ\,mol^{-1}K^{-2}}$ ($256\ \mathrm{mJ\,kg^{-1}K^{-2}}$) experimentally in the itinerant strongly exchange enhanced Pauli paramagnet $LaCo_9Si_4$. Since γ can be written as $\gamma = \pi^2 k_B^2 N(E_F)(1+\lambda)/3$ [139], they estimated a spin fluctuation mass enhancement $\lambda_{spin} \sim 3.3$. Looking further, similar families of magnetic materials of the $NaZn_{13}$ structure showed the itinerant strongly exchange enhanced Pauli paramagnet $CeNi_9Si_4$ and the compound $LaNi_9Si_4$ [165], which is a simple Pauli paramagnetic metal, had a γ value of $150\ \mathrm{mJ\,mol^{-1}K^{-2}}$ ($192\ \mathrm{mJ\,kg^{-1}K^{-2}}$) compared to $33\ \mathrm{mJ\,mol^{-1}K^{-2}}$ ($42\ \mathrm{mJ\,kg^{-1}K^{-2}}$), respectively. In this case the mass enhancement is not restricted to ferromagnetic systems, and is likely a result of spin fluctuations. For the La(Fe,Mn,Si)$_{13}$(-H) materials measured here and shown in Figure 6.8, λ_{spin} is estimated as ~ 4.5 for the zero or low Mn containing samples.

As summarised in section 2.1.5, the dominant effect of hydrogen on the magnetic properties of La(Fe,Si)$_{13}$ is not the change in the density of states, but rather the renormalisation of spin fluctuations due to the change in the volume influencing the magnetovolume coupling, which is responsible for the increase in T_C [88]. Using Mossbauer spectroscopy, Fujita *et al.* [108] attributed the change in the magnetic state of $LaFe_{13x}Si_x$-H_y solely to the volume expansion caused by hydrogen absorption, such that the role of the additional electrons from the incorporated hydrogen does not affect bands near the Fermi energy. However, measurements of the thermopower of $LaFe_{11.6}Si_{1.4}$ and $LaFe_{11.6}Si_{1.4}$-$H_{1.6}$, across the metamagnetic transition and at low temperatures [166], suggest a broadening of the DOS as a result of hydrogenation, and also indicate an additional electron scattering mechanism that enters at low temperatures

which could be suppressed in magnetic field. The scattering responsible for the enhanced γ is likely related to the low temperature features previously observed in the thermopower. Band structure calculations show that at low temperatures, the free energy well associated with the FM state narrows as well as deepens with hydrogenation [88, 110], consistent with an increase of T_C and suppression of spin fluctuations. Since γ is lower in the hydrogenated compounds, this suggests that one mechanism producing the enhanced γ relates to spin fluctuations. This is consistent with the field dependence of γ discussed in section 6.4.

6.3.2 The phonon contribution: Debye temperature

The values in Figure 6.9, calculated from β using Eqn. 2.4, show that within the uncertainties of the experiment θ_D is constant with Fe/Mn/Si content but increases by about 5 to 10% as hydrogen is incorporated and the lattice expands (the maximum incorporation of hydrogen increases the unit cell volume by about 1% [88]). The absolute value of θ_D depends on the material density and also the average sound velocity, and therefore on the elastic moduli; thus it is far from straightforward to predict θ_D from the available experimental data [167]. Nevertheless, Fujita *et al.* [88], determining θ_D from specific heat on $LaFe_{11.7}Si_{1.3}$ as a function of hydrogen content, find $\theta_D \sim 350$ K for all samples. Wang *et al.* [142] report $\theta_D = 317$ K, 330 K and 336 K for $LaFe_{13-x}Si_x$ with $x = 1.3$, 1.7 and 2, respectively. The measurements given in Figure 6.9 are therefore generally consistent with the literature values, adding validity to the fitting process used to extract the other parameters, γ and α. Between Ref. [88] and [142] there is considerable variability for samples of the same nominal composition. The variation in Si site occupancy could affect the absolute value of θ_D: as there are two Fe sites, and in principle the Si site occupancy might depend on sample processing strategy, Fujita and Yako discuss whether there is preferential occupancy, calculating whether one site is more energetically favourable [79]. It is likely that site disorder is a contributing factor to the discrepancies between reported measurements. Indeed, between $LaFe_{13-x}Si_x$ with $x = 1.2$ and $x = 1.6$ there is a noticeable change, with θ_D for $x = 1.6$ approximately 14 K lower than $x = 1.2$ and the non-hydrogenated $La(Fe,Mn,Si)_{13}$ samples with comparative Si contents.

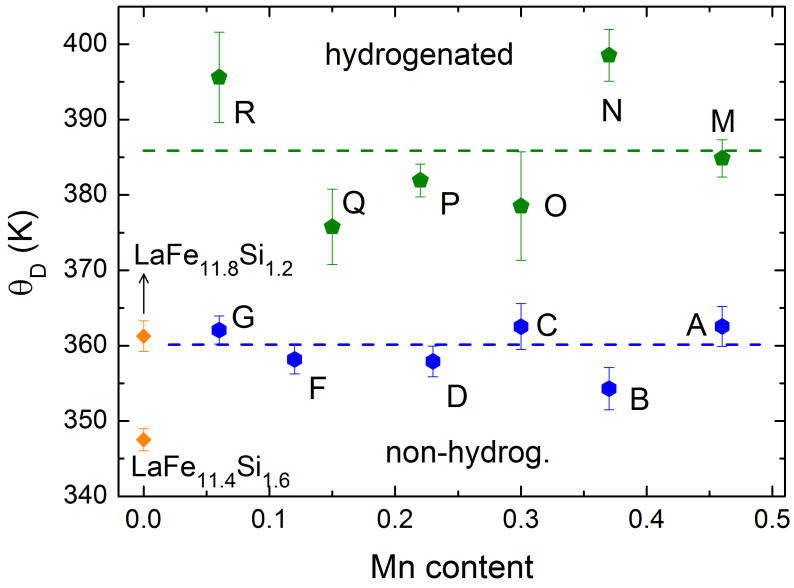


Figure 6.9: θ_{D} with Mn composition, as calculated from the coefficient β.

However it is not entirely unreasonable that this may be within the error of the model fitting.

6.3.3 The spin wave contribution

The hydrogenated sample set has an unmeasurably small spin wave heat capacity component α (Figure 6.10(a)); this is also clear from Figure 6.6(b) where a deviation from linear fit of c_p/T versus T^2 is absent. In the non-hydrogenated samples there are significant deviations below 5 K due to the finite $T^{3/2}$ term, and the extracted α value shows an increasing trend with Mn doping. The spin wave stiffness, D, is calculated from α using Eqn. 2.6, and for the non-hydrogenated samples increases with increasing Mn content, as shown in Figure 6.10(b). However, the variation across the samples is subtle. Due to the negligible α in the hydrogenated samples, D calculated from Eqn. 2.6 tends to infinity. As such, these values are not included in Figure 6.10(b).

Previous measurements of D for $LaFe_{11.44}Si_{1.56}H_x$, calculated from low temperature variations in the magnetisation, give $D = 52$ meV Å^2 for $x = 0$ and 91 meV Å^2 for $x = 1.6$ [91]. This

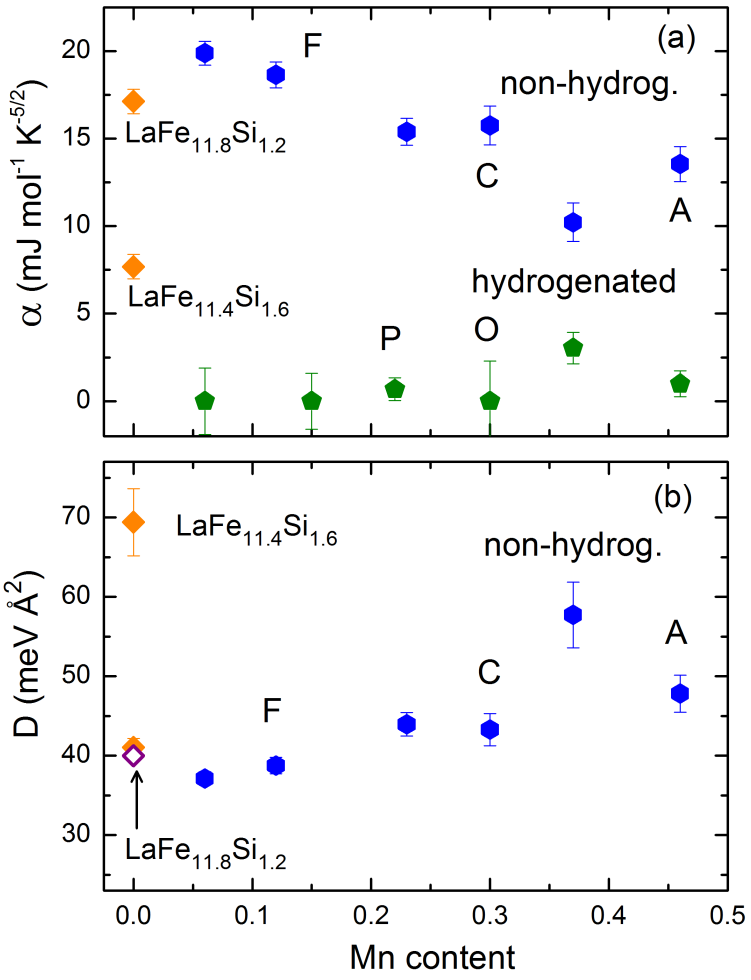


Figure 6.10: (a) Extracted α for both the hydrogenated and non-hydrogenated composition sets, and (b) Derived spin wave stiffness, D, values for the non-hydrogenated set only, with Mn content. Also included in both plots are $LaFe_{11.8}Si_{1.2}$ and $LaFe_{11.4}Si_{1.6}$, obtained in the same way from the low temperature heat capacity measurement (closed diamonds), compared with that for $LaFe_{11.8}Si_{1.2}$ obtained by neutron scattering (open) [168].

result was explained by the increased thermal stabilisation of the FM moment with increased hydrogen content, leading to an increase in the spin wave stiffness, in tandem with the increase of T_C. The results in Figure 6.10 are consistent with these findings: the hydrogenated results imply a substantial increase in D which cannot reliably be calculated from the negligible α component. The samples $LaFe_{13-x}Si_x$ with $x = 1.2$ and 1.6 demonstrate that D shows a strong dependence on silicon content, which for $x = 1.2$ has been corroborated by results from neutron scattering [168]. Therefore, as anticipated from a quick inspection of Figure 6.7, it is the spin-wave component that results in the principal separation between the two c_p curves, as has been seen by the minor variation between their Sommerfeld coefficients and Debye temperatures. Since the set of $La(Fe,Mn,Si)_{13}$ samples has a systematic variation, albeit minor, in Si content, which increases with Mn (Si content varying from 1.20 to 1.32 for compositions G to A, see Table 6.1), the dominance of Si on the spin-wave contribution cannot be ruled out, and in fact the apparent increase of D with increasing Si is consistent with the trend of the two $LaFe_{13-x}Si_x$ samples.

6.4 Magnetic field dependence of the specific heat contributions

Following the thermopower measurements on the system, suggesting the suppression of an electron scattering mechanism at low temperatures by magnetic field [166], investigating the dependence of c_p on applied field will help determine whether these same or similar scattering mechanisms might be contributing to the enhancement of γ. In section 6.3.3, it has already become clear that the spin-wave component is absent (or at least negligible) with hydrogen. In Figure 6.11, the specific heat is shown for sister sample pair C and O, with 0.30 Mn content, roughly in the middle of the series, within a number of applied field strengths between $\mu_0 H = 0$ and 8 T. The principal differences between the two samples in zero field are again clear, with sample O showing a linear trend in c_p/T versus T^2 axes, with a shallower slope and smaller intercept in comparison to sample C. As the field is increased there is a downward shift in the

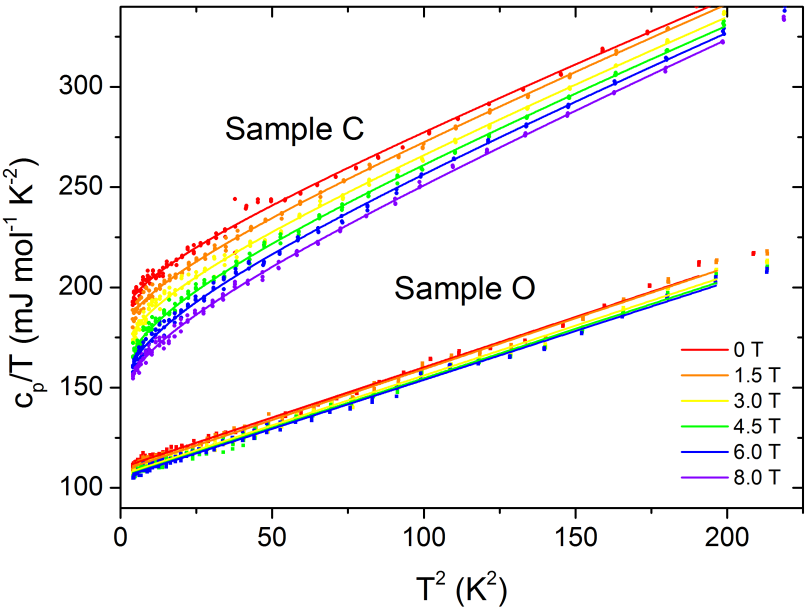


Figure 6.11: Specific heat data (symbols) for samples C and O, the respective non-hydrogenated and hydrogenated pair with Mn content 0.30, for several applied magnetic field values, with axes c_p/T against T^2. The fittings to the Debye model from 2 to 14 K are included (lines).

plots for both samples. This shift is however much more significant for non-hydrogenated C. The shift is indicative of a decreasing γ, since neither the gradients for both samples at higher T, above $T^2 = 100$ K^2, nor the existence of deviation from linearity at the low temperature limit appear significantly changed with H.

These observations are shown clearly after parameter extraction in Figure 6.12(a). Between 0 and 8 T, γ extracted for C decreases by 26%. The decrease for sample O is by contrast considerably less (4% between 0 and 6 T). As a result, the application of H appears to suppress γ for C towards that for (mostly invariant) O. The results of two other samples are also shown, G and R, the non-hydrogenated and hydrogenated samples respectively both with an Mn content of 0.06. A similar pattern is evident: a small decrease for R and a considerable decrease for G towards the γ of R. In this case, the decrease is smaller than C (16% between 0 and 6 T), in agreement with the suppression of the non-hydrogenated γ towards the hydrogenated, since the zero-field value of G is closer to R than C is to O. These results suggest

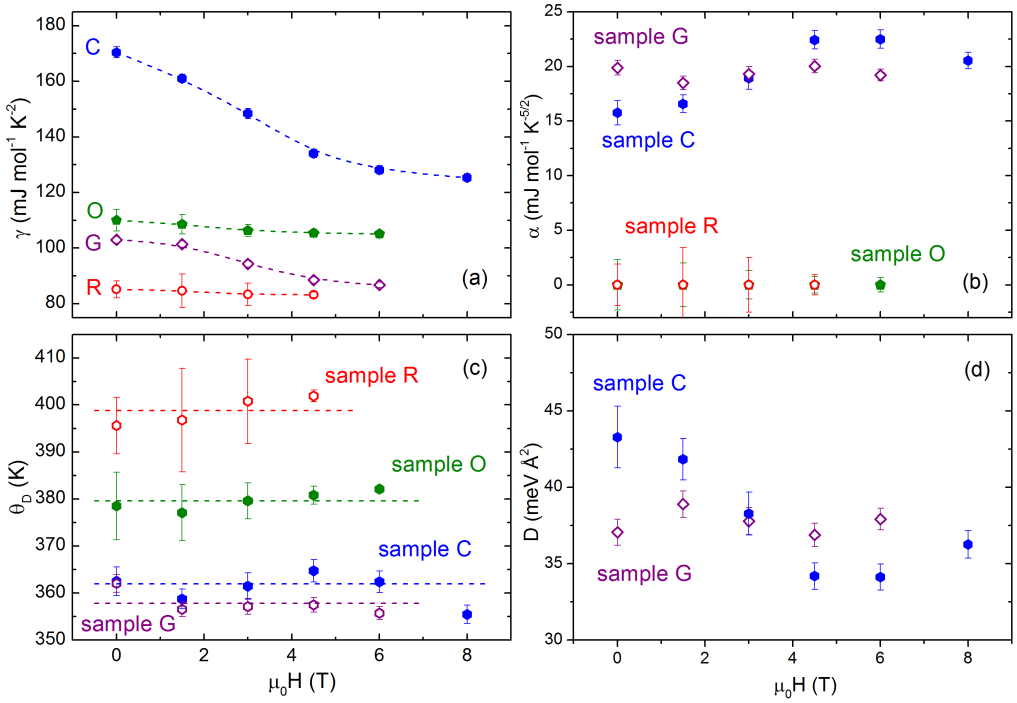


Figure 6.12: (a) γ, (b) α, (c) θ_{D} and (d) D in field for compositions C and O, and F and R, the equivalent composition pairs without and with interstitial hydrogen, respectively.

that the enhanced values for γ in the non-hydrogenated compositions have a magnetic origin, for which the enhancement is greater with more Mn-doping, and is significantly diminished in the hydrogenated forms. This origin is most likely from enhanced scattering from spin waves which are suppressed in field. Consistent with this scenario, spin waves were undetected in the hydrogenated samples and in these samples no significant dependence of γ on field was observed.

Figure 6.12(c) suggests that within the error, there is no dependence of θ_{D} on applied field. This is to be expected since at low T, away from the magnetovolume transition, the magnetic field has no effect on the lattice.

The impact of H on the spin wave component, α, and the resultant calculation of spin wave stiffness, D, is shown for the two pairs of samples in Figure 6.12(b) and (d) respectively. As expected, the values of α for hydrogenated samples O and R remain negligible, as they are

in zero field, resulting in a D value which cannot be reliably extracted for all field strengths. Regarding the non-hydrogenated samples, C shows what appears to be a slight increase in α with H, and therefore a decrease in D. However, sample G appears to show no dependence with H, suggesting that the same is true for C but, due to the α extraction during the fitting of the three parameters being the least robust, difficulty of its accurate extraction is not represented in the data. Indeed, spin wave theory suggests that we should observe D to be independent of field.

Finally, γ, θ_{D} and D are shown separately for the two Mn-free and H-free $LaFe_{13-x}Si_x$ compositions in Figure 6.13. Both samples show a similar decrease of γ with H, therefore the extent of suppression in field appears to be independent of Si/Fe content. The additional enhancement with increased Si can then be said not to be magnetic in origin. As with the Mn-doped samples, both θ_{D} and D are consistent with constant behaviour, most convincingly for $x = 1.2$, with the maximum variation of θ_{D} for $x = 1.6$ approximately 2.5%, well within the range of variation (which is approximated to being constant) measured across the non-hydrogenated set of samples in zero field.

6.5 Summary

The $La(Fe,Mn,Si)_{13}$(-H) series shows considerable differences in low temperature specific heat with composition and the state of hydrogenation. This is shown to be due to variations in all three heat capacity contributions: electronic, lattice and spin wave. The former, represented by the Sommerfeld coefficient, γ, is greatly enhanced for all compositions over that predicted from density functional theory calculations, by between a factor of 5 to 11, depending on Mn content. This is likely due to a mass enhancement of the d-band electrons (which are not apparent in DFT calculations). For low or zero Mn contents, the enhancement is by the lower limit of this range and is weakly affected by variations in hydrogen or Si content. For increasing Mn content up to 0.46 atoms per unit formula, γ for both non-hydrogenated and hydrogenated

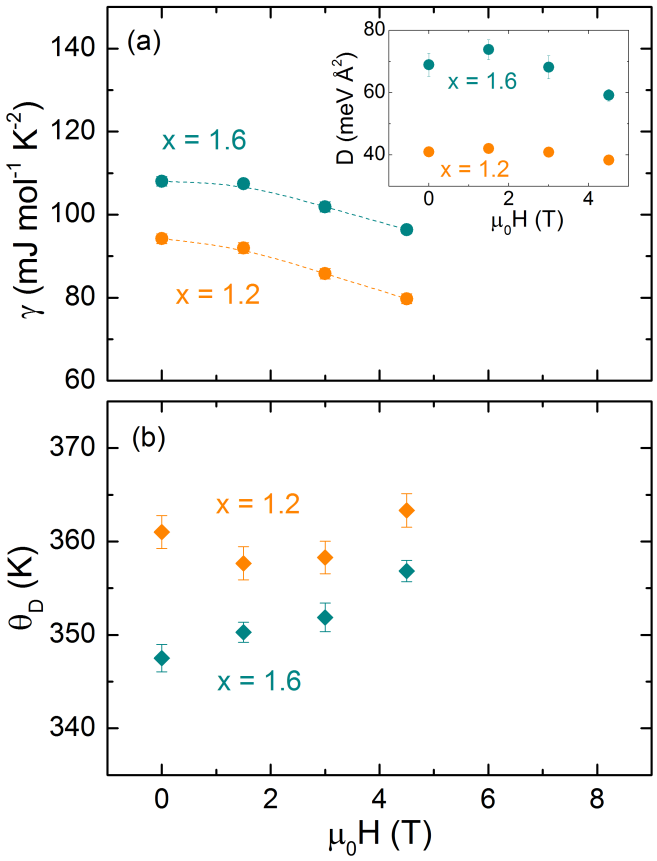


Figure 6.13: (a) γ, (b) θ_{D} and inset to (a) D as a function of H for $LaFe_{11.8}Si_{1.2}$ and $LaFe_{11.4}Si_{1.6}$, labelled $x = 1.2$ and $x = 1.6$, respectively

samples increases considerably and linearly, by over a factor of two and approximately 50% for the former and latter sets, respectively, suggesting an additional enhancement mechanism for increased Mn which is suppressed somewhat by hydrogen.

The suppression of γ with increasing field in non-hydrogenated samples, towards that of their corresponding hydrogenated versions, suggests that this additional enhancement is likely to be the result of a scattering mechanism of magnetic origin, which is present and more significant with increased Mn doping, and absent in the hydrogenated form. Therefore, the base enhancement, which in general is not affected by hydrogen, H or the composition may correspond to electron-electron or electron-phonon interactions. The further enhancement occurring with Mn-doping appears to be directly related to the spin fluctuations, which are

a defining feature of the itinerant electron metamagnetic transition in this system. The suppression with hydrogen is consistent with the deepening and narrowing of the ferromagnetic free energy minimum in the hydrogenated state, which leads to a reduction of spin fluctuations.

This suppression is also evident in Mn-free non-hydrogenated samples, for which the extent of suppression is little affected by variations in Si content. The spin wave contribution to the specific heat is absent (within resolution of the equipment) for hydrogenated samples, but finite, with a suggested but subtle decrease, with increasing Mn in the non-hydrogenated compounds. The Debye temperature is shown to be consistent with the literature and independent of Mn/Fe/Si content, with a 5-10% increase when the samples are hydrogenated and the lattice expands.

These results demonstrate that cooperative effects, such as those between the magnetic, electronic and phonon lattices manifest at the paramagnetic to ferromagnetic transition, are also present within the ferromagnetic state at low temperature and suggest that the enhanced interactions studied may provide an interesting playground for other exotic effects.

7 | Conclusions and Future Work

In this chapter, I summarise the key findings and implications of the thesis, and discuss several promising further research options.

7.1 Summary of Results

The findings of this thesis have added to the knowledge base of a well known compound in which the easy tunability of the working temperature around room temperature, without significant detriment to the large MCE properties, makes it a frontrunner for future magnetic cooling applications. Magnetisation measurements of the $La(Fe,Si)_{13}$ first-order, magnetic field induced paramagnetic (PM) to ferromagnetic (FM) magnetocaloric transition show dynamic effects in response to the applied field rate. These are shown to fall into two regimes, untangling the conflicting claims in the literature: the regime at fast field rate is dominated by the material's ability to thermally equilibrate with the bath and results in an extrinsic hysteresis increase; in the slow field rate regime, the transition is sharp and temporal relaxation, between the two phases, dominates. The rate of relaxation, in constant field, H, and temperature, T, increases when the transition is partially induced by field before H is held constant. This increase is linear with H, and cannot be explained by the JMA model, which assumes the rate is independent of the extent of material already transformed. Instead the increasing relaxation rate is indicative of a change in the global free energy and local-scale

dipole interactions.

Relaxation of the sample from PM to a fully FM state is possible, but requires a sample to have a low demagnetising factor. With high demagnetising factor, the relaxation arrests in a mixed state, in agreement with previous results. Extending these findings, physical gaps in the solid material (i.e. from cracks) were shown to lead to considerable slowing of the relaxation, demonstrating that sample connectivity is important and local demagnetising fields formed at these new edges play a large role in impeding the progression of the transition. However, if the sample shape is retained after breaks are introduced, relaxation to full FM is able to occur and the transition remains sharp. Therefore, magnetic dipole coupling across the cracks, and within the material, from the local field created is an important driving mechanism of the growth. The demagnetising factor is shown to dominate the nucleation of both the PM to FM and FM to PM transitions, with regards to the spatial location of nucleation on the sample shape and the critical field. This work has demonstrated that methods to take advantage of this result, through the choice of sample shape, can lead to a reduced hysteresis, which is one of the desired aims in the magnetocalorics field with regards to technological application. These conclusions were confirmed by scanning Hall probe imaging measurements.

The relaxation rate decreases with increasing temperature and disappears at the critical point, T_{crit}, at which the transition becomes second-order. This is in correspondence with the decrease and disappearance of the latent heat, indicating that changes in the separation of the free energy landscape minima are reflected in the rate of growth of the FM phase. The relaxation rate is described as a measure of first-order character strength. The contributions of the extrinsic and intrinsic hystereses in the field driven transition and their evolution with temperature are explicitly shown, where the former is found to remain constant across the range of T where the material is first-order, and then decrease above T_{C}. Substitution of Mn on the Fe sites decreases the first-order character, broadening the transition and decreasing the separation between T_{crit} and T_{C}. This is also demonstrated by the reduction of the relaxation rate as a function of increasing Mn, in addition to a decrease in the entropy change due to the latent heat release, which shows consistency with the Clausius-Clapeyron analysis of the

first-order contribution from magnetisation data. The comparison of T_{crit} with samples which have been hydrogenated (as reported in the literature) highlights the substantial role that interstitial hydrogen plays in reducing the first-order character. The decrease of latent heat is concurrent with an increase in the peak of the heat capacity, with increasing temperature above T_{C}. These trends, with comparison to the relaxation rate, reveal the role that the creation of latent heat at the phase boundary, and the change in T it affords on the surrounding material, has on the growth behaviour at the local scale.

Switching to more fundamental matters, the Sommerfeld coefficient measurements, extracted from the low temperature specific heat, show a considerable enhancement of the electronic specific heat over the values predicted from density functional theory calculations in the literature, by a factor of approximately 5, demonstrating that such theoretical calculations do not represent the full picture regarding the electron interaction processes present. The enhancement increases significantly with increased doping of Mn up to a factor of 11. This further enhancement is reduced when samples are hydrogenated. The extracted spin wave component is also negligible for hydrogenated samples. Complementary results of the magnetic field dependence of the Sommerfeld coefficient indicate that there is a base electron mass enhancement, likely due to electron-phonon coupling, and an extra enhancement in Mn containing samples, which is suppressed in field and with the addition of hydrogen, which appears to be magnetic in origin. The enhancement with Mn is not directly correlated with the strength of the first order character at T_{C}. Therefore, these effects, although providing rich information about the properties in the FM state, do not shed light on the MCE directly.

7.2 Future Work

Many areas addressed in this thesis have significant scope for further study. However, I believe that there are three particular areas which merit more detailed study. I will summarise these in terms of the research questions following on from the work of this thesis, and suggest how

these can be answered.

7.2.1 Study of sample shape benefits in a working cycle context

This work has gone into great detail with regards to reducing hysteresis in $LaFe_{13-x}Si_x$ using sample shape, under isothermal conditions. However, it is not conclusive with regards to the impact these findings will have in a real cooling cycle, such as the active magnetic regenerator (AMR), where there are adiabatic and isofield stages. Understanding how the hysteresis and the finite time to undergo transition will translate into such a cycle is important. As mentioned in section 4.4, an adiabatic step should still allow complete transformation within a $\mu_0 H = 0$ to 2 T applied field change, before the isofield, work extraction step.

However, for smaller field changes, which are desired to reduce the amount of Nd-Fe-B required for permanent magnets in this technology, the transition will predominantly take place during the isofield process, i.e. the thermally driven transition induced by the sample returning to the bath temperature and thus crossing most of the transition (see step 2 of Figure 1.2 for an example). This is particularly true for the isofield stage, after field removal, since the unavoidable limit of zero field will be met before full the transition has taken place adiabatically, if the FM to PM transition begins below 1.76 T. This is likely to be the case for other MCE material systems as well. Unlike the field-induced transition, the thermally-induced transition has not been covered in detail within this work. Adiabatic magnetisation or demagnetisation capabilities are not currently available to me. However, appropriate simulations of the adiabatic transition, using the information obtained from the results of this thesis and the literature, complemented by experimental studies of the thermal transition and the thermal step around the AMR cycle are possible. Carrying out measurements of the thermal, isofield transition, with variables sample shape, field strength and thermal environment, will be informative concerning application purposes relevant to my isothermal results.

Extending this beyond current capabilities, measurements in a prototype heat pump set-up,

with both rapid application/removal of field and heat transfer fluid, would be necessary to help clarify the advantages afforded by sample shape. Cooling system designs themselves are expected to require specific refrigerant shapes and fluid flow designs for the practical separation of the hot and cold heat reservoirs and most efficient transfer of heat energy. Methods to incorporate beneficial shape designs with existing cooling pump designs are vital to observe the potential efficiency improvements possible.

7.2.2 Multicaloric combinations

Two of the principal aims of this thesis were to better understand and control the magnitude of the required fields and the hysteresis. Similar issues are present in other caloric systems, for example, the electrocaloric effect (ECE) or the barocaloric effect (BCE). An interesting further development to address and perhaps overcome these issues focuses on the careful combination of these. Liu *et al.* [56] demonstrated an artificial reduction in hysteresis via a combination of magnetic field and pressure induced (from its large BCE) transitions in Heusler alloys. A similar result has been carried out using in FeRh films coupled to a ferroelectric $BaTiO_3$ substrate by combining MCE and ECE in Ref. [57], in which the authors show that the hysteresis loss is instead transferred into the elastic cycle.

Since $La(Fe,Si)_{13}$ exhibits the barocaloric effect, a multicaloric cycle in this material is expected to be similarly advantageous. An in-depth study of both the MCE and BCE is required to determine whether such methods can lead to both an improvement in efficiency and the accessibility of a large MCE within small field ranges suitable for cheap permanent magnet use. This extra control via pressure may also allow a more practical method to increase the working temperature range, whereby the pressure is continually changed to move T_C to the desired value, or a pressure gradient creates a range of T_C within one composition of material. This would avoid the need to control this by only the composition (i.e. a cascaded set of difference compositions with difference T_C). Using a pressure cell incorporated within the VSM, which allows applied hydrostatic pressures up to 1.3 GPa, these questions can be

investigated systematically within $La(Fe,Si)_{13}$, with further development into other material systems which are much more inhibited by hysteresis and broadness in the transition. I have been awarded a one-year EPSRC prize scholarship which will, in part, involve investigation of these effects.

7.2.3 Further understanding of the enhanced Sommerfeld coefficient and implication on the MCE

The systematic study of the low temperature heat capacity contributions leaves several questions unanswered with regards to the exact mechanisms and coupling effects which lead to these enhancements. Several avenues are very promising, such as broadening the work by making a direct comparison with other compositional changes in this system, e.g. by cobalt doping, and its correlation with the MCE properties. In addition, investigating other MCE systems (particularly itinerant electron systems) will be very informative for understanding both MCE mechanisms and the interactions present at low temperature. Further comparisons can be made of the spin-wave heat capacity. Neutron diffraction studies (as is given for one example composition) will help clarify their variation with temperature, as will results extracted from saturation magnetisation measurements and the $M_s - aT^{3/2}$ behaviour describing the spin wave stiffness, under different field and compositional variations. This will help compare the consistency between several methods of spin wave stiffness determination, and in these materials will give a greater understanding of their presence and role with regards to the Sommerfeld coefficient enhancements observed.

Further extensions which would be important to this study are studying the effect of the heat capacity and the γ, α and β components under pressure, and theoretical approaches that describe the enhancement mechanisms beyond current density functional theory predictions.

7.3 Publications of work conducted during Ph.D.

E. Lovell, K. Morrison, A. M. Pereira, A. D. Caplin, O. Gutfleisch, L. F. Cohen, Scanning Hall probe imaging of $LaFe_{13x}Si_x$, *Adv. Sci. Tech.* **93**, 219-224 (2014)

E. Lovell, A. M. Pereira, A. D. Caplin, J. Lyubina, L. F. Cohen, Dynamics of the first-order metamagnetic transition in magnetocaloric $La(Fe,Si)_{13}$: reducing hysteresis, *Adv. Energy Mater.* **5**, 1401639 (2015)

V. Basso, M. Kuepferling, C. Curcio, C. Bennati, A. Barcza, M. Katter, M. Bratko, E. Lovell, J. Turcaud, L. F. Cohen, Specific heat and entropy change at the first order phase transition of $La(Fe\text{-}Mn\text{-}Si)_{13}$-H compounds, *J. Appl. Phys.* **118**, 053907 (2015)

E. Lovell, M. Bratko, A. D. Caplin, A. Barcza, M. Katter, L. Ghivelder, L. F. Cohen, Magnetic relaxation dynamics driven by the first-order character of magnetocaloric $La(Fe,Mn,Si)_{13}$, *Phil. Trans. R. Soc. A* **374**, 20150307 (2016)

K. Zeissler, M. Chadha, E. Lovell, L. F. Cohen, W. R. Branford, Low temperature and high field regimes of connected kagome artificial spin ice: the role of domain wall topology, *Sci. Rep.* **6**, 30218 (2016)

E. Lovell, L. Ghivelder, A. Nicotina, J. Turcaud, M. Bratko, A. D. Caplin, V. Basso, A. Barcza, M. Katter, L. F. Cohen, Low temperature specific heat in hydrogenated and Mn doped $La(Fe,Si)_{13}$, *Phys. Rev. B* **94**, 134405 (2016)

A. Waske, E. Lovell, A. Funk, K. Sellschopp, A. Rack, L. Giebeler, P. F. Gostin, S. Fähler, L. F. Cohen, The impact of surface morphology on the magnetovolume transition in magnetocaloric $LaFe_{11.8}Si_{1.2}$, *APL Mater.* **4**, 106101 (2016)

M. Bratko, E. Lovell, A. D. Caplin, V. Basso, A. Barcza, M. Katter, L. F. Cohen, Determining the first-order character of $La(Fe,Mn,Si)_{13}$, *Phys. Rev. B* **95**, 064411 (2017)

In progress:

M. Bratko, E. Lovell, A. D. Caplin, A. Barcza, M. Katter, L. F. Cohen, Studies of the avalanche behaviour of La(Fe,Mn,Si)13: resolving the nature of the magnetic transition and its dependence on thermal environment (in preparation to be submitted to Scientific Reports)

Bibliography

[1] M. Isaac, D. P. van Vuuren, Modeling global residential sector energy demand for heating and air conditioning in the context of climate change, Energy Policy 37, 597-521 (2009)

[2] P. Weiss, A. Piccard, Le phénomène magnétocalorique, J. Phys. (Paris), 7, 103-109 (1917)

[3] A. M. Tischin, Y. I. Spichkin, The Magnetocaloric Effect and Its Applications, Series in Condensed Matter Physics (CRC Press) (2003)

[4] E. Ambler, R. P. Hudson, Magnetic cooling, Rep. Prog. Phys. 18, 251-303 (1955)

[5] V. K. Pecharsky, K. A. Gschneidner Jr., Giant Magnetocaloric Effect in $Gd_5Si_2Ge_2$, Phys. Rev. Lett. 78, 4494-4497 (1997)

[6] K. A. Gschneidner Jr., V. K. Pecharsky, A. O. Tsokol, Recent developments in magnetocaloric materials, Rep. Prog. Phys. 68, 1479-1539 (2005)

[7] V. Franco, J. S. Blázquez, B. Ingale, A. Conde, The Magnetocaloric Effect and Magnetic Refrigeration Near Room Temperature: Materials and Models, Annu. Rev. Mater. Res. 42, 305-342 (2012)

[8] O. Gutfleisch, M. A. Willard, E. Brück, C. H. Chen, S. G. Sankar, J. P. Liu, Magnetic Materials and Devices for the 21st Century: Stronger, Lighter, and More Energy Efficient, Adv. Mater. 23, 821-842 (2011)

[9] A. Smith, C. R. H. Bahl, R. Bjørk, K. Engelbrecht, K. K. Nielsen, N. Pryds, Materials Challenges for High Performance Magnetocaloric Refrigeration Devices, Adv. Energy Mater. 2, 1288-1318 (2012)

[10] M. W. Zemansky, Heat and Thermodynamics, McGraw-Hill Book Company, Inc., U.S.A. (1957)

[11] M. Shimizu, Itinerant electron metamagnetism, J. Physique 43, 155-163 (1982)

[12] J. M. D. Coey, Magnetism and Magnetic Materials, Cambridge (2010)

[13] J. C. Slater, Introduction to Chemical Physics, McGraw-Hill Book Company, Inc., U.S.A. (1939)

[14] O. Gutfleisch, T. Gottschall, M. Fries, D. Benke, I. Radulov, K. P. Skokov, H. Wende, M. Gruner, M. Acet, P. Entel, M. Farle, Mastering hysteresis in magnetocaloric materials, Phil. Trans. R. Soc. A 374, 20150308 (2016)

[15] V. Provenzano, A. J. Shapiro, R. D. Shull, Reduction of hysteresis losses in the magnetic refrigerant $Gd_5Ge_2Si_2$ by the addition of iron, Nature 429, 853-857 (2004)

[16] L. F. Bates, The hysteresis cycle and its interpretation, Proc. Phys. Soc. 53, 468 (1941)

[17] L. F. Bates, E. G. Harrison, The Adiabatic Temperature Changes Accompanying Magnetization in Low and Moderate Fields: A Further Study of Iron, Proc. Phys. Soc. 60, 225 (1948)

[18] K. A. Gschneidner Jr., V. K. Pecharsky, Thirty years of near room temperature magnetic cooling: Where we are today and future prospects, Int. J. Refrig. 31, 945-961 (2008)

[19] V. K. Pecharsky, K. A. Gschneidner Jr., Y. Mudryk, D. Paudyal, Making the most of the magnetic and lattice entropy changes, J. Magn. Magn. Mater. 321, 3541-3547 (2009)

[20] A. Planes, L. Mañosa, M. Acet, Magnetocaloric effect and its relation to shape-memory properties in ferromagnetic Heusler alloys, J. Phys.: Condens. Matter 21, 233201 (2009)

[21] A. Fujita, Y. Akamatsu, K. Fukamichi, Itinerant electron metamagnetic transition in $La(Fe_xSi_{1-x})_{13}$ intermetallic compounds, J. Appl. Phys. 85, 4756-4758 (1999)

[22] A. Giguère, M. Foldeaki, B. Ravi Gopal, R. Chahine, T. K. Bose, A. Frydman, J. A. Barclay, Direct Measurement of the 'Giant' Adiabatic Temperature Change in $Gd_5Si_2Ge_2$, Phys. Rev. Lett. 83, 2262-2265 (1999)

[23] L. Caron, Z. Q. Ou, T. T. Nguyen, D. T. Cam Thanh, O.Tegus, E. Brück, On the determination of the magnetic entropy change in materials with first-order transitions, J. Magn. Magn. Mater. 321, 3559-3566 (2009)

[24] J. S. Amaral, V. S. Amaral, On estimating the magnetocaloric effect from magnetization measurements, J. Magn. Magn. Mater. 322, 1552-1557 (2010)

[25] V. I. Zverev, A. M. Tishin, M. D. Kuz'min, J. Appl. Phys. 107, 043907 (2010)

[26] K. G. Sandeman, Scr. Mater. 67, 566 (2012)

[27] Barclay J. A. Barclay, W. A. Steyert, Active magnetic regenerator, US Patent 4332135A, 1 June (1982)

[28] C. Zimm, A. Jastrab, A. Sternberg, V. Pecharsky, K. Gschneidner Jr., M. Osborne, I. Anderson, Description and performance of a near-room temperature magnetic refrigerator, Adv. Cryog. Engin. 43, 1759 (1998)

[29] F. C. Chen, R. W. Murphy, V. C. Mei, G. L. Chen, Thermodynamic Analysis of Four Magnetic Heat-Pump Cycles, J. Eng. Gas Turbine Power 114, 715-720 (1992)

[30] C. Zimm, A. Boeder, J. Chell, A. Sternberg, A. Fujita, S. Fujieda, K. Fukamichi, Design and performance of a permanent-magnet rotary refrigerator, Int. J. Refrig. 29, 1302-1306 (2006)

[31] A. Waske, L. Giebeler, B. Weise, A. Funk, M. Hinterstein, M. Herklotz, K. Skokov, S. Fähler, O. Gutfleisch, J. Eckert, Asymmetric first-order transition and interlocked particle state in magnetocaloric $La(Fe,Si)_{13}$, Phys. Status Solidi RRL 9, 136 (2015)

[32] A. Bartok, M. Kustov, L. F. Cohen, A. Pasko, K. Zehani, L. Bessais, F. Mazaleyrat, M. LoBue, Study of the first paramagnetic to ferromagnetic transition in as prepared samples of Mn-Fe-P-Si magnetocaloric compounds prepared by different synthesis routes, J. Magn. Magn. Mater. 400, 333-338 (2016)

[33] J. Lyubina, R. Schäfer, N. Martin, L. Schultz, O. Gutfleisch, Novel Design of $La(Fe,Si)_{13}$ Alloys Towards High Magnetic Refrigeration Performance, Adv. Mater. 22, 3735 (2010)

[34] J. Lyubina, U. Hannemann, L. F. Cohen, M. P. Ryan, Novel $La(Fe,Si)_{13}$/Cu Composites for Magnetic Cooling, Adv. Energy Mater. 2, 1323-1327 (2012)

[35] Z. Q. Ou, L. Zhang, N. H. Dung, L. van Eijck, A. M. Mulders, M. Avdeev, N. H. van Dijk, E. Brück, Neutron diffraction study on the magnetic structure of Fe_2P-based $Mn_{0.66}Fe_{1.29}P_{1-x}Si_x$ melt-spun ribbons, J. Magn. Magn. Mater. 340, 80-85 (2013)

[36] N. H. Dung, L. Zhang, Z. Q. Ou, E. Brück, From first-order magneto-elastic to magneto-structural transition in $(Mn,Fe)_{1.95}P_{0.50}Si_{0.50}$ compounds, Appl. Phys. Lett. 99, 092511 (2011)

[37] H. Yibole, F. Guillou, L. Zhang, N. H. van Dijk, E. Brück, Direct measurement of the magnetocaloric effect in MnFe(P,X) (X = As, Ge, Si) materials, J. Phys. D: Appl. Phys 47, 075002 (2014)

[38] M. P. Annaorazov, K. A. Asatryan, G. Myalikgulyev, S. A. Nikitin, A. M. Tishin, A. L. Tyurin, Alloys of the Fe-Rh system as a new class of working material for magnetic refrigerators, Cryogenics 32, 867-872 (1992)

[39] A. R. Dinesen, S. Linderoth, S. Mørup, Direct and indirect measurement of the magnetocaloric effect in a $La_{0.6}Ca_{0.4}MnO_3$ ceramic perovskite, J. Magn. Magn. Mater. 253, 28-34 (2002)

[40] H. Wada, Y. Tanabe, Giant magnetocaloric effect of $MnAs_{1-x}Sb_x$, Appl. Phys. Lett. 79, 3302-3304 (2001)

[41] F. X. Hu, B. G. Shen, J. R. Sun, Magnetic entropy change in $Ni_{51.5}Mn_{22.7}Ga_{25.8}$ alloy, Appl. Phys. Lett. 76, 3460-3462 (2000)

[42] T. Gottschall, K. P. Skokov, B.Frincu, O. Gutfleisch, Large reversible magnetocaloric effect in Ni-Mn-In-Co, Appl. Phys. Lett. 106, 021901 (2015)

[43] T. Gottschall, K. P. Skokov, D. Benke, M. E. Gruner, O. Gutfleisch, Contradictory role of the magnetic contribution in inverse magnetocaloric Heusler materials, Phys. Rev. B 93, 184431 (2016)

[44] R. Y. Umetsu, K. Endo, A. Kondo, K. Kindo, W. Ito, X. Xu, T. Kanomata, R. Kainuma, Magnetoresistance and Transformation Hysteresis in the $Ni_{50}Mn_{34.4}In_{15.6}$ Metamagnetic Shape Memory Alloy, Mater. Trans. 54, 291-296 (2013)

[45] M. P. Annaorazov, S. A. Nikitin, A. L. Tyurin, K. A. Asatryan, A. K. Dovletov, Anomalously high entropy change in FeRh alloy, J. Appl. Phys. 79, 1689-1695 (1996)

[46] X. Moya, S. Kar-Narayan, N. D. Mathur, Caloric materials near ferroic phase transitions, Nat. Mater. 13, 439-450 (2014)

[47] H. Baumgartner, Elektrische Sättigungserscheinungen und elektrokalorischer Effekt von Kaliumphosphat KH_2PO_4, Helv. Phys. Acta 23, 651-696 (1950)

[48] X. Li, X. S. Qian, H. Gu, X. Chen, S. G. Lu, M. Lin, F. Bateman, Q. M. Zhang, Giant electrocaloric effect in ferroelectric poly(vinylidenefluoride-trifluoroethylene) copolymers near a first-order ferroelectric transition, Appl. Phys. Lett. 101, 132903 (2012)

[49] S. Kar-Narayan, M. D. Mathur, Predicted cooling powers for multilayer capacitors based on various electrocaloric and electrode materials, Appl. Phys. Lett. 95, 242903 (2009)

[50] P. Lloveras, E. Stern-Taulats, M. Barrio, J. L. Tamarit, S. Crossley, W. Li, V. Pomjakushin, A. Planes, L. Mañosa, N. D. Mathur, X. Moya, Giant barocaloric effects at low pressure in ferrielectric ammonium sulphate, Nat. Commun. 6, 8801 (2015)

[51] L. Mañosa, D. González-Alonso, A. Planes, E. Bonnot, M. Barrio, J. L. Tamarit, S. Aksoy, M. Acet, Giant solid-state barocaloric effect in the Ni-Mn-In magnetic shape-memory alloy, Nat. Mater. 9, 478-481 (2010)

[52] L. Mañosa, D. González-Alonso, A. Planes, M. Barrio, J. L. Tamarit, I. S. Titov, M. Acet, A. Bhattacharyya, S. Majumdar, Inverse barocaloric effect in the giant magnetocaloric La-Fe-Si-Co compound, Nat. Commun. 2, 595 (2011)

[53] L. G. de Medeiros Jr., N. A. de Oliveira, A. Troper, Barocaloric and magnetocaloric effects in $La(Fe_{0.89}Si_{0.11})_{13}$, J. Appl. Phys. 103, 113909 (2008)

[54] X. Moya, E. Defay, V. Heine, N. D. Mathur, Too cool to work, Nature Phys. 11, 202-205 (2015)

[55] A. Fujita, S. Fujieda, K. Fukamichi, H. Mitamura, T. Goto, Itinerant-electron metamagnetic transition and large magnetovolume effects in $La(Fe_xSi_{1-x})_{13}$ compounds, Phys. Rev. B 65, 014410 (2001)

[56] J. Liu, T. Gottschall, K. P. Skokov, J. D. Moore, O. Gutfleisch, Giant magnetocaloric effect driven by structural transitions, Nat. Mater. 11, 620-626 (2012)

[57] Y. Liu, L. C. Phillips, R. Mattana, M. Bibes, A. Barthélémy, B. Dkhil, Large reversible caloric effect in FeRh thin films via a dual-stimulus multicaloric cycle, Nat. Commun. 7, 11614 (2016)

[58] L. Pál, First-order magnetic phase transitions, Acta. Phys. Hung. 27, 47-85 (1969)

[59] Y. Imry, M. Wortis, Influence of quenched impurities on first-order phase transitions, Phys. Rev. B 19, 3580-3585 (1979)

[60] A. Arrott, J. E. Noakes, Approximate equation of state for nickel near its critical temperature, Phys. Rev. Lett. 19, 786-789 (1967)

[61] A. B. Pippard, The elements of classical thermodynamics, Cambridge University Press (1963)

[62] M. Avrami, Kinetics of Phase Change. I. General Theory, J. Chem. Phys. 7, 1103-1112 (1939)

[63] M. Avrami, Kinetics of Phase Change. II. Transformation-Time Relations for Random Distribution of Nuclei, J. Chem. Phys. 8 212-224 (1940)

[64] M. Perez, Gibbs-Thomson effects in phase transformations, Scr. Mater. 52, 709-712 (2005)

[65] Y. I. Dzhezherya, A. I. Tovstolytkin, A remarkable transformation of magnetic resonance spectra as a result of a mutual influence of coexisting para- and ferromagnetic phases, J. Phys.: Condens. Matter 19, 246212 (2007)

[66] C. P. Bean, D. S. Rodbell, Magnetic disorder as a first-order phase transformation, Phys. Rev. 126, 104-109 (1962)

[67] J. S. Amaral, S. Das, V. S. Amaral, The mean-field theory in the study of ferromagnets and the magnetocaloric effect (2011)

[68] V. Basso, The magnetocaloric effect at the first-order magneto-elastic phase transition, J. Phys.: Condens. Matter 23, 226004 (2011)

[69] H. N. Bez, K. K. Nielsen, P. Norby, A. Smith, C. R. H. Bahl, Magneto-elastic coupling in $La(Fe,Mn,Si)_{13}H_y$, AIP Adv. 6, 056217 (2016)

[70] S. Schmitt, N. Grewe, T. Jabben, Itinerant and local-moment magnetism in strongly correlated electron systems. Phys. Rev. B 85, 024404 (2012)

[71] E. P. Wohlfarth, P. Rhodes, Collective electron metamagnetism, Philos. Mag. 7, 1817-1824 (1962)

[72] H. Yamada, Metamagnetic transition and susceptibility maximum in an itinerant-electron system, Phys. Rev. B 47, 11211-11219 (1993)

[73] H. Yamada, K. Terao, Negative mode-mode coupling among spin fluctuations and the magneto-volume effect in an itinerant-electron ferromagnet, J. Phys.: Condens. Matter 6, 10805-10809 (1994)

[74] H. Yamada, K. Fukamichi, T. Goto, Itinerant-electron metamagnetism and strong pressure dependence of the Curie temperature, Phys. Rev. B 64, 024413 (2001)

[75] P. Entel, M. Schröter, A novel theoretical description of volume instabilities in itinerant magnetic systems, Physica B 161, 160-164 (1989)

[76] T. T. M. Palstra, J. A. Mydosh, G. J. Nieuwenhuys, A. M. van der Kraan, K. H. J. Buschow, Study of the critical behaviour of the magnetization and electrical resistivity in cubic La(Fe,Si)$_{13}$ compounds, J. Magn. Magn. Mater. 36, 290-296 (1983)

[77] V. Raghavan, Fe-La-Si (Iron-Lanthanum-Silicon), J. Phase Equilib. 22, 158-159 (2001)

[78] F. Wang, G. J. Wang, F. X. Hu, A. Kurbakov, B. G. Shen, Z. H. Cheng, Strong interplay between structure and magnetism in the giant magnetocaloric intermetallic compound LaFe$_{11.4}$Si$_{1.6}$: a neutron diffraction study, J. Phys.: Condens. Matter 15, 5269-5278 (2003)

[79] A. Fujita, H. Yako, Stability of metallic, magnetic and electronic states in NaZn$_{13}$-type La(Fe$_x$Si$_{1-x}$)$_{13}$ magnetocaloric compounds, Scr. Mater. 67, 578-583 (2012)

[80] F. X. Hu, B. G. Shen, J. R. Sun, Z. H. Cheng, G. H. Rao, X. X. Zhang, Influence of negative lattice expansion and metamagnetic transition on magnetic entropy change in the compound LaFe$_{11.4}$Si$_{1.6}$, Appl. Phys. Lett. 78, 3675-3677 (2001)

[81] J. Liu, M. Krautz, K. Skokov, T. G. Woodcock, O. Gutfleisch, Systematic study of the microstructure, entropy change and adiabatic temperature change in optimized La-Fe-Si alloys, Acta Mater. 59, 3602-3611 (2011)

[82] A. Fujita, K. Fukamichi, Giant Volume Magnetostriction due to the Itinerant Electron Metamagnetic Transition in La(Fe-Si)$_{13}$ Compounds, IEEE Trans. Magn. 35, 3796-3798 (1999)

[83] D. T. Cam Thanh, E. BrÃijck, O. Tegus, J. C. P. Klaasse, T. J. Gortenmulder, K. H. J. Buschow, Magnetocaloric effect in MnFe(P,Si,Ge) compounds, J. Appl. Phys. 99, 08Q107 (2006)

[84] B. G. Shen, J. R. Sun, F. X. Hu, H. W. Zhang, Z. H. Cheng, Recent Progress in Exploring Magnetocaloric Materials, Adv. Mater. 21, 4545-4564 (2009)

[85] K. P. Skokov, V. V. Khovaylo, K. -H. Müller, J. D. Moore, J. Liu, O. Gutfleisch, Magnetocaloric materials with first-order phase transition: thermal and magnetic hysteresis in $LaFe_{11.8}Si_{1.2}$ and $Ni_{2.21}Mn_{0.77}Ga_{1.02}$ (invited), J. Appl. Phys. 111, 07A910 (2012)

[86] S. Fujieda, A. Fujita, K. Fukamichi, Large magnetocaloric effect in $La(Fe_xSi_{1-x})_{13}$ itinerant-electron metamagnetic compounds, Appl. Phys. Lett. 81, 1276-1278 (2002)

[87] R. Bjørk, C. R. H. Bahl, M. Katter, Magnetocaloric properties of $LaFe_{13-x-y}Co_xSi_y$ and commercial grade Gd, J. Magn. Magn. Mater. 322, 3882-3888 (2010)

[88] A. Fujita, S. Fujieda, Y. Hasegawa, K. Fukamichi, Itinerant-electron metamagnetic transition and large magnetocaloric effects in $La(Fe_xSi_{1-x})_{13}$ compounds and their hydrides, Phys. Rev. B 67, 104416 (2003)

[89] S. Fujieda, A. Fujita, K. Fukamichi, Y. Yamazaki, Y. Iijima, Giant isotropic magnetostriction of itinerant-electron metamagnetic $La(Fe_{0.88}Si_{0.12})_{13}H_y$ compounds, Appl. Phys. Lett. 79, 653-655 (2001)

[90] A. Fujita, S Fujieda, K. Fukamichi, Influence of spin fluctuations on thermodynamics of itinerant-electron metamagnetic transition in $La(Fe_{0.88}Si_{0.12})_{13}$ compound, J. Magn. Magn. Mater. 272-276, e629-e630 (2004)

[91] A. Fujita, K. Fukamichi, Control of large magnetocaloric effects in metamagnetic $La(Fe_xSi_{1-x})_{13}$ compounds by hydrogenation, J. Alloys Compd. 404, 554-558 (2005)

[92] A. Fujita, K. Fukamichi, Enhancement of isothermal entropy change due to spin fluctuations in itinerant-electron metamagnetic $La(Fe_{0.88}Si_{0.12})_{13}$ compound, J. Alloys Compd. 408-412, 62-65 (2006)

[93] M. D. Kuz'min, M. Richter, Mechanism of the strong magnetic refrigerant performance of $LaFe_{13-x}Si_x$, Phys. Rev. B 76, 092401 (2007)

[94] M. E. Gruner, W. Keune, B. Roldan Cuenya, C. Weis, J. Landers, S. I Makarov, D. Klar, M. Y. Hu, E. E. Alp, J. Zhao, M. Krautz, O. Gutfleisch and H. Wende, Phys. Rev. Lett. 114, 057202 (2015)

[95] S. Fujieda, A. Fujita, K. Fukamichi, Control of Large Magnetocaloric Effects and Hysteresis of $La_{1-z}Ce_z(Fe_{0.86}Si_{0.14})_{13}$ Compounds, IEEE Trans. Magn. 41, 2787-2789 (2005)

[96] S. Fujieda, A. Fujita, K. Fukamichi, Reduction of hysteresis loss and large magnetocaloric effects in substituted compounds of itinerant-electron metamagnets $La(Fe_xSi_{1-x})_{13}$, J. Magn. Magn. Mater. 321, 3567-3570 (2009)

[97] F. X. Hu, L. Chen, J. Wang, L. F. Bao, J. R. Sun, B. G. Shen, Particle size dependent hysteresis loss in $La_{0.7}Ce_{0.3}Fe_{11.6}Si_{1.4}C_{0.2}$ first-order systems, Appl. Phys. Lett. 100, 072403 (2012)

[98] S. Fujieda, A. Fujita, K. Fukamichi, Reduction of hysteresis loss in itinerant-electron metamagnetic transition by partial substitution of Pr for La in $La(Fe_xSi_{1-x})_{13}$, J. Magn. Magn. Mater. 310, e1004-e1005 (2007)

[99] K. Morrison, J. Lyubina, J. D. Moore, A. D. Caplin, K. G. Sandeman, O. Gutfleisch, L. F. Cohen, Contributions to the entropy change in melt-spun $LaFe_{11.6}Si_{1.4}$, J. Phys. D: Appl. Phys. 43, 132001 (2010)

[100] K. Morrison, M. Bratko, J. Turcaud, A. Berenov, A. D. Caplin, L. F. Cohen, A calorimetric method to detect a weak or distributed latent heat contribution at first order magnetic transitions, Rev. Sci. Instrum. 83, 033901 (2012)

[101] C. Xu, G. D. Li, L. G. Wang, Itinerant-electron metamagnetic transition and giant magnetocaloric effect in $La_{0.8}Ce_{0.2}Fe_{11.4}Si_{1.6}$ compound, J. Appl. Phys. 99, 123913 (2006)

[102] A. Fujita, S. Fujieda, K. Fukamichi, Relative cooling power of $La(Fe_xSi_{1-x})_{13}$ after controlling the Curie temperature by hydrogenation and partial substitution of Ce, J. Magn. Magn. Mater. 310, e1006-e1007 (2007)

[103] F. Wang, Y. F. Chen, G. J. Wang, B. G. Shen, The effect of Mn substitution in $LaFe_{11.7}Si_{1.3}$ compound on the magnetic properties and magnetic entropy changes, J. Phys. D: Appl. Phys. 36, 1-3 (2003)

[104] F. X. Hu, X. L. Qian, J. R. Sun, G. J. Wang, X. X. Zhang, Z. H. Cheng, B. G. Shen, Magnetic entropy change and its temperature variation in compounds $La(Fe_{1-x}Co_x)_{11.2}Si_{1.8}$, J. Appl. Phys. 92, 3620-3623 (2002)

[105] J. Liu, J. D. Moore, K. P. Skokov, M. Krautz, K. LÃűwe, A. Barcza, M. Katter, O. Gutfleisch, Exploring $La(Fe,Si)_{13}$-based magnetic refrigerants towards application, Scr. Mater. 67, 584-589 (2012)

[106] M. Krautz, K. Skokov, T. Gottschall, C. S. Teixeira, A. Waske, J. Liu, L. Schultz, O. Gutfleisch, Systematic investigation of Mn substituted $La(Fe,Si)_{13}$ alloys and their hydrides for room-temperature magnetocaloric application, J. Alloys Compd. 598, 27-32 (2014)

[107] A. Fujita, S. Fujieda, K. Fukamichi, Y. Yamazaki Y. Iijima, Giant Magnetic Entropy Change in Hydrogenated $La(Fe_{0.88}Si_{0.12})_{13}H_y$ Compounds, Mater. Trans. 43, 1202-1204 (2002)

[108] A. Fujita, S. Fujieda, K. Fukamichi, Influence of hydrogenation on the electronic structure and the itinerant-electron metamagnetic transition in strong magnetocaloric compound $La(Fe_{0.88}Si_{0.12})_{13}$, J. Magn. Magn. Mater. 321, 3553-3558 (2009)

[109] S. Fujieda, A. Fujita and K. Fukamichi, Strong Pressure Effect on the Curie Temperature of Itinerant-Electron Metamagnetic $La(Fe_{0.88}Si_{0.12})_{13}H_y$ and $La_{0.7}Ce_{0.3}(Fe_{0.88}Si_{0.12})_{13}H_y$, Mater. Trans. 50, 483 (2009)

[110] Z. Gercsi, K. G. Sandeman, A. Fujita, Electronic structure and metamagnetic transition of interstitially doped $LaSiFe_{12}$, arXiv:1407.7975[cond-mat.mtrl-sci]

[111] A. Barcza, M. Katter, V. Zellmann, S. Russek, S. Jacobs, C. Zimm, Stability and Magnetocaloric Properties of Sintered La(Fe,Mn,Si)$_{13}$H$_z$ Alloys, IEEE Trans. Magn. 47, 3391-3394 (2011)

[112] M. Krautz, J. D. Moore, K. P. Skokov, J. Liu, C. S. Teixeira, R. Schäfer, L. Schultz, O. Gutfleisch, Reversible solid-state hydrogen-pump driven by magnetostructural transformation in the prototype system La(Fe,Si)$_{13}$H$_y$, J. Appl. Phys. 112, 083918 (2012)

[113] J. Lyubina, K. Nenkov, L. Schultz, O. Gutfleisch, Multiple Metamagnetic Transitions in the Magnetic Refrigerant La(Fe,Si)$_{13}$H$_x$, Phys. Rev. Lett. 101, 177203 (2008)

[114] S. I. Makarov, M. Krautz, S. Salamon, K. Skokov, C. S. Teixeira, O. Gutfleisch, H. Wende, W. Keune, Local electronic and magnetic properties of pure and Mn-containing magnetocaloric LaFe$_{13-x}$Si$_x$ compounds inferred from Mössbauer spectroscopy and magnetometry, J. Phys. D: Appl. Phys. 48, 305006 (2015)

[115] J. D. Moore, K. Morrison, K. G. Sandeman, M. Katter, L. F. Cohen, Reducing extrinsic hysteresis in first-order La(Fe,Co,Si)$_{13}$ magnetocaloric systems, Appl. Phys. Lett. 95, 252504 (2009)

[116] M. Kuepferling, C. P. Sasso, V. Basso, Rate dependence of the magnetocaloric effect in La-Fe-Si compounds, EPJ Web. Conf. 40, 06010 (2013)

[117] A. Fujita, T. Kondo, M. Kano, H. Yako, Shape-anisotropic heterogeneous nucleation and magnetic Gibbs-Thomson effect in itinerant-electron metamagnetic transition of La(Fe$_{0.88}$Si$_{0.12}$)$_{13}$ magnetocaloric compound, Appl. Phys. Lett. 102, 041913 (2013)

[118] A. Fujita, S. Fujieda, K. Fukamichi, Influence of Supercooling on the Thermally Induced First-Order Magnetic Transition in Magnetocaloric Compound La(Fe$_{0.88}$Si$_{0.12}$)$_{13}$, IEEE Trans. Magn. 47, 3387 (2011)

[119] H. Zhang, F. Wang, T. Zhao, S. Zhang, J. R. Sun, B. G. Shen, Thermally activated itinerant metamagnetic transition in LaFe$_{11.7}$Si$_{1.3}$, Phys. Rev. B 70, 212402 (2004)

[120] H. Yako, S. Fujieda, A. Fujita, K. Fukamichi, Influence of Demagnetizing Effect on the Kinetics of the Itinerant Electron Metamagnetic Transition in Magnetic Refrigerant $La(Fe_{0.88}Si_{0.12})_{13}$, IEEE Trans. Magn. 47, 2482 (2011)

[121] M. D. Kuz'min, Factors limiting the operation frequency of magnetic refrigerators, Appl. Phys. Lett. 90, 251916 (2007)

[122] N. T. Trung, J. C. P. Klaasse, O. Tegus, D. T. Cam Thanh, N. H. J. Bushow, E. Brück, Determination of adiabatic temperature change in MnFe(P,Ge) compounds with pulse-field method, J. Phys. D: Appl. Phys. 43, 015002 (2010)

[123] A. Fujita, H. Yako, Kinetics of thermally induced first-order magnetic transition in $La(Fe_{0.88}Si_{0.12})_{13}$ itinerant electron metamagnet, J. Alloys Compd. 577, S48-S51 (2013)

[124] M. Kuepferling, C. Bennati, F. Laviano, G. Ghigo, V. Basso, Dynamics of the magneto structural phase transition in $La(Fe_{0.9}Co_{0.015}Si_{0.085})_{13}$ observed by magneto-optical imaging, J. Appl. Phys. 115, 17A925 (2014)

[125] J. Lieb, J. E. Snyder, T. A. Lograsso, D. Schlagel, D. C. Jiles, Dynamics of the magnetic field-induced first-order magnetic-structural phase transformation of $Gd_5(Si_{0.5}Ge_{0.5})_4$, J. Appl. Phys. 95, 6915-6917 (2004)

[126] J. D. Moore, G. K. Perkins, K. Morrison, L. Ghivelder, M. K. Chattopadhyay, S. B. Roy, P. Chaddah, K. A. Gschneidner Jr., V. K. Pecharsky, L. F. Cohen, Local probing of arrested kinetics in Gd_5Ge_4, J. Phys. Condens. Matter 20, 465212 (2008)

[127] X. Xu, T. Kihara, M. Tokunaga, A. Matsuo, W. Ito, R. Y. Umetsu, K. Kindo, R. Kainuma, Magnetic field hysteresis under various sweeping rates for Ni-Co-Mn-In metamagnetic shape memory alloys, Appl. Phys. Lett. 103, 122406 (2013)

[128] M. Manekar, S. B. Roy, Nucleation and growth dynamics across the antiferromagnetic to ferromagnetic transition in $(Fe_{0.975}Ni_{0.025})_{50}Rh_{50}$: analogy with crystallization, J. Phys.: Condens. Matter 20, 325208 (2008)

[129] D. X. Chen, E. Pardo, A. Sanchez, Demagnetizing Factors of Rectangular Prisms and Ellipsoids, IEEE Trans. Magn. 38, 1742-1752 (2002)

[130] A. Smith, K. K. Nielsen, D. V. Christensen, C. R. H. Bahl, R. Bjørk, J. Hattel, The demagnetizing field of a nonuniform rectangular prism, J. Appl. Phys. 107, 103910 (2010)

[131] V. Christensen, R. Bjørk, K. K. Nielsen, C. R. H. Bahl, A. Smith, S. Clausen, Spatially resolved measurements of the magnetocaloric effect and the local magnetic field using thermography, J. Appl. Phys. 108, 063913 (2010)

[132] R. Bjørk, C. R. H. Bahl, Demagnetizing factor for a powder of randomly packed spherical particles, Appl. Phys. Lett. 103, 102403 (2013)

[133] P. V. Trevizoli, J. R. Barbosa Jr., P. A. Oliveira, F. C. Canesin, R. T. S. Ferreira, Assessment of demagnetization phenomena in the performance of an active magnetic regenerator, Int. J. Refrig. 35, 1043-1054 (2012)

[134] R. Caballero-Flores, V. Franco, A. Conde, L. F. Kiss, Influence of the demagnetizing field on the determination of the magnetocaloric effect from magnetization curves, J. Appl. Phys. 105, 07A919 (2009)

[135] B. Schwarz, N. Mattern, J. D. Moore, K. P. Skokov, O. Gutfleisch, J.Eckert, Influence of sample geometry on determination of magnetocaloric effect for $Gd_{60}Co_{30}Al_{10}$ glassy ribbons using direct and indirect methods, J. Magn. Magn. Mater. 323, 1782-1786 (2011)

[136] C. Romero-Muñiz, J. J. Ipus, J. S. Blázquez, V. Franco, A. Conde, Influence of the demagnetizing factor on the magnetocaloric effect: Critical scaling and numerical simulations, Appl. Phys. Lett. 104, 252405 (2014)

[137] M. Zou, Y. Mudryk, V. K. Pecharsky, K. A. Gschneidner Jr., D. L. Schlagel, T. A. Lograsso, Crystallography, anisotropic metamagnetism, and magnetocaloric effect in $Tb_5Si_{2.2}Ge_{1.8}$, Phys. Rev. B 75, 024418 (2007)

[138] M. S. Reis, R. M. Rubinger, N. A. Sobolev, M. A. Valente, K. Yamada, K. Sato, Y. Todate, A. Bouravleuv, P. J. von Ranke, S. Gama, Influence of the strong magnetocrys-

talline anisotropy on the magnetocaloric properties of MnP single crystal, Phys. Rev. B 77, 104439 (2008)

[139] H. P. Myers, Introductory Solid State Physics, Taylor & Francis (1997)

[140] A. G. Gurevich and G. A. Melkov, Magnetization Oscillations and Waves, CRC Press, Boca Raton (1996)

[141] H. Michor, M. El-Hagary, M. Della Mea, M. W. Pieper, M. Reissner, G. Hilscher, S. Khmelevskyi, P. Mohn, G. Schneider, G. Giester and P. Rogl, Itinerant electron metamagnetism in $LaCo_9Si_4$, Phys. Rev. B 69, 081404 (2004)

[142] G. J. Wang, F. Wang, N. L. Di, B. G. Shen, Z. H. Cheng, Hyperfine interactions and band structures of $LaFe_{13-x}Si_x$ intermetallic compounds with large magnetic entropy changes, J. Magn. Magn. Mater. 3030, 84-91, (2006)

[143] Z. Gercsi, Magnetic coupling in transition-metal-doped $LaSiFe_{11.5}TM_{0.5}$ (TM=Cr, Mn, Co and Ni), Europhys. Lett. 110, 47006 (2015)

[144] M. Katter, V. Zellmann, G. Reppel, K. Uestuener, Magnetocaloric Properties of $La(Fe,Co,Si)_{13}$ Bulk Material Prepared by Powder Metallurgy, IEEE Trans. Magn. 44, 3044 (2008)

[145] R. S. Popović, Hall Effect Devices. IOP Publishing Ltd. (1991)

[146] G. K. Perkins, Y. V. Bugoslavsky, X. Qi, J. L. MacManus-Driscoll, A. D. Caplin, High Field Scanning Hall Probe Imaging of High Temperature Superconductors, IEEE Trans. Appl. Supercond. 11, 3186-3189 (2001)

[147] Quantum Design PPMS Heat Capacity Option Manual

[148] J. S. Hwang, K. J. Lin, C. Tien, Measurement of heat capacity by fitting the whole temperature response of a heatpulse calorimeter, Rev. Sci. Instrum. 68, 94-101 (1997)

[149] J. C. Lashley, M. F. Hundley, A. Migliori, K. L. Sarrao, P. G.Pagliuso, T. W. Darling, M. Jaime, J. C. Cooley, W. L. Hults, L. Morales, D. J. Thoma, J. L. Smith, J. Boerio-Goates,

B. F. Woodfield, G. R. Stewart, R. A. Risher, N. E. Phillips, Critical examination of heat capacity measurements made on a Quantum Design physical property measurement system, Cryogenics 43, 369-378 (2003)

[150] M. Bratko, E. Lovell, A. D. Caplin, V. Basso, A. Barcza, M. Katter, L. F. Cohen, Determining the first-order character of La(Fe,Mn,Si)$_{13}$, Phys. Rev. B 95, 064411 (2017)

[151] E. Lovell, A. M. Pereira, A. D. Caplin, J. Lyubina, L. F. Cohen, Dynamics of the first-order metamagnetic transition in magnetocaloric La(Fe,Si)$_{13}$: reducing hysteresis, Adv. Energy Mater. 5, 1401639 (2015)

[152] J. D. Moore, G. K. Perkins, Y. Bugoslavsky, M. K. Chattopadhyay, S. B. Roy, P. Chaddah, V. K. Pecharsky, K. A. Gschneidner Jr., L. F. Cohen, Reducing the operational magnetic field in the prototype magnetocaloric system Gd_5Ge_4 by approaching the single cluster size limit, Appl. Phys. Lett. 88, 072501 (2006)

[153] E. Lovell, M. Bratko, A. D. Caplin, A. Barcza, M. Katter, L. Ghivelder, L. F. Cohen, Magnetic relaxation dynamics driven by the first-order character of magnetocaloric La(Fe,Mn,Si)$_{13}$, Phil. Trans. R. Soc. A 374, 20150307 (2016)

[154] K. Morrison, J. Lyubina, J. D. Moore, K. G. Sandeman, O. Gutfleisch, L. F. Cohen, A. D. Caplin, Magnetic refrigeration: phase transitions, itinerant magnetism and spin fluctuations, Philos. Mag. 92, 292-303 (2012)

[155] V. Basso, M. Küpferling, C. Curcio, C. Bennati, A. Barcza, M. Katter, M. Bratko, E. Lovell, J. Turcaud, L. F. Cohen, Specific heat and entropy change at the first order phase transition of La(Fe-Mn-Si)$_{13}$-H compounds, J. Appl. Phys. 118, 053907 (2015)

[156] F. Macià, G. Abril, J. M. Hernandez, J. Tejada, The role of thermal coupling on avalanches in manganites, J. Phys.: Condens. Matter 21, 406005 (2009)

[157] L. Ghivelder, G. G. Eslava, R. S. Freitas, G. Leyva, F. Parisi, Avalanche-like metamagnetic transition in (LaNd)CaMnO manganites, J. Alloys Compd. 680, 494-499 (2016)

[158] E. Lovell, L. Ghivelder, A. Nicotina, J. Turcaud, M. Bratko, A. D. Caplin, V. Basso, A. Barcza, M. Katter, L. F. Cohen, Low temperature specific heat in hydrogenated and Mn doped La(Fe,Si)$_{13}$, Phys. Rev. B (in press)

[159] F. Wang, Y. F. Chen, G. J. Wang, J. R. Sun, B. G. Shen, Large magnetic entropy change and magnetic properties in La(Fe$_{1-x}$Mn$_x$)$_{11.7}$Si$_{1.3}$H$_y$ compounds, Chinese Phys. 12, 911-914 (2003)

[160] F. Wang, J. G. Wang, J. R. Sun, B. G. Shen, Magnetic properties and magnetocaloric effect in Nd$_x$La$_{1-x}$Fe$_{11.5}$Al$_{1.5}$ compounds, Chinese Phys. B 17, 3087-3092 (2008)

[161] M. J. Rice, Electron-electron scattering in transition metals, Phys. Rev. Lett. 20, 1439-1141 (1968)

[162] J. R. Schrieffer, Effect of virtual spin waves on the properties of strongly paramagnetic metals, J. Appl. Phys. 39, 642-648 (1968)

[163] A. Fujita, K. Fukamichi, J. T. Wang, Y. Kawazoe, Large magnetovolume effects and band structure of itinerant-electron metamagnetic La(Fe$_x$Si$_{1-x}$)$_{13}$ compounds, Phys. Rev. B 68, 104431 (2003)

[164] M. J. Rice, Itinerant electron correlation and the ideal Lorenz number of transition metals, Phys. Lett. 26A, 86-87 (1967)

[165] H. Michor, E. Bauer, M. El-Hagary, C. Dusek, P. Rogl, G. Hilscher, Kondo-lattice behaviour of CeNi$_9$Si$_4$, Physica B 329, 572-573 (2003)

[166] U. Hanneman, J. Lyubina, M. Ryan, N. Alford, L. F. Cohen, Thermopower of LaFe$_{13-x}$Si$_x$ alloys, Europhys. Lett. 100, 57009 (2012)

[167] Q. Chen, B. Sundman, Calculation of Debye temperature for crystalline structures - a case study on Ti, Zr, and Hf, Acta Mater. 49, 947-961 (2001)

[168] Private communication with K. Morrison

A | Acronyms and Abbreviations

AFM:	antiferromagnet(ic)
AMR:	active magnetic regenerator
BCE:	barocaloric effect
CC:	Clausius-Clapeyron (method)
DFT:	density functional theory
DOS:	density of states
DSC:	differential scanning calorimetry
ECE:	electroncaloric effect
JMA:	Johnson-Mehl-Avrami (model)
FIB:	focused ion beam
FM:	ferromagnet(ic)
IEM:	itinerant electron metamagnetism
MCE:	magnetocaloric effect
PM:	paramagnet(ic)
PPMS:	physical property measurement system
PTFE:	polytetrafluoroethylene
SDM:	slope difference method
SEM:	scanning electron microscopy
SHPI:	scanning Hall probe imaging
VSM:	vibrating sample magnetometry

aust.:	austenite
hexag.:	hexagonal
non-hydrog.:	non-hydrogenated
mart.:	martensite
monoc.:	monoclinic
ortho.:	orthorhombic
tetrag.:	tetragonal

B | Hall Sensor Fabrication and Characterisation

This appendix gives further details of the fabrication methods used to make the Hall probe sensors used for this work, following the outline in section 3.4.1, in addition to several details concerning the characteristics of the InSb epilayers used.

B.1 InSb/GaAs epilayer characterisation

The epilayers on which Hall sensors are fabricated are InSb of 2.5 μm thickness, doped with Te, on a GaAs substrate, provided by QinetiQ, with growth number ME1926. The carrier density, n, and carrier mobility, μ can be calculated from the following equations.

The response of the Hall resistance, R_{H}, defined as V_{H}/I (where V_{H} is the Hall voltage, defined in section 3.4), to applied field, B, in a semiconductor film is determined by the charge carrier (e.g. electrons or holes) density, n, by:

$$\frac{dR_{\mathrm{H}}}{dB} = \frac{1}{net} \tag{B.1}$$

Where e is the electron charge, 1.6×10^{-19} coulombs, and t is the film thickness. μ can be

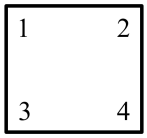


Figure B.1: An example of a film in square geometry with measurement labels, 1 to 4, as described in the text. V_{H} would be measured by applying current between 1 and 4, measuring the voltage between 2 and 3, and applying the field out of the page.

calculated from the resistivity, ρ, using the following equations:

$$\rho = \frac{1}{ne\mu} \tag{B.2}$$

$$R_{\mathrm{s}} = \rho/t \tag{B.3}$$

Where R_{s} is the sheet resistance, in the geometric resistance unit $\Omega/\Box$. R_{s} can be calculated using the van der Pauw method, from:

$$R_{\mathrm{s}} = \frac{\pi}{ln2}\frac{(R_{\mathrm{a}} - R_{\mathrm{b}})}{2} f\Big(\frac{R_{\mathrm{a}}}{R_{\mathrm{b}}}\Big) \tag{B.4}$$

Where R_{a} and R_{b} are the four-point resistances measured in the two directions, $(V_1 - V_2)/I_{34}$ and $(V_2 - V_4)/I_{13}$ respectively, where the former refers to applying a current from corners 3 to 4 and measuring the voltage between 1 and 2, as shown in Figure B.1, and $f\frac{R_{\mathrm{a}}}{R_{\mathrm{b}}}$ is a geometric-dependent value which for simple square geometries can be treated as unity [145].

The mobility, μ, is often cited as the principal material-dependent characteristic determining the sensitivity of R_{H} to magnetic field. Sensitivity of a sensor scales with the noise (i.e. a large sensitivity means a device is less sensitive) and is proportional to $\frac{1}{\mu d}$, where d is the sensor size [145]. μ and n measured for the InSb wafer as a function of T is shown in Figure B.2.

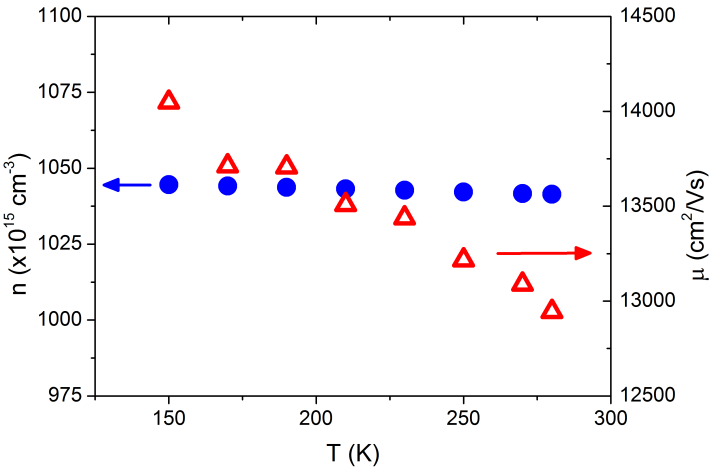


Figure B.2: The carrier number density, n, and mobility, μ, as a function of temperature for the QinetiQ InSb film ($t = 2.5$ μm). The invariant n makes sensors from this wafer very reliable as the dR_{H}/dB characteristic is very insensitive to T.

B.2 Sensor fabrication

In order to achieve the desired maximum sensor active area size of 5 μm by 5 μm, within close proximity to the corner of the 2.5 μm thick InSb epilayer wafers, two methods are used in conjunction. In order to fit the dimensions required for the Hall probe imaging rig, wafers of the size 4×4 to 5×5 mm^2 are used.

B.2.1 Diamond-tip scribing

Firstly, a diamond-tip stepper motor-controlled scribe is used to carve valleys into the film, to a minimum depth of 3 μm. This depth is chosen in order to etch fully through the InSb layer to the substrate and create the electrical conduction leads, shown in Figure 3.2, between which any cross-conduction is isolated. In this instance, 'coarse' refers to any the features on the scale of 10 μm and larger, and therefore all of the insulation channels, except the finer cross detail at the corner.

The tip has a angle of 90° with a tip width of approximately $1-2$ μm, and contacts the film vertically from above. Therefore a channel depth of 3 μm will give a width of 6 μm, which limits the smallest reliable features permitted.

The InSb sensor to be fabricated rests on a capacitor plate which gives sensitivity to the force of the diamond tip on the film by the same method as for the scanning Hall probe imaging rig detailed in section 3.4.2. A feedback mechanism allows control of the force between the tip and film. The tip is then passed across the film multiple times with the set contact force, until the required depth is obtained. A common number of passes to reach depths of > 3 μm is 2000, moving at a velocity of 1000 $\mu\mathrm{m\,s^{-1}}$. This process allows fast and large-scale (several millimetres) creation of isolating valleys, and is used, as the first step of fabrication, to approach the isolation channels to the corner of the InSb film.

B.2.2 Focused Ion Beam lithography

Focused Ion Beam (FIB) lithography uses the impact of accelerated gallium ions to etch channels into surfaces, with high precision in both depth and width: sub-micrometre features are easily achievable. This method is used to continue the coarse isolation channels from the diamond tip scribing step, and fabricate the fine details (< 10 μm) of the sensor. A step-by-step sensor-fabrication process is shown in Figure B.3.

Active area sizes as small as 5 μm are easily attainable and can be placed between 20 μm and 40 μm from the corner. A finite separation between corner and active area is required to protect the sensor from physical damage by contact of the corner with the sample, during the imaging process. With the sensor at a 5° angle, the increased distance of the active area from the sample surface, and thus the compromise of resolution, is minimal. Although smaller areas are possible, they are limited by the depth required being of the order of the width, which requires a greater intensity of ion beam and will cause degradation to the surrounding regions of film or ion-implantation, both which will adversely affect the Hall effect properties,

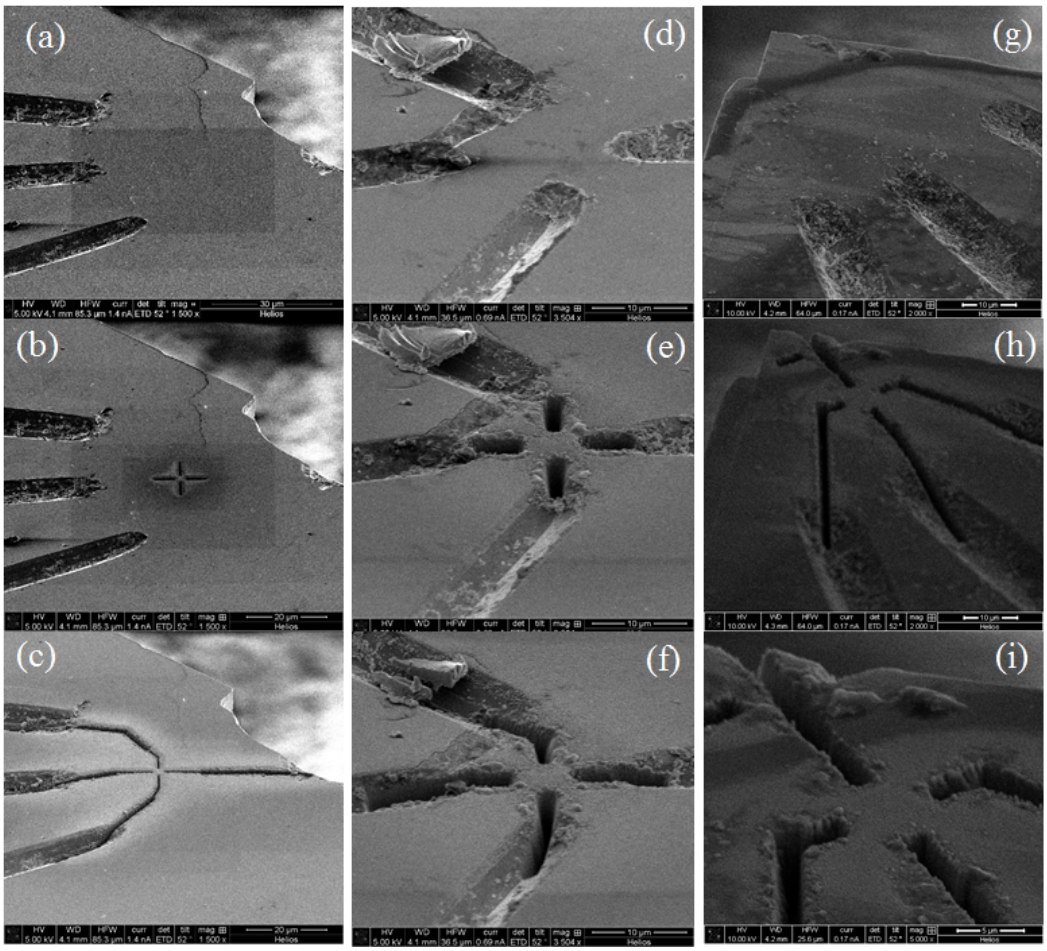


Figure B.3: Scanning electron microscopy images showing several examples, step-by-step, of the FIB sensor fabrication process on InSb: (a) to (c), and (g) to (i) Starting with (a) and (g), the wafers, post diamond tip scribing of the coarse approach isolation channels, and finishing in (c) and (i) with the finished sensor, with 5×5 μm^2 active area. The steps of (d) to (f) show the same result but as an adaptation from a previous diamond tip scribed 15×15 μm^2 sensor. For all images, damage of the film around the etched areas can be seen.

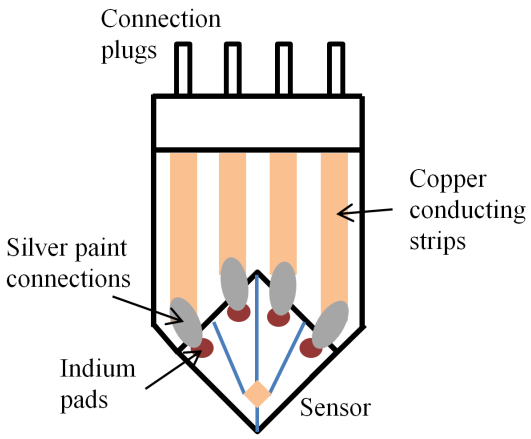


Figure B.4: Schematic of the sensor mount board (which is demonstrated in imaging position in Figure 3.3(b)).

e.g. n and μ.

B.2.3 Sensor mounting

In order to be compatible with the Hall probe imaging rig, the sensor is mounted onto a sensor mount board as shown in Figure B.4. This allows the active area to be the closest point to a sample. To achieve reliable ohmic contact (mechanically stable at the full range of T from room temperature to 4.2 K), indium contact pads are fused onto the four InSb channels by heating above the melting point of indium, 430 K, then cooling. Subsequent conduction from the indium to the sensor mount board contact pads is achieved with silver paint. Each board is designed to be easily inserted, using the 4-pin plug, into the Hall probe imaging rig.

C | Copyright Permissions

AMERICAN PHYSICAL SOCIETY LICENSE TERMS AND CONDITIONS

Sep 07, 2016

This Agreement between Edmund Lovell ("You") and American Physical Society ("American Physical Society") consists of your license details and the terms and conditions provided by American Physical Society and Copyright Clearance Center.

License Number	3943660818664
License date	Sep 07, 2016
Licensed Content Publisher	American Physical Society
Licensed Content Publication	Physical Review B
Licensed Content Title	Itinerant-electron metamagnetic transition and large magnetocaloric effects in $\mathrm{La}({\mathrm{Fe}}_{x}{\mathrm{Si}}_{1\ensuremath{-}x}{)}_{13}$ compounds and their hydrides
Licensed Content Author	A. Fujita et al.
Licensed Content Date	Mar 20, 2003
Licensed Content Volume Number	67
Type of Use	Thesis/Dissertation
Requestor type	Student
Format	Print, Electronic
Portion	chart/graph/table/figure
Number of charts/graphs/tables/figures	2
Portion description	Figure 3, Figure 14
Rights for	Main product
Duration of use	Life of Current Edition
Creation of copies for the disabled	no
With minor editing privileges	no
For distribution to	Worldwide
In the following language(s)	Original language of publication
With incidental promotional use	no
The lifetime unit quantity of new product	0 to 499
The requesting person/organization is:	Edmund Lovell
Order reference number	
Title of your thesis / dissertation	Magnetocaloric properties of La(FeSi)13 compounds
Expected completion date	Sep 2016
Expected size (number of pages)	200
Requestor Location	Edmund Lovell H702, Blackett Laboratory Imperial College

Reply all | Delete Junk | ...

Re: Permission to use figure in Ph.D. thesis

AF

Asaya Fujita <asaya-fujita@aist.go.jp>

Fri 09/09/2016 10:25

To: Lovell, Edmund

Reply all

Inbox

Dear Edmund,

Sure, yes! you can use these figures freely.
I hope your writing of thesis , as well as defense,
goes well without any barriers.

Asaya

> Dear Dr Asaya Fujita
>
> I am completing my PhD thesis at Imperial College London, UK (working with Lesley), entitled 'Magnetocaloric properties of La(FeSi)13 compounds'. I seek your permission to reprint, in my thesis, two of your figures:
>
> In the paper: A. Fujita, S. Fujieda, Y. Hasegawa, K. Fukamichi, Itinerant-electron metamagnetic transition and large magnetocaloric effects in La(FexSi1-x)13 compounds and their hydrides, Phys. Rev. B 67, 104416 (2003)
>
> The figures to be reproduced are: Figure 3 and Figure 14
>
> I have already been given copyright permission from American Physical Society, but part of their terms and conditions states that I must get permission from the authors, hence my email to you.
>
> If you could respond as soon as you are able I would be very grateful.
>
> We met in London at the Royal Society multicalorics meeting, and I really like your work, it has been extremely useful and informative for my PhD!
>
> Best wishes,
> Edmund Lovell

Reply all | Delete Junk | ...

RE: Permission to reproduce figures for PhD thesis

AP

AIPRights Permissions <Rights@aip.org>

Fri 09/09, 21:05

Lovell, Edmund

Reply all

Inbox

Action Items

Dear Dr. Lovell:

Thank you for requesting permission to reproduce material from AIP Publishing publications.

Material to be reproduced:

S. Fujieda, A. Fujita, K. Fukamichi,
'Large magnetocaloric effect in La(FexSi1-x)13 itinerant-electron metamagnetic compounds'
Appl. Phys. Lett. 81, 1276-1278 (2002)
Figures 2, 3, 4 and 5

For use in the following manner:

Reproduced in your PhD thesis at Imperial College London and included in its institutional repository.

Permission is granted subject to these conditions:

1. AIP Publishing grants you non-exclusive world rights in all languages and media. This permission extends to all subsequent and future editions of the new work.

2. The following notice must appear with the material (please fill in the citation information):

"Reproduced from [FULL CITATION], with the permission of AIP Publishing."

When reusing a full article, the notice must be printed on the first page of the reprinted article or book chapter. When reusing figures, photographs, covers, or tables, the notice may appear in the caption, in a footnote, or in the reference list.

In cases where the new publication is licensed under a Creative Commons license, the full notice as stated above must appear with the reproduced material.

3. If the material is published in electronic format, we ask that a link be created pointing back to the abstract of the article on the journal website. This can be accomplished through the use of the article's DOI.
4. This permission does not apply to any materials credited to another source.

5. If you have not already done so, please attempt to obtain permission from at least one of the authors. The authors' contact information can usually be obtained from the article.

Please let us know if you have any questions.

Sincerely,

RE: Permission to reproduce figures for PhD thesis

藤田麻哉 <asaya-fujita@aist.go.jp>

Wed 21/09/2016 12:49

To: Lovell, Edmund <e.lovell12@imperial.ac.uk>;

Dear Edmund,

I approve.

Asaya

差出人: Lovell, Edmund <e.lovell12@imperial.ac.uk>
送信日時: 2016年9月21日 20:37:48
宛先: 藤田麻哉
件名: Fw: Permission to reproduce figures for PhD thesis

Dear Asaya,

I realise I also need permission from one of the authors to use four figures, from the following paper, in my thesis.

S. Fujieda, A. Fujita, K. Fukamichi,
'Large magnetocaloric effect in La(FexSi1-x)13 itinerant-electron metamagnetic compounds'
Appl. Phys. Lett. 81, 1276-1278 (2002)

Figures 2, 3, 4 and 5

If you could let me know as soon as possible that would be great!

Many thanks,
Edmund

From: AIPRights Permissions <Rights@aip.org>
Sent: 09 September 2016 21:04
To: Lovell, Edmund
Subject: RE: Permission to reproduce figures for PhD thesis

Dear Dr. Lovell:

Thank you for requesting permission to reproduce material from AIP Publishing publications.

Material to be reproduced:

S. Fujieda, A. Fujita, K. Fukamichi,
'Large magnetocaloric effect in La(FexSi1-x)13 itinerant-electron metamagnetic compounds'
Appl. Phys. Lett. 81, 1276-1278 (2002)
Figures 2, 3, 4 and 5

For use in the following manner:

Reproduced in your PhD thesis at Imperial College London and included in its institutional repository.

Permission is granted subject to these conditions:

AMERICAN PHYSICAL SOCIETY LICENSE TERMS AND CONDITIONS

Sep 07, 2016

This Agreement between Edmund Lovell ("You") and American Physical Society ("American Physical Society") consists of your license details and the terms and conditions provided by American Physical Society and Copyright Clearance Center.

License Number	3943671121268
License date	Sep 07, 2016
Licensed Content Publisher	American Physical Society
Licensed Content Publication	Physical Review B
Licensed Content Title	Mechanism of the strong magnetic refrigerant performance of ${\mathrm{LaFe}}_{13\ensuremath{-}x}{\mathrm{Si}}_{x}$
Licensed Content Author	Michael D. Kuz'min and Manuel Richter
Licensed Content Date	Sep 5, 2007
Licensed Content Volume Number	76
Type of Use	Thesis/Dissertation
Requestor type	Student
Format	Print, Electronic
Portion	chart/graph/table/figure
Number of charts/graphs/tables/figures	1
Portion description	Figure 1
Rights for	Main product
Duration of use	Life of Current Edition
Creation of copies for the disabled	no
With minor editing privileges	no
For distribution to	Worldwide
In the following language(s)	Original language of publication
With incidental promotional use	no
The lifetime unit quantity of new product	0 to 499
The requesting person/organization is:	Edmund Lovell
Order reference number	
Title of your thesis / dissertation	Magnetocaloric properties of La(FeSi)13 compounds
Expected completion date	Sep 2016
Expected size (number of pages)	200
Requestor Location	Edmund Lovell H702, Blackett Laboratory Imperial College South Kensington London, SW7 2AZ

Reply all | Delete Junk | ...

Re: Permission to use figure in Ph.D. thesis

MK

Michael Kuzmin <mdkuzmin@gmail.com>

Fri 09/09/2016 10:23

To: Lovell, Edmund

Reply all

Inbox

Dear Edmund,

you have my permission to reproduce Figure 1 of our paper "Mechanism of the strong
magnetic refrigerant performance of LaFe13-xSix", Phys. Rev. B 76, 092401 (2007),
in your PhD thesis.

Good luck with it.

Michael Kuzmin

On Fri, Sep 9, 2016 at 11:16 AM, Lovell, Edmund <e.lovell12@imperial.ac.uk> wrote:
> Dear Prof Michael Kuz'min,
>
>
> I am completing my PhD thesis at Imperial College London, UK (working with
> Lesley), entitled 'Magnetocaloric properties of La(FeSi)13 compounds'. I
> seek your permission to reprint, in my thesis, one of your figures:
>
> In the paper: M. D. Kuz'min, M. Richter, Mechanism of the strong magnetic
> refrigerant performance of LaFe13-xSix, Phys. Rev. B 76, 092401 (2007)
>
> The figure to be reproduced is Figure 1
>
> I have already been given copyright permission from American Physical
> Society, but part of their terms and conditions states that I must get
> permission from the authors, hence my email to you.
>
> If you could respond as soon as you are able I would be very grateful.
>
> Best wishes,
> Edmund Lovell
>
>

Re: Permission to reproduce figures for PhD thesis

Kathryn Shaw <Kathryn.Shaw@iop.org> on behalf of Permissions <permissions@iop.org>

Thu 08/09/2016 12:33

To: Lovell, Edmund <e.lovell12@imperial.ac.uk>;

1 attachments (24 KB)

IOP Permission Requests.docx;

Dear Edmund Lovell,

Thank you for your request to reproduce IOP Publishing material in your thesis.

Regarding:

Figure 1b (Fangwei Wang et al 2003 J. Phys.: Condens. Matter 15 5269)

Figure 2 (K Morrison et al 2010 J. Phys. D: Appl. Phys. 43 132001)

Figure 2b (N T Trung et al 2010 J. Phys. D: Appl. Phys. 43 015002)

We are happy to grant permission for the use you request on the terms set out below.

Conditions

Non-exclusive, non-transferrable, revocable, worldwide, permission to use the material in print and electronic form will be granted **subject to the following conditions:**

· Permission will be cancelled without notice if you fail to fulfil any of the conditions of this letter.

· You will make reasonable efforts to contact the author(s) to seek consent for your intended use. Contacting one author acting expressly as authorised agent for their co-authors is acceptable.

· You will reproduce the following prominently alongside the material:

o the source of the material, including author, article title, title of journal, volume number, issue number (if relevant), page range (or first page if this is the only information available) and date of first publication. This information can be contained in a footnote or reference note; or

o a link back to the article (via DOI); and

o if practical and IN ALL CASES for works published under any of the Creative Commons licences the words "© IOP Publishing. Reproduced with permission. All rights reserved""

· The material will not, without the express permission of the author(s), be used in any way which, in the opinion of IOP Publishing, could distort or alter the author(s)' original intention(s) and meaning, be prejudicial to the honour or reputation of the author(s) and/or imply endorsement by the author(s) and/or IOP Publishing.

· Payment of £0 is received in full by IOP Publishing prior to use.

This permission does not apply to any material/figure which is credited to another source in our publication or has been obtained from a third party. Express permission for such materials/figures must be obtained from the copyright owner.

If you have any questions, please feel free to contact our Permissions team at permissions@iop.org.

I should be grateful if you would acknowledge receipt of this email.

Permission to use figure in Ph.D. thesis

Lovell, Edmund

Fri 09/09/2016 14:08

To: jfzw2001@163.com <jfzw2001@163.com>;

Dear Dr Wang Fang

I am completing my PhD thesis at Imperial College London, UK, entitled 'Magnetocaloric properties of La(FeSi)13 compounds'. I seek your permission to reprint, in my thesis, one of your figures:

F. Wang, G. J. Wang, F. X. Hu, A. Kurbakov, B. G. Shen, Z. H. Cheng, 'Strong interplay between structure and magnetism in the giant magnetocaloric intermetallic compound LaFe11.4Si1.6: a neutron diffraction study', J. Phys.: Condens. Matter 15, 5269-5278 (2003).

The figure to be reproduced is: Figure 1(b).

I have already been given copyright permission from IOP Publishing, but part of their terms and conditions states that I must get permission from the authors, hence my email to you.

If you could respond as soon as you are able I would be very grateful.

Best wishes,
Edmund Lovell

Re: Permission to use figure in thesis

Kelly Morrison <K.Morrison@lboro.ac.uk>

Thu 08/09/2016 14:28

To: Lovell, Edmund <e.lovell12@imperial.ac.uk>;

Sure - of course.

Good luck!

From: Lovell, Edmund <e.lovell12@imperial.ac.uk>
Sent: 08 September 2016 14:24:39
To: Kelly Morrison
Subject: Permission to use figure in thesis

Hi Kelly

I'm just getting together permissions etc for my thesis. I'm planning to use one of your figures and have already been given copyright permission from IOP Publishing, but part of their terms and conditions states that I must get permission from the authors too, hence my email.

The figure is... Figure 2, in:

K. Morrison, J. Lyubina, J. D. Moore, A. D. Caplin, K. G. Sandeman, O. Gutfleisch, L. F. Cohen, 'Contributions to the entropy change in melt-spun LaFe11.6Si1.3', J. Phys. D: Appl. Phys. 43, 132001 (2010).

If you could respond as soon as you are able I would be very grateful. Getting to the end now, exciting!

Of course you could be mean and deny me permission for a laugh!

Best wishes,
Ed

Reply all | Delete Junk | ...

RE: Permission to use figure in Ph.D. thesis

ET

Ekkes Brück - TNW <E.H.Bruck@tudelft.nl>
Today, 10:08
Lovell, Edmund; 'Trung (thanh.trung.nguyen@philips.com)'

Reply all

Inbox

Action Items

Dear Edmund,
No problem,
Best regards
Ekkes

From: Lovell, Edmund [mailto:e.lovell12@imperial.ac.uk]
Sent: vrijdag 9 september 2016 11:00
To: Ekkes Brück - TNW
Subject: Permission to use figure in Ph.D. thesis

Dear Prof. Ekkes Brück

I am completing my PhD thesis at Imperial College London, UK (working with Lesley), entitled 'Magnetocaloric properties of La(FeSi)13 compounds'. I seek your permission to reprint, in my thesis, a figure from Nguyen Thanh Trung's following paper:

From N. T. Trung, J. C. P. Klaasse, O. Tegus, D. T. Cam Thanh, N. H. J. Bushow, E. Brück, 'Determination of adiabatic temperature change in MnFe(P,Ge) compounds with pulse-field method', J. Phys. D: Appl. Phys. 43, 015002 (2010).

The figure to be reproduced is Figure 2(b).

I have already been given copyright permission from IOP Publishing, but part of their terms and conditions states that I must get permission from the authors. I have tried to contact Nguyen but wasn't able to find a recent address so my email did not get through. Are you happy to give permission on the authors' behalf, or if not are you able to forward this message on?

If you could respond as soon as you are able I would be very grateful.

Best wishes,
Edmund Lovell

AIP PUBLISHING LLC LICENSE
TERMS AND CONDITIONS

Sep 07, 2016

This Agreement between Edmund Lovell ("You") and AIP Publishing LLC ("AIP Publishing LLC") consists of your license details and the terms and conditions provided by AIP Publishing LLC and Copyright Clearance Center.

License Number	3943641154384
License date	Sep 07, 2016
Licensed Content Publisher	AIP Publishing LLC
Licensed Content Publication	Journal of Applied Physics
Licensed Content Title	Specific heat and entropy change at the first order phase transition of La(Fe-Mn-Si)13-H compounds
Licensed Content Author	Vittorio Basso,Michaela Küpferling,Carmen Curcio, et al.
Licensed Content Date	Aug 4, 2015
Licensed Content Volume Number	118
Licensed Content Issue Number	5
Type of Use	Thesis/Dissertation
Requestor type	Student
Format	Print and electronic
Portion	Figure/Table
Number of figures/tables	1
Title of your thesis / dissertation	Magnetocaloric properties of La(FeSi)13 compounds
Expected completion date	Sep 2016
Estimated size (number of pages)	200
Requestor Location	Edmund Lovell H702, Blackett Laboratory Imperial College South Kensington London, SW7 2AZ United Kingdom Attn: Edmund Lovell
Billing Type	Invoice
Billing Address	Edmund Lovell H702, Blackett Laboratory Imperial College South Kensington London, United Kingdom SW7 2AZ Attn: Edmund Lovell
Total	0.00 GBP

Terms and Conditions

AIP Publishing LLC -- Terms and Conditions: Permissions Uses

AIP Publishing hereby grants to you the non-exclusive right and license to use and/or distribute the Material according to the use specified in your order, on a one-time basis, for the specified term, with a maximum distribution equal to the number that you have ordered. Any links or other content accompanying the Material are not the subject of this license.

AIP PUBLISHING LLC LICENSE TERMS AND CONDITIONS

Sep 07, 2016

This Agreement between Edmund Lovell ("You") and AIP Publishing LLC ("AIP Publishing LLC") consists of your license details and the terms and conditions provided by AIP Publishing LLC and Copyright Clearance Center.

License Number	3943680398818
License date	Sep 07, 2016
Licensed Content Publisher	AIP Publishing LLC
Licensed Content Publication	Applied Physics Letters
Licensed Content Title	Shape-anisotropic heterogeneous nucleation and magnetic Gibbs-Thomson effect in itinerant-electron metamagnetic transition of La(Fe0.88Si0.12)13 magnetocaloric compound
Licensed Content Author	A. Fujita,T. Kondo,M. Kano, et al.
Licensed Content Date	Jan 31, 2013
Licensed Content Volume Number	102
Licensed Content Issue Number	4
Type of Use	Thesis/Dissertation
Requestor type	Student
Format	Print and electronic
Portion	Figure/Table
Number of figures/tables	2
Title of your thesis / dissertation	Magnetocaloric properties of La(FeSi)13 compounds
Expected completion date	Sep 2016
Estimated size (number of pages)	200
Requestor Location	Edmund Lovell H702, Blackett Laboratory Imperial College South Kensington London, SW7 2AZ United Kingdom Attn: Edmund Lovell
Billing Type	Invoice
Billing Address	Edmund Lovell H702, Blackett Laboratory Imperial College South Kensington London, United Kingdom SW7 2AZ Attn: Edmund Lovell
Total	0.00 GBP

Terms and Conditions

AIP Publishing LLC -- Terms and Conditions: Permissions Uses

AIP Publishing hereby grants to you the non-exclusive right and license to use and/or distribute the Material according to the use specified in your order, on a one-time basis, for the specified term,

JOHN WILEY AND SONS LICENSE TERMS AND CONDITIONS

Sep 07, 2016

This Agreement between Edmund Lovell ("You") and John Wiley and Sons ("John Wiley and Sons") consists of your license details and the terms and conditions provided by John Wiley and Sons and Copyright Clearance Center.

License Number	3943671432398
License date	Sep 07, 2016
Licensed Content Publisher	John Wiley and Sons
Licensed Content Publication	Advanced Materials
Licensed Content Title	Novel Design of La(Fe,Si)13 Alloys Towards High Magnetic Refrigeration Performance
Licensed Content Author	Julia Lyubina,Rudolf Schäfer,Norbert Martin,Ludwig Schultz,Oliver Gutfleisch
Licensed Content Date	Aug 20, 2010
Licensed Content Pages	5
Type of use	Dissertation/Thesis
Requestor type	University/Academic
Format	Print and electronic
Portion	Figure/table
Number of figures/tables	1
Original Wiley figure/table number(s)	Figure 1(a) inset
Will you be translating?	No
Title of your thesis / dissertation	Magnetocaloric properties of La(FeSi)13 compounds
Expected completion date	Sep 2016
Expected size (number of pages)	200
Requestor Location	Edmund Lovell H702, Blackett Laboratory Imperial College South Kensington London, SW7 2AZ United Kingdom Attn: Edmund Lovell
Publisher Tax ID	EU826007151
Billing Type	Invoice
Billing Address	Edmund Lovell H702, Blackett Laboratory Imperial College South Kensington London, United Kingdom SW7 2AZ Attn: Edmund Lovell
Total	0.00 GBP
Terms and Conditions	

TERMS AND CONDITIONS

AIP PUBLISHING LLC LICENSE
TERMS AND CONDITIONS

Sep 07, 2016

This Agreement between Edmund Lovell ("You") and AIP Publishing LLC ("AIP Publishing LLC") consists of your license details and the terms and conditions provided by AIP Publishing LLC and Copyright Clearance Center.

License Number	3943680742445
License date	Sep 07, 2016
Licensed Content Publisher	AIP Publishing LLC
Licensed Content Publication	Applied Physics Letters
Licensed Content Title	Reducing extrinsic hysteresis in first-order La(Fe,Co,Si)13 magnetocaloric systems
Licensed Content Author	J. D. Moore,K. Morrison,K. G. Sandeman, et al.
Licensed Content Date	Dec 23, 2009
Licensed Content Volume Number	95
Licensed Content Issue Number	25
Type of Use	Thesis/Dissertation
Requestor type	Student
Format	Print and electronic
Portion	Figure/Table
Number of figures/tables	2
Title of your thesis / dissertation	Magnetocaloric properties of La(FeSi)13 compounds
Expected completion date	Sep 2016
Estimated size (number of pages)	200
Requestor Location	Edmund Lovell H702, Blackett Laboratory Imperial College South Kensington London, SW7 2AZ United Kingdom Attn: Edmund Lovell
Billing Type	Invoice
Billing Address	Edmund Lovell H702, Blackett Laboratory Imperial College South Kensington London, United Kingdom SW7 2AZ Attn: Edmund Lovell
Total	0.00 GBP

Terms and Conditions

AIP Publishing LLC -- Terms and Conditions: Permissions Uses

AIP Publishing hereby grants to you the non-exclusive right and license to use and/or distribute the Material according to the use specified in your order, on a one-time basis, for the specified term, with a maximum distribution equal to the number that you have ordered. Any links or other content accompanying the Material are not the subject of this license.

JOHN WILEY AND SONS LICENSE TERMS AND CONDITIONS

Sep 07, 2016

This Agreement between Edmund Lovell ("You") and John Wiley and Sons ("John Wiley and Sons") consists of your license details and the terms and conditions provided by John Wiley and Sons and Copyright Clearance Center.

License Number	3943650006624
License date	Sep 07, 2016
Licensed Content Publisher	John Wiley and Sons
Licensed Content Publication	Advanced Energy Materials
Licensed Content Title	Materials Challenges for High Performance Magnetocaloric Refrigeration Devices
Licensed Content Author	Anders Smith,Christian R.H. Bahl,Rasmus Bjørk,Kurt Engelbrecht,Kaspar K. Nielsen,Nini Pryds
Licensed Content Date	Sep 11, 2012
Licensed Content Pages	31
Type of use	Dissertation/Thesis
Requestor type	University/Academic
Format	Print and electronic
Portion	Figure/table
Number of figures/tables	1
Original Wiley figure/table number(s)	Figure 4
Will you be translating?	No
Title of your thesis / dissertation	Magnetocaloric properties of La(FeSi)13 compounds
Expected completion date	Sep 2016
Expected size (number of pages)	200
Requestor Location	Edmund Lovell H702, Blackett Laboratory Imperial College South Kensington London, SW7 2AZ United Kingdom Attn: Edmund Lovell
Publisher Tax ID	EU826007151
Billing Type	Invoice
Billing Address	Edmund Lovell H702, Blackett Laboratory Imperial College South Kensington London, United Kingdom SW7 2AZ Attn: Edmund Lovell
Total	0.00 GBP
Terms and Conditions	

TERMS AND CONDITIONS

AIP PUBLISHING LLC LICENSE TERMS AND CONDITIONS

Sep 07, 2016

This Agreement between Edmund Lovell ("You") and AIP Publishing LLC ("AIP Publishing LLC") consists of your license details and the terms and conditions provided by AIP Publishing LLC and Copyright Clearance Center.

License Number	3943681423223
License date	Sep 07, 2016
Licensed Content Publisher	AIP Publishing LLC
Licensed Content Publication	Journal of Applied Physics
Licensed Content Title	Magnetocaloric materials with first-order phase transition: thermal and magnetic hysteresis in LaFe11.8Si1.2 and Ni2.21Mn0.77Ga1.02 (invited)
Licensed Content Author	K. P. Skokov,V. V. Khovaylo,K.-H. Müller, et al.
Licensed Content Date	Feb 10, 2012
Licensed Content Volume Number	111
Licensed Content Issue Number	7
Type of Use	Thesis/Dissertation
Requestor type	Student
Format	Print and electronic
Portion	Figure/Table
Number of figures/tables	2
Title of your thesis / dissertation	Magnetocaloric properties of La(FeSi)13 compounds
Expected completion date	Sep 2016
Estimated size (number of pages)	200
Requestor Location	Edmund Lovell H702, Blackett Laboratory Imperial College South Kensington London, SW7 2AZ United Kingdom Attn: Edmund Lovell
Billing Type	Invoice
Billing Address	Edmund Lovell H702, Blackett Laboratory Imperial College South Kensington London, United Kingdom SW7 2AZ Attn: Edmund Lovell
Total	0.00 GBP

Terms and Conditions

AIP Publishing LLC -- Terms and Conditions: Permissions Uses

AIP Publishing hereby grants to you the non-exclusive right and license to use and/or distribute the Material according to the use specified in your order, on a one-time basis, for the specified term,

9/7/2016 Rightslink® by Copyright Clearance Center

Copyright Clearance Center RightsLink® Home Account Info Help Live Chat

IEEE Requesting permission to reuse content from an IEEE publication

Title: Influence of Demagnetization Effect on the Kinetics of the Itinerant Electron Metamagnetic Transition in Magnetic Refrigerant ${\rm La}{({\rm Fe}_{0.88}{\rm Si}_{0.12})}_{13}$
Author: H. Yako
Publication: Magnetics, IEEE Transactions on
Publisher: IEEE
Date: 0 Oct. 2011
Copyright © 2011, IEEE

Logged in as:
Edmund Lovell
LOGOUT

Thesis / Dissertation Reuse

The IEEE does not require individuals working on a thesis to obtain a formal reuse license, however, you may print out this statement to be used as a permission grant:

Requirements to be followed when using any portion (e.g., figure, graph, table, or textual material) of an IEEE copyrighted paper in a thesis:

1) In the case of textual material (e.g., using short quotes or referring to the work within these papers) users must give full credit to the original source (author, paper, publication) followed by the IEEE copyright line © 2011 IEEE.
2) In the case of illustrations or tabular material, we require that the copyright line © [Year of original publication] IEEE appear prominently with each reprinted figure and/or table.
3) If a substantial portion of the original paper is to be used, and if you are not the senior author, also obtain the senior author's approval.

Requirements to be followed when using an entire IEEE copyrighted paper in a thesis:

1) The following IEEE copyright/ credit notice should be placed prominently in the references: © [year of original publication] IEEE. Reprinted, with permission, from [author names, paper title, IEEE publication title, and month/year of publication]
2) Only the accepted version of an IEEE copyrighted paper can be used when posting the paper or your thesis on-line.
3) In placing the thesis on the author's university website, please display the following message in a prominent place on the website: In reference to IEEE copyrighted material which is used with permission in this thesis, the IEEE does not endorse any of [university/educational entity's name goes here]'s products or services. Internal or personal use of this material is permitted. If interested in reprinting/republishing IEEE copyrighted material for advertising or promotional purposes or for creating new collective works for resale or redistribution, please go to http://www.ieee.org/publications_standards/publications/rights/rights_link.html to learn how to obtain a License from RightsLink.

If applicable, University Microfilms and/or ProQuest Library, or the Archives of Canada may supply single copies of the dissertation.

BACK CLOSE WINDOW

Copyright © 2016 Copyright Clearance Center, Inc. All Rights Reserved. Privacy statement. Terms and Conditions.
Comments? We would like to hear from you. E-mail us at customercare@copyright.com

https://s100.copyright.com/AppDispatchServlet#formTop 1/1